Electronic Thesis and Dissertation Repository

6-13-2013 12:00 AM

Microbially induced magnesium carbonation reactions as a strategy for carbon sequestration in ultramafic mine tailings

Jenine McCutcheon, *The University of Western Ontario*

Supervisor: Dr. Gordon Southam, *The University of Western Ontario*
A thesis submitted in partial fulfillment of the requirements for the Master of Science degree in Geology
© Jenine McCutcheon 2013

Follow this and additional works at: https://ir.lib.uwo.ca/etd

Part of the Biogeochemistry Commons

Recommended Citation

MICROBIALLY INDUCED MAGNESIUM CARBONATION REACTIONS AS A
STRATEGY FOR CARBON SEQUESTRATION IN ULTRAMAFIC MINE TAILINGS

Thesis format: Integrated Article

by

Jenine <u>McCutcheon</u>

Graduate Program in Earth Sciences

A thesis submitted in partial fulfillment
of the requirements for the degree of
Master of Science

The School of Graduate and Postdoctoral Studies
The University of Western Ontario
London, Ontario, Canada

© Jenine McCutcheon 2013

Abstract

The atmospheric carbon dioxide (CO_2) concentration has increased due to anthropogenic fossil fuel combustion, causing higher global temperatures and other negative environmental effects. CO_2 sequestration through carbonate mineralisation provides a stable, long term carbon sink. A natural hydromagnesite playa (Atlin, British Columbia, Canada) demonstrates the ability of phototrophic microorganisms to accelerate magnesium carbonate mineralisation. The site's biogeochemistry was modeled in a 10 m flow-through bioreactor carbonation experiment, allowing for hydromagnesite precipitation conditions to be refined. Ultramafic mine tailings are a target substrate for carbonation reactions due to their high magnesium content. A synthetic mine leach water, designed from the results of a chrysotile leaching experiment, was added to the bioreactor in a second carbonation experiment. This demonstrated the microorganisms' ability to precipitate hydromagnesite and magnesite using atmospheric CO_2. The achieved carbon storage rate of 65 t C/ha/year has the potential to offset net carbon emissions of mining operations.

Co-Authorship Statement

Chapter 2 constitutes the material included in a manuscript for submission to *Environmental Science and Technology*. The authors include J. McCutcheon, I.M. Power, A.L. Harrison, G.M. Dipple, and G. Southam. McCutcheon drafted the manuscript, prepared the figures, ran the carbonation experiment, preformed electron microscopy, and completed water and mineralogical analyses. Power contributed to the design of this study, as well as data analysis and interpretation. Harrison advised on determining the feedstock water chemistry, and determining mineral saturation indices. Power and Harrison contributed to fieldwork and revision of the manuscript. Dipple and Southam are the project leads, providing academic leadership for the research program. Southam advised on all aspects of this research and manuscript revisions.

Chapter 3 contains the material that will be submitted as a manuscript to an undetermined journal. The authors include J. McCutcheon, I.M. Power, A.L. Harrison, G.M. Dipple, and G. Southam. McCutcheon drafted the manuscript, prepared the figures, ran the carbonation experiment, preformed electron microscopy, and completed water analyses. Power contributed to the design of this study, completed mineral analyses, and advised on data analysis and interpretation. Harrison advised on determining mineral saturation indices. Dipple and Southam are the project leads, providing academic leadership for the research program. Southam advised on all aspects of this research and manuscript revisions.

Acknowledgments

I would like to take this opportunity to thank those who contributed to this thesis and supported me along the way. First and foremost, I would like to thank my supervisor, Gord Southam, for the tremendous support and guidance he has provided since taking me on as an undergraduate in my Honours thesis. From the first lecture of your class, during which you explained how to think like a bacterium, I was inspired by the enthusiastic and creative way in which you approach scientific questions. Thank you for encouraging me to pursue my athletic goals alongside my academic ones, and for always knowing just how much to let me struggle before helping me solve a problem. I am a better scientist, and person, as a result.

I would also like to thank all of the Southam lablings who have helped me through this project. Jer, when Gord asked you to "get me started" on my thesis, I'm sure you didn't realize this would entail becoming my personal TA and lab technique demonstrator extraordinaire for two solid years. Thank you for the patience with which you answered each and every one of my many questions, and making each day an adventure. To the other lablings (Chris, Andrea, Maija, Scampi, Alex, Liane, Kelly, Jess, and Nahed) it was a pleasure working alongside you. To my roommate Bry, thank you for your friendship and support over the past 3 years, and for taking on Graduate School with me.

The success of this project is largely due to collaboration with Dr. G.M. Dipple's laboratory at the University of British Columbia. I would like to thank Dr. Ian Power for his advice and input throughout the progression of this project. Your enthusiasm and expertise on this subject have made you an excellent mentor. Thank you for your help with X-ray diffraction and water chemistry. I would like to thank Anna Harrison, my UBC counterpart on this carbonation adventure, for all of the chemistry help she provided for the design of my project. I couldn't have asked for a better hole digging partner in the field.

I would also like to extend my gratitude to all of the laboratory technicians who assisted me with laboratory techniques and analyses, including: Tim Goldhawk and Todd Simpson (scanning electron microscopy); Monique Durr and Dr. Charlie Wu (water chemistry and X-ray fluorescence); Dr. Roberta Flemming (X-ray diffraction interpretation); and Stephen Wood (thin section preparation). I would like to give a special thank you to Monique for the

time she took to solve my many water chemistry mysteries. Thank you to Mag van Hal and the rest of the greenhouse staff for accommodating my project over the last two years. A special thanks to Dr. Elizabeth Webb for being my Advisory Committee member. I would also like to express my appreciation for everything the Earth Sciences administration staff has helped me with over the last several years.

I would like to thank my track coaches Sylvia Kontra and John Allan for everything they have done for me over the last six years. Sylvia: for your endless support and generosity in helping me pursue my goals on and off the track. John: for our many little chats when you knew I needed them most. To my throwing siblings: nothing will ever replace being greeted by your insanity at the end of each day.

Finally, to my family, thank you for all of your love, support, and patience. To my parents: thank you for instilling a curiosity and appreciation of the natural world in me at such a young age. I would like to extend a special thank you to my Dad for the construction of the bioreactor used in this project, without which this study would not have been possible.

Table of Contents

List of Tables

List of Figures

List of Appendices

List of Abbreviations

% parts per hundred

˚C Celsius

$\Delta G°_f$ Gibbs free energy of formation

µL microlitre

µm micrometre

µXRD micro X-ray diffraction

cf. compare or contrast with

CPD critical point drying

ddH_2O dionized distilled water

DIC dissolved inorganic carbon

DO dissolved oxygen

EDS energy dispersive x-ray spectroscopy

EPS extracellular polymeric substances

g grams

Ga Gigannum (billion years)

GADDS General area detection diffraction system

h hours

ha hectare

IC ion chromatography

ICP-AES inductively coupled plasma-atomic emission spectroscopy

kJ kilojoules

kV kilovolt

L litre

LOI loss on ignition

M moles per litre

mA milliampere

mg milligram

mL millilitre

mM millimoles per litre

mol moles

mS/cm millisiemens per centimetre

nm nanometre

pH $-\log[H^+]$

ppm parts per million

SEM scanning electron microscopy

SI saturation index

spp. species (plural)

XRF x-ray fluorescence

XRD x-ray diffractometer

Chapter 1

1   Introduction

Human activity has led to the concentration of carbon dioxide (CO_2) in Earth's atmosphere to increase by over 100 ppm since the start of the Industrial Revolution in 1750 (Figure 1.1) (IPCC 2007). This alteration of atmospheric chemistry has resulted in changes to Earth's climate, negatively impacting the environment in many ways. The changes include melting of the polar ice caps, increasing global air temperatures, decreased global snow pack and snow cover, and sea level rise (Figure 1.2) (IPCC 2007). The severity of these environmental concerns will continue to increase with human population and carbon emission growth, unless net anthropogenic CO_2 production is decreased through preventative or remediation strategies. Due to the carbon dependent nature of society and the limited use of alternative energy resources in comparison to carbon-based fuels, it is unlikely that efforts to decrease emissions will be sufficient to maintain an atmospheric CO_2 concentration that is sustainable through time and safe for the environment (Broecker 2007). As a result, CO_2 sequestration methods need to be improved in order to mitigate the damage human activity is causing to the planet.

1.1   Atmospheric Chemistry, greenhouse gases, and climate change

Although it is known that the composition of Earth's atmosphere has changed drastically since the planet's formation 4.6 Ga, there are large segments of geologic time for which the chemistry of the atmosphere is unclear (Cloud 1968; Kasting 1993; Ekart et al. 1999; Bekker et al. 2004; Canfield 1998; Pearson and Palmer 2000; Retallack 2001; Canfield 2005; Kump 2008; Shaw 2008; Falkowski and Isozaki 2008). In the Early Archean, Earth likely had an atmosphere composed of N_2, CO_2, and CH_4 based on geologic evidence and computer modelling (Kasting 1993). One of the most notable changes in atmospheric composition was the Great Oxidation Event (GOE), which occurred between 2.45 and 2.32 Ga (Bekker et al. 2004). This initial oxygenation started in the shallow ocean. Accumulation of any substantial atmospheric oxygen did not occur until the late Neoproterozoic (750-500 Ma) and the Carboniferous (360-200 Ma)
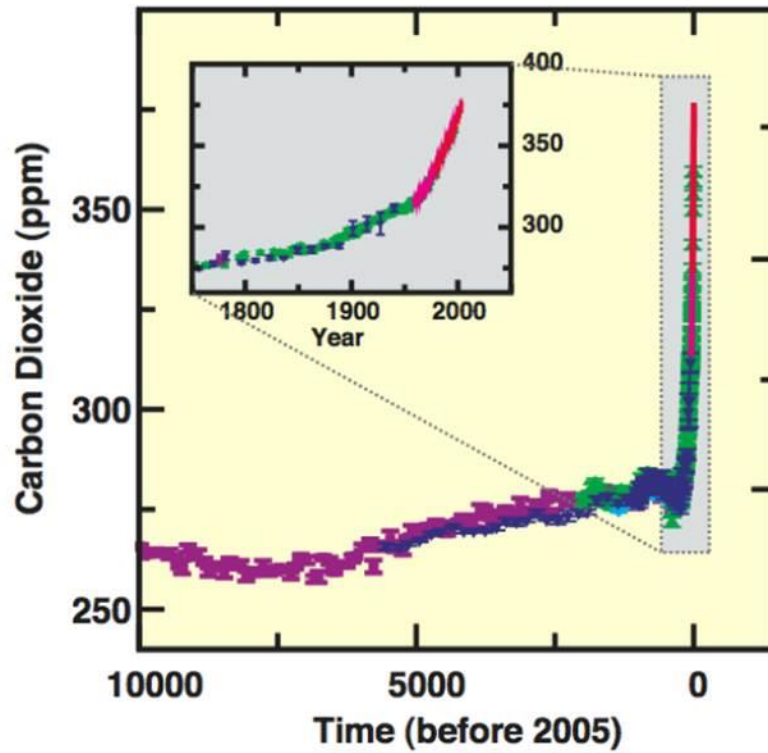
Figure 1.1 Ice core and atmospheric measurements of the concentration of carbon dioxide in the atmosphere for the past 10 000 years. Carbon dioxide levels since just prior to the start of the Industrial Revolution (1750) (inlay) (from IPCC 2007).
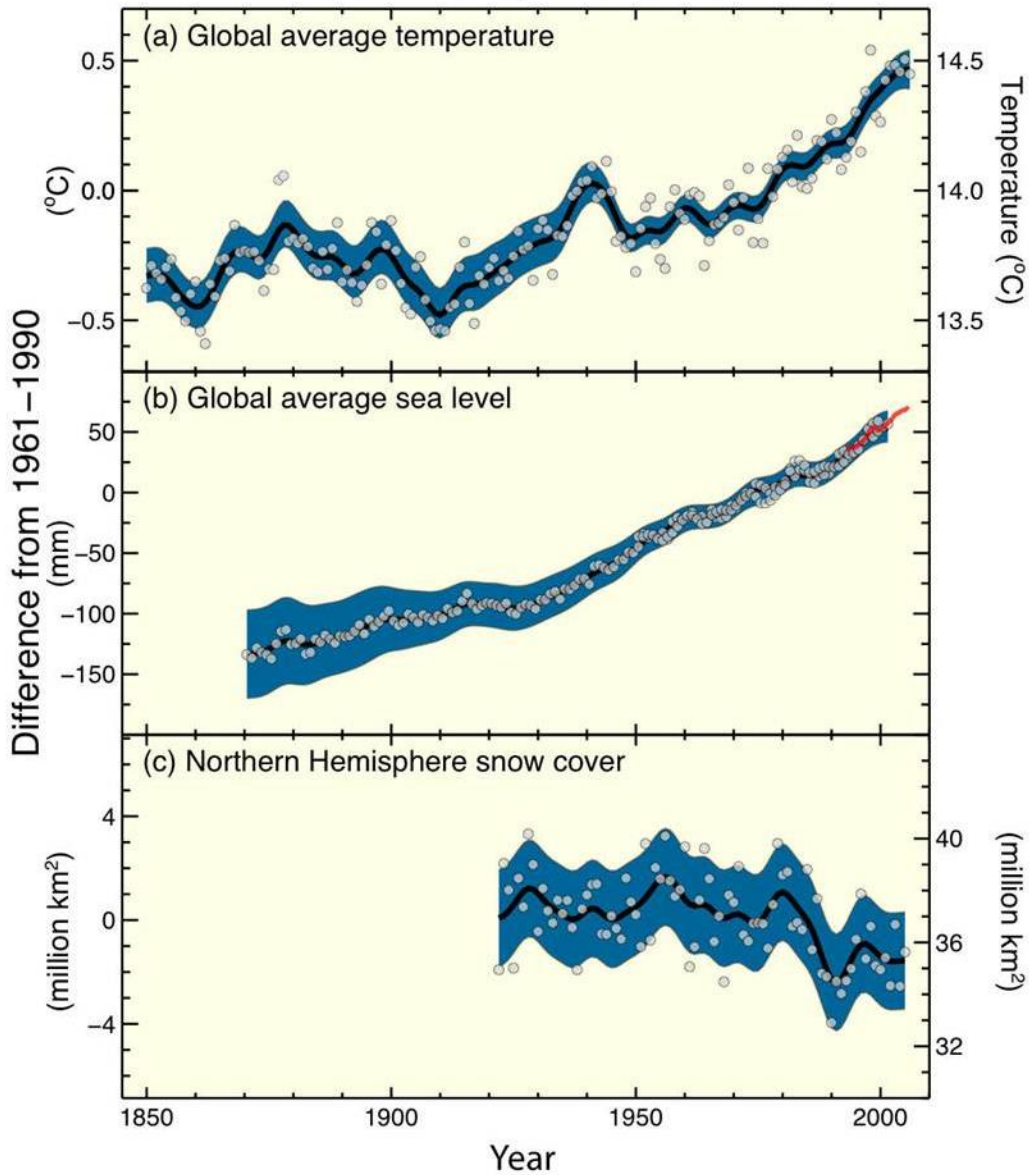
Figure 1.2 Changes to a) the global average surface air temperature since 1850, b) global average sea level since 1870, and c) the area of snow cover present in the Northern Hemisphere in March-April since 1920. The shaded areas indicate the uncertainty of these measurements (from IPCC 2007).

(Canfield 1998; Canfield 2005; Falkowski and Isozaki 2008). The proportion of the atmosphere made up by oxygen has varied between 10 and 30 % since the Carboniferous, fluctuating due to the balance between the generation of oxygen through primary productivity, and its consumption through oxygenation of organic carbon (Falkowski and Isozaki 2008). At 20.95%, oxygen is currently the second most abundant gas in Earth's atmosphere next to nitrogen (Ackerman and Knox 2007). Nitrogen (N_2), a stable gas with an atmospheric residence time of 1 Ga, currently constitutes 78.08% of the atmosphere (Berner 2006; Ackerman and Knox 2007). The following constituents make up the remaining atmosphere: argon (Ar) (0.93%), CO_2 (0.035%), and trace amounts of $H_2O_{(g)}$, hydrogen (H_2), neon (Ne), helium (He), methane (CH_4), krypton (Kr) and chlorofluorocarbons (CFCs) (Ackerman and Knox 2007).

The composition of the atmosphere plays an important role in governing Earth's climate (IPCC 2007; Shaw 2008; Lacis et al. 2010). The atmosphere is largely transparent to the shortwave radiation generated by the sun, allowing this energy to reach, and warm, the surface of the Earth. This warming, however, does not solely account for the habitable temperatures experienced on Earth's surface. Infrared radiation emitted by the Earth is absorbed by atmospheric gases, largely water vapour and CO_2, which can then be re-emitted in all directions including back down towards Earth's surface. This radiative process, known as the greenhouse effect, has been acknowledged for almost two centuries, and is important for keeping many of Earth's habitats above freezing by increasing surface temperatures by approximately 33°C (Ackerman and Knox 2007).

Greenhouse gases, those which absorb infrared radiation but not solar radiation, include H_2O, CO_2, CH_4, N_2O, CFCs, and ozone (O_3) (Ackerman and Knox 2007; IPCC 2007; Lacis et al. 2010). Water accounts for 75% of the total greenhouse effect in the form of vapour (50%) and clouds (25%) (Lacis et al. 2010). Water is highly mobile in the atmosphere, being able to evaporate, condense, and precipitate in response to changes in temperature and pressure. Carbon dioxide is responsible for 20% of the total greenhouse effect, with other minor greenhouse gases making up the final 5% (Lacis et al. 2010). By these data it would appear that water is the most critical greenhouse gas; however, CO_2 and the other minor greenhouse gases are the most important in terms of controlling global temperatures. This is due to their inability to condense under atmospheric conditions, which limits the ability of these gases to move and change in the

atmosphere. This key difference in comparison to water is evident in their atmospheric residence times. On average, any given water molecule remains in the atmosphere for only 10 days, while a molecule of CO_2 will remain in the atmosphere for 0.01 million years (Bolin and Rodhe 1973; Berner 2006). The addition of CO_2 to the atmosphere results in an increased greenhouse effect through greater infrared radiation absorption and re-radiation by the atmosphere (Lacis et al. 2010). Since these gases do not condense and precipitate from the atmosphere, they generate a constant, base level of warming. This warming causes air temperatures high enough for water vapour and clouds to exist in the atmosphere, which can then cause the remaining 75% of the total greenhouse effect. When the concentrations of CO_2 and other non-condensable greenhouse gases increase through human activity, the magnitude of the base level warming increases, generating a radiatively forced increase in the amount of warming caused by water. The important role CO_2 plays in Earth's climate can be seen in models in which CO_2 and other non-condensing greenhouse gases are removed from the atmosphere (Lacis et al. 2010). In a 50 year timeframe of a CO_2-free atmosphere, Earth's surface temperatures would decrease by 34.8°C to a global average of -21°C. The amount of sea ice would increase by ten times, causing an increase in Earth's albedo from 29% to 41.8% (Lacis et al. 2010).

Studies such as that of Lacis et al. (2010) demonstrate the importance of CO_2 to Earth's climate, making it critical to understand how human activity is contributing to the presence of this gas in the atmosphere. Carbon dioxide in the atmosphere has increased from a Pre-Industrial (1750) concentration of 280 ppm to 390 ppm (IPCC 2007; Lacis 2010). This increased value is well outside the range of 180-300 ppm documented in ice cores from the last 650 000 years, and well above the 280 ppm concentration which is common for an interglacial maximum such as the one currently taking place (Lacis et al. 2010). The rate of increase of atmospheric CO_2 is greater than any other time known in geologic history (Archer et al. 2009; Lacis et al. 2010). Fossil fuel burning is the primary source of this CO_2; with cement production and land use change by deforestation, urbanization, and agricultural activity also playing a role (IPCC 2007; Le Quéré et al. 2009). Despite the fact that CO_2 has been in the atmosphere through most of Earth's history, no past natural events are known to have caused a concentration increase similar to the anthropogenic one currently taking place. For example, the estimates of annual volcanic CO_2 emissions of 0.13-0.44 Gt are well exceeded by the estimates of annual anthropogenic CO_2 production of 35 Gt (Friedlingstein et al. 2010; Gerlach 2011).

Understanding the role that CO_2 plays in Earth's climate is also critical for selecting a target concentration for atmospheric CO_2 in order to mitigate the climate change currently taking place. Suggested targets range from 200-500 ppm over the next few centuries (Harvey 2007; Hansen et al. 2008). The current value of 390 ppm exceeds the threshold value of 350 ppm which is thought to be the critical point above which the environment may not be able to recover to its Pre-Industrial Revolution state. These targets are based on climate models which attempt to predict how the atmosphere, ocean, and biosphere will react to increasing atmospheric CO_2 and the resulting environmental effects. The uncertainty in these simulations is largely due to the complexity of Earth as a system, and the number of feedback loops involved. For example, global warming is causing a decrease in snow pack and sea ice (IPCC 2007). This results in a decrease in Earth's albedo, resulting in further warmer and more melting. The oceans are absorbing 80% of the warming effect caused by climate change, resulting in sea level rise due to expansion of the water (IPCC 2007). The addition of freshwater to the ocean through ice melting, particularly around Greenland, is altering ocean circulation patterns which is influencing precipitation patterns around the world (Stammer 2008).

The severity of these and other effects are all dependent on the quantity of CO_2 produced and the rate at which it enters the atmosphere (Archer and Brovkin 2008; Archer et al. 2009). Equilibration of the atmosphere with the ocean will likely take between two and twenty centuries, and will delay a portion of the resulting warming effects (Archer et al. 2009). Invasion of CO_2 to the oceans will cause a drop in pH, resulting in large-scale dissolution of marine calcium carbonate deposits and drastic marine ecosystem change (Broecker and Takahashi 1978; Archer et al. 1998; Archer et al. 2009). This disruption in oceanic chemistry will take thousands of years to neutralise. After the oceans have consumed the maximum amount of CO_2 possible, 20-60% of total anthropogenic CO_2 emissions will remain in the atmosphere (Archer and Brovkin 2008; Archer et al. 2009). This fraction will take several thousand years to be absorbed by the lithosphere through chemical weathering of silicate minerals (Berner et al 1983; Berner and Kothavala 2001; Walker et al. 1981). Another factor adding to the complexity of the problem is the increasingly important role that non-CO_2 greenhouse gases, such as methane, will play in climate change (Harvey 2007; Montzka et al. 2011).

1.2 Carbon cycling and sequestration

With the increasing concentration of atmospheric CO_2, it is important to understand how carbon is exchanged among components of Earth as a system. The movement of carbon between air, water, soil, biomass, and rock involves a complex set of pathways which occur over a large range of timescales. Transport of carbon between air, water, soil, and biomass takes place relatively quickly, and is collectively known as the short term carbon cycle (Houghton 2007). This cycle involves photosynthesis, respiration, decomposition, and the exchange of CO_2 between the atmosphere and ocean surface water. In contrast, cycling of carbon between short-term sinks and geologic reservoirs takes millions of years. This is known as the long term carbon cycle and consists of volcanism, subduction, weathering, and carbon storage in deep sea sediments and carbonaceous rocks (Jones and Cox 2001; Berner 2003). The long term carbon cycle is responsible for the formation of fossil fuel deposits and is the dominant factor controlling atmospheric CO_2 concentrations over geologic time scales (Lacis et al. 2010).

Due to the amount of CO_2 being produced by human activity and the long residence time of CO_2 in the atmosphere, steps need to be made to mitigate this environmental problem. Approximately half of all anthropogenic CO_2 emissions are sequestered naturally by the oceans, biosphere, and lithosphere, with the rest remaining in the atmosphere (Cox et al. 2000; Le Quéré et al. 2009). However, the amount of natural sequestration is decreasing, indicating a limit to Earth's ability to buffer anthropogenic CO_2 emissions. Reduction of anthropogenic CO_2 production is the ideal solution; however, the magnitude of current global emissions makes it unrealistic that prevention alone will be sufficient. This has resulted in extensive research investigating a range of strategies for storing anthropogenic carbon.

Carbon capture and storage (CCS) involves collecting, concentrating, transporting, and storing CO_2 as a method to reduce net emissions from fossil fuel burning (Holloway 2005; IPCC 2005; Plasynski et al. 2009). Emissions produced through power generation and industrial processes are the main target for CCS because of the magnitude of CO_2 produced from single sources, unlike emissions generated in the transportation sector. Carbon dioxide capture requires power plants to have technology for trapping and purifying CO_2, which is expensive to develop and lowers overall plant efficiency due to the additional energy needed to operate the CO_2 capture process. The cost of capturing the CO_2 accounts for 75% of the total financial cost of CCS

(Plasynski et al. 2009). Once CO_2 is captured, purified, and compressed, it needs to be transported to a suitable reservoir for storage (IPCC 2005). The distance between the CO_2 source and the reservoir can determine whether a particular CO_2 source is a suitable target for CCS, due to the cost of building the pipeline for transportation. Possible storage locations include depleted oil and gas reservoirs, deep saline aquifers, and coal beds that are not economical for mining (IPCC 2005; Bachu 2007; Plasynski et al. 2009). Carbon dioxide is injected into porous sedimentary rocks after the oil and gas they contain has been removed, a practice sometimes implemented to enhance hydrocarbon recovery. Once injected, the CO_2 exists as a liquid and is less dense than water, causing it to rise to the top of the reservoir. This makes it critical for the reservoir, usually located at a depth of at least 800 m below the surface, to be sealed by an impermeable layer of rock called the cap rock (IPCC 2005). Even with little regional seismic activity and a good cap rock such as shale or clay, there is potential for leaks through lateral movement of the injected CO_2. Over time, the CO_2 will dissolve in the rock formation water, causing it to sink to the bottom of the reservoir; where, over millions of years, it will precipitate as carbonate minerals. Carbon dioxide injection sites need to be carefully selected and monitored for the presence of leaks, which can pose hazards to people, ecosystems, and groundwater sources (IPCC 2005).

The deep ocean is another reservoir being investigated for CO_2 storage (IPCC 2005). Due to the recent increase of atmospheric CO_2, there is already a net flux of carbon from the atmosphere to the ocean of approximately 0.6-2 Gt/year (Takahashi et al. 1997; Houghton 2007). The equilibration between the atmosphere and the ocean has resulted in the oceans taking in 140 Gt of anthropogenic carbon over the past 200 years, causing a 0.1 pH drop in the surface of the oceans (IPCC 2005). Injection of CO_2 on a scale that would make any impact on atmospheric CO_2 levels would result in a pH decrease immediately surrounding the injection site, which over time would circulate throughout the entire ocean. This is concerning due to the environmental effects already seen as a result of the slight acidification occurring in the shallow ocean today. On the scale of months, reduced calcification, growth, and reproduction of shelly marine organisms has been observed, demonstrating the risk involved in using the oceans as a storage site for anthropogenic CO_2 (IPCC 2005).

Biological storage of carbon is another method being considered. Vegetation annually removes 1 Gt of carbon from the atmosphere, a value which could be increased through reforestation and soil restoration strategies (Plasynski et al 2009). Soil degradation caused by commercial agriculture has resulted in many soils containing less organic carbon than undisturbed soils (Lah 2003; Lah 2004; Plasynski et al. 2009). There is potential for terrestrial vegetation and depleted soils to act as a sink for 30-60 billion tonnes of carbon. Unfortunately, the residence time of carbon in soil and vegetation is short due to continuous exchange of CO_2 with the atmosphere. In contrast, carbonate minerals are the most stable, long term form of carbon storage. On the scale of 1 Ma, almost all anthropogenic carbon emissions will become stored in carbonate minerals (Kump et al. 2000). As a result, carbonate mineralisation as a method of carbon sequestration is worth further investigation.

1.3   **Silicate weathering and carbonate mineralisation**

Volcanic and plutonic igneous processes generate a wide range of silicate rock formations, constituting 42.5% of continental outcrops (Suchet et al. 2003). These rocks weather by reacting with carbonic acid found in soil, rain, and groundwater (Berner 1992). Carbonic acid naturally forms by the dissolution of CO_2 in water, releasing protons which react with silicate minerals. The rate of chemical weathering through this process is partially dependent on mineral chemistry and structure (Goldich, 1938). Mafic rocks such as basalt and peridotite react with CO_2 faster than their felsic counterparts, with basalt accounting for as much as 35% of CO_2 consumed through silicate weathering (Dessert et al. 2003; Kelemen and Matter 2008; Kelemen et al. 2011). In addition to surface weathering, low temperature hydrothermal alteration (0-60$^{\mathrm{o}}$C) of basalt plays an important role in ocean floor absorption of CO_2 (Alt and Teagle 1999). This transfer of carbon to the lithosphere is important during ocean crust subduction and carbon transfer to the mantle.

On the scale of geologic time, silicate weathering regulates the concentration of atmospheric CO_2 and has absorbed a total of 90 million Gt of carbon (Sundquist 1993; Lackner 2002). Of the silicate minerals that weather to produce carbonates, olivine and serpentine are favourable because these reactions are exothermic (Equations 1 and 2) (Alexander et al. 2007).

$$Mg_2SiO_4 + 2\ CO_2 \rightarrow 2\ MgCO_3 + 2\ SiO_2 \qquad\qquad \Delta G°_f = \text{-64 kJ/mol} \quad (1)$$

$$Mg_3Si_2O_5(OH)_4 + 3\ CO_2 \rightarrow MgCO_3 + 2\ SiO_2 + 2\ H_2O \qquad \Delta G°_f = \text{-67 kJ/mol} \quad (2)$$

The primary concern for using mineral carbonation as a method of carbon sequestration is that it naturally occurs at a rate that is too low to have an influence on anthropogenic CO_2 emissions. As a result, strategies for accelerating this chemical process have been investigated. These primarily consist of increasing the surface area of the minerals being reacted and subjecting them to high temperatures and pressures in the presence of concentrated CO_2 (Kelemen and Matter 2008; Zevenhoven et al. 2008; Fagerlund et al. 2009; Koukouzas et al. 2009; Lammers et al. 2011; Kelemen et al. 2011). These methods of sequestering CO_2 in carbonates are currently not practical for large-scale use due to the financial and energy resources required for applying the heat and pressure treatments.

While industrial carbonate mineralisation is expensive, passive carbonate reactions have potential because they require less financial and energy input. Mine tailing storage sites are a target for passive carbonation because they often consist of ultramafic waste rock, especially in the cases of diamond, nickel, asbestos, and chromium mining (Wilson et al. 2009a; Wilson et al. 2009b; Wilson et al. 2010; Wilson et al. 2011; Pronost et al. 2012). An advantage of using mine tailings is that the rock has already been milled during the mining process, exposing greater amounts of reactive mineral surfaces than what would occur in the rock prior to processing. Passive carbonate mineral formation has been documented in milled chrysotile waste rock piles at Clinton Creek Asbestos Mine (Yukon, Canada), Cassiar (British Columbia, Canada),and Black Lake Mine (Québec, Canada); processed kimberlite at the Diavik Diamond Mine (Northwest Territories, Canada); and Mount Keith Nickel Mine (Western Australia). The carbonate minerals found at these sites consist primarily of hydrated magnesium carbonates. Targeting mine sites for carbonation is advantageous because of the infrastructure already present due to the primary mining activity. As environmental protocols in the mining sector become stricter, it will benefit these operations to have a carbon storage strategy in use. This passive carbonation has potential for greater carbonate mineralisation rates if the geochemical conditions needed for mineral formation are encouraged.

One method of increasing carbonate formation rates is to inject CO_2 into the tailings piles (Harrison et al. 2013). This increases the acidity of the system, resulting in an increase in both the tailings' weathering rate and the availability of cations for carbonate mineral precipitation. The more critical result of CO_2 injection is the increased availability of CO_2, which is the rate limiting factor in carbonate formation (Vermilyea 1969; Pokrovsky and Schott 2000; Pokrovsky and Schott 2004; Wilson et al. 2010; Harrison et al. 2013). The concentration of CO_2 in the injection gas, the humidity of the gas, and the temperature influence the carbonation rate (Provost et al. 2011). Like CCS, the need for transporting concentrated CO_2 to the tailings facility and successfully injecting it into the tailings pile is a challenge. As with any method of carbon storage involving concentrated CO_2, the concern of large scale CO_2 leaks would have to be addressed.

1.4   **Microbial carbonate mineralisation**

The role of microorganisms in carbonate mineral precipitation has been known for a century (Drew 1913). Over geologic time, the rock record exhibits evidence of microbially mediated carbonation, the oldest of which are Precambrian stromatolites preserved in limestone and dolostone (Riding 2000; Aloisi 2008). It is unclear if microbes were involved in the formation of the first stromatolites (3.45 Ga and earlier), but Late Archean (2.8-1.0 Ga) specimens display a range of cellular morphologies providing evidence of significant microbial activity (Thompson and Ferris 1990; Aloisi 2008). Of the carbonation reactions in which microbes are involved, calcium carbonate mineralisation reactions are the most studied. These processes, taking place in the oceans, lakes, soils, caves, and groundwater, are primarily enabled by phototrophic microbes such as the cyanobacteria *Synechococcus* and *Triodesmium* which alter the water chemistry and induce carbonate precipitation (Thompson and Ferris 1990; Riding 2000; Kranz et al. 2010). Cyanobacteria are a phylum of diverse gram-negative phototrophic Bacteria (Rippka et al. 1979). These organisms evolved in the Precambrian and are responsible for the formation of Archean, Proterozoic, and modern stromatolites (Canfield 2005; Altermann et al. 2006). Horizontal gene transfer has resulted in modern cyanobacteria having a combination of photosystem 1 and photosystem 2, acquired from green sulfur bacteria and purple sulfur bacteria, respectively (Nisbet and Fowler 1999). They contain the pigments chlorophyll-*a*, phycobilin, and phycocyanin; the latter of which is responsible for the blue-green colour common to these

organisms (Stanier and Cohen-Bazire 1977). Although some cyanobacteria use H_2S for anoxygenic photosynthesis, most cyanobacteria use oxygenic photosynthesis (Equation 3) (Cohen et al. 1975).

$$6 \, CO_2 + 6 \, H_2O \rightarrow C_6H_{12}O_6 + 6 \, O_2 \qquad\qquad (3)$$
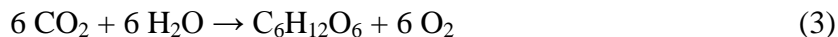
The cells of cyanobacteria can be filamentous or coccoid in morphology, and can exist as individuals or in colonies (Komárek et al. 2003). They live in a wide range of habitats including lakes, oceans, soils, and porous rocks. When cyanobacteria form benthic communities with other microbes in aquatic environments, they can form microbial mats (Stal et al. 1985). These form as a semi-consolidated mass of stratified microorganisms which organize themselves within the mat based on metabolism. Microenvironments within the mat allow for both aerobic and anaerobic organisms to live within the mat a short distance from each other (Nisbet and Fowler 1999). Microbial mats often contain trapped sediment or precipitated minerals which help to consolidate the structure. The laminated nature of these microbe-sediment structures makes them good analogues for Precambrian stromatolites (Canfield 2005; Altermann et al. 2006).

In contrast to calcium carbonate, microbially induced dolomite $[CaMg(CO_3)_2]$ precipitation occurs in anoxic environments and is mediated by the metabolic activity of iron-reducing, sulfate-reducing, and methanogenic bacteria (van Lith et al. 2003; Roberts et al. 2004; Kenward et al. 2009). The cell walls and extracellular polysaccharides of these microbes appear to act as nucleation sites for dolomite precipitation, as mineral formation does not occur under the same geochemical conditions in the absence of cells.

Magnesium carbonate precipitation occurs in association with cyanobacteria and diatoms in alkaline aquatic environments (Renaut 1993; Braithwaite and Zedef 1994; López-García et al. 2005; Power et al. 2007). This process, which occurs in association with cyanobacteria, is strongly controlled by pH and alkalinity, but is incompletely understood in terms of the biogeochemical conditions required for magnesium carbonate formation (Thompson and Ferris 1990; Shiraishi 2012). Since magnesium is one of the main cations produced through the weathering of ultramafic mine tailings, understanding the conditions needed for optimal precipitation of magnesium carbonate minerals from mine tailings leachate is worth further investigation.

1.5   Study objectives

This study focuses on the biogeochemical conditions required for magnesium carbonate mineral precipitation from solution. Two experiments were conducted using a greenhouse-scale model wetland that represented the conditions that would be present in a mine tailings carbonation pond. The wetland was designed to allow for both temporal and spatial examination of magnesium carbonate precipitation. The microbial mats used to inoculate the system were collected from a wetland near Atlin, British Columbia, Canada, that is known for natural magnesium carbonate mineral precipitation (Power et al. 2007).

In Chapter 2, the biogeochemical conditions found in the Atlin wetland were recreated in the model system. A magnesium- and bicarbonate-rich solution was added to the system over the course of a 7 week carbonation experiment. Analysis of the water chemistry, mineralogy, and microbiology of the bioreactor allowed for mineralisation and carbon storage rates to be deduced. These results aid in constraining the conditions necessary for magnesium carbonate precipitation.

In Chapter 3, chrysotile collected from waste rock in an abandoned open pit mine at Clinton Creek, Yukon, Canada were used in a leaching trial. The fibres were allowed to react with six different concentrations of sulfuric acid for 6 weeks, during which the pH of all the reactions was monitored. Chemical and structural changes in the chrysotile fibres were determined. These results, combined with aqueous chemistry data, allowed for an understanding of the transfer of magnesium from solid form to solution. This information about the release of magnesium from tailings is important for understanding its availability for carbonation reactions, and was used in a carbonation experiment similar to the one in Chapter 2. With the leaching chemistry as a guideline, a feedstock solution was added to the model wetland. This experiment modeled magnesium carbonate mineralisation as it would occur at a mine tailings storage facility. The information gathered in this study provides insight for the use of magnesium carbonate mineralisation as a strategy for mining operations to reduce their net greenhouse gas emissions.

1.6   References

Ackerman, S.A. and Knox, J. A. 2007. Meterology: Understanding the atmosphere 2nd Edition. Thomson Brooks/Cole, Belmont, pp 467.

Alexander, G., Maroto-Valer, M.M., and Gafarova-Aksoy, P. 2007. Evaluation of reaction variables in the dissolution of serpentine for mineral carbonation. Fuel, **86**: 273-281.

Aloisi, G. 2008. The calcium carbonate saturation state in cyanobacterial mats throughout Earth's history. Geochimica et Cosmochimica Acta, **72**: 6037-6060.

Alt, J.C. and Teagle, D.A.H. 1999. The uptake of carbon during alteration of oceanic crust. Geochimica et Cosmochimica Acta, **63**: 1527-1535.

Altermann, W., Kazmierczak, J., Oren, A., and Wright, D.T. 2006. Cyanobacterial calcification and its rock-building potential during 3.5 billion years of Earth history. Geobiology, **4**: 147-166.

Archer, D. and Brovkin, V. 2008. The millennial atmospheric lifetime of anthropogenic CO_2. Climate Change, **90**: 283-297.

Archer, D., Kheshgi, H., and Maier-Reimer, E. 1998. Dynamics of fossil fuel CO2 neutralization by marine CaCO3. Global Biogeochemical Cycles, **12**: 259-276.

Archer, D., Eby, M., Brovkin, V., Ridgwell, A., Cao, L., Mikolajewicz, U., Caldeira, K., Matsumoto, K., Munhoven, G., Montenegro, A., and Tokos, K. 2009. Atmospheric lifetime of fossil fuel carbon dioxide. Annual Review of Earth and Planetary Sciences, **37**: 117-134.

Bachu, S. 2007. Carbon dioxide storage capacity in uneconomic coal beds in Alberta, Canada: Methodology, potential and site identification. International Journal of Greenhouse Gas Control, **1**: 374-385.

Bekker, A., Holland, H.D., Wang, P.L., Rumble, D., Stein, H.J., Hannah, J.L., Coetzee, L.L., and Beukes, N.J. 2004. Dating the rise of atmospheric oxygen. Nature, **427**: 117-120.

Berner, R.A. 1992. Weathering, plants, and the long-term carbon cycle. Geochimica et Cosmochimica Acta, **56**: 3225-3231.

Berner, R.A. 2003. The long-term carbon cycle, fossil fuels and atmospheric composition. Nature, **426**: 323-326.

Berner, R.A. 2006. Geological nitrogen cycling and atmospheric N_2 over Phanerozoic time. Geology, **34**: 413-415.

Berner, R.A. and Kothavala, Z. 2001. GEOCARB III: a revised model of atmospheric CO2 over Phanerozoic time. American Journal of Science, **301**: 182-204.

Berner, B.A., Lasaga A.C., and Garrels R.M. 1983. The carbonate-silicate geochemical cycle and its effect on atmospheric carbon dioxide over the past 100 million years. American Journal of Science, **283**: 641-683.

Bolin, B. and Rodhe, H. 1973. A note on the concepts of age distribution and transit time in natural reservoirs. Tellus, **25**: 58-62.

Braithwaite, C.J.R. and Zedef, V. 1994. Living hydromagnesite stromatolites from Turkey. Sedimentary Geology, **92**: 1-5.

Broecker, W.S. 2007. CO_2 arithmetic. Science, **315**: 1371.

Broecker, W.S. and Takahashi, T. 1978. Neutralization of fossil fuel CO_2 by marine calcium carbonate. In: Andersen, N.R. and Malahoff, A. (eds). The fate of fossil fuel CO_2 in the oceans. Plenum, New York, pp. 213-248.

Canfield, D.E. 1998. A new model for Proterozoic ocean chemistry. Nature, **396**: 450-453.

Canfield, D.E. 2005. The early history of atmospheric oxygen: Homage to Robert A. Garrels. Annual Review of Earth and Planetary Sciences, **33**: 1-36.

Cloud, P.E. 1968. Atmospheric and hydrospheric evolution of the primitive earth. Science, **160**: 729-736.

Cohen, Y., Padan, E., and Shilo, M. 1975. Facultative anoxygenic photosynthesis in cyanobacterium *Oscillatoria limnetica*. Journal of Bacteriology, **123**: 855-861.

Cox, P.M., Betts, R.A., Jones, C.D., Spall, S.A., and Totterdell, I.J. 2000. Acceleration of global-warming due to carbon cycle feedbacks. Nature, **408**: 184-187.

Dessert, C., Dupré, B., Gaillardet, J., François, L.M., and Allègre, C.J. 2003. Basalt weathering and the impact of basalt weathering on the global carbon cycle. Chemical Geology, **202**: 257-273.

Drew, G.H. 1913. On the precipitation of calcium carbonate in the sea by marine bacteria, and on the action of denitrifying bacteria in tropical and temperate seas. Journal of the Marine Biological Association of the United Kingdom, **9**: 479-524.

Ekart, D.D., Cerling, T.E., Montañez, I.P., and Tabor, N.J. 1999. A 400 million carbon isotope record of pedogenic carbonate: Implications for paleoatmospheric carbon dioxide. Science, **299**: 805-827.

Fagerlund, J., Teir, S., Nduagu, E., and Zevenhoven, R. 2009. Carbonation of magnesium silicate mineral using a pressurised gas/solid process. Energy Procedia, **1**: 4907-4914.

Falkowski, P.G. and Isozaki, Y. 2008. The story of O_2. Geology, **322**: 540-542.

Friedlingstein, P., Houghton, R.A., Marland, G., Hackler, J., Boden, T.A., Conway, T.J., Canadell, J.G., Raupach, M.R., Ciais, P., and Le Quéré, C. 2010. Update on CO_2 emissions. Nature Geoscience, **3**: 811-812.

Gerlach, T. 2011. Volcanic versus anthropogenic carbon dioxide. EOS Transactions, **92**: 201-208.

Goldich, S.S. 1938. A study of rock-weathering. Journal of Geology, **46**: 17-58.

Hansen, J., Sato, M., Kharecha, P., Beerling, D., Berner, R., Masson-Delmotte, V., Pagani, M., Raymo, M., Royer, D. L., and Zachos, J. C. 2008. Target atmospheric CO_2: Where should humanity aim? The Open Atmospheric Science Journal, **2**: 217-231.

Harrison, A.L., Power, I.M., and Dipple, G.M. 2013. Accelerated carbonation of brucite in mine tailings for carbon sequestration. Environmental Science & Technology, **47**: 126-134.

Harvey, L.D.D. 2007. Dangerous anthropogenic interference, dangerous climatic change, and harmful climatic-change: non-trivial distinctions with significant policy implications. Climate Change, **82**: 1-25.

Holloway, S. 2005. Underground sequestration of carbon dioxide - a viable greenhouse gas mitigation option. Energy, **30**: 2318-2333.

Houghton, R.A. 2007. Balancing the global carbon budget. Annual Review of Earth and Planetary Sciences, **35**: 313-347.

IPCC, 2005. IPCC Special report on carbon dioxide capture and storage. Prepared by Workng Group III of the Intergovernmental Panel on Climate Change [Metz, B., Davidson, O., de Coninck, H.C., Loos, M. and Leyer, L.A. (eds)]. Cambridge University Press, Cambridge, United Kingdom and New York, NY, USA, pp. 442.

IPCC, 2007. Climate Change 2007: The physical science basis. Contribution of Working Group I to the Fourth Assessment Report of the Intergovernmental Panel on Climate Change [Solomon, S., Qin, D., Manning, M., Chen, Z., Marquis, M., Averyt, K.B., Tignor, M., and Miller, H.L. (eds)]. Cambridge University Press, Cambridge, United Kingdom and New York, NY, USA, pp. 96.

Jones, C.D. and Cox, P.M. 2001. Modeling the volcanic signal in the atmospheric CO_2 record. Global Biogeochemical Cycles, **15**: 453-465.

Kasting, J.F. 1993. Earth's Early Atmosphere. Science, **259**: 920-926.

Kelemen, P.B. and Matter, J. 2008. In situ carbonation of peridotite for CO_2 storage. Proceedings of the National Academy of Sciences of the United States of America, **104**: 17295-17300.

Kelemen, P.B., Matter, J., Streit, E.E., Rudge, J.F., Curry, W.B., and Blusztajn, J. 2011. Rates and mechanisms of mineral carbonation in peridotite- natural processes and preicpes for enhanced, in situ CO2 capture and storage. Annual Review of Earth and Planetary Sciences, **39**: 545-576.

Kenward, P.A., Goldstein, R.H., González, L.A., and Roberts J.A. 2009. Precipitation of low-temperature dolomite from an anaerobic microbial consortium: the role of methanogenic Archaea. Geobiology, **7**: 556-565.

Komárek, J. 2003. Coccoid and colonial cyanobacteria. In: Wehr, J.D. and Sheath, R.G. (eds) Freshwater algae of North America: Ecology and Classification. Elsevier Sciences, San Diego, pp. 59-116.

Komárek, J., Kling, H., and Komárková, J. 2003. Filamentous cyanobacteria. In: Wehr, J.D. and Sheath, R.G. (eds) Freshwater algae of North America: Ecology and Classification. Elsevier Sciences, San Diego, pp. 117-196.

Koukouzas, N., Gemeni, V., and Ziock, H.J. 2009. Sequestration of CO_2 in magnesium silicates, in Western Macedonia, Greece. International Journal of Mineral Processing, **93**: 179-186.

Kranz, S.A., Wolf-Gladrow, D., Nehrke, G., Langer, G., and Rost, B. 2010. Calcium carbonate precipitation induced by the growth of the marine cyanobacterium *Trichodesmium*. Limnology and Oceanography, **55**: 2563-2569.

Kump, L.R., Brantley, S.L., and Arthur, M.A. 2000. Chemical weathering, atmospheric CO_2, and climate. Annual Reviews in Earth and Planetary Sciences, **28**: 611-667.

Kump, L.R. 2008. The rise in atmospheric oxygen. Nature, **451**: 277-278.

Lacis, A.A., Schmidt, G.A., Rind, D., and Ruedy, R.A. 2010. Atmospheric CO_2: Principle control knob governing Earth's temperature. Science, **330**: 356-359.

Lackner, K.S. 2002. Carbonate chemistry for sequestering fossil carbon. Annual Review of Energy and the Environment, **27**: 193-232.

Lah, R. 2003. Global potential of soil carbon sequestration to mitigate the greenhouse effect. Critical Reviews in Plant Sciences, **22**: 151-184.

Lah, R. 2004. Soil carbon sequestration to mitigate climate change. Geoderma, **123**: 1-22.

Lammers, K., Murphy, R., Riendeau, A., Smirnov, A., Schoonen, M.A.A., and Strongin, D.R. 2011. CO_2 sequestration through mineral carbonation of iron oxyhydroxides. Environmental Science and Technology, **45**: 10422-10428.

Le Quéré, C., Raupach, M.R., Canadell, J.G., and Marland, G. 2009. Trends in the sources and sinks of carbon dioxide. Nature Geoscience, **2**: 831-836.

López-García P., Kazmierczak, J., Benzerara, K., Kempe S., Guyot, F., and Moreira, D. 2005. Bacterial diversity and carbonate precipitation in the giant microbialites from the highly alkaline Lake Van, Turkey. Extremophiles, **9**: 263-274.

Montzka, S.A., Dlugokencky, E.J., and Butler, J.H. 2011. Non-CO_2 greenhouse gases and climate change. Nature, **476**: 43-50.

Nisbet, E.G. and Fowler, C.M.R. 1999. Archaean metabolic evolution of microbial mats. Proceedings of the Royal Society of London Biological Sciences, **266**: 2375-2382.

Pearson, P.N. and Palmer, M.R. 2000. Atmospheric carbon dioxide concentrations over the past 60 million years. Nature, **406**: 695-699.

Plasynski, T. 2009. Progress and new developments of carbon capture and storage. Critical Reviews in Plant Sciences, **28**: 123-138.

Pokrovsky, O. S. and Schott, J. 2000. Kinetics and mechanism of forsterite dissolution at 25°C and pH from 1 to 12. Geochimica et Cosmochimica Acta, **64**: 3313-3325.

Pokrovsky, O. S. and Schott, J. 2004. Experimental study of brucite dissolution and precipitation in aqueous solutions: surface speciation and chemical affinity control. Geochimica et Cosmochimica Acta, **68**: 31-45.

Power, I.M., Wilson, S.A., Thom, J.M., Dipple, G.M., and Southam, G. 2007. Biologically induced mineralisation of dypingite by cyanobacteria from an alkaline wetland near Atlin, British Columbia, Canada. Geochemical Transactions, **8**, 13.

Pronost, J., Beaudoin, G., Lemieux, J.-M., Hébert, R., Constantin, M, Marcouiller, S., Klein, M., Duchesne, J., Molson, J.W., Larchi, F., and Maldague, X. 2012. CO_2-depleted warm air venting from chrysotile milling waste (Thetford Mines, Canada): Evidence for in-situ carbon capture from the atmosphere. Geology, **40**: 275-278.

Renaut, R.W. 1993. Morphology, distribution, and preservation potential of microbial mats in the hydromagnesite-magnesite playas of the Cariboo Plateau, British Columbia, Canada. Hydrobiologia, **267**: 75-98.

Retallack, G.J. 2001.A 300-million-year record of atmospheric carbon dioxide from fossil plant cuticles. Nature, **411**: 287-290.

Riding, R. 2000. Microbial carbonates: the geological record of calcified bacterial-algal mats and biofilms. Sedimentology, **47**: 179-214.

Rippka, R., Deruelles, J.B., Waterbury, J.B., Herdman, M., and Stanier, R.Y. 1979. Generic assignments, strain histories and properties of pure culture of cyanobacteria. Journal of General Microbiology, **111**: 1-61.

Roberts, J.A., Bennett, P.C., González, L.A., Macpherson, G.L., and Milliken, K.L. 2004. Microbial precipitation of dolomite in methanogenic groundwater. Geology, **32**: 277-180.

Shaw, G.H. 2008. Earth's atmosphere – Hadean to Early Proterozoic. Chemie der Erde, **68**: 235-264.

Shiraishi, F. 2012. Chemical conditions favoring photosynthesis-induced $CaCO_3$ precipitation and implications for microbial carbonate formation in the ancient ocean. Geochimica et Cosmochimica Acta, **77**: 157-174.

Stal, L.J., van Gemerden, H., and Krumbein, W.E. 1985. Structure and development of benthic marine microbial mat. Microbiology Ecology, **31**: 111-125.

Stammer, D. 2008. Response of the global ocean to Greenland and Antarctic ice melting. Journal of Geophysical Research, **113**: C06022.

Stanier, R.Y. and Cohen-Bazire, G. 1977. Phototrophic prokaryotes: The cyanobacteria. Annual Review of Microbiology, **31**: 225-274.

Suchet, P. A., Probst, J.-L., and Ludwig, W. 2003. Worldwide distribution of continental rock lithology: implications for the atmosphere/soil CO_2 uptake by continental weathering and alkalinity river transport to the oceans. Global Biogeochemical Cycles, **17**: 1038-1052.

Sundquist, E.T. 1993. The global carbon-dioxide budget. Science, **259**: 934-941.

Takahashi, T., Feely, R.A., Weiss, R.F., Wanninkhof, R.H., Chipman, D.W., Sutherland, S.C., and Takahashi, T.T. 1997. Global air-sea flux of CO2: an estimate based on sea-air pCO_2 difference. Proceedings of the National Academy of Sciences, **94**: 8292-8299.

Thompson, J.B. and Ferris, F.G. 1990. Cyanobacterial precipitation of gypsum, calcite, and magnesite from natural alkaline water. Geology, **18**: 995-998.

van Lith, Y., Warthmann, R., Vasconcelos, C., and Mckenzie, J.A. 2003. Sulfate-reducing bacteria induce low-temperature Ca-dolomite and high Mg-calcite precipitation. Geobiology, **1**: 71-79.

Vermilyea, D.A. 1969. The dissolution of MgO and $Mg(OH)_2$ in aqueous solutions. Journal of Electrochemical Society, **116**: 1179-1183.

Walker, J.C.G., Hays, P.B., and Kasting, J.F. 1981. A negative feedback mechanism for the long-term stabilization of Earth's surface temperature. Journal of Geophysical Research, **86**: 9776-9782.

Wilson, S.A., Raudsepp, M., and Dipple, G.M. 2009. Quantifying carbon fixation in trace minerals from processed kimberlite: A comparative study of quantitative methods using

X-ray powder diffraction data with applications to the Diavik Diamond Mine, Northwest Territories, Canada. Applied Geochemistry, **24**: 2312-2331.

Wilson, S.A., Dipple, G.M., Power, I.M., Thom, J.M., Anderson, R.G., Raudsepp, M., Gabite, J.E., and Southam, G. 2009. Carbon dioxide fixation within mine wastes of ultramafic-hosted ore deposits: examples from the Clinton Creek and Cassiar chrysotile deposits, Canada. Economic Geology, **104**: 95-112.

Wilson, S.A., Barker, S.L.L., Dipple, G.M., and Atudorei, V. 2010. Isotopic disequilibrium during uptake of atmospheric CO_2 into mine process waters: implications for CO_2 sequestration. Environmental Science and Technology, **44**: 9522-9529.

Wilson, S.A., Dipple, G.M., Power, I.M., Barker, S.L.L., Fallon, S.J., and Southam, G. 2011. Subarctic weathering of mineral wastes provides a sink for atmospheric CO_2. Environmental Science and Technology, **45**: 7727-7736.

Zevenhoven, R., Teir, S., and Eloneva S. 2008. Heat optimization of a staged gas-solid mineral carbonation process for long-term CO_2 storage. Energy, **33**: 362-370.

Chapter 2

2   A greenhouse-scale photosynthetic microbial bioreactor for mineral carbonation

2.1   Introduction

Since the start of the Industrial Revolution, the atmospheric concentration of CO_2 has been increasing due to human activity. The change in concentration from 280 ppm to 390 ppm is primarily due to the burning of fossil fuels, although land use change and deforestation are also factors (IPCC 2007; Lacis et al. 2010). The additional CO_2 in the atmosphere is causing a range of environmental problems, resulting in extensive research in the field of carbon storage. Sequestering anthropogenic CO_2 in carbonate minerals was first proposed by Seifritz in 1990. Carbonate minerals offer a stable medium for storing CO_2 over geological time scales and require limited monitoring. These advantages over other types of CO_2 storage have resulted in extensive research of both industrial and passive mineral carbonation methods (Lackner et al. 1995; Hansen et al. 2005; Schuiling and Krijgsman, 2006; Wilson et al. 2006; Gerdemann et al. 2007; Wilson et al. 2009; Köhler et al. 2010; Power et al. 2010; Power et al. 2011; Renforth and Manning 2011; Bea et al. 2012; Renforth 2012; Washbourne et al. 2012; Harrison et al. 2013). Due to the monetary and energy costs involved, industrial mineral carbonation is currently not practical for large scale use. Passive processes such as enhanced weathering and subsequent carbonate precipitation taking place at low temperatures and pressures require less energy input than industrial carbonation (Power et al. 2010). Biological processes that accelerate mineral carbonation at ambient conditions may offer an alternative means of storing significant quantities of anthropogenic CO_2 and aid in reducing net greenhouse gas emissions (Power et al. 2011).

The involvement of microorganisms in carbonate mineral precipitation has been acknowledged for a century (Drew 1913). Microbially mediated carbonation is evident in many parts of the geologic record, with Precambrian stromatolites preserved in limestone and dolostone providing the earliest evidence (Riding 2000; Aloisi 2008). Although the role of microbes in the formation of the first stromatolites (3.45 Ga and earlier) is still disputed, Late Archean (2.8-1.0 Ga)

specimens contain evidence of significant microbial activity (Thompson and Ferris 1990; Aloisi 2008). Calcium carbonate mineral precipitation is the most studied carbonation reaction in which microbes are involved, and has been documented in environmental settings such as oceans, lakes, soils, caves, and groundwater (Riding 2000). These reactions are primarily enabled by phototrophic microbes, including cyanobacteria such as *Synechococcus* and *Triodesmium*, which alter the water chemistry and induce carbonate precipitation (Thompson and Ferris 1990; Kranz et al. 2010). Microbially induced dolomite [$CaMg(CO_3)_2$] precipitation is mediated by the metabolic activity of iron-reducing, sulfate-reducing, and methanogenic bacteria in anoxic environments (van Lith et al. 2003; Roberts et al. 2004; Kenward et al. 2009). The cell walls and extracellular polysaccharides of these microbes provide sites for dolomite crystal nucleation, as mineral formation does take place abiotically under the same geochemical conditions. Magnesium carbonate precipitation associated with cyanobacteria and diatoms has been documented in several alkaline aquatic environments (Renaut 1993; Braithwaite and Zedef 1994; López-García et al. 2005; Power et al. 2007). Magnesium carbonate precipitation, like biogenic calcium carbonate formation, is strongly affected by pH and alkalinity; however, the biogeochemical conditions required for magnesium carbonation are not completely refined (Thompson and Ferris 1990; Shiraishi 2012).

This study examined the ability of a natural cyanobacteria dominated consortium to accelerate magnesium carbonate precipitation from solution in a flow through bioreactor. This was completed by simulating the geochemical and microbial growth conditions of a natural wetland located near Atlin, British Columbia, Canada, a field site known for the precipitation of magnesium carbonate minerals including hydromagnesite [$Mg_5(CO_3)_4(OH)_2 \cdot 4H_2O$], nesquehonite [$MgCO_3 \cdot 3H_2O$], and dypingite [$Mg_5(CO_3)_4(OH)_2 \cdot 5H_2O$] (Figure 2.1, 2.2) (Power et al. 2007; Power et al. 2009). In contrast to previous studies, this investigation examines this biogeochemical process on a much larger scale, making it more representative of the reactions occurring in natural systems and demonstrating the resilience of these microbial 'mats'. The linear experimental bioreactor design used in this study allowed for both temporal and spatial examination of magnesium carbonate precipitation.

22
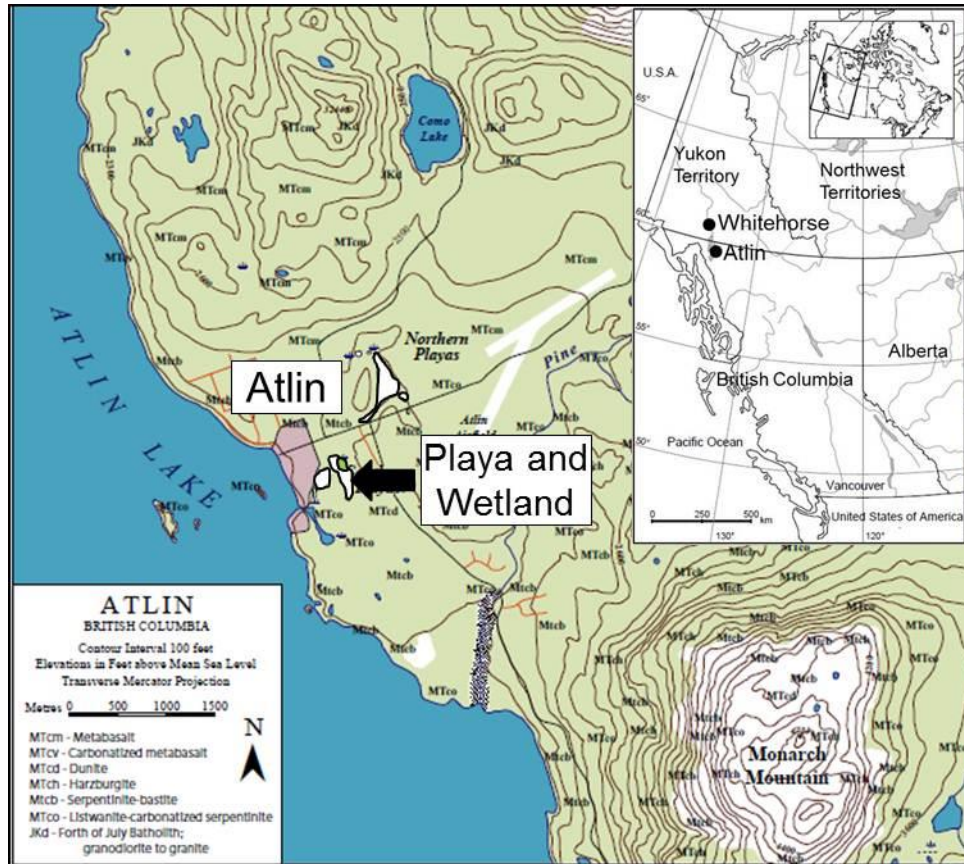
Figure 2.1 Location of the magnesium carbonate mineral playa and wetland modeled in this investigation near Atlin, British Columbia, Canada (modified from Power et al. 2009).
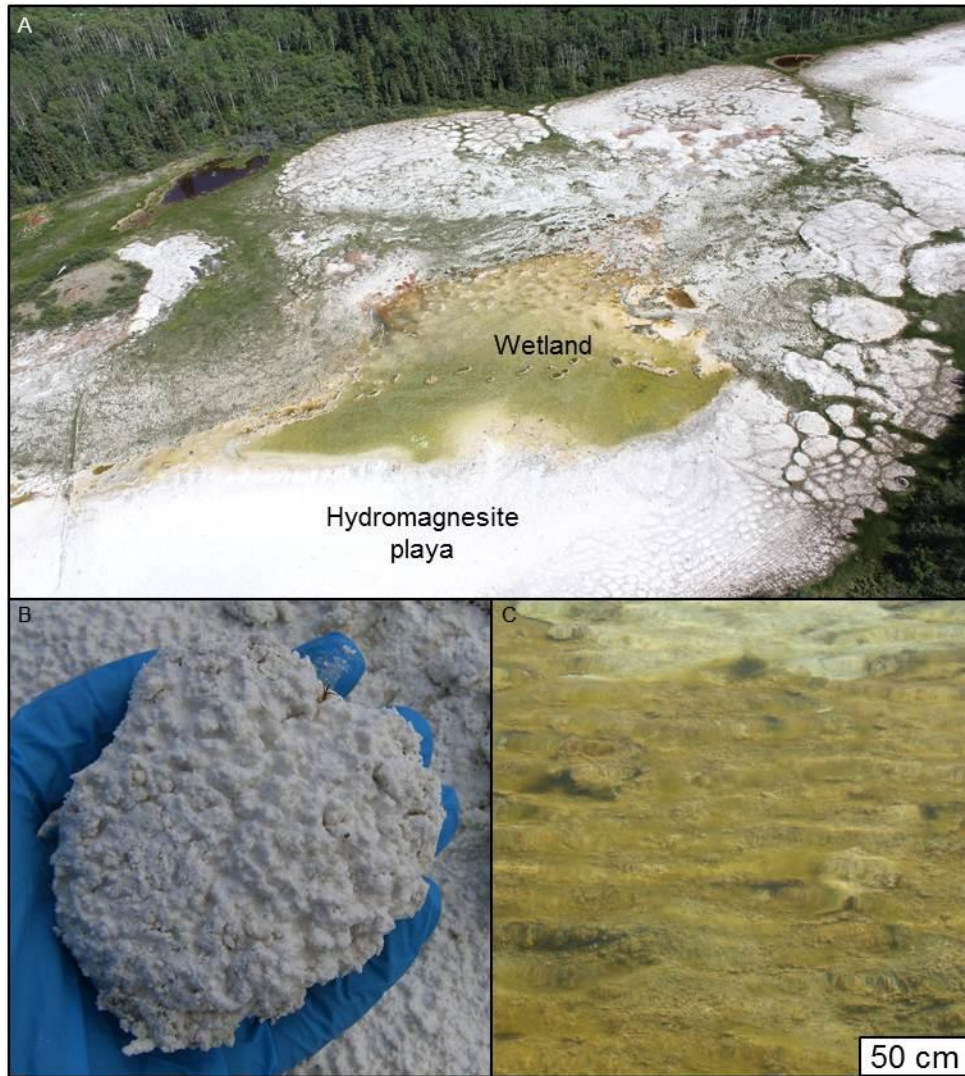
Figure 2.2 A) Aerial photograph of the Atlin hydromagnesite playa and associated wetland. B) sample of the unconsolidated hydromagnesite that makes up the playa. C) phototrophic microbial mats in the wetland. (Photograph A) taken by I.M. Power, 2012).

2.2 **Methods**

2.2.1 Site description and sampling

Samples of benthic microbial mats (20 dm^3) and the underlying carbonaceous sediments (20 dm^3) were collected from a wetland that is part of a natural hydromagnesite playa found near Atlin, British Columbia (59°34'30" N, 133°41'60" W) (Figure 2.1). The playa consists of mounds of hummocky hydromagnesite and is surrounded by ophiolitic country rock composed primarily of serpentinised harzburgite (Figure 2.2) (Hansen et al. 2005). Minor carbonitised harzburgite, dunite lenses, and pyroxenite veins are also present in the local bedrock. Weathering of the country rock produces the magnesium-rich groundwater that feeds the wetland, which has an average water depth of 30 cm and an area of approximately 0.5 ha (Power et al. 2007). The wetland water had a pH of 8.6, conductivity of 5.0 mS/cm, and dissolved oxygen (DO) concentration of 9.3 mg/L at the time of sampling.

2.2.2 Bioreactor construction and preparation

After transport, the carbonaceous sediment samples had a pH of 8.7, conductivity of 2.5 mS/cm, and a DO content of 2.5 mg/L. The sediments were placed in the bottom of the bioreactor, which was constructed from 15 cm diameter polyvinyl chloride pipe (Figure 2.3). The gravity driven flow-through channel had a volume of 155 L, a length of 10 m, and a surface area of 1.5 m^2. The bioreactor was located in a greenhouse which maintained a minimum air temperature of 18°C and received at least 14 h of light/day through combined natural and artificial lighting. The microbial mat samples were layered on top of the sediments, all of which was submerged below 5 cm of growth medium. The microbial mats were allowed to re-establish in the bioreactor for 8 weeks, hereafter called the 'growth phase', in 100 L of phosphorus-enriched BG-11 medium (Appendix A) prior to starting experimentation (Vonshak 1986). At the start of the carbon mineralisation experiment, hereafter called the 'carbonation phase', the 'spent' BG-11 medium was gradually replaced by a feedstock containing 10.12 g/L MgSO$_4$·7H$_2$O (41.07 mM magnesium) and 6.92 g/L NaHCO$_3$ (82.4 mM bicarbonate), comparable to the Atlin wetland waters (Power et al. 2007). Using dypingite as the target mineral product (Reaction 1), six 'cycles' of carbon fixation (Reaction 2) were required to produce the requisite hydroxyl and carbonate anions (Reaction 3) for each molecule of dypingite precipitated (Power et al. 2007). Using the classic phytoplankton biomass formula [(CH$_2$O)$_{106}$(NH$_4$)$_{16}$(H$_3$PO$_4$)] (Peters et al.

2005) the nutrient supplement required to meet the minimum amount of photosynthesis for magnesium carbonate precipitation is 42% of the concentration of the standard BG-11 medium recipe, assuming 100% efficiency of photosynthetically driven dypingite formation (Appendix A). The feedstock solution containing both magnesium and nutrients was added at the 0 m position of the channel at a rate of 5 L/day for 7 weeks using a Masterflex® peristaltic pump. A drain at the other end of the bioreactor allowed the solution to flow passively out of the system. Outflow volume was tracked in order to quantify evaporation.

$$5 \; Mg^{2+} + 4 \; CO_3^{2-} + 2 \; OH^- + 5 \; H_2O \rightarrow Mg_5(CO_3)_4(OH)_2 \cdot 5H_2O \tag{1}$$

$$HCO_3^- + H_2O \rightarrow CH_2O + O_2 + OH^- \tag{2}$$

$$HCO_3^- + OH^- \rightarrow CO_3^{2-} + H_2O \tag{3}$$

2.2.3 *Water chemistry analysis*

Water chemistry was monitored at 0 m, 2 m, 4 m, 6 m, and 8 m down the length the bioreactor from the feedstock solution inflow point, as well as in the solution flowing out of the system (Figure 2.3). Weekly pH, conductivity, and DO measurements were taken at each of these locations. The pH was measured using a Mettler Toledo EL2 pH meter, with a Mettler Toledo LE407 electrode calibrated using buffer solutions 4, 7, and 10 with analytical pH measurement uncertainties of ± 0.01 pH units. Conductivity was measured using a Mettler Toledo conductivity/temperature EL3 meter equipped with a Mettler Toledo LE703 electrode. The probe was calibrated using 84 μS/cm, 1413 μS/cm, and 12.88 mS/cm conductivity standards and has a measurement error of ± 0.5% of the measured value. DO was measured using a Traceable digital oxygen/temperature meter calibrated using atmospheric oxygen. The probe has an accuracy of ± 0.4 mg/L.

A hydrochloric acid titration was completed using 0.45 μm-filtered water samples (10 mL) collected from each sampling point in order to determine alkalinity (Lahav et al. 2001). This was completed by measuring the pH of the water, followed by the addition of aliquots of 1.0 N HCl with a Gilson pipet. After the addition of each aliquot, ranging in volume from 20-75 μL, the pH was re-measured. Acid was added until the pH dropped below 3.0. Alkalinity, the ability of a

26
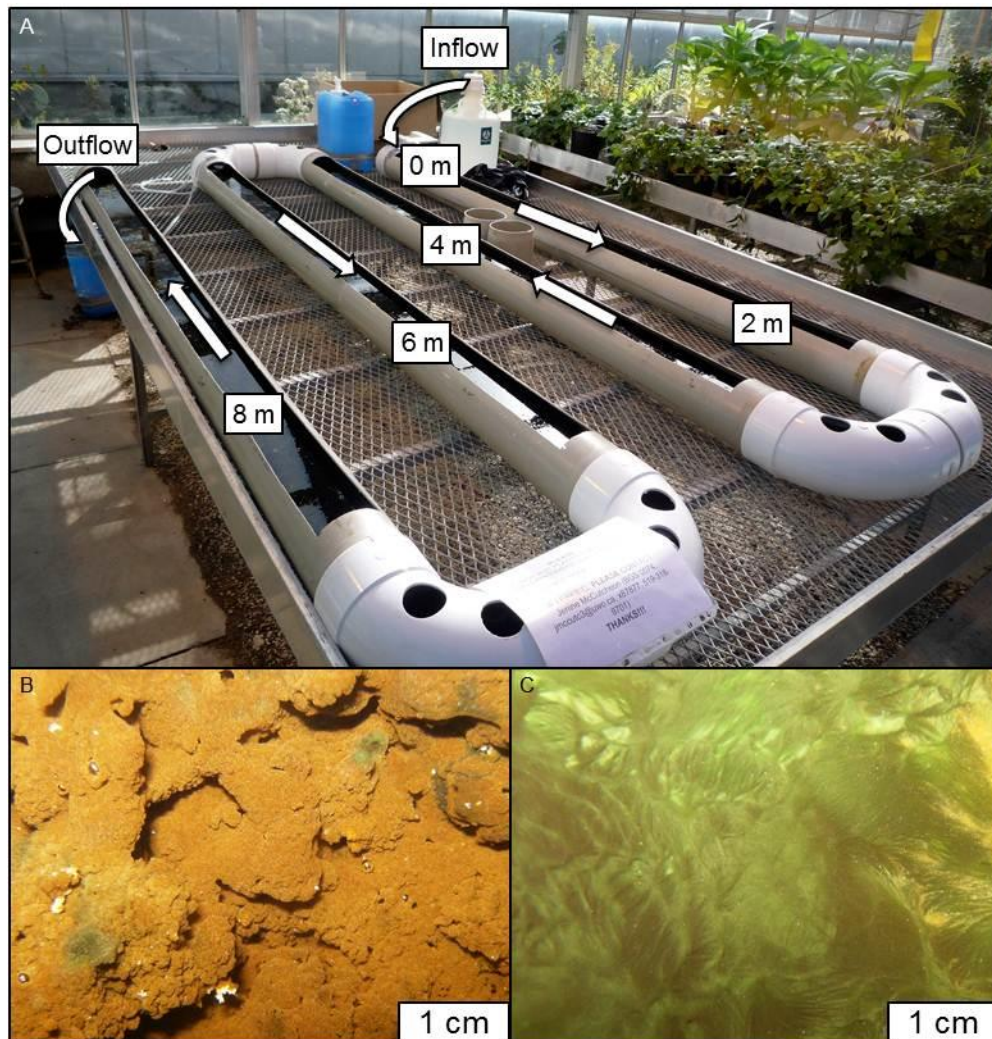
Figure 2.3 A) The gravity driven bioreactor inoculated with microbial mats from the Atlin wetland for the carbonation experiment. The magnesium- and bicarbonate-rich feedstock solution was added to one end of the system using a peristaltic pump. The inflow solution was able to flow passively through the bioreactor and out a valve in the other end. Arrows indicate the direction of flow. Sampling points are marked in metres from the start of the channel. B) and C) Microbial mats in the bioreactor after the carbonation phase near the start and the end of the channel, respectively.

liquid to neutralise acid, was calculated as mM of HCO_3^- using the volume of acid added to each sample.

Major ion concentrations were determined weekly for each sample location from 15 mL 0.45 μm-filtered water samples. Cation analysis was completed using inductively coupled plasma-atomic emission spectroscopy (ICP-AES) with a Perkin-Elmer Optima 300DV, while a Dionex IC 3000 equipped with a Dionex IonPac AS14A column (4×250 mm) was used for anion analysis by ion chromatography (IC). Ion concentrations were also determined for the field site using filter-sterilised water samples collected at the time of microbial mat and sediment samples. Ion concentrations were measured with the following detection limits and measurement uncertainties, respectively: Mg^{2+} (0.03 μg/mL, 14.9%), Ca^{2+} (0.06 μg/mL, 16.6%), Na^+ (0.01 μg/mL 27.3%), Si^{4+} (0.05 μg/mL, 39.4%), K^+ (0.02 μg/mL, 11.7%), NO_3^- (0.05 μg/mL, 28.8%), PO_4^{3-} (0.09 μg/mL, 24.7%), NO_2^- (0.06 μg/mL, 40.7%), SO_4^{2-} (0.03 μg/mL, 25.7%), and Cl^- (0.01 μg/mL, 23.5%).

Samples of water were collected from each sampling location in the bioreactor to determine water hardness, which is a measure of the presence of multivalent cations such as calcium and magnesium. The 10 mL water samples were filter-sterilised using Fisher Brand® 0.45 μm syringe filters. One ManVer 2 Hardness Pillow sachet was added to each sample, after which the pH was adjusted to 10.3 using 0.1 M NaOH. A 0.02 M ethylenediaminetetraacetic acid (EDTA) solution was added to each sample in 100 μL aliquots using a Gilson pipet. The solution was continuously stirred on a magnetic stir plate while the EDTA was being added. This was continued until the solution exhibited a colour change from blue to pink. The volume of EDTA added was used to calculate the hardness of the water samples, with every 100 μL added equivalent to 10 mg/L of calcium. Since there is minimal calcium in the samples, this value was converted to magnesium using molar mass.

Mineral saturation indices were determined by analysing the water chemistry data with PHREEQC Interactive version 3.0.2.7614 (Parkhurst and Appelo 1999). Water sample pH and ion concentration values were used along with the llnl.dat database for thermodynamic constants in order to identify mineral supersaturation in the bioreactor (Appendix B). This information was

used to characterise how carbonate mineral formation is affected by changes in pH, and the availability of Mg^{2+} and dissolved inorganic carbon species.

2.2.4   *Microbe and mineral characterisation*

Microbial mat samples were collected after the experiment at 0.5 m, 4 m, and 8 m along the length of the bioreactor as representatives of upstream, midstream, and downstream mats in the system. These samples were fixed with $2\%_{(aq)}$ glutaraldehyde and dehydrated with an ethanol concentration series of 25%, 50%, 75%, and $3 \times 100\%$ for 20 min at each concentration. The samples were then critical point dried using a Tousimis, Samdri-PVT-3B critical point dryer. The samples were mounted on stainless steel stubs with adhesive carbon tabs and coated with 4 nm of osmium with a Filgen OPC80T osmium plasma coater prior to scanning electron microscopy (SEM) using Zeiss Leo 1530 and 1540 XB microscopes. Elemental data, for mineral grains observed within the microbial mat samples, were collected using an Oxford Instruments INCA x-sight energy dispersive spectrometer (EDS) in conjunction with the 1540 XB microscope.

A microbial mat sample (dry weight = 2 g) collected 0.5 m from the start of the bioreactor at the end of the experiment, dried at 60°C, and powdered with a mortar and pestle was analysed with micro X-ray diffraction (μXRD). A Bruker axs D8 Discover 300 μm capillary micro X-ray diffractometer with CoKα radiation was used, operating at 35 kV and 45 mA and equipped with a General Area Detector Diffraction System (GADDS). Mineral phases were determined by interpreting the raw data using DIFFRAC^{plus} Eva software.

2.2.5   *Abiotic control*

A flask containing 1 L of the magnesium- and bicarbonate-rich solution added to the bioreactor was placed under the same conditions as the carbonation system for 4 weeks. The flask was monitored for abiotic mineral precipitation to ensure that any mineral formation occurring in the carbonation experiment is due to the presence of the microorganisms. Samples from the abiotic control were examined with SEM-EDS in the same manner as the microbial mat samples.

2.3   **Results**

2.3.1   Water chemistry

By the end of the 8-week growth phase, the pH increased to an average of 9.7 in the bioreactor (Figure 2.4). At the beginning of the carbonation phase, the pH declined with the addition of the pH 8.3, buffered magnesium- and bicarbonate-rich feedstock solution, stabilising at approximately pH 9.2. The decrease in pH was more dramatic at the start of the channel, with the water becoming more basic down the length of the bioreactor (Figure 2.4).

By the end of the growth phase, the DO had increased from 2.5 mg/L to 20.6 mg/L (Figure 2.5). During the first week of the carbonation phase, the DO concentration decreased to a system average of 9.8 mg/L. The average DO concentration in the feedstock solution was 6.9 mg/L, increasing to 11.7 mg/L upon entering the bioreactor at the 0 m mark, and continuing to rise to 19.6 mg/L by 6 m along the bioreactor channel. This increase in oxygen concentration along the first 6 m was followed by a decrease over the last 4 m, dropping to 10.8 mg/L in the system outflow (Figure 2.5).

A total of 260 L of the magnesium- and bicarbonate-rich growth solution was added to the start of the bioreactor over the course of the carbonation phase. The volume of water flowing out of the bioreactor was tracked and indicated that a total of 102 L, or 39%, of the water evaporated from the system over the course of the experiment. This water loss was taken into account for the conductivity, ICP, and IC results. Ion concentration analyses indicated major changes in water chemistry along the length of the bioreactor, including nutrient limitation in the lower 4 m of the bioreactor throughout the carbonation phase (Figure 2.6; Table 2.1). Phosphate and nitrate concentrations both decreased from respective inflow values of 0.30 and 0.46 mM to 0.0 mM in the bioreactor outflow water.

During the growth phase, the conductivity of the bioreactor was constant at 3.3 mS/cm (Figure 2.7). During the first week of the carbonation phase, the conductivity of the inflow solution was 9.9 mS/cm, dropping to 5.0 mS/cm upon being added at the 0 m sampling point, and reaching a 4.0 mS/cm by the end of the bioreactor. The magnitude of the drop in conductivity decreased over the course of the carbonation phase, with the average inflow conductivity of 10.0 mS/cm dropping to 8.4 mS/cm upon addition to the system, and reaching 7.7 mS/cm in the bioreactor

outflow water (Figure 2.7). Hardness, which is closely related to conductivity, also decreased in this manner (Figure 2.8). The average hardness of the inflow solution was 55.9 mM 'magnesium'. Although this value also includes other cations such as calcium, it primarily represents magnesium because magnesium was the main cation in the system. The hardness decreased along the bioreactor from the inflow value to an average outflow value of 7.7 mM, which is a reduction of 86.2%. As with conductivity, hardness concentrations decreased the greatest amount at the start of the bioreactor and during the first week of the carbonation phase.

Alkalinity decreased by 34% along the whole length of the bioreactor over the course of the carbonation phase, with two-thirds of this decrease occurring in the first 2 m of the channel (Figure 2.9). Similar to conductivity, the alkalinity exhibited the greatest decrease in comparison to the experiment as a whole during the first week of the carbonation phase. During the first week, the conductivity dropped from the inflow average of 69.4 mM as HCO_3^- to 43.5 mM immediately after addition to the system and to 32.5 mM by the end of the bioreactor channel, which is a decrease of 53.1%. This rate of alkalinity consumption decreased both along the length of the bioreactor and with time. Magnesium decreased in a similar manner to alkalinity and conductivity. Over the whole length of the bioreactor, the magnesium concentration decreased from the inflow value of 38.3 mM to 10.6 mM, which is a drop of 72.4% for the entire duration of the carbonation phase (2.10; Table 2.1). During the first week of the carbonation phase, the concentration of magnesium decreased from the average inflow value of 38.3 mM to 16.3 mM immediately upon addition to the start of the bioreactor, and to 3.7 mM by the outflow, which was a 90.4% decrease in magnesium concentration (Figure 2.10; Table 2.1). The magnesium concentrations for the first 2 m of the first week of the carbonation phase were used to calculate the optimum magnesium mineral precipitation and carbon storage rate values below.

Using the water chemistry data outlined above, saturation indices were determined for potential mineral precipitates using PHREEQC. Although dypingite was used as the target magnesium carbonate mineral product, the saturation index for hydromagnesite was used as a guide for carbonation potential because thermodynamic data are not available for dypingite. In theory, a saturation index (SI) value greater than zero indicates that the mineral is able to form; however, for many minerals including hydromagnesite, mineral formation may be kinetically inhibited without the addition of heat or pressure beyond that of ambient conditions, or a biological

31

process. This explains why no hydromagnesite precipitated in the feedstock solution, even though it had a SI value of 2.16 (Figure 2.11, Appendix B). The solution SI value for hydromagnesite increased immediately upon addition to the bioreactor, followed by changes within the system over both space and time (Figure 2.11). At each sampling point, the SI value exhibited an increase over the first 4 weeks of the carbonation phase, followed by a decrease at the end of the experiment. One week into the carbonation phase (day 63), the 0 m sampling location had the highest hydromagnesite SI value which was followed by a continuous decrease down the length of the bioreactor. In the other three sets of data analysed, the hydromagnesite SI value increased from 0 m to the 2 m sampling point. In these three time course data sets, the 2 m position had the highest SI value and preceded a decline down the remaining length of the system. The highest hydromagnesite SI value identified was 6.14 and occurred at the 2 m sampling point 4 weeks into the carbonation phase (day 84).

2.3.2   *Microbe and mineral characterisation*

Scanning electron microscopy of the microbial mats indicated variations in microbial and mineral content along the length of the bioreactor. Filamentous cyanobacteria and diatoms dominated all of the microbial communities sampled, with some heterotrophic bacteria also present. The 0.5 m sample contained abundant platy crystals of hydromagnesite that reached 7 µm in diameter and were associated with large quantities of extra-cellular polymeric substances (EPS) (Figure 2.12). The hydromagnesite was identified using µXRD and SEM-EDS (Figure 2.13). Hydromagnesite is a slightly less hydrated magnesium carbonate mineral than the target mineral dypingite. The aragonite identified using µXRD was likely derived from the underlying carbonaceous sediments adhered as a clotted texture to the bottom of the microbial mat. No aragonite was observed with SEM as only the top, 'growing' surface of the mat was sampled for electron microscopy. The cyanobacteria were identified as straight, cylindrical filaments reaching up to 300 µm in length and lacking constrictions at the cross-walls; such attributes were comparable to those of *Lyngbya* spp. observed in samples collected from the wetland.

Table 2.1 Average concentrations (mM) of major cations and anions at each of the seven sampling locations during the carbonation phase and for the field site at the time of sampling.

Sample Point	Ion concentration (mM)									
	Mg^{2+}	Ca^{2+}	Na^+	Si^{4+}	K^+	NO_3^-	PO_4^{3-}	NO_2^-	SO_4^{2-}	Cl^-
Inflow	38.298	0.076	89.848	1.872	0.385	0.461	0.301	0.004	52.514	0.322
0 m	27.207	0.053	99.624	0.640	1.338	0.165	0.108	0.081	51.681	0.496
2 m	22.432	0.048	94.833	0.317	1.403	0.081	0.053	0.091	37.543	0.579
4 m	16.972	0.037	79.264	0.205	1.349	0.043	0.028	0.068	41.124	0.565
6 m	14.414	0.037	73.737	0.218	1.274	0.026	0.017	0.043	43.600	0.580
8 m	11.734	0.032	67.936	0.198	1.311	0.006	0.004	0.021	44.596	0.633
Outflow	10.563	0.027	66.207	0.169	1.256	0.005	0.003	0.000	36.932	0.656
Field site	45.386	0.258	2.723	1.477	0.245	645.057	ND	0.753	ND	ND

ND: not detected
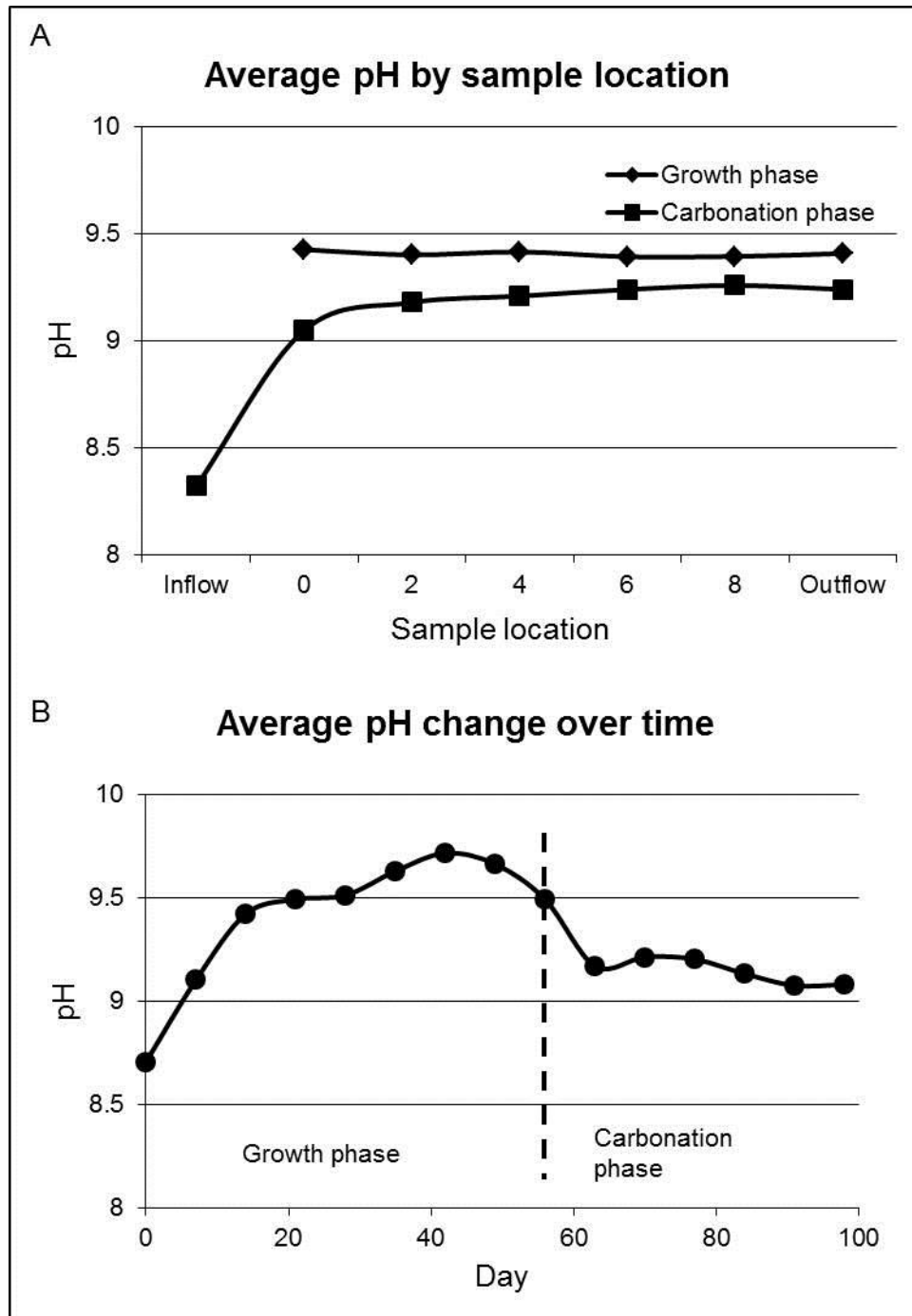
Figure 2.4 Changes in pH for both the growth and carbonation phases of the experiment over A) space and B) time as an average of the 7 samples measured at each time point.
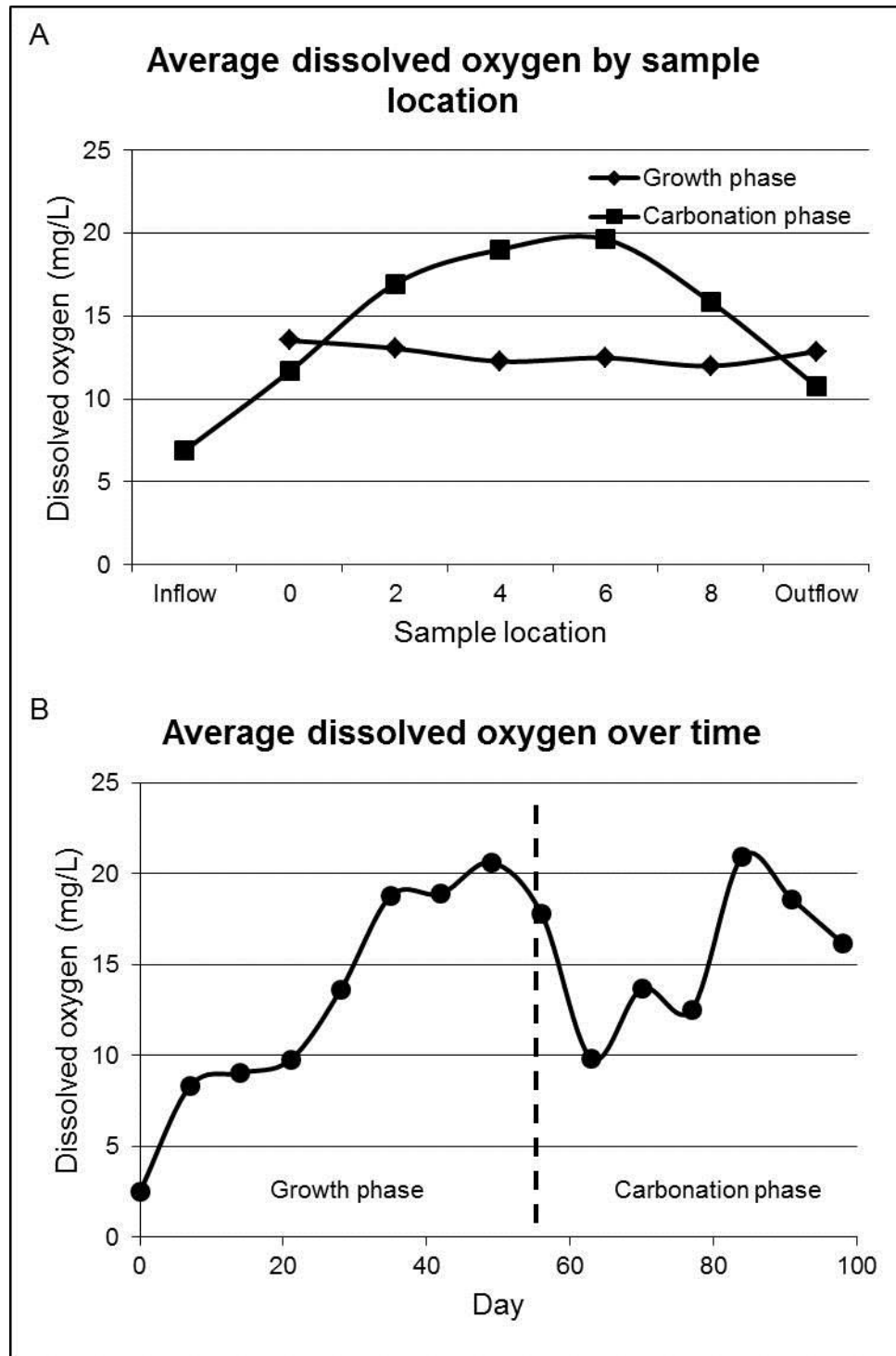
Figure 2.5 Changes in dissolved oxygen concentration (mg/L) for both the growth and carbonation phases of the experiment over A) space and B) time as an average of the 7 samples measured at each time point.
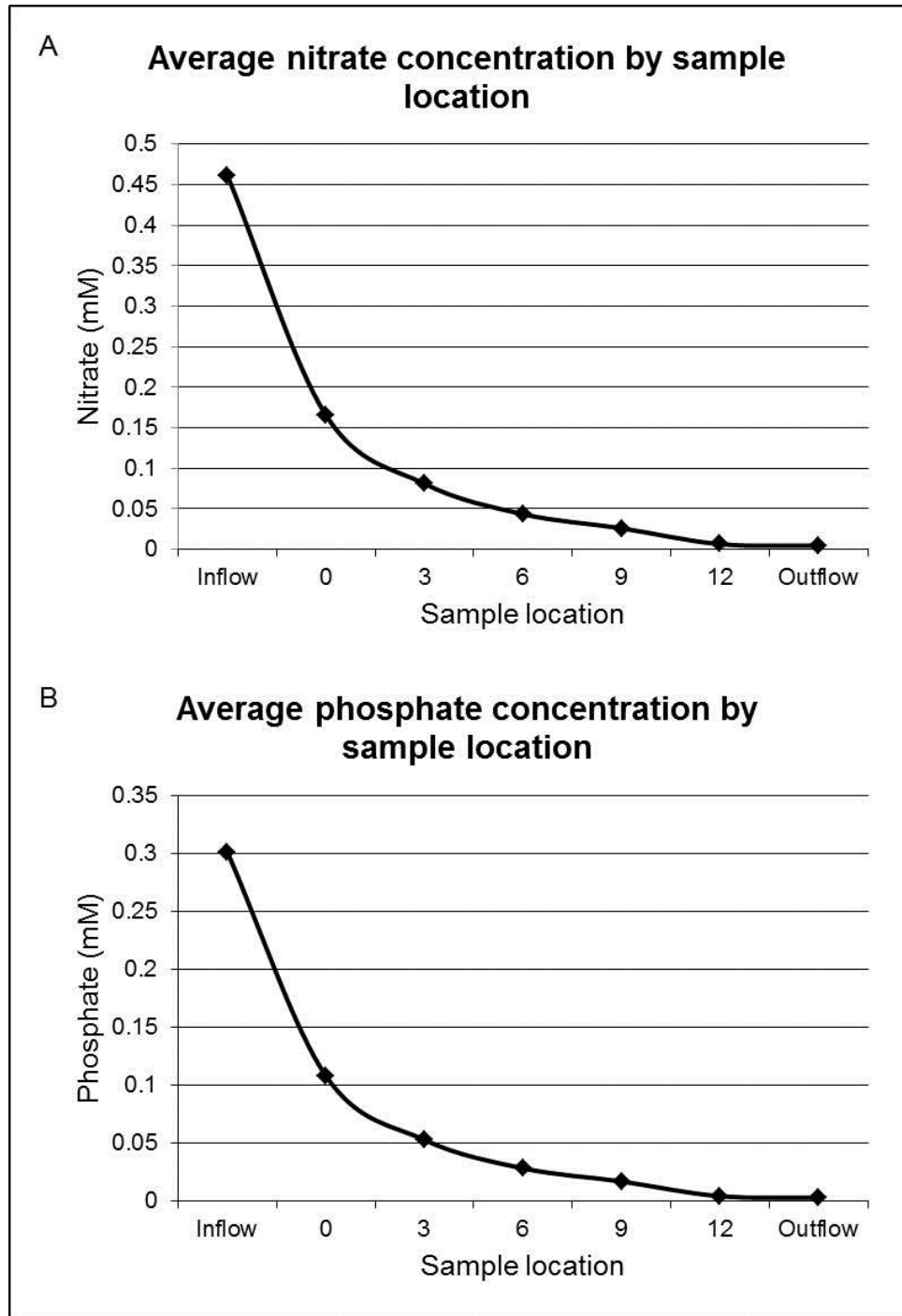
Figure 2.6 Average A) nitrate and B) phosphate concentrations (mM) by sampling point in the bioreactor during the carbonation phase.
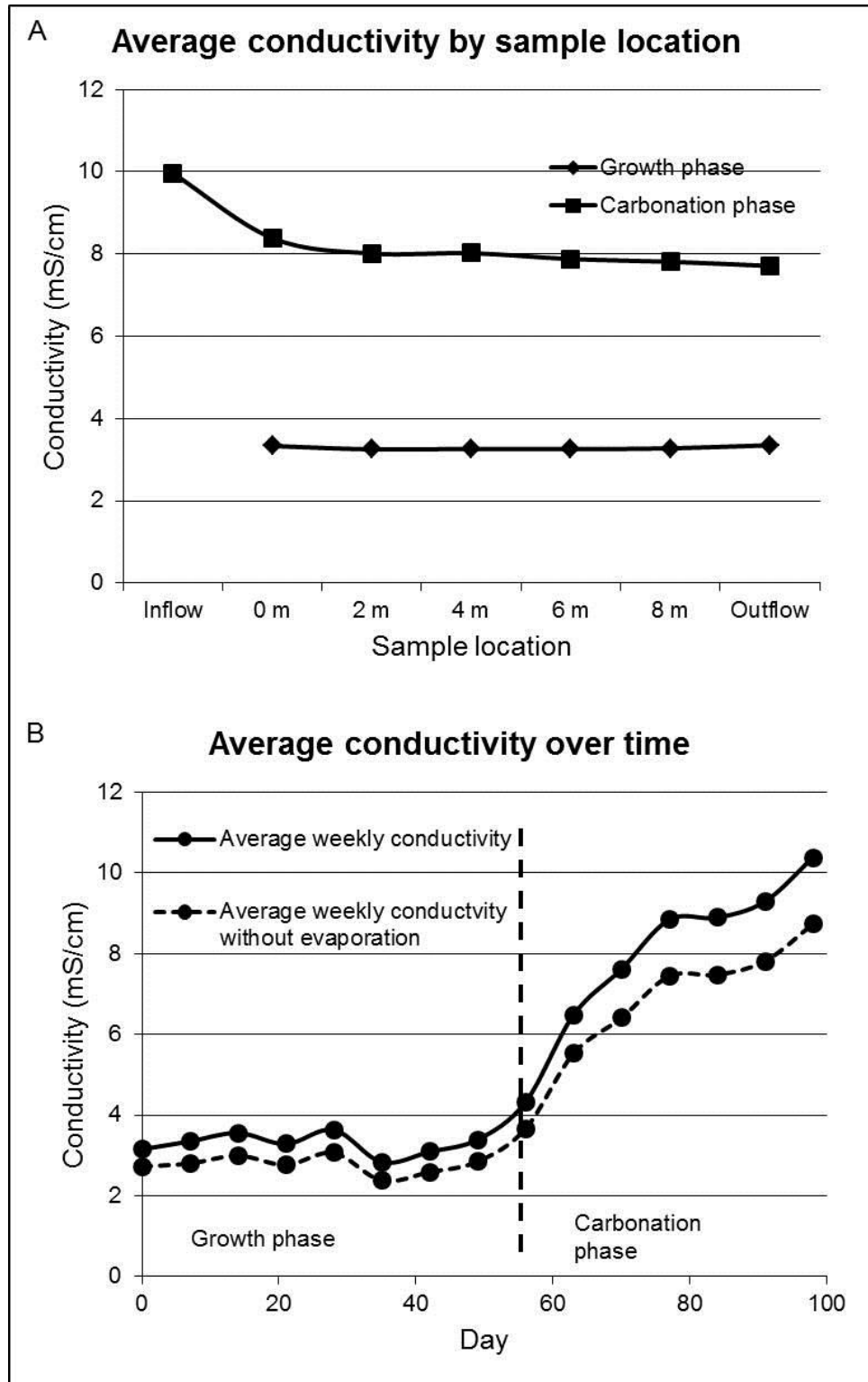
Figure 2.7 Changes in conductivity (mS/cm) for both the growth and carbonation phases of the experiment over A) space and B) time as an average of the 7 samples measured at each time point.
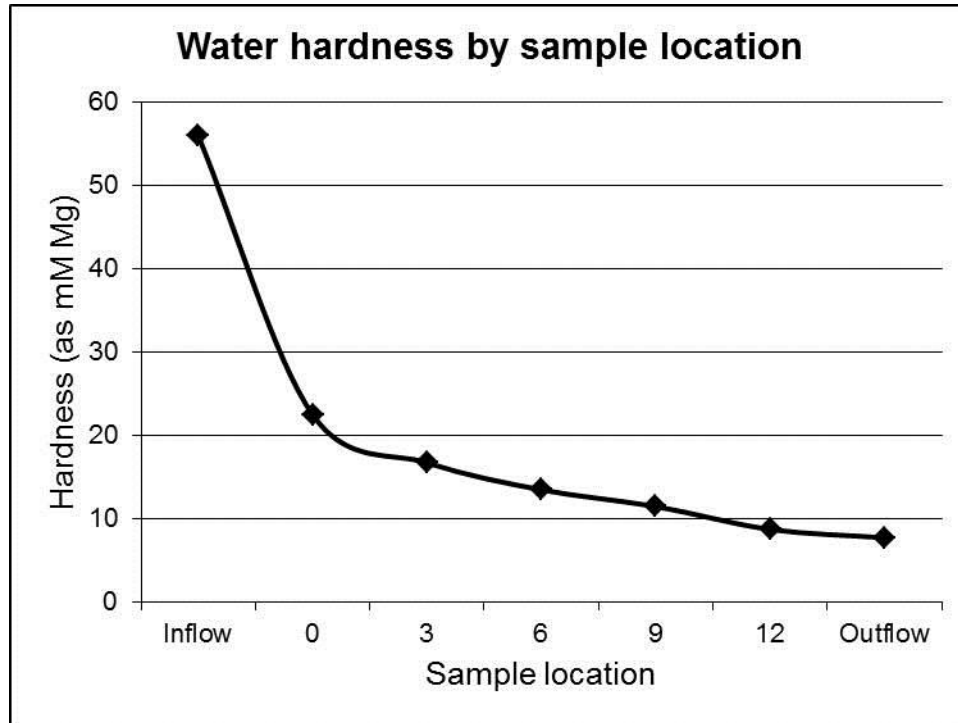
Figure 2.8 Average water hardness (as mM Mg) by sample location in the bioreactor during the carbonation phase.
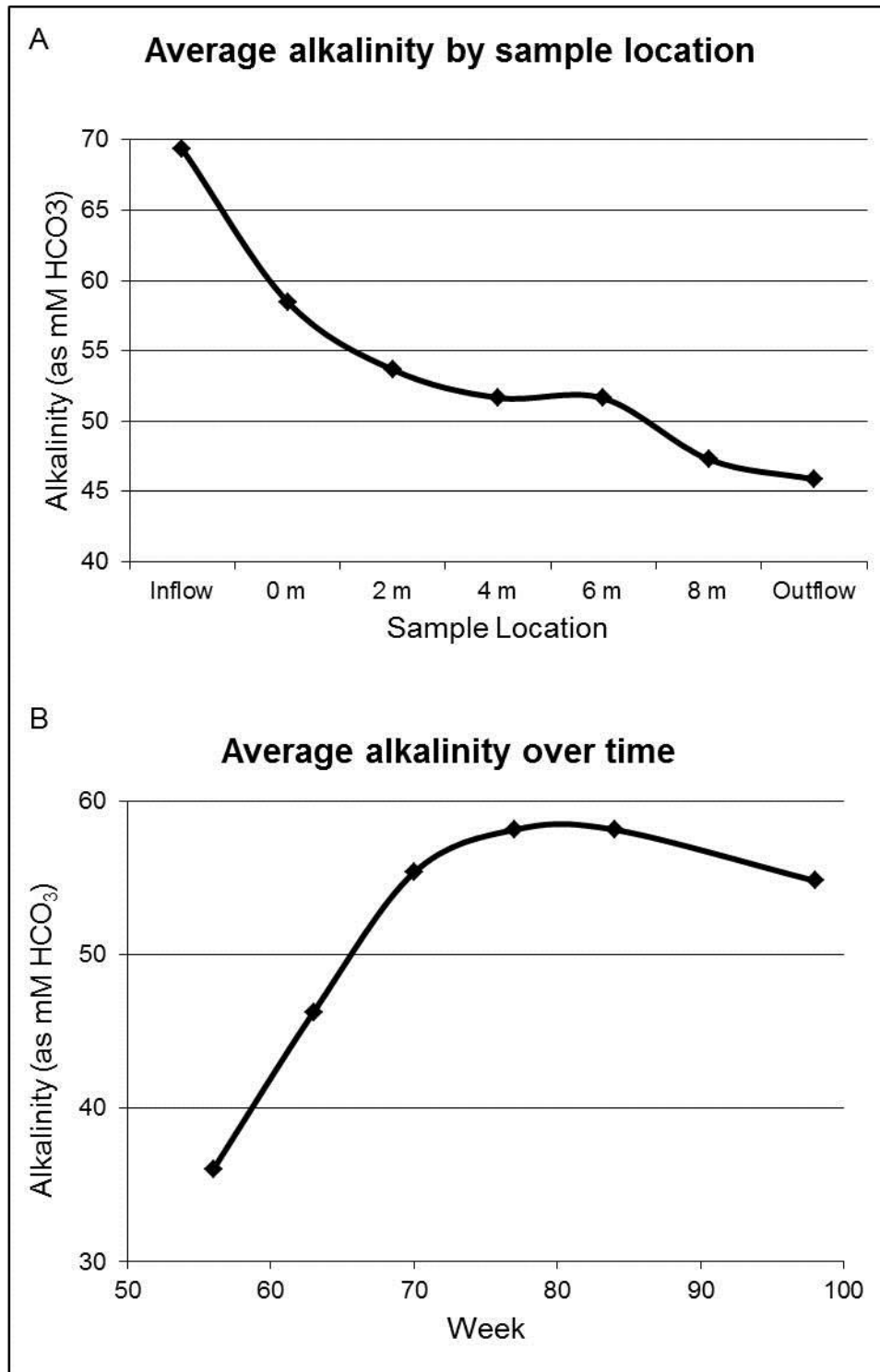
Figure 2.9 Change in alkalinity (as mM HCO_3^-) during the carbonation phase of the experiment over A) space and B) time as an average of the 7 samples measured at each time point.
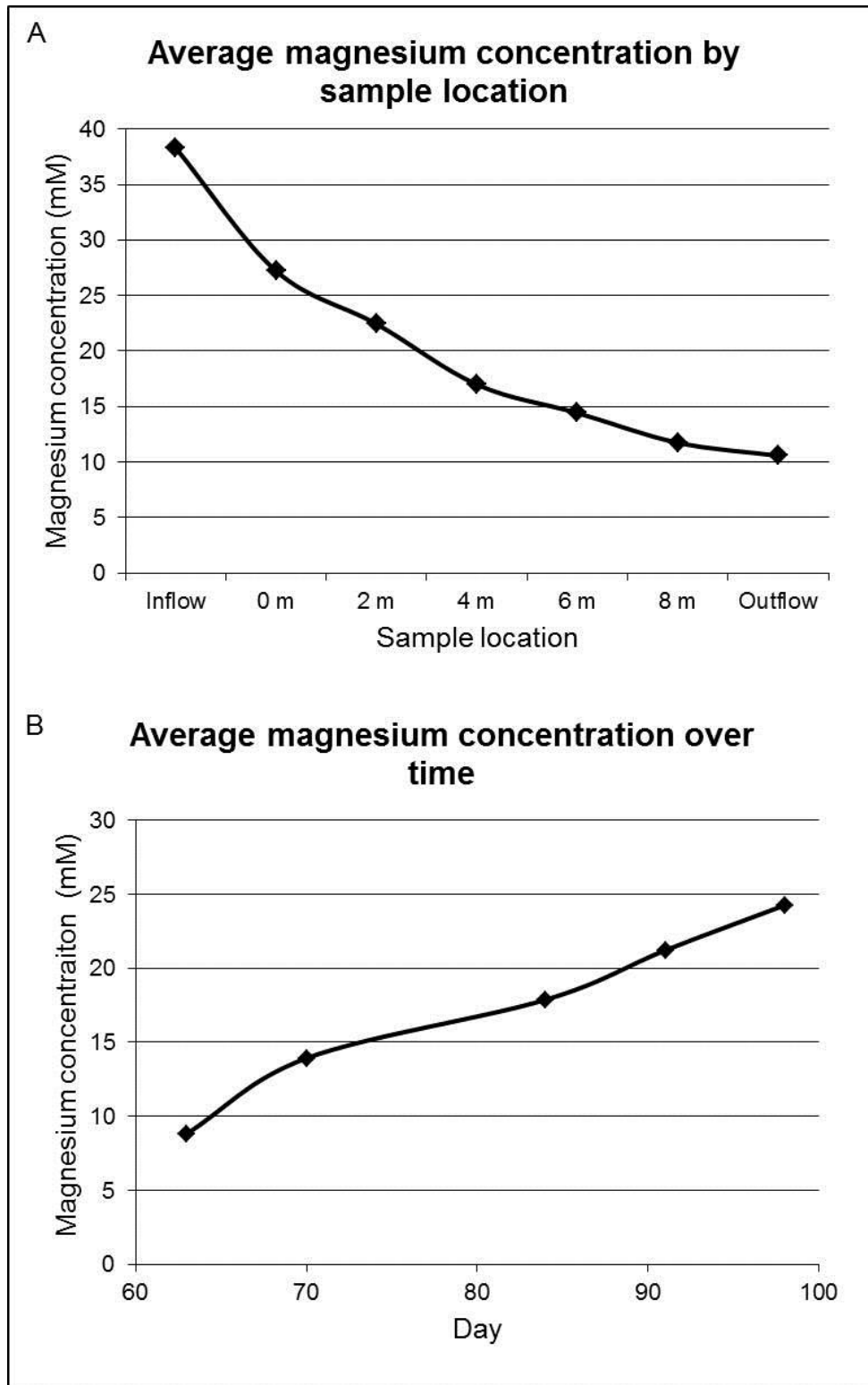
Figure 2.10 Change in magnesium concentration (mM) during the carbonation phase of the experiment over A) space and B) time as an average of the 7 samples measured at each time point.
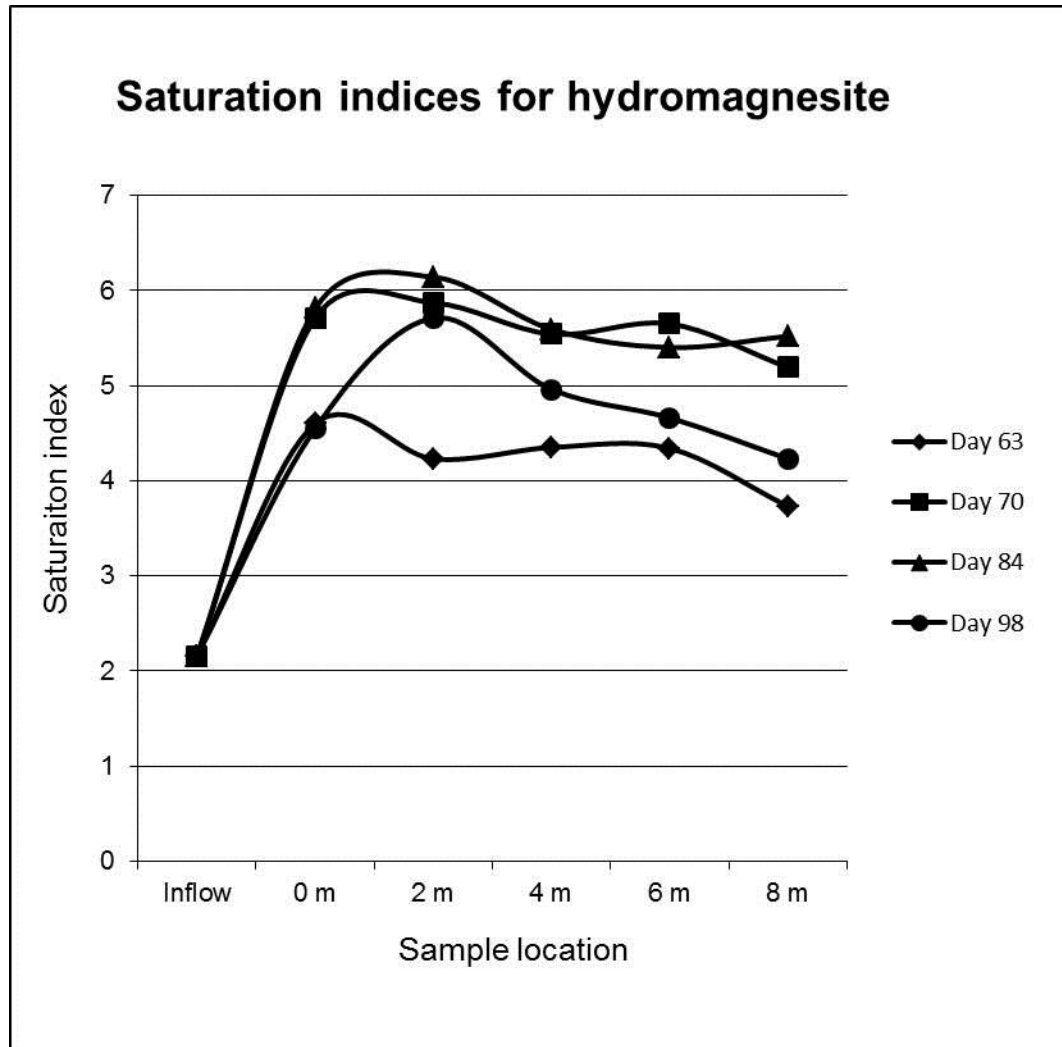
Figure 2.11 Saturation index values generated using PHREEQC for hydromagnesite by sampling point for four sets of chemistry data collected during the carbonation phase.
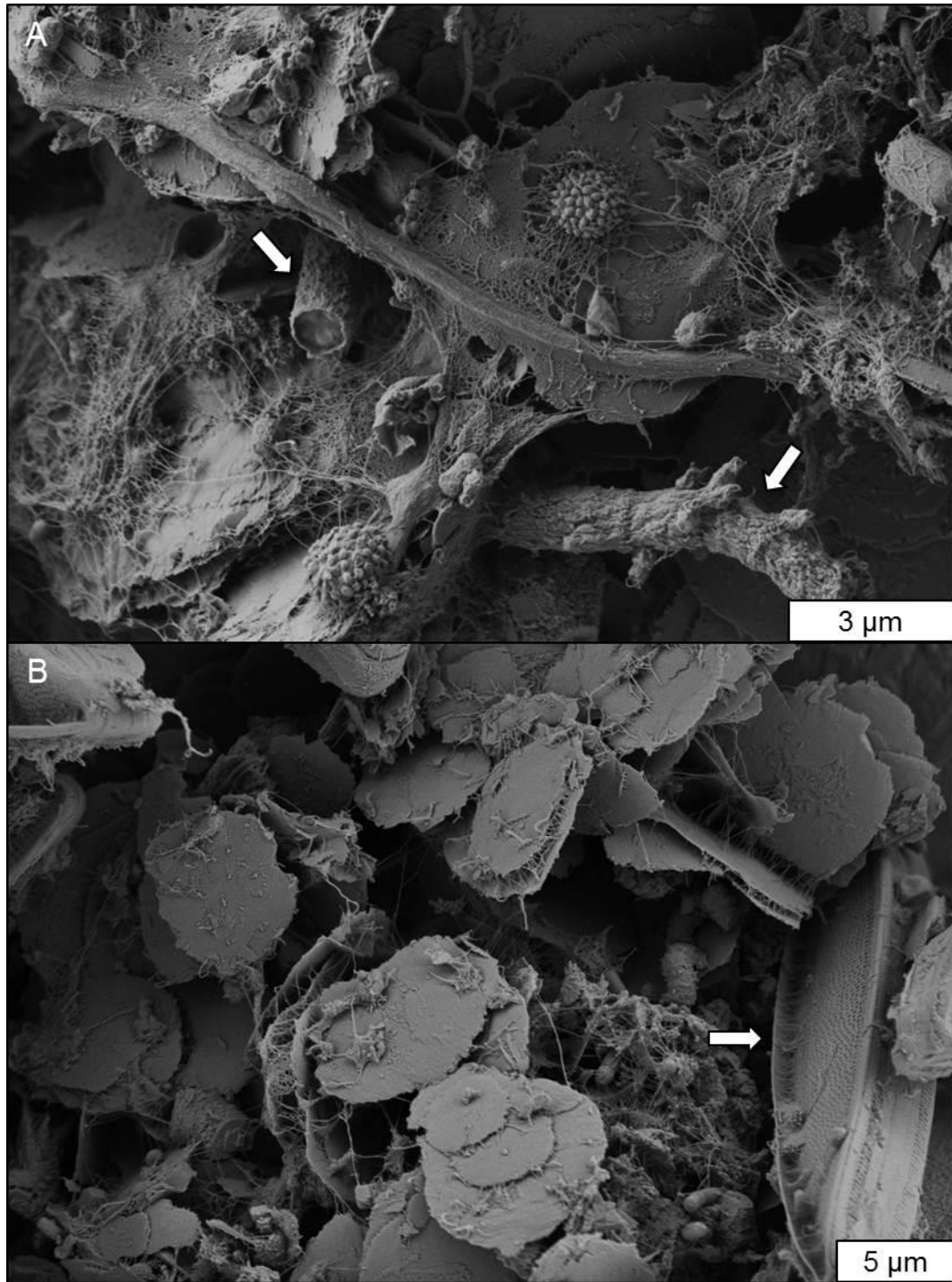
Figure 2.12 Scanning electron micrographs of microbial mat samples collected from the beginning of the bioreactor showing A) hydromagnesite crystals and cyanobacteria (arrows); B) platy hydromagnesite crystals and diatoms (arrow) coated in extracellular polymeric substances.
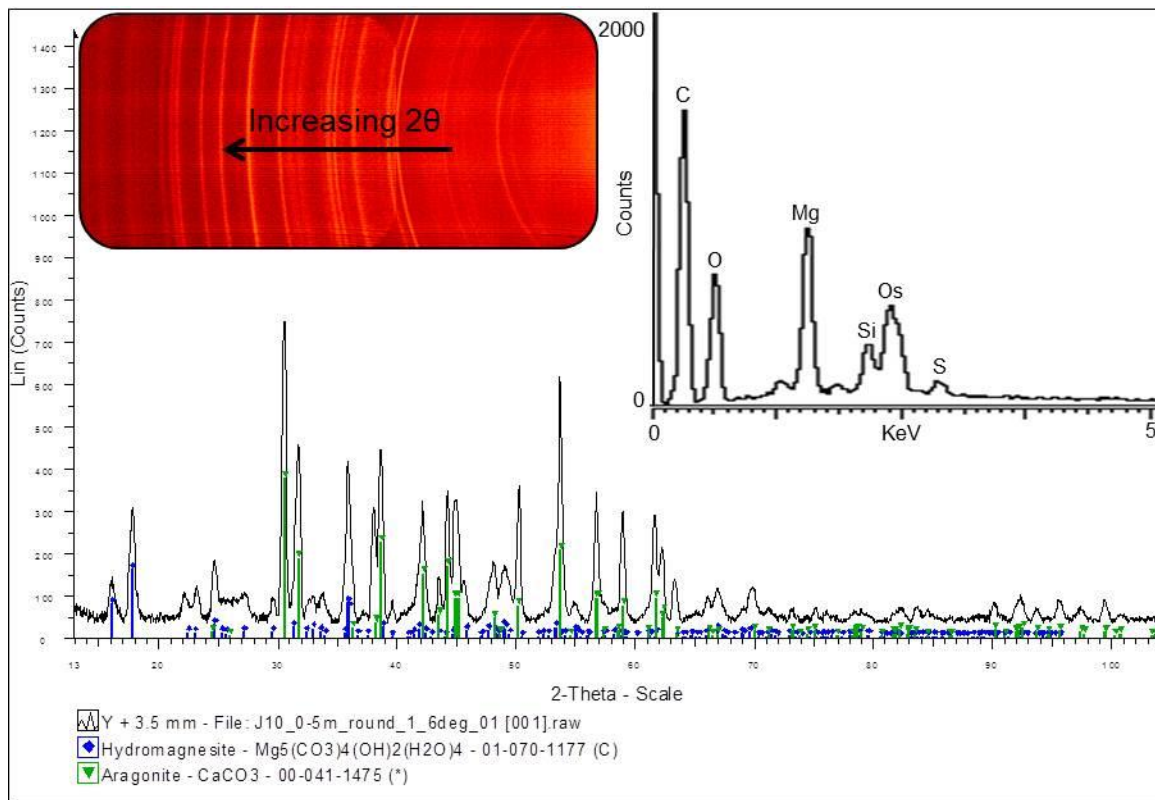
Figure 2.13 Micro X-ray diffraction pattern and General Area Detection Diffraction System (GADDS) image (left inset) of the hydromagnesite and aragonite identified in the microbial mat. Right inset: Spectrum indicating magnesium carbonate precipitation when the platy mineral crystals were analyzed with SEM-EDS.

Samples collected from 4 m and 8 m along the channel did not contain any evidence of new, surficial hydromagnesite mineralisation and less EPS than the 0.5 m sample (Figure 2.14). The 4 m sample was dominated by filamentous cyanobacteria with the same morphology as the 0.5 m sample; while filamentous cyanobacteria with cylindrical, helically coiled trichomes (cf. *Spirulina*) reaching 100 μm in length dominated the 8 m sample. These helical microbes were present in minor amounts in the upstream and midstream cultures. The 8 m mat contained much less EPS and few diatoms than the other two samples (Figure 2.14).

2.3.3   Abiotic control

Evaporative conditions in the abiotic control resulted in the formation of minor nesquehonite, comparable to that observed in the natural wetland, which was not observed in the bioreactor (Figure 2.15) (Power et al. 2007). This occurred after more than 12% of the water in the control flask had evaporated, and the pH of the remaining solution increased from 8.3 to 9.1.
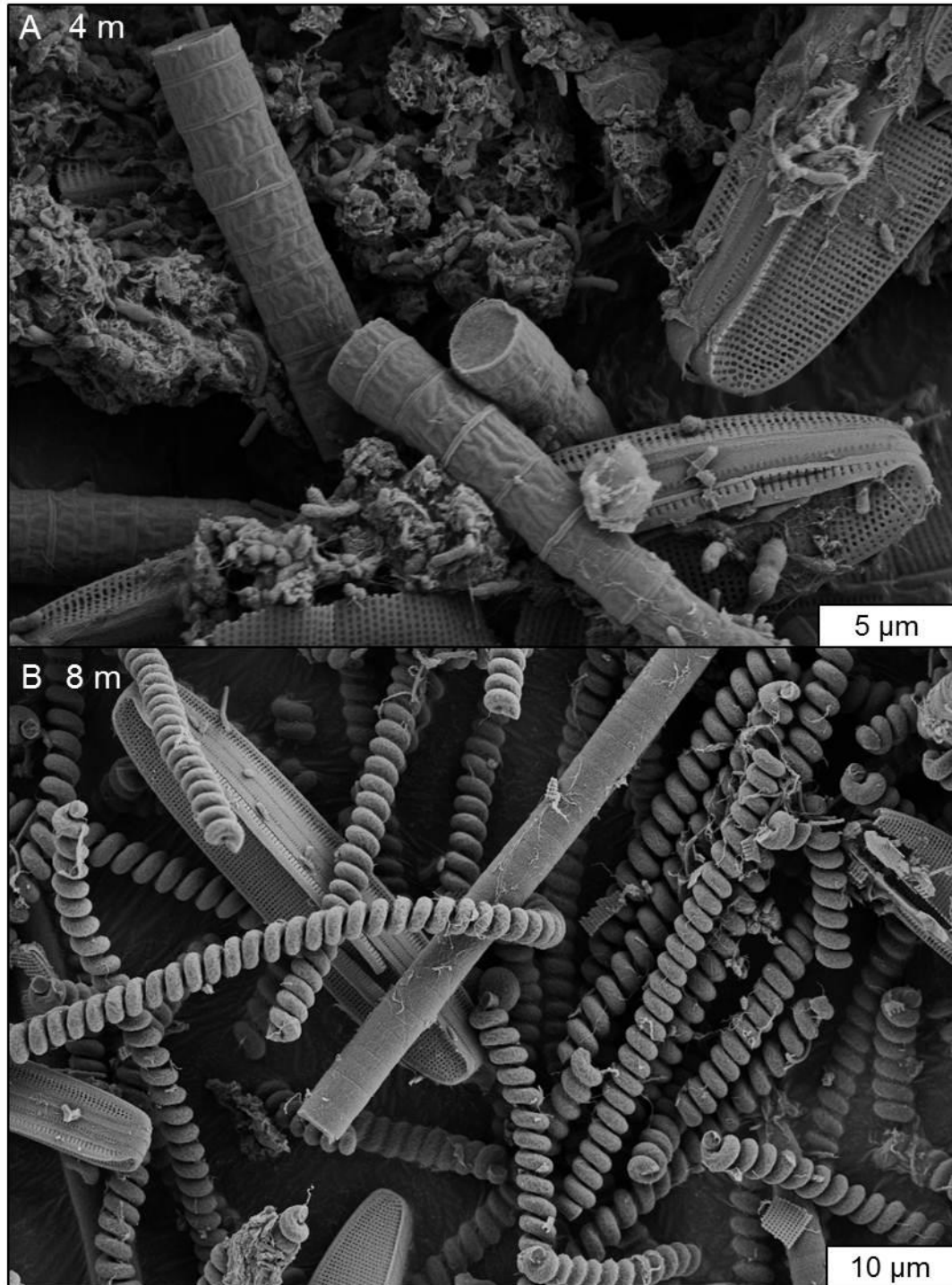
Figure 2.14 Scanning electron microscopy of A) cyanobacterial filaments and diatoms from a mat sample collected 4 m from the start of the bioreactor channel showing no evidence of carbonate precipitation; and B) helical cf. *Spirulina* cyanobacterial filaments and diatoms in the microbial mat sample collected from 8 m down the bioreactor channel.
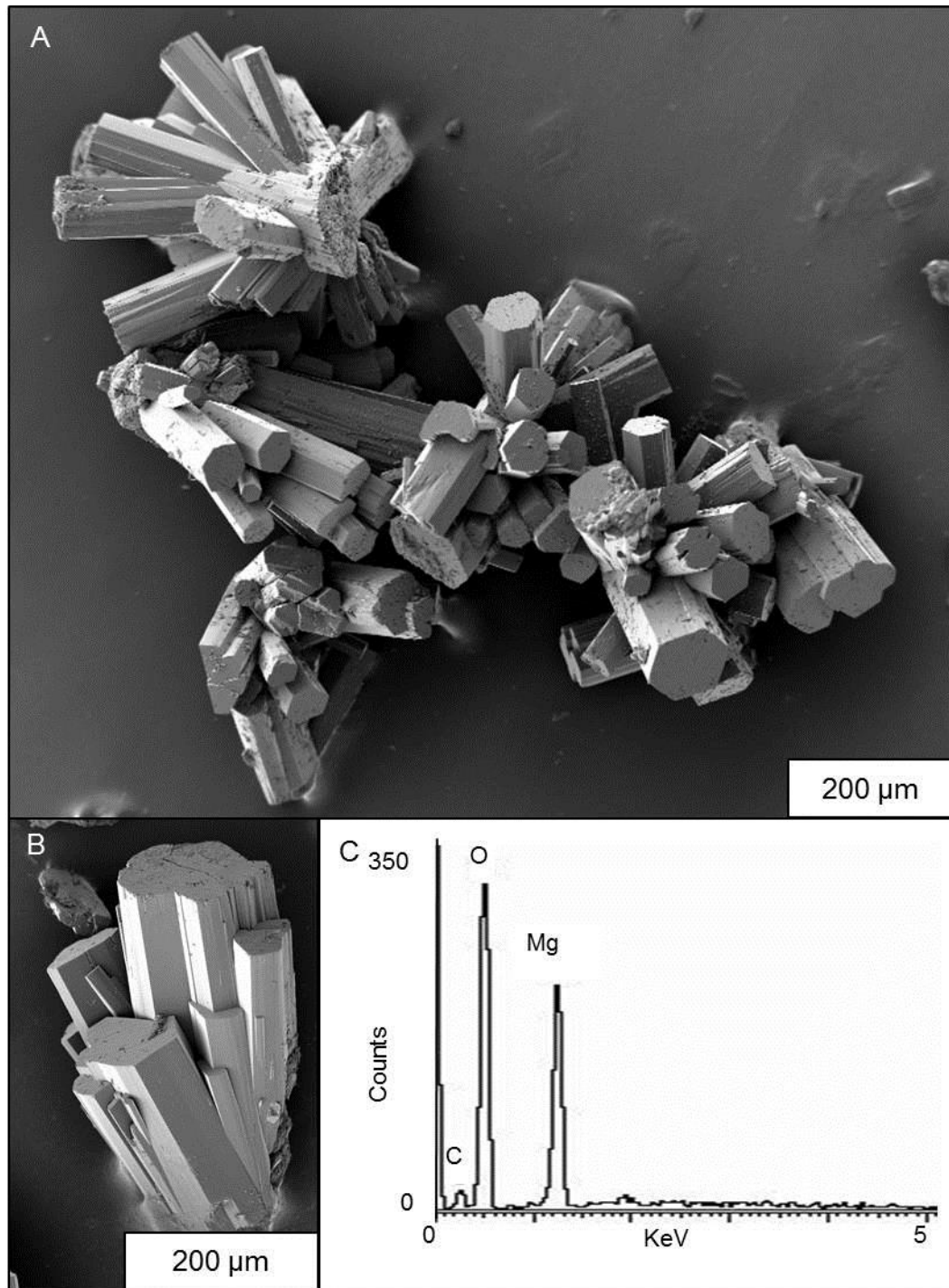
Figure 2.15 A) and B) Crystals of the mineral phase produced by the abiotic control which are comparable in morphology and C) chemistry to nesquehonite identified by Power et al. (2009) as an evaporative mineral at the Atlin field site.

2.4   **Discussion**

2.4.1   Water chemistry as an indication of carbonate mineral precipitation

The observed increase in pH and DO during the growth phase likely corresponds to an increase in photosynthetic activity in the system as the microbial community established itself in the bioreactor. The drop in DO during the first week of the carbonation phase may be due to the onset of carbonate mineral precipitation preventing photosynthesis by shielding the mats from sunlight. The increase in DO along the first 6 m of the bioreactor during the experiment likely corresponds to a decrease in the amount of carbonation taking place, allowing for uninhibited photosynthesis. This increase in photosynthetic activity is likely responsible for driving the pH up along the length of the bioreactor. Beyond 6 m, the observed DO decrease matches the lack of nutrients, particularly phosphate and nitrate, in the lower portion of the system; as well as an increase in the amount of heterotrophic metabolism taking place in the bioreactor.

The trends of pH and DO indicate that mineral precipitation from the inflow solution occurred immediately upon its addition to the start of the bioreactor. This is strongly complemented by evidence provided by the changes in conductivity, hardness, alkalinity, and dissolved magnesium concentration over the course of the carbonation phase. Conductivity and hardness were both used as indicators of the presence of magnesium, since it was the primary cation in the inflow solution. Both of these parameters exhibited a large decrease from the inflow solution value at the very start of the bioreactor channel. The alkalinity as mM of HCO_3^- and magnesium concentrations both demonstrated the same pattern.

The rate of decline of conductivity, hardness, alkalinity, and the concentrations of magnesium, phosphate, and nitrate decreased with increasing distance down the bioreactor (Figure 2.6-2.10). The similarity of how all of these parameters changed can be explained by the observations made with SEM, and is closely linked to mineral precipitation. The first 2 m of the bioreactor had access to the highest concentrations of nutrients allowing the most photosynthesis and growth. This microbial growth was accompanied by extensive EPS (extra-cellular polymeric substances) production. EPS is

important for both the chemical and physical conditions required for cyanobacterium accelerated carbonate mineralisation (Dittrich et al. 2003; Bissett et al. 2008; Obst et al. 2009a; Obst et al. 2009b; Power et al. 2011). Excess EPS, found in the upstream SEM sample, forms under nutrient-rich conditions and can generate localized microenvironments of cation supersaturation around cyanobacteria cells (Dittrich et al. 2003; Obst et al. 2009a; Obst et al. 2009b). Photosynthetically generated OH^- anions increases the pH value of the water directly around the cells, which increases the concentration of CO_3^{2-} resulting in increased carbonate supersaturation (Reactions 2 and 3) (Dittrich et al. 2003; Obst et al. 2009b; Power et al. 2011). This localized increase in alkalinity can increase pH of the water surrounding the cell by one unit in comparison to the pH measured for the system as a whole (Bissett et al. 2008). In addition, cations such as magnesium are attracted to the negatively charged surface of the microbial cells (Beveridge 1988). This localized combination of a high pH, dissolved carbonate, and magnesium ions in the first 2 m of the bioreactor resulted in the greatest amount of mineral carbonation observed in the system. The coupled generation of microbial biomass and mineral precipitation at the start of the bioreactor caused the large decline seen in so many of the parameters observed in this region of the system, in comparison to the downstream part of the model wetland. The lack of nutrients in the downstream portion of the bioreactor would have inhibited the generation of the biogeochemical conditions needed for carbonation through the lack of EPS production. This is consistent with other investigations, which have demonstrated that cyanobacteria generate less EPS under nutrient starved conditions (Obst and Dittrich 2005). In addition, previous studies have shown that carbonate precipitation is found only in cyanobacteria cultures in the growth phase of their life cycle, while no mineralisation takes place in stationary or dying cultures (Obst et al. 2009b). Cyanobacteria in the downstream portion of the bioreactor would have entered a stationary growth phase due to nutrient limitations. This progression of microbial growth habit is also reflected in the presence of diatoms in the bioreactor. The concentration of Si, critical to the formation of silica-based diatom frustules, decreased along the length of the system from the inflow concentration (1.872 mM) to 0.169 mM in the outflow solution (Table 2.1). This decrease coincides with the visible decline in diatom abundance down the length of the system.

The rate of magnesium addition to the system appears to have exceeded the rate of removal through mineral precipitation. This is evident by the continuous, linear increase in overall average magnesium concentration in the bioreactor (Figure 2.10B). A possible reason that mineralisation rate may have been restricted is the other role that EPS plays in carbonate precipitation, which is the generation of nucleation sites (Obst et al. 2009a; Obst et al. 2009b). Excess EPS produced during the growth phase would have stimulated hydromagnesite precipitation upon addition of the $Mg\text{-}HCO_3$ solution at the start of the carbonation phase. Once these biogenic nucleation sites became occupied by mineral crystals, further carbonate precipitation would have become dependent on the generation of new EPS.

Using the water chemistry data collected during the carbonation phase and the observations made with SEM, the SI values calculated for hydromagnesite can be explained. Since no hydromagnesite precipitated in the inflow solution, a SI value greater than 2.16 must be required for hydromagnesite to form. Based on the measured magnesium concentrations, hydromagnesite formation occurred at the very start of the carbonation phase in the upper portion of the bioreactor. At this time, the SI values for hydromagnesite were 4.6 and 4.23 for the 0 m and 2 m sampling points, respectively (Figure 2.11). This indicates that an SI value of ~ 4.2 is sufficient to induce hydromagnesite precipitation. It appears, however, that the conditions needed for mineral formation are far from straightforward. If an SI value of 4.2 was all that was needed for hydromagnesite precipitation, mineralisation would have been observed everywhere in the bioreactor, because all of the sampling points in the system exhibited an SI value greater than 4.2 at some point during the carbonation phase (Figure 2.11). Since hydromagnesite was not observed with SEM in all samples, another factor beyond water chemistry must play a role, one of which may be the availability of nucleation sites. At the beginning of the carbonation phase, the first few metres of the bioreactor had access to the highest concentrations of magnesium and dissolved carbon, as well as the most nutrients for the required EPS production. With all of these factors in place, hydromagnesite was able to form, even though the SI value was only ~4.2. This value, much lower than the maximum calculated SI value of 6.14, was sufficient for mineralisation. In contrast, on day 84, the 8 m sampling point had a SI value of 5.52, and

49

yet no hydromagnesite was observed in that location. Based on water chemistry alone, the conditions at that site should have been conducive to mineral precipitation, but the lack of nucleation sites, resulting from nutrient limiting conditions prevented hydromagnesite formation.

Another potential cause of this discrepancy in carbonate mineralisation is the balance between the three chemical factors on which the hydromagnesite saturation index is primarily dependent: magnesium concentration, dissolved inorganic carbon concentration (alkalinity), and pH. Different solution chemistries can have the same SI value through the balance between these factors. For instance, on day 70, the 6 m point in the bioreactor had a pH of 9.21, a magnesium concentration of 17.81 mM, and an alkalinity of 56.0 mM; resulting in a SI value of 5.65. In contrast, the 2 m sampling point on day 98 had a pH of 9.09, a magnesium concentration of 38.06 mM, and an alkalinity of 57.50 mM; generating a SI value of 5.71. Although these SI values are similar, they are generated by different chemistries. It appears that a higher pH is sufficient to drive up the SI value in the case of a lower magnesium concentration and a lower alkalinity, but does not actually compensate by resulting in successful hydromagnesite formation. All three factors must be optimised for magnesium carbonation mineralisation.

2.4.2   *Quantifying mineral precipitation rate*

The mineralisation rate was used to determine the rate of carbon storage in the precipitated hydromagnesite. The maximum rate of hydromagnesite precipitation achieved within the upper 2 m of the bioreactor during the first week (13.1 g/day) translates to a carbon storage rate of 33 t of C/ha/year in combined mineral and biological storage (Reaction 4-13). The average rate for the first 2 m of the bioreactor (7.7 g/day) over the course of the experiment was 16 t of C/ha/year. Based on the nutritional analysis, the bioreactor has potential for greater carbon storage if the biogeochemical conditions in the system are modified to encourage continued growth of cyanobacteria to enable magnesium carbonation throughout the entire system. Improving nutrient availability in the system would increase photosynthesis, EPS production, and alkalinity, would thus result in a greater carbonation rate.

$$Average\ inflow\ [Mg^{2+}]\ -\ day\ 63\ [Mg^{2+}]\ at\ 2\ m\ sampling\ location = [Mg^{2+}] \quad (4)$$
$$removed\ from\ solution$$
$$971.0\ mg/L - 286.9\ mg/L = 684.1\ mg/L$$

$$[Mg^{2+}] \times volume = mass\ of\ Mg\ removed\ from\ solution \quad (5)$$
$$684.1\ mg/L \times 35.00\ L = 23944\ mg = 23.94\ g$$

$$Mass\ Mg \div molar\ mass\ Mg = moles\ Mg\ removed\ from\ solution \quad (6)$$
$$23.94\ g \div 24.305\ g/mol = 0.9850\ mol\ of\ Mg$$

$$5\ Mg\ atoms\ needed\ per\ crystal\ of\ hydromagnesite\ produced: \quad (7)$$
$$Moles\ Mg \div 5 = moles\ hydromagnesite\ produce = 0.9850\ mol \div 5 = 0.1970$$
$$mol$$

$$10\ CO_2\ consumed\ for\ every\ hydromagnesite\ produced: \quad (8)$$
$$0.1970\ mol \times 10 = 1.970\ mol\ CO_2\ consumed$$

$$Moles\ CO_2 \times molar\ mass\ of\ CO_2 = mass\ of\ CO_2\ consumed \quad (9)$$
$$1.970\ mol \times 44\ g/mol = 86.69\ g\ CO_2\ consumed$$

$$Mass\ of\ CO_2 \div microbial\ mat\ surface\ area = mass\ CO_2\ consumed/unit\ area \quad (10)$$
$$86.69\ g \div 0.37\ m^2 = 234.3\ g/m^2$$

$$Duration = 7\ days,\ annual\ rate: \quad (11)$$
$$234.3\ g/m^2 \times (365/7) = 12217\ g\ of\ CO_2/m^2/year = t\ of\ CO_2/km^2/year$$

$$In\ hectares/year: \quad (12)$$
$$12217\ t\ of\ CO_2/km^2/year \div 100 = 122.17\ g\ of\ CO_2/ha/year$$

$$Annual\ rate \times (molar\ mass\ of\ C \div molar\ mass\ of\ CO_2)\ as\ tonnes: \quad (13)$$
$$122.17\ g\ of\ CO_2/ha/year \times (12.01\ g/mol \div 44.01\ g/mol) = 33.34\ t\ of\ C/ha/year$$

2.4.3 Applications to carbon sequestration

Similar to other studies of microbially generated carbonates, the potential for stable carbon storage observed in this study may have applications to mining operations that produce ultramafic tailings (Wilson et al. 2009; Power et al. 2010; Ramanan et al. 2010). Large-scale storage of CO_2 in carbonate minerals could be achieved if magnesium leached from the tailings was made accessible to a microbial consortium similar to that used in this study (Power et al. 2010). This could be achieved by developing a 'carbonation pond' containing these microbes, which would, in turn, facilitate carbonate mineralisation using atmospheric CO_2 and magnesium leached from the tailings. This

method of carbon sequestration is of particular interest because it represents an inexpensive, low risk, long-term storage strategy; and would provide mining operations with a method for reducing their net greenhouse gas emissions.

2.5   Conclusion

The biogeochemical conditions of the field site wetland were successfully re-created in the greenhouse bioreactor. The microbial community used in this experiment enabled magnesium carbonation precipitation in the form of hydromagnesite platelets. The water chemistry data collected demonstrated the importance of both chemical and physical factors to carbonate precipitation. A high magnesium concentration and high alkalinity are required along with a high pH (>9) in order to create the degree of supersaturation needed for hydromagnesite formation. These conditions can occur in the form of microenvironments directly around microbial cells. The most important physical factor for mineralisation is the presence of nucleation sites, which in this case occurred as EPS generated in locations rich in essential nutrients. The fastest rate of hydromagnesite precipitation documented in the bioreactor translated to a carbon sequestration rate of 33 t C/ha/year. This model has the potential to achieve a greater carbon storage rate if the nutrient availability is increased throughout the system, allowing for continuous microbial growth and EPS production. This biogeochemical process has potential as a carbon storage strategy at mine sites with magnesium-rich, ultramafic tailings.

2.6   References

Aloisi, G. 2008. The calcium carbonate saturation state in cyanobacterial mats throughout Earth's history. Geochimica et Cosmochimica Acta, **72**: 6037-6060.

Bea, S.A., Wilson, S.A., Mayer, K.U., Dipple, G.M., Power, I.M., and Gamazo, P. 2012. Reactive transport modeling of natural carbon sequestration in ultra-mafic mine tailings. Vadose Zone Journal, **11**.

Beveridge. T.J. 1988. The bacterial surface - general considerations towards design and function. Canadian Journal of Microbiology, **34**: 363-372.

Bissett, A., Reimer, A., de Beer, D., Shiraishi, F., and Arp, G. 2008. Metabolic microenvironmental control by photosynthetic biofilms under changing macroenvironmental temperature and pH conditions. Applied Environmental Microbiology, **74**: 6306-6312.

Braithwaite, C.J.R. and Zedef, V. 1994. Living hydromagnesite stromatolites from Turkey. Sedimentary Geology, **92**: 1-5.

Dittrich, M., Müller, B., Mavrocordatos, D., and Wehril, B. 2003. Induced calcite precipitation by cyanobacterium Synechococcus. Acta Hydrochimica Hydrobiologica, **31**: 162-169.

Drew, G.H. 1913. On the precipitation of calcium carbonate in the sea by marine bacteria, and on the action of denitrifying bacteria in tropical and temperate seas. Journal of Marine Biology Association UK, **9**: 479-524.

Gerdemann, S.J., O'Connor, W.K., Dahlin, D.C., Penner, L.R., and Rush, H. 2007. Ex situ aqueous mineral carbonation. Environmental Science and Technology, **41**: 2587-2593.

Hansen, L.D., Dipple, G.M., Gordon, T.M., and Kellett, D.A. 2005. Carbonated serpentinite (listwanite) at Atlin, British Columbia: A geological analogue to carbon dioxide sequestration. Canadian Mineralogist, **43**: 225-239.

Harrison, A.L., Power, I.M., and Dipple, G.M. 2013. Accelerated carbonation of brucite in mine tailings for carbon sequestration. Environmental Science & Technology, **47**: 126-134.

IPCC, 2007. Climate Change 2007: The physical science basis. Contribution of Working Group I to the Fourth Assessment Report of the Intergovernmental Panel on Climate Change [Solomon, S., Qin, D., Manning, M., Chen, Z., Marquis, M., Averyt, K.B., Tignor, M., and Miller, H.L. (eds)]. Cambridge University Press, Cambridge, United Kingdom and New York, NY, USA, pp. 96.

Kenward, P.A., Goldstein, R.H., González, L.A., and Roberts J.A. 2009. Precipitation of low-temperature dolomite from an anaerobic microbial consortium: the role of methanogenic Archaea. Geobiology, **7**: 556-565.

Köhler, P., Hartmann, J., and Wolf-Gladrow, D.A. 2010. Geoengineering potential of artificially enhanced silicate weathering of olivine. Proceedings of the National Academy of Sciences of the United States of America, **107**: 20228-20233.

Kranz S.A., Wolf-Gladrow, D., Nehrke, G., Langer, G., and Rost, B. 2010. Calcium carbonate precipitation induced by the growth of the marine cyanobacterium. *Trichodesmium*. Limnology and Oceanography, **55**: 2563-2569.

Lacis, A.A., Schmidt, G.A., Rind, D., and Ruedy, R.A. 2010. Atmospheric CO_2: Principle control knob governing Earth's temperature. Science, **330**: 356-359.

Lackner, K.S., Wendt, C.H., Butt, D.P., Joyce Jr., E.L., and Sharp, D.H. 1995. Carbon dioxide disposal in carbonate minerals. Energy, **20**:1153-1170.

Lahav, O., Morgan, B.E., and Loewenthal, R.E. 2001. Measurement of pH, alkalinity and acidity in ultra-soft waters. Water SA, **27**: 423-431.

López-García P., Kazmierczak, J., Benzerara, K., Kempe S., Guyot, F., and Moreira, D. 2005. Bacterial diversity and carbonate precipitation in the giant microbialites from the highly alkaline Lake Van, Turkey. Extremophiles, **9**: 263-274.

Obst, M., Dittrich M. 2005. Living under an atomic force microscope: An optimized approach for *in vivo* investigations on surface alterations towards biomineral nucleation on cyanobacterial cells. Geobiology, **5**: 179-193.

Obst, M., Wehrli, B., and Dittrich, M. 2009. $CaCO_3$ nucleation by cyanobacteria: Laboratory evidence for a passive, surface-induced mechanism. Geobiology, **7**: 324-347.

Obst, M., Dynes, J.J., Lawrence, J.,R., Swerhone, G.D.W., Benzerara, K., Karunakaran, C., Kaznatcheev, K., Tyliszczak, T. and Hitchock, A.P. 2009. Precipitation of amorphous $CaCO_3$ (aragonite-like) by cyanobacteria: A STXM study of the influence of EPS on the nucleation process. Geochimica et Cosmochimica Acta. **72**: 4180-4198.

Parkhurst, D.L. and Appelo, C.A.J. 1999. User's guide to PHREEQC (version 2) - A computer program for speciation, batch-reaction, one-dimensional transport and inverse geochemical calculations. Water-Resources Investigations Report 99-4259, U.S. Geologic Survey, Denver.

Peters, K.E., Walters, C.C., and Moldowan, J.M. 2005. *The Biomarker Guide Volume I Biomarkers and Isotopes in the Environment and Human History*; Cambridge University Press: Cambridge, U.K., pp 1155.

Power, I.M., Wilson, S.A., Thom, J.M., Dipple, G.M., and Southam, G. 2007. Biologically induced mineralisation of dypingite by cyanobacteria from an alkaline wetland near Atlin, British Columbia, Canada. Geochemical Transactions, **8**: 13.

Power, I.M., Wilson, S.A., Thom, J.M., Dipple, G.M., Gabites, J.E., and Southam, G. 2009. The hydromagnesite playas of Atlin, British Columbia, Canada: A biogeochemical model for CO_2 sequestration. Chemical Geology, **260**: 286-300.

Power, I.M., Dipple, G.M., and Southam, G. 2010. Bioleaching of ultramafic tailings by *Acidithiobacillus* spp. for CO_2 sequestration. Environmental Science & Technology, **44**: 456-462.

Power, I.M., Wilson, S.A., Small, D.P., Dipple, G.,M.; Wan, W.K., and Southam, G. 2011. Microbially mediated mineral carbonation: Roles of phototrophy and heterotrophy. Environmental Science & Technology, **45**: 9061-9068.

Ramanan, R., Kannan, K., Deshkar, A., Yadav, R., and Chakrabarti, T. 2010. Enhanced algal CO_2 sequestration through calcite deposition by *Chlorella* sp. *Spirulina platensis* in a mini-raceway pond. Bioresource Technology, **101**: 2616-2622.

Renaut, R.W. 1993. Morphology, distribution, and preservation potential of microbial mats in the hydromagnesite-magnesite playas of the Cariboo Plateau, British Columbia, Canada. Hydrobiologia, **267**: 75-98.

Renforth, P. 2012. The potential of enhanced weathering in the UK. International Journal of Greenhouse Gas Control, **10**: 229-243.

Renforth, P., and Manning, D.A.C. 2011. Laboratory carbonation of artificial silicate gels enhanced by citrate: Implications for engineered pedogenic carbonate formation. International Journal of Greenhouse Gas Control, **5**: 1578-1586.

Riding, R. 2000. Microbial carbonates: the geological record of calcified bacterial-algal mats and biofilms. Sedimentology, **47**: 179-214.

Roberts, J.A., Bennett, P.C., González, L.A., Macpherson, G.L., and Milliken, K.L. 2004. Microbial precipitation of dolomite in methanogenic groundwater. Geology, **32**: 277-180.

Schuiling, R.D. and Krijgsman, P. 2006. Enhanced weathering: An effective and cheap tool to sequester CO_2. Climatic Change, **74**: 349-354.

Seifritz, W. 1990. CO_2 disposal by means of silicates. Nature, **345**: 486.

Shiraishi, F. 2012. Chemical conditions favoring photosynthesis-induced $CaCO_3$ precipitation and implications for microbial carbonate formation in the ancient ocean. Geochimica et Cosmochimica Acta, **77**: 157-174.

Thompson, J.B. and Ferris, F.G. 1990. Cyanobacterial precipitation of gypsum, calcite, and magnesite from natural alkaline water. Geology, **18**: 995-998.

van Lith, Y.; Warthmann, R.; Vasconcelos, C.; Mckenzie, J.A. 2003. Sulfate-reducing bacteria induce low-temperature Ca-dolomite and high Mg-calcite precipitation. Geobiology, **1**: 71-79.

Vonshak, A. 1986. Laboratory techniques for the cultivation of microalgae. In: Richmond, A. (eds). CRC handbook of microalgae mass culture. CRC Press Inc., Bocca Raton, pp. 117.

Washbourne, C.L., Renforth, P., and Manning, D.A.C. 2012. Investigating carbonate formation in urban soils as a method for capture and storage of atmospheric carbon. Science of the Total Environment, **431**: 166-175.

Wilson, S.A., Raudsepp, M., and Dipple, G.M. 2006. Verifying and quantifying carbon fixation in minerals from serpentine-rich mine tailings using the Rietveld method with X-ray powder diffraction data. American Mineralogist, **91**: 1331-1341.

Wilson, S.A., Dipple, G.M., Power, I.M., Thom, J.M., Anderson, R.G., Raudsepp, M., Gabites, J.E., and Southam, G. 2009. Carbon dioxide fixation within mine wastes of ultramafic-hosted ore deposits: Examples from the Clinton Creek and Cassiar chrysotile deposits, Canada. Economic Geology, **104**: 95-112.

Chapter 3

3 Optimization of bioreactor conditions for carbon dioxide sequestration in magnesium carbonate minerals

3.1 Introduction

Fossil fuels combustion since the start of the Industrial Revolution in the mid-1700s has caused the concentration of atmospheric carbon dioxide (CO_2) to increase from 280 ppm to 390 ppm and is resulting in a range of environmental problems (IPCC 2007; Lacis et al. 2010). Research investigating strategies for sequestering carbon is being conducted, with geologic storage in carbonate minerals being of particular interest due to the stability and longevity of these minerals as a carbon sink over geologic time (Wilson et al. 2009a; Köhler et al. 2010; Power et al. 2010; Power et al. 2011a; Renforth and Manning 2011; Bea et al. 2012; Renforth 2012; Washbourne et al. 2012; Harrison et al. 2013). Carbonation of ultramafic rocks, particularly serpentine, has potential to act as a large carbon sink due to the abundance of serpentine on Earth's surface (Park et al. 2003; Wilson et al. 2009b). This process happens slowly when occurring at natural, abiotic rates; however, it can be accelerated in the presence of certain microorganisms. Previous studies have demonstrated, on a small-scale, the ability of some phototrophic microbes to increase the rate of magnesium carbonate mineral precipitation from ultramafic mine tailings, with the tailings acting as the source of magnesium (Power et al. 2009; Power et al. 2010; Power et al. 2011b). Ultramafic tailings are a waste product of many large-scale nickel, diamond, and asbestos mining operations. It has been proposed that they could be utilised by mining companies as a method to reduce net carbon emissions due to the large volumes of tailings produced annually.

Carbonate mineral formation in ultramafic tailings has been studied in detail at several mine sites around the world (Al et al. 2000; Paktunc and Davé, 2002; Huot et al., 2003; Wilson et al., 2009a; Wilson, et al. 2009b; Wilson et al. 2010). These tailings provide an excellent substrate for carbonate mineralisation because the ore extraction process significantly increases the surface area of the tailing minerals (White et al., 1996; Molson

et al., 2005). Increased exposure of reactive surfaces allows for higher weathering and carbonation reaction rates than those observed for natural, ultramafic bedrock. Due to their stability, carbonate minerals will likely be the final sink for a large proportion of the CO_2 produced by human activity over a timeframe of 1 Ma (Seifritz, 1990; Lackner et al., 1995; Kump et al. 2000; Lackner, 2003). As a result, various methods of accelerating mine tailing carbonation reactions have been explored. Passive carbonation has been observed at active and historic tailing storage sites with the potential for greater carbonate mineralisation rates if the geochemical conditions needed for mineral formation are encouraged (Wilson 2009; Wilson et al. 2009a; Wilson et al. 2009b; Wilson et al. 2010; Wilson et al. 2011; Pronost et al. 2011). Passive carbonate mineral formation has been documented in milled chrysotile waste rock piles at Clinton Creek Asbestos Mine (Yukon, Canada), Cassiar (British Columbia, Canada), Black Lake Mine (Québec, Canada); processed kimberlite at the Diavik Diamond Mine (Northwest Territories, Canada); and Mount Keith Nickel Mine (Western Australia). The carbonates found at these sites consist primarily of hydrated magnesium carbonate minerals.

High temperature and pressure industrial processes for mineral carbonation have been studied for a range of geologic materials (Zevenhoven et al. 2008; Fagerlund et al. 2009; Koukouzas et al. 2009; Lammers et al. 2011). Exposure of materials such as basalt, serpentine, steel slag, and iron oxyhydroxides to elevated temperatures (600°C) and highly pressurized (160 bar) CO_2 results in rapid carbonate mineral formation. Although this strategy of sequestering CO_2 in carbonates is effective, it is currently not practical for large scale use due to the financial and energy resources required. Consequently, other methods of carbonate mineral acceleration are being examined.

Injection of CO_2 into tailings piles is a low temperature and pressure method of abiotically increasing carbonation reaction rates (Harrison et al. 2013). Increasing the concentration of CO_2 accelerates carbonate mineralisation by increasing the acidity of the system, which in turn increases the rate of weathering of the tailings and cation availability for carbonate mineral precipitation reactions. The other, more beneficial result of CO_2 injection is the increased availability of CO_2, which is the rate-limiting factor in carbonate mineralisation (Vermilyea 1969; Pokrovsky and Schott 2000;

Pokrovsky and Schott 2004; Wilson et al. 2010; Harrison et al. 2013). Carbonation rate is dependent on the proportion of CO_2 in the injection gas, the humidity of the gas, and temperature (Pronost et al. 2011). A challenge for utilising this method at a tailings facility is developing the infrastructure required for transporting CO_2 to the tailings pile and successfully injecting it into the tailings. As with any method of carbon storage involving concentrated CO_2, the concern of a large-scale CO_2 leak would have to be addressed.

Biological methods of accelerating mine tailings carbonate mineralisation rates have also been explored (Power et al. 2010; Power et al. 2011a; Power et al. 2011b). The ability of microbes to generate the alkaline water conditions needed for carbonate mineral supersaturation have been studied in natural systems. Cyanobacteria produce hydroxyl (OH^-) anions through photosynthesis, driving up the pH of the water. The hydroxyl ions react with bicarbonate to form water and carbonate ions [CO_3^{2-}] which can subsequently react with divalent cations to form minerals (Pentecost 1995; Thompson and Ferris 1990). This process is also aided by the physical presence of the microbes, which can act as nucleation sites by attracting cations to the net negative charge on the surface of cells (Schultze-Lam et al. 1996). Cations such as magnesium are able to attach to negatively charged extracellular organics possessing carboxyl groups, generating a microenvironment with a high magnesium concentration immediately around the cell (Nothdurft et al. 2005; Power et al. 2009). A high magnesium concentration is important because free magnesium in solution is generally surrounded by a hydration shell of six water molecules in octahedral coordination (Kluge and Weston 2005). Disrupting the hydration shell is important as it allows the magnesium to react with carbonate ions in carbonate mineralisation reactions.

3.1.1   *Description of Chrysotile Sampling Site*

The Clinton Creek Asbestos Mine in Yukon Territory, Canada is located 77 km northwest of Dawson City (Figure 3.1). Between 1967 and 1978 Cassiar Asbestos Corporation Limited mined chrysotile asbestos from four open pits at this location, producing 60 million tons of tailings over the life of the mine at an average stripping ratio of 11:2 (Wilson 2010; Yukon Government 2010). The bedrock is composed of

serpentinite and peridotite (harzbergite, lherzolite, dunite, and pyroxenite) (Htoon 1979). Most of the peridotite has been serpentised to chrysotile and antigorite, with the fibrous chrysotile present in veins cutting through the non-fibrous serpentine wall rock.

Carbonate minerals found in the Clinton Creek tailings include nesquehonite [$MgCO_3 \cdot 3H_2O$], dypingite [$Mg5(CO_3)_4(OH)_2 \cdot 5H_2O$], and hydromagnesite [$Mg5(CO_3)_4(OH)_2 \cdot 4H_2O$] (Wilson et al. 2009b). Nesquehonite is found as an evaporative crust, while dypingite and hydromagnesite have been observed as cement between silt- to cobble-sized serpentinite grains within the tailings.

In addition to the magnesium carbonate mineralisation found in the tailings piles at Clinton Creek Mine, more unique carbonate mineralisation is present in the form of microbialites (Power et al. 2011a). 'Microbialite' is a term given to organo-sedimentary structures in which sediments are trapped, bound, and/or precipitated by microbial activity (Burner and Moore 1987; Winsborough and Golubic 1987). These structures are found in the Porcupine Pit pond and could only have formed after the mine closed in 1978 (Power et al. 2011a). The microbialites are primarily composed of aragonite, which appears to begin growth as acicular crystals. These engulf microorganisms such as diatoms, algae, and cyanobacteria, preserving them in the sedimentary structure. Macroscopically, the microbialites are columnar, reaching 15 cm in height; and exhibit a mm-scale spherical texture (Power et al. 2011a).

This study quantifies the removal of magnesium from ultramafic mine tailings in leaching reactions with sulfuric acid. The resulting solution chemistry was used as a precursor for biogenic magnesium carbonation reactions using a phototrophic, halophilic microbial consortium. Using a linear experimental design; changes in water chemistry, mineralogy, and the microbial community were examined over space and time. This information was used to determine the rate of carbon storage. In contrast to the carbonation experiment completed in Chapter 2, no soluble inorganic carbon was provided for the carbonate precipitation reactions, forcing the system to utilise atmospheric CO_2. Magnesium was added at a concentration five times higher than in Chapter 2, 'challenging' the carbonation abilities of the system. To combat the nutrient limitation conditions

documented in the first carbonation experiment, a higher nutrient concentration was added to the bioreactor in two locations during this experiment, in an attempt to stimulate carbonate mineral formation throughout the system.
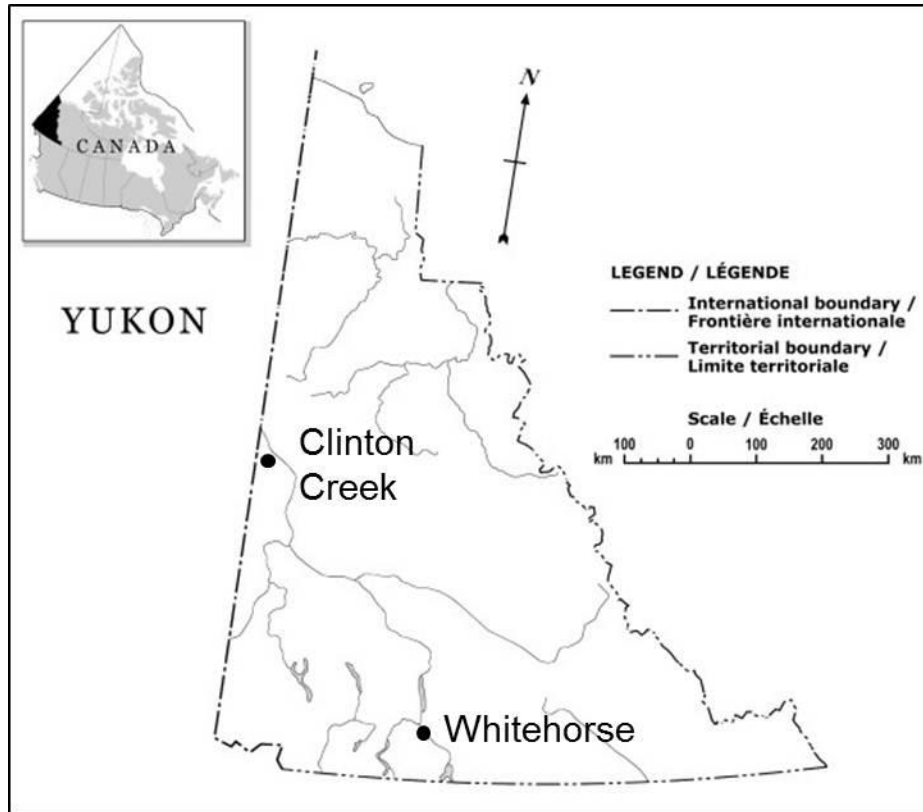
Figure 3.1 Location of the Clinton Creek chrysotile mine located in Yukon Territory, Canada (modified from Natural Resources Canada).

Figure 3.2 A) The Porcupine open pit and B) tailings pile at Clinton Creek Mine, Yukon, Canada. C) Veins of chrysotile fibres cutting through the serpentine wall rock at Clinton Creek.

3.2   **Methods**

3.2.1   *Characterisation of chrysotile samples*

A TM Engineering Ltd. ring mill was used to powder 50 g of chrysotile fibres collected from the Porcupine open pit at Clinton Creek Asbestos Mine. Major oxide composition and loss on ignition (LOI) of this material were determined for a 2.0 g sample via X-ray fluorescence (XRF) using a PANalytical PW-2400 Wavelength Dispersive X-ray Fluorescence Spectrometer at the Biotron Institute for Experimental Climate Research Analytical Chemistry Facility. X-ray diffraction (XRD) was used to determine mineral composition for a 2.0 g sample of powdered chrysotile using a Bruker D8 Focus Bragg-Brentano diffractometer at the University of British Columbia. A step size of $0.03°$ over a range of $3\text{-}80°2\theta$ was used with a dwell time of 0.7 s/step. This machine is equipped with a long fine focus Co X-ray tube, which was operated at 35 kV and 40 mA with a take-off angle of $6°$. A Lynx Eye positive sensitive detector was used to collect the data. Mineral phases were determined by interpreting the raw data using DIFFRAC^{plus} Eva software.

Polished thin sections of rock samples collected from the mine site were examined with plane polarised, cross polarised, and reflected light microscopy using a Nikon Eclipse LV 100 POL petrographic microscope at the High Resolution Earth and Planetary Materials Imaging Facility in the Department of Earth Sciences. Samples were characterised in terms of grain size, shape, and textural features. Thin sections were also examined by scanning electron microscopy and energy dispersive spectroscopy (SEM-EDS) using a Zeiss Leo 1540 XB microscope equipped with an Oxford Instruments INCA x-sight energy dispersive spectrometer for elemental analysis. The sections were coated with 10 nm of osmium using a Filgen OPC80T osmium plasma coater prior to SEM-EDS at 10 kV and a working distance of 12 mm.

3.2.2   *Leaching experiment*

Seven leaching experiments were conducted in 125 mL Erlenmeyer flasks, each containing 5 g of the powdered chrysotile and 100 mL of liquid. The acid concentrations were selected to create molar acid/chrysotile ratios of 0.25, 0.5, 1, 2, 3, and 4. Throughout the results of this experiment, the flasks will be identified by their

acid/chrysotile ratios. A flask containing chrysotile and 100 mL of E-Pure ddH$_2$O acted as a control. The flasks were placed on a New Brunswick Scientific shaker table operating at 100 rpm. The pH of each flask was measured at the start of the experiment, followed by pH measurements at 4 h, 8 h, 24 h, followed by daily measurements for 3 weeks, and then intermittent measurements over the following 3 weeks until the all of the flasks reached equilibrium as indicated by a constant pH. This leaching reaction consumes protons from the acid releasing soluble magnesium (Equation 1) (Stumm 1992; Park and Fan 2004).

$$Mg_3Si_2O_5(OH)_4 + 3\ H_2SO_4 \rightarrow 3\ Mg^{2+} + 2\ Si(OH)_4 + H_2O + 3\ SO_4^{2-} \qquad (4)$$
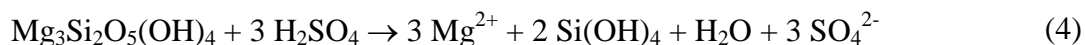
3.2.3   *Post-experiment characterisation of the tailings*

Once the flasks reached equilibrium, a sample of the solid material in each flask was filtered first using Whatman® No. 1 filter paper and then Whatman® 0.45 μm sterile cellulose nitrate membrane filters using a vacuum system. Each sample was air dried at room temperature for 120 h, after which it was powdered using the ring mill. This material was analysed for major oxides and LOI using XRF to allow for comparison to the pre-experiment chemical composition. The chemically weathered chrysotile fibres were characterised using SEM-EDS with the same microscope described above. For this analysis, fibres were mounted on Electron Microscopy Sciences stainless steel stubs with adhesive carbon tabs and coated with 5 nm of osmium. The SEM was operated at 1 kV and a working distance of 4 mm for imaging, and 10 kV and a working distance of 8 mm for EDS analysis.

Water samples collected from each flask were filtered using 0.1 μm Fisherbrand® syringe filters and submitted for cation and anion concentration analysis. Cation analysis was completed using inductively coupled plasma-atomic emission spectroscopy (ICP-AES) with a Perkin-Elmer Optima 300DV, while a Dionex IC 3000 equipped with a Dionex IonPac AS14A column (4 × 250 mm) was used for anion analysis by ion chromatography (IC). Ion concentrations were measured with the following detection limits and measurement uncertainties, respectively: Mg^{2+} (0.03 μg/mL, 14.9%), Ca^{2+} (0.06 μg/mL, 16.6%), Na$^+$ (0.01 μg/mL 27.3%), Si^{4+} (0.05 μg/mL, 39.4%), K$^+$ (0.02

μg/mL, 11.7%), NO_3^- (0.05 μg/mL, 28.8%), PO_4^{3-} (0.09 μg/mL, 24.7%), NO_2^- (0.06 μg/mL, 40.7%), SO_4^{2-} (0.03 μg/mL, 25.7%), and Cl^- (0.01 μg/mL, 23.5%). These data was used to develop the recipe for the synthetic leachate solution used in the microbial carbonation experiment in this chapter.

3.2.4 *Microbial mat collection and carbonation bioreactor preparation*

The 10 m-long bioreactor system used in Chapter 2 was also used for this experiment (Figure 3.3). The volume of mat material was reduced by approximately 75% between experiments in order to stimulate growth of 'fresh' mats without any mineral content at the mat surface for the second bioreactor experiment. The mats were maintained using standard BG-11 medium during the time between experiments (Appendix A) (Vonshak 1986).

3.2.5 *Carbonation experiment*

The water chemistry identified with ICP-AES and IC for flask 1 was used as a guide for generating a synthetic mine tailings leach solution (Appendix C). This solution was used as the Mg source for studying microbially assisted magnesium carbonate mineralisation in the bioreactor. The purpose of the experiment was to conduct a realistic model of this biogeochemical process as it would occur at a mine tailings storage facility. The target magnesium concentration was 5000 ppm (205.76 mM), which is comparable to the concentration of 4932 ppm measured in flask 1. The leach solution was added to one end of the bioreactor, referred to as the 0 m sampling point, using a Masterflex® peristaltic pump (Figure 3.3). A drain at the other end of the bioreactor allowed the solution to flow passively out of the system. Outflow volume was tracked in order to quantify evaporation. For the first 21 days of the experiment, the inflow rate was 1 L/day. This was followed by an 11 day rest period during which the leach solution was not added. When it was started again, the inflow rate was 1 L/day for one week, with the following 4 weeks having flow rates of 2 L/day, 3 L/day, 4 L/day, and 5 L/day, respectively. Air temperatures were documented on all sampling days (Appendix C).

Based on the chemistry of the leachate solution the nutrient requirements of the microbial community in the experimental system were calculated (Appendix C). With dypingite as

the target mineral (Reaction 2), the number of cycles of carbon fixation (Reaction 3) required to make the necessary hydroxyl and carbonate anions (Reaction 4) per molecule of dypingite produced was calculated as ten (Power et al. 2007). This process requires four more photosynthetic cycles than the carbonation experiment in Chapter 2 due to the lack of bicarbonate in the feedstock solution to act as the carbon source for mineralisation. The classic phytoplankton biomass formula $[(CH_2O)_{106}(NH_4)_{16}(H_3PO_4)]$ was used to determine the required nutrient supplement (Peters et al. 2005).

$$5\ Mg^{2+} + 4\ CO_3^{2-} + 2\ OH^- + 5\ H_2O \rightarrow Mg_5(CO_3)_4(OH)_2 \cdot 5H_2O \tag{2}$$

$$HCO_3^- + H_2O \rightarrow CH_2O + O_2 + OH^- \tag{3}$$

$$HCO_3^- + OH^- \rightarrow CO_3^{2-} + H_2O \tag{4}$$

The modified BG-11 (Vonshak 1986) solution (Appendix C) was added at 0 m and 5 m with a second peristaltic pump at the same flow rates as the leach solution described above. Due to problems with excess microbial growth in the system described below, the concentration of the BG-11 solution was reduced partway through the experiment. For the first 21 days of the experiment the full strength BG-11 solution was used. During the following 'rest period', standard BG-11 medium was added to the system while no leach solution was added. From day 32 to 46, the weeks in which the flow rate was 1 L/day and 2 L/day respectively, a BG-11 solution with half the concentration of the original was used. At this point in the experiment, one of the peristaltic pumps broke. With only one pump to add both the leach solution and the BG-11 solution, the BG-11 concentration was doubled back to its original concentration and added only at the 0 m sampling location. In this way, the same amounts of nutrients were added, but only at one inflow point rather than two. This increased concentration was used from day 46 to day 60, which were the weeks during which the inflow rate was 3 L/day and 4/L day, respectively. For the final week of the experiment (day 60 to 67), the half-strength concentration of BG-11 was used during the 5 L/day inflow rate.
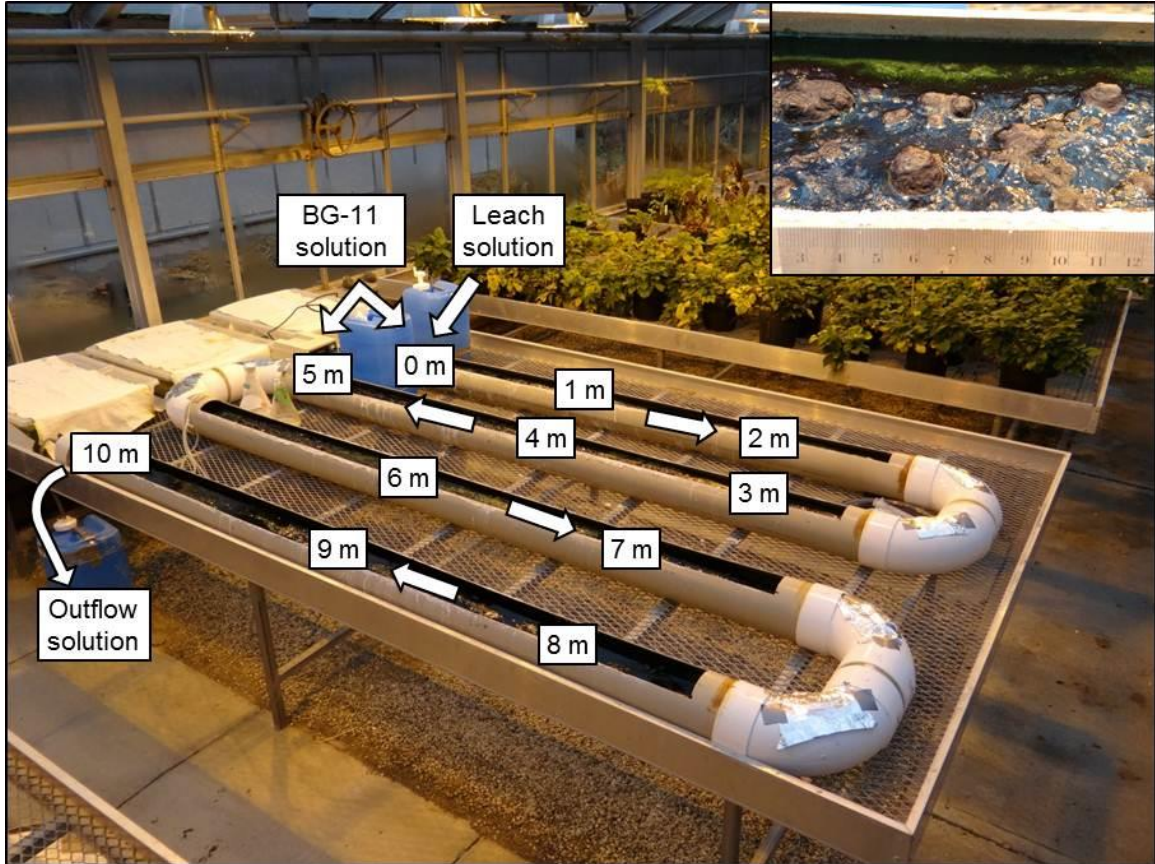
Figure 3.3 The bioreactor inoculated with microbial mats from the wetland near Atlin, British Columbia for the carbonation experiment. The magnesium-rich leach solution was added using a peristaltic pump at one end of the channel (0 m), while the BG-11 nutrient solution was added at 0 m and 5 m. The gravity driven system allows for the solution to flow passively through the bioreactor and out a valve in the other end. Arrows indicate the direction of flow. Sampling points are marked in metres from the start of the channel. Excess microbial growth occurred during the experiment, causing the mats to fill the fluid phase and grow out of the water (inset).

3.2.6 *Water chemistry analysis*

Water chemistry was monitored at every metre (0-10 m) along the bioreactor, as well as in the solution flowing out of the system. Weekly pH, conductivity, and DO were measured at each sampling location. The pH was measured using a Mettler Toledo EL2 pH meter, with a Mettler Toledo LE407 electrode calibrated using buffer solutions 4, 7, and 10 with analytical pH measurement uncertainties of $\pm$ 0.01 pH units. Conductivity was measured using a Mettler Toledo conductivity/temperature EL3 meter equipped with a Mettler Toledo LE703 electrode. The probe was calibrated using 84 μS/cm, 1413 μS/cm, and 12.88 mS/cm conductivity standards and has a measurement error of $\pm$ 0.5% of the measured value. Dissolved oxygen (DO) was measured using a Traceable digital oxygen/temperature meter calibrated using atmospheric oxygen. The accuracy of this probe is $\pm$ 0.4 mg/L.

A hydrochloric acid titration was completed using 10 mL water samples filtered with 0.45 μm Fisherbrand® syringe filters (Lahav 2001). Eleven samples were taken from within the bioreactor, from 0-10 m, as well as from the BG-11 growth medium, the leachate solution, and the water in the outflow collection jug at the end of the bioreactor. The initial pH of each water sample was measured, followed by the addition of aliquots of 1.0 N HCl using a Gilson pipet. After each aliquot, ranging in volume from 20-75 μL, was added the pH was re-measured. Acid addition was continued until the pH dropped below 3.0. Alkalinity, the ability of a liquid to neutralize acid, was calculated using the volume of acid added as mM of HCO_3^-.

Major cation and anion concentrations were determined weekly for each sampling point ICP-AES and IC as described above in the leaching experiment. Due to the high concentration, magnesium was analysed using IC instead of ICP-AES. Water samples were analysed for total dissolved inorganic carbon (DIC) concentration using a Lachat IL550 TOC-TN analyser at the University of British Columbia. Dissolved carbon species in 100 μL water samples were released from solution by reacting the samples with a 10% H_3PO_4 solution, producing $CO_{2(g)}$, which was measured with an infrared detector.

Saturation indices (SI) were determined for possible mineral products by analysing the water chemistry data using PHREEQC Interactive version 3.0.2.7614 (Parkhurst and Appelo 1999). The llnl.dat database for thermodynamic constants was used to identify mineral supersaturation in the bioreactor for the measured water sample pH and ion concentrations values. This information was used to understand how changes in pH, and the availability of Mg^{2+} and dissolved inorganic carbon species influence carbonate mineral formation.

3.2.7   *Microbe and mineral characterisation*

Microbial mat samples were collected after the experiment at the 0 m, 5 m, and 10 m positions in the bioreactor as representatives of upstream, midstream, and downstream mats in the system. Samples were collected on day 14, day 28, and day 67. Additional samples were collected at 1 m intervals on day 67 at the end of the experiment. All samples were fixed with 2%$_{(aq)}$ glutaraldehyde and dehydrated with ethanol (25, 50, 75, 100% × 3 for 20 min each) prior to critical point drying (Tousimis, Samdri-PVT-3B). The samples were coated with 4 nm of osmium before examination with SEM-EDS using the Zeiss Leo 1540 microscope.

Microbial mat samples were collected at 0 m, 5 m, and 10 m on day 28 and day 67 for mineral analysis with XRD. A sample was also collected on day 0, prior to starting the experiment. The mats were air dried in petri dishes, and powdered with a mortar and pestle. The samples were analysed in the same way as the mine tailings sample described above.

3.3   **Results**

3.3.1   *Characterisation of chrysotile*

Chemical analysis of the powdered chrysotile fibres using XRF indicated that magnesium is the most abundant cation in the fibres with MgO constituting 37.58% of the sample (Table 3.1). Silicon and iron were the next most abundant cations, with SiO and FeO making up 31.1% and 5.82% of the fibres, respectively. These findings are consistent

with the XRD results, which indicated the presence of chrysotile $[Mg_3(Si_2O_5)(OH)_4]$, magnetite $[Fe_3O_4]$, magnesite $[MgCO_3]$, and chalcopyrite $[CuFeS_2]$ (Figure 3.4).

Petrographic and SEM characterisation of the Clinton Creek rock samples showed that the chrysotile fibres are present as veins ranging in width from a few microns to over 2 mm (Figure. 3.5). These are small compared to some observed in the field, which were cm-scale in width (Figure 3.2). Under cross-polarized light, the chrysotile veins exhibit first order birefringence. The veins are present in fractures cutting through the wall rock, and occasionally crosscut each other or branch into multiple veins. The fibres in the veins mostly occur perpendicular to the wall rock; however, fibres with inclined contacts with the wall rock are also visible. The wall rock consists of non-fibrous serpentine minerals including chrysotile and antigorite. These observations are consistent with other mineralogical characterisations of the Clinton Creek chrysotile mineralisation (Htoon 1979). Closer examination of the chrysotile with SEM-EDS indicated the presence of Mg- and Ca-carbonate interspersed within both the vein and wall rock serpentine (Figure 3.6). In both cases, the relative abundance of carbonate in the serpentine can be seen based on the contrast between the minerals. Mineral grains which appear black under plane- and cross-polarized light are bright grey when viewed with reflected light (Figure 3.7). These grains are irregularly shaped and often contain what appear to be crystals of non-fibrous serpentine (Figure 3.7). When analysed with SEM-EDS, most of the grains are composed of Fe and O, which is consistent with the magnetite identified with XRD. Some of these grains exhibit zoning between multiple metals; including Fe, Cr, Cu, Al, and Zn (Figure 3.7). Based on the observations made using petrography and SEM-EDS, the mineral abundances in these rocks have been determined to be 90% serpentine (chrysotile >> antigorite), 7% Mg- and Ca-carbonates, and 3% metal oxides.

3.3.2   *Leaching experiment*

The starting pH values for all the leaching flasks were very acidic. Flasks 0.25, 0.5, and 1 had pH values of 1.3, 1.0, and 0.5 respectively; with flasks 2, 3, and 4 all having pH values of 0 (Figure 3.8). The changes in pH of the leaching flasks varied with acid concentration. The rate at which the pH changed decreased with increasing acid concentration, with the flasks 0.25, 0.5, 1, and 2 showing pH increases in the first 4 hours

of the experiment. The acidity was neutralised in flasks 0.25, 0.5 and 1; these flasks exhibited a pH greater than 7 after 79, 96, and 480 hours, respectively. Flasks 2 and 3 demonstrated minimal acid neutralization, and only reached respective pH values of 1.9 and 0.75 after the full 1008 h of the experiment. The pH of flask 4 never increased from 0. The control flask had a starting pH value of 7.1 that fluctuated for the first 72 h before increasing for the remainder of the experiment to an end value of 8.32.

Chemical analysis of the waters produced during the leaching experiment with ICP-AES and IC demonstrated the release of elements from the chrysotile samples into solution (Table 3.2). Water from the control flask contained low concentrations of leached ions, with magnesium having the highest concentration of 20 ppm. Most of the metals, including aluminum, copper, chromium, manganese, vanadium, and zinc; were not leached from the fibres in the control flask. Flasks 0.25, 0.5, and 1 showed similar results, with little to no metal being released into solution by the tailings. Calcium and magnesium were leached more readily from the fibres (Table 3.2). The concentration of magnesium released into solution increased with increasing acid concentration, with the transition between flask 3 and flask 4 being an exception. Flask 3 contained the highest concentration of magnesium (10 493 ppm). However, the chemistry in flask 1, which contained a magnesium concentration of 4 932 ppm, was selected as the target for the carbonation experiment synthetic leach solution because it contained the highest concentration of magnesium of the flasks that reached a neutral pH. Although the flasks containing higher acid concentrations generated more soluble magnesium, they did not achieve the neutral to alkaline pH conditions required for survival of the cyanobacteria used in the bioreactor carbonation experiment. The high sulfate concentrations generated in all of the acidic flasks is a result of the sulfuric acid used to conduct the leaching, and not a product of the chrysotile.

The proportion of MgO in the control flasks and flask 0.25 were very similar to that of the fresh fibres, indicating little leaching of magnesium (Table 3.1). As the concentration of acid increased, the amount of magnesium remaining in the fibres decreased. A similar pattern was observed for CaO, MnO, Al_2O_3, and Cr_2O_3 (Table 3.1). There is little evidence of iron being leached from the fibres in any but the two strongest acid

concentrations in flasks 3 and 4. Both iron and magnesium show slightly less leaching in flask 4 than flask 3.

SEM of the leached chrysotile fibres indicated a change in the mineralogy and structure of the natural sample (Figure 3.9-3.11, Appendix D). The unleached 'fresh' chrysotile appears as continuous fibres 100-500 nm in diameter, reaching lengths of over 300 μm. When analysed with EDS, these fibres match the MgSiO chemistry expected of chrysotile. The fibres were accompanied by grains of iron oxide up to 40 μm is diameter. The fibres in the control flask were similar in appearance to the fresh fibres (Figure 3.9, Appendix D). The fibres in flask 0.25 were still intact, showing little evidence of chemical weathering. As the acid concentration increases, the fibres began to exhibit evidence of chemical weathering. They occurred as less continuous fragments and were accompanied by secondary minerals, such as magnesium, calcium, and sodium sulfates, which were not observed in the samples of fresh fibres or those leached with weaker concentrations of H_2SO_4 (Figure 3.11).

Table 3.1 Major oxide composition of chrysotile fibres before and after leaching with sulfuric acid. Those leached with acid are specified by the acid/chrysotile ratio used for each experiment. A control of chrysotile fibres leached with ddH2O was also analysed.

Sample	SiO_2	TiO_2	Al_2O_3	Fe_2O_3	MnO	MgO	CaO	K_2O	Na_2O	P_2O_5	Cr_2O_3	LOI	Total
Fresh Chrysotile Fibres	31.10	0.00	0.21	5.82	0.15	37.58	3.06	0.00	< 0.01	0.01	0.16	21.87	99.96
0.25	33.09	0.02	0.43	5.93	0.19	37.38	1.87	0.02	< 0.01	< 0.01	0.12	21.19	100.23
0.5	34.27	0.02	0.65	6.14	0.18	34.17	2.04	0.02	< 0.01	< 0.01	0.11	22.29	99.89
1	34.37	0.01	0.52	6.22	0.11	24.93	2.09	0.02	< 0.01	< 0.01	0.11	31.41	99.79
2	43.38	0.02	0.17	5.83	0.05	8.43	2.20	0.02	< 0.01	0.01	0.06	39.85	100.02
3	34.27	0.01	0.09	3.96	0.05	7.15	1.95	0.01	< 0.01	< 0.01	0.06	51.93	99.48
4	24.52	0.01	0.09	4.25	0.05	8.29	1.48	0.02	< 0.01	< 0.01	0.06	60.54	99.31
ddH$_2$O Control	30.96	0.01	0.52	5.03	0.18	38.42	2.71	0.01	< 0.01	< 0.01	0.10	22.16	100.10

LOI = loss on ignition
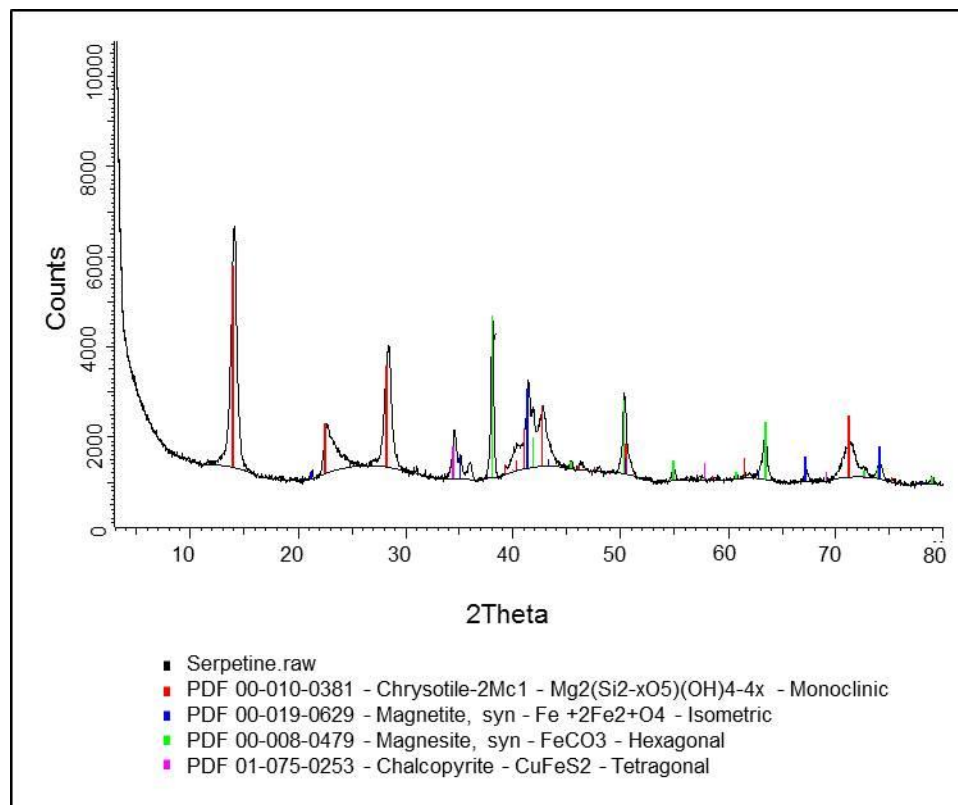
Figure 3.4 XRD pattern of the chrysotile collected from the Clinton Creek Asbestos Mine for use in the leaching experiment. Chrysotile, magnetite, magnesite, and chalcopyrite were identified.
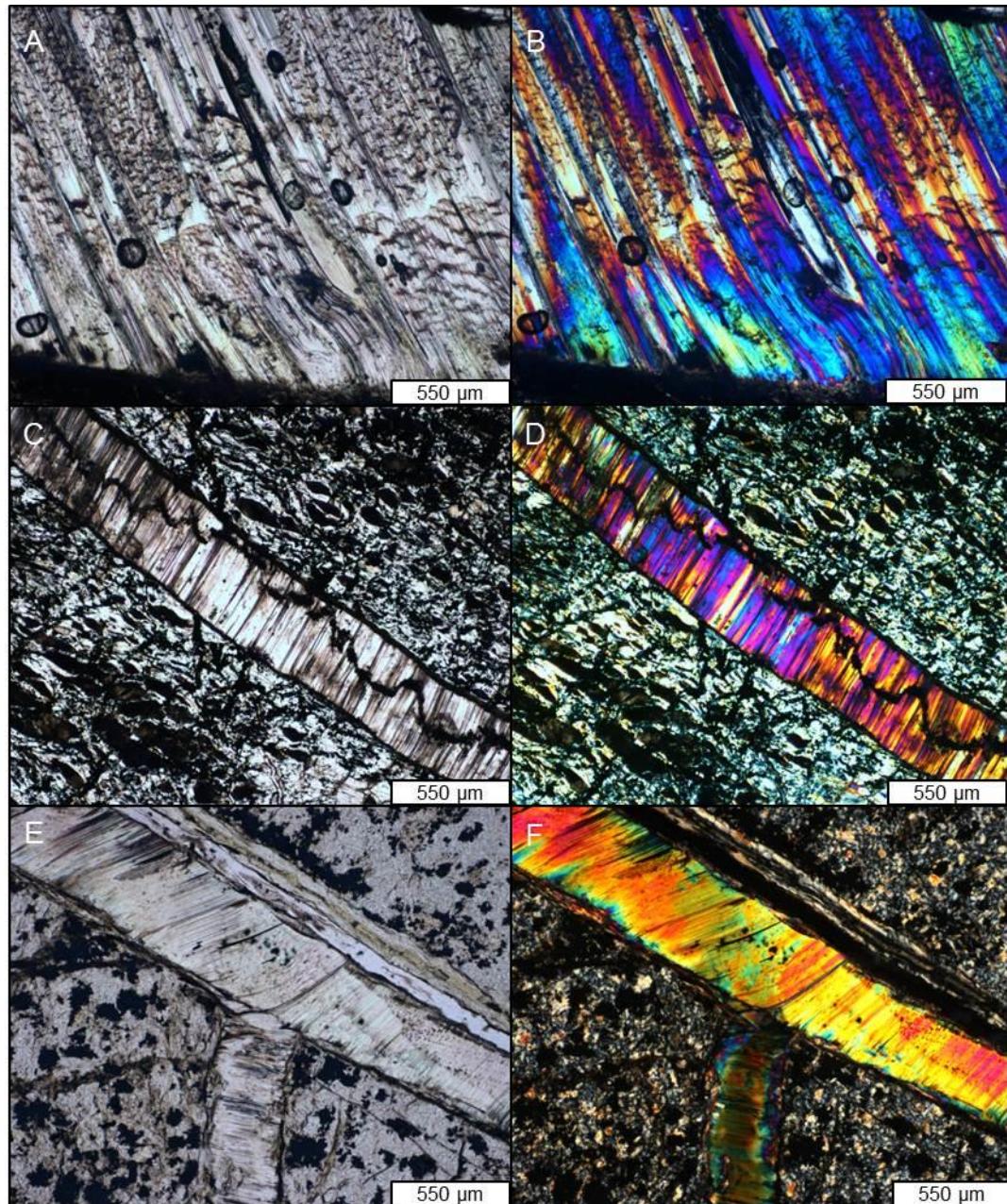
Figure 3.5 Plane polarized (A, C, and E) and cross polarized (B, D, and F) petrographic images of large (A and B), small (C and D), and branched (E and F) chrysotile veins in the Clinton Creek samples. The fibres can be parallel (C and D) or inclined (E and F) to the wall rock.
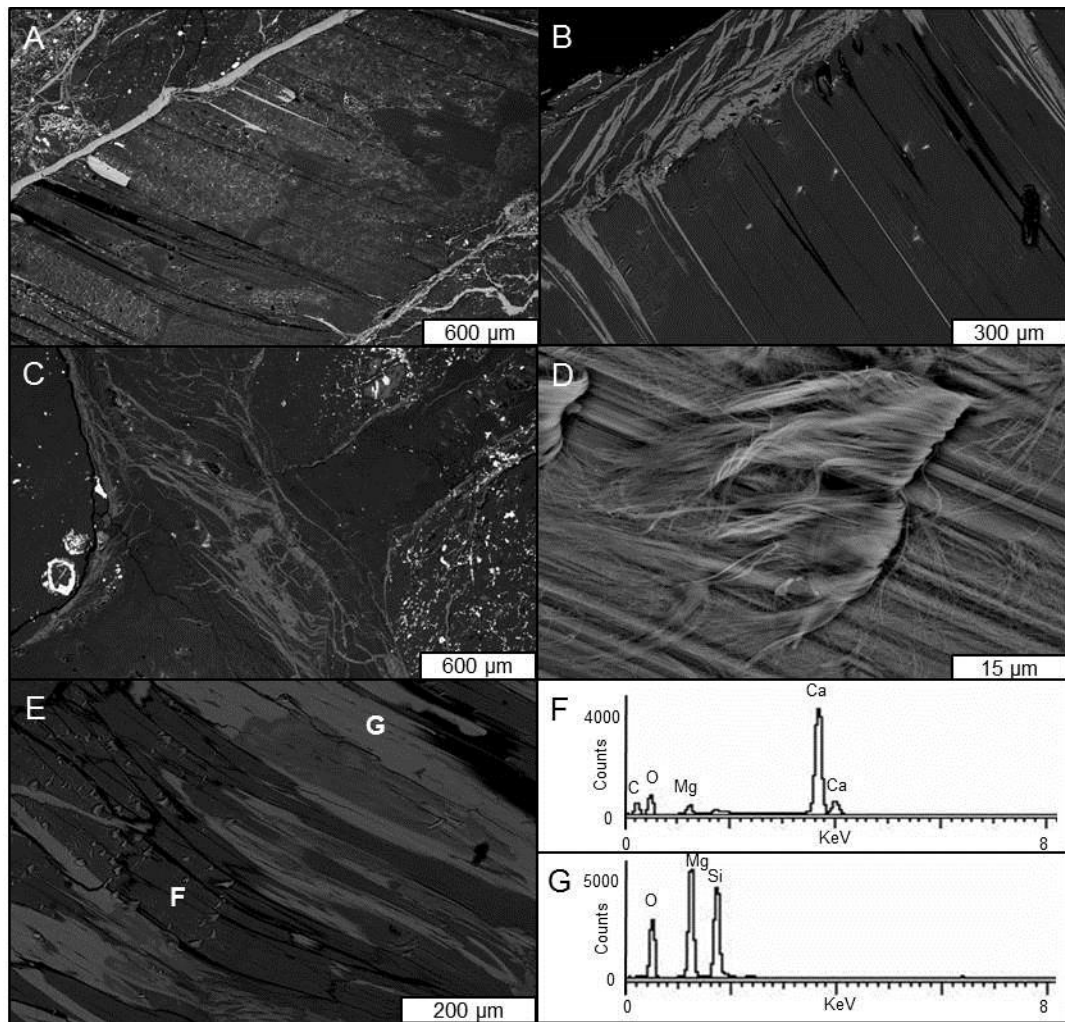
Figure 3.6 A)-E) Backscatter electron images of fibrous chrysotile in the Clinton Creek rocks. The fibres are present in veins, running through non-fibrous serpentine wall rock. C) A branched vein of chrysotile. D) High magnification of the chrysotile fibres on the surface of the thin section. E) A portion of a chrysotile vein showing carbonate alteration. The chrysotile and carbonate are labeled as F and G, respectively; and correspond to the EDS spectra in F) and G).
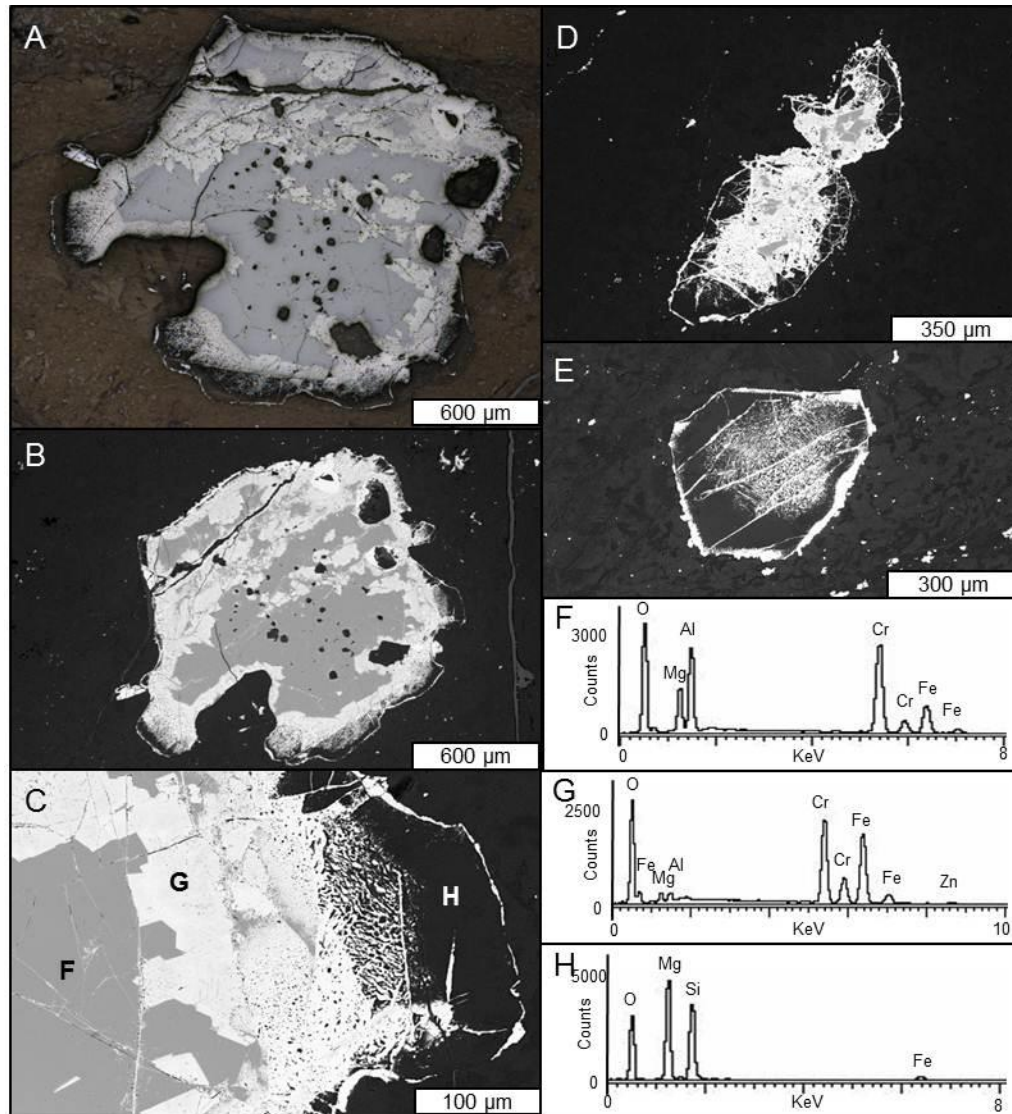
Figure 3.7 A) Reflected light petrography and B) and C) scanning electron microscopy of a large, zoned metal oxide grain found in the Clinton Creek serpentine. EDS for the different zones visible in C) are shown in F)-H). D) and E) SEM of metal oxide grains (bright) containing serpentine (dark grey).
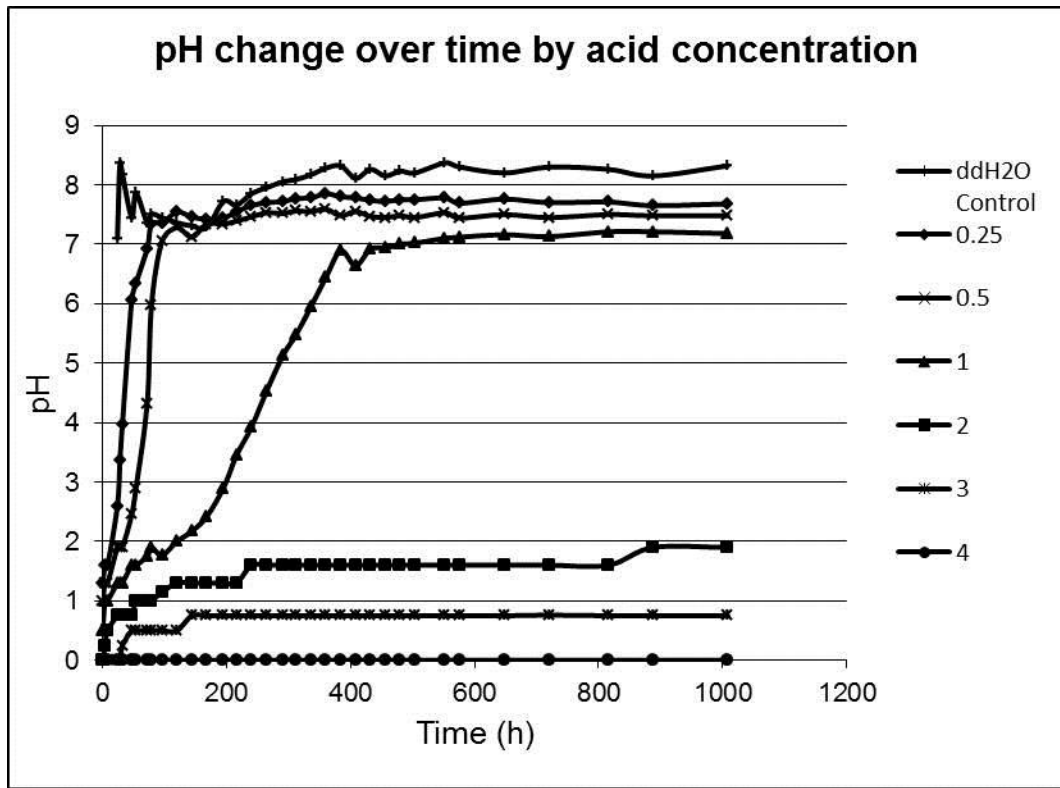
Figure 3.8 Change in pH over time for each of the acid concentrations used in the leaching experiment.

Table 3.2 Concentrations (ppm) of major cations and anions for each of the acid concentrations used in the leaching experiment.

	Ion concentration (ppm)									
Flask	Al^{3+}	Ca^{2+}	Cr^{3+}	Cu^{2+}	Fe^{2+}	K^+	Mg^{2+}	Mn^{2+}	Na^+	Pb^{4+}
0.25	ND	375	ND	ND	ND	1.25	1028	0.11	1.31	ND
0.5	ND	320	ND	ND	ND	0.34	2281	4.50	1.57	ND
1	ND	476	ND	ND	ND	0.34	4932	20.1	1.43	ND
2	60.0	579	8.78	0.08	290	0.32	10241	30.2	1.51	ND
3	60.5	451	8.59	0.05	394	0.41	10493	28.7	5.62	ND
4	54.2	427	7.79	0.03	404	0.34	9380	25.6	1.46	ND
ddH$_2$O Control	ND	10	ND	ND	0.100	1.24	20.0	ND	0.22	ND

	Ion concentration (ppm)									
Flask	Si^{4+}	V^{5+}	Zn^{2+}	Br^-	Cl^-	F^-	NO_2^-	NO_3^-	PO_4^{3-}	SO_4^{2-}
0.25	58.8	0.02	ND	0.50	1.70	0.05	ND	0.10	< 9.0	6396
0.5	57.3	0.03	ND	0.53	1.40	0.07	0.70	0.11	< 9.0	14193
1	52.4	0.08	0.02	ND	0.19	0.19	ND	ND	< 9.0	28900
2	79.2	0.56	0.32	ND	0.28	0.94	2.74	ND	< 9.0	66533
3	53.7	0.53	0.47	ND	1.71	0.46	3.09	0.70	< 9.0	100500
4	41.6	0.50	0.31	3.50	6.03	0.30	ND	ND	< 9.0	125833
ddH$_2$O Control	9.5	ND	ND	ND	1.51	0.30	ND	ND	ND	7.13

ND: not detected
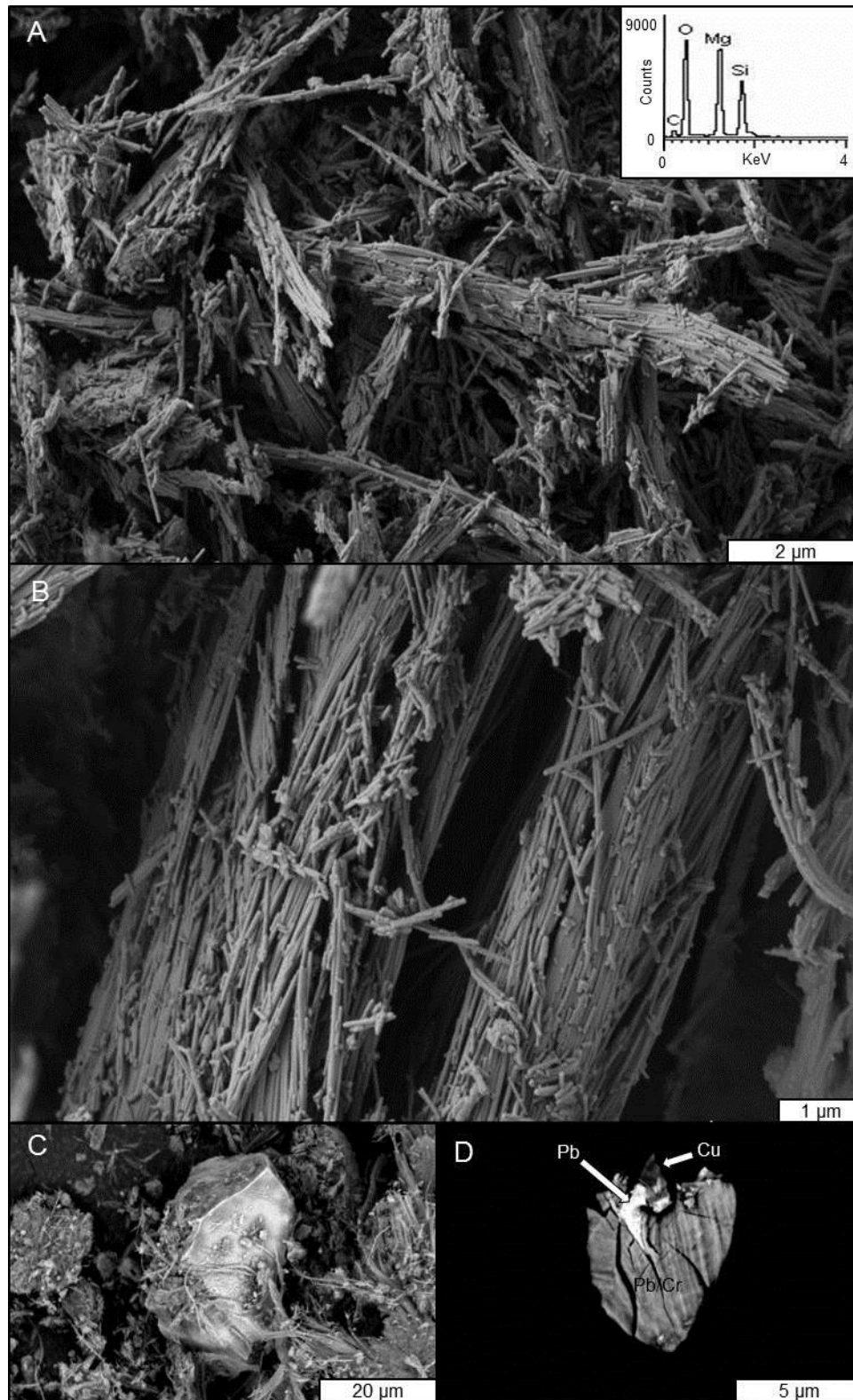
Figure 3.9 A) and B) Scanning electron micrographs of the 'fresh' chrysotile fibres composed of Mg-Si-O and minor C (EDS in inset in of A) used in the leaching experiment. C) Iron oxide and D) Pb-Cr-Cu grains found in the chrysotile tailings.
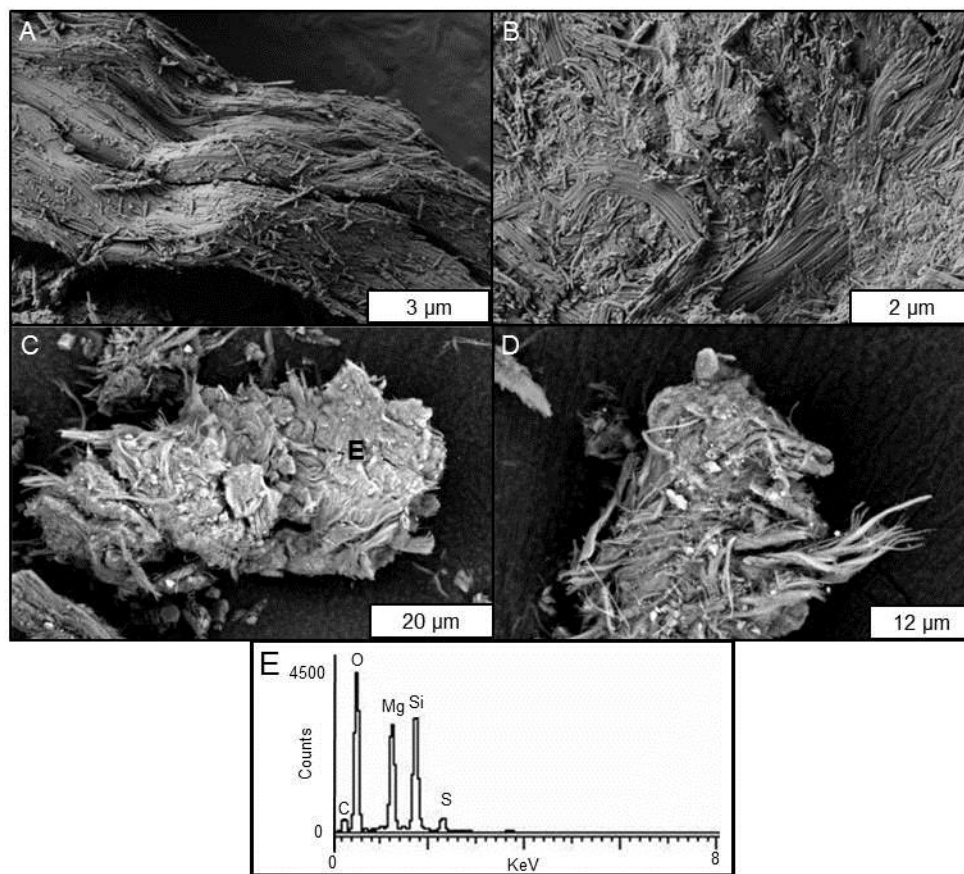
Figure 3.10 A-D) Scanning electron micrographs of chrysotile fibres sampled from flask 1 at the end of the leaching experiment. E) Energy dispersive spectroscopy of the chrysotile fibres.
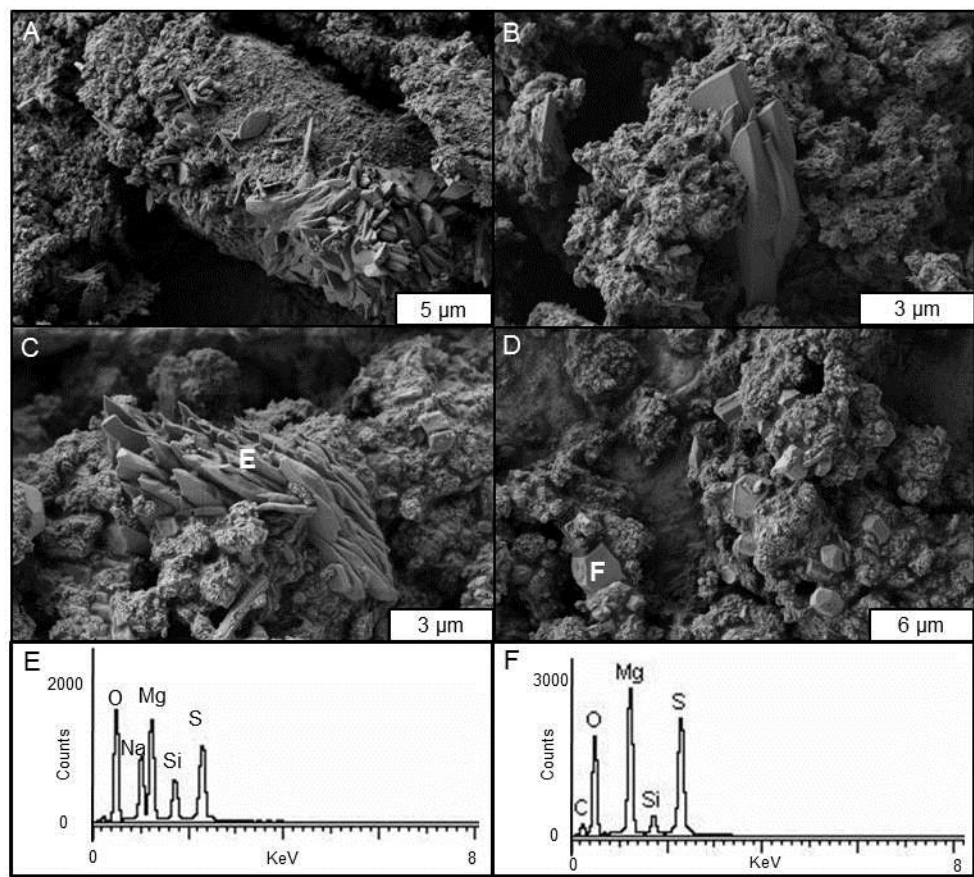
Figure 3.11 A-D) Scanning electron micrographs of the leached tailings sampled from flask 4. The chrysotile fibres have been chemically weathered generating amorphous material. (C-F) Magnesium and sodium sulfate minerals are also present.

3.3.3   Water chemistry analysis

The volume of water flowing out of the bioreactor was tracked. It indicated that a total of 124 L, or 45%, of the water added to the system evaporated over the course of the experiment. This water loss was taken into account for mass balance calculations for the system and for conductivity, ICP, IC, and alkalinity, and DIC results.

The average concentration of dissolved oxygen in the bioreactor as a whole was 15.2 mg/L at the beginning of the experiment, followed by a drop to 5.9 mg/L by day 21 (Figure 3.12). The decrease during the first 3 weeks corresponded to the growth of a pellicle on the surface of the water in the bioreactor. This excess growth formed a seal between the experimental system and the atmosphere, limiting gas exchange and causing the water in the bioreactor to become suboxic. Over the first 3 weeks, DO concentrations as low as 1.3 mg/L were measured. At the 3 week time point, the system was given time to recover. This was done by stopping the addition of the synthetic leach solution, giving the bioreactor a reduced concentration of BG-11, and removing the pellicle daily to allow re-oxygenation of the water. This was achieved after 11 days, at which point the experiment was continued. At that time, the average DO concentration in the bioreactor was 9.0 mg/L, with no sample location having a concentration lower than 5.9 mg/L. The average DO concentration fluctuated between 15.1 mg/L and 21.0 mg/L for the rest of the experiment (Figure. 3.12). The average DO concentrations in the BG-11 and leach solution were 5.2 mg/L and 7.4 mg/L, respectively. The average DO concentration at the inflow location (0 m) was 12.4 mg/L for the entire experiment. Overall, the DO concentration increased down the length of the bioreactor, with averages from sample points 1 through 10 m ranging from 13.99 mg/L up to 16.52 mg/L. The concentration dropped to 9.2 mg/L in the outflow solution, probably due to heterotrophic activity in the catch basin.

The average pH in the bioreactor at the start of the experiment was 9.8 (Figure. 3.13). The pH dropped slightly over the course of the experiment; however, the system average was always above 9.4. The pH dropped during the first 3 weeks of the experiment,

corresponding to the formation of the pellicle described above, followed by higher pH values for the remainder of the experiment. The pH increased slightly down the length of the bioreactor (Figure 3.13B). Over the duration of the experiment, the 0 m sampling location had an average pH of 9.5, increasing to 9.7 by the end of the bioreactor channel. The only location that exhibited a decrease in pH was the 5 m sampling location, which corresponded to the second BG-11 inflow location; the BG-11 and leach solutions had pH values of 5.9 and 8.1, respectively (Figure 3.13).

Overall, the conductivity in the bioreactor increased over the course of the experiment from the time zero value of 8.0 mS/cm (Figure 3.14A). A small peak is visible at day 21 when average conductivity in the bioreactor is plotted over time, corresponding to the pellicle formation and associated drop in DO. This is followed by a decrease in conductivity during the 11 day rest period during which the leach solution was not added. Once the magnesium-rich solution was restarted, the conductivity increased over time to a final system average of 11.1 mS/cm (Figure 3.14). Note, this increase matches the time course of the experiment (day 32 to 67) during which the inflow rate of the leach solution was increased on a weekly basis. The conductivity displayed a linear decrease down the length of the bioreactor (Figure 3.14B). The leach solution was the primary source of conductivity with an average of 18.1 mS/cm, with the full strength and half strength BG-11 solutions having conductivity values of 6.6 mS/cm and 3.7 mS/cm, respectively. This means that the ions being added at the 0 m point in the bioreactor result in as much as 24.7 mS/cm of conductivity. The 0m location had an average conductivity of 9.5 mS/cm over the course of the experiment (Figure 3.14). This value decreased linearly to 6.8 mS/cm by the 10 m location.

The alkalinity, which reflects any dissolved constituents in the system that can accept a proton, changed over both space and time. The average alkalinity for the system at the start of the experiment was 36.8 mM HCO_3^- (Figure 3.15A). The alkalinity decreased over time to a system average of 5.5 as mM HCO_3^- by the end of the experiment. The alkalinity decreased at a faster rate during the second part of the experiment when the leach solution and nutrient inflow rate was increased on a weekly basis, compared to the first 3 weeks of the experiment (Figure 3.15A). Down the length of the bioreactor, the

alkalinity changed in reference to the leach and BG-11 solution input locations, with the lowest alkalinity values measured for samples from within the bioreactor being at the points of solution inflow (0 m and 5 m). The alkalinity increased from 0 m to 2 m, followed by a decrease until 5 m (Figure 3.15B). Beyond the second BG-11 inflow location, the alkalinity rose again to a system high of 23.7 mM HCO_3^- at 8 m, followed by a decrease over the remaining length of the bioreactor and in the outflow solution. Alkalinity was below detection in the BG-11 and leach solutions and therefore was not calculated.

The portion of the alkalinity that is specific to carbon species in solution is reflected in the DIC concentration, which demonstrated a pattern similar to that of the overall alkalinity. The concentration of DIC decreased over time, with the system average dropping from 27.1 to 3.6 as mM carbon from the start to the end of the experiment (Figure 3.16A). The rate of DIC decrease was greater during the second half of the experiment. Like the alkalinity, the DIC had low points at 0 m, 5 m and in the outflow solution; with high points in between the locations where the BG-11 growth solution was added (Figure 3.16B).

The magnesium concentration, which was used as an indicator of mineral precipitation in the bioreactor, increased over the course of the experiment. (Table 3.3, Figure 3.17A). The average concentration at the start of the experiment was 2.60 mM, which increased to 68.80 mM by the end of the experiment. This increase occurred slowly over the first 39 days of the experiment, followed by a much faster increase during the last 28 days when the magnesium inflow rate was increased. Before the experiment, the magnesium concentration was consistent throughout the bioreactor, with all sampling locations having a concentration between 2.50 mM and 2.67 mM. Down the length of the bioreactor, the magnesium concentration decreased throughout the experiment (Table 3.4, Figure 3.17B). For the first 39 days of the experiment, the system was able to precipitate enough magnesium carbonate to reduce the magnesium concentration to equal or less than the time zero concentration. Over time, a greater length of the bioreactor was needed for this to happen. Most of the decrease in magnesium concentration took place immediately upon addition of the leach solution to the 0 m location in the bioreactor

(Table 3.4). The leach solution had a concentration of 196.12 mM compared to the concentration at the 0 m location of 45.72 mM. On the last sampling day of the experiment (day 67), the magnesium concentration did not come close to approaching the time zero value; however, a continuous decrease in magnesium can still be seen down the length of the system.

In contrast to chapter 2, nutrient limitation did not occur in the bioreactor during the carbonation experiment. The average nitrate concentration increased over time from 3.07 mM on day 7 to 20.75 mM by the end of the experiment (Table 3.3, Figure 3.18A). The full strength BG-11 contained 74.87 mM, while the half strength contained 30.67 mM. The half strength value is not exactly half of the full strength value due to the analytical error of the measurements (also applicable to the phosphate values below). This input of nitrate decreased down the length of the bioreactor from 15.60 mM at the 0 m location to 3.56 mM in the outflow solution (Table 3.4, Figure 3.18B). The nitrate concentration over the first 5 m was much higher than the values for the last 5 m of the bioreactor, likely due to the removal of the second inflow partway through the experiment.

The average phosphate concentration in the bioreactor decreased over the course of the experiment (Table 3.3, Figure 3.19A). The system average on day 7 of the experiment was 0.18 mM, which decreased until day 39. From day 39 to the end of the experiment, the average phosphate concentration was steady, though low, at 0.02 mM (Figure 3.19A). The full and half strength BG-11 solutions had concentrations of 6.10 mM and 2.28 mM respectively, which were reduced to an average concentration of 0.05 mM at the 0 m sampling location (Table 3.4, Figure 3.19B). The nitrate concentration fluctuated down the length of the bioreactor, with a system low location average at 2 m of 0.03 mM, and a system high location average of 0.12 mM, which corresponds to the second BG-11 inflow location. Beyond 5 m, the phosphate content decreased continuously to a concentration of 0.05 mM at the 10 m sampling location.

Using the water chemistry data outlined above, saturation indices were determined for potential mineral precipitates using PHREEQC (Figure 3.20 and 3.21; Appendix E). Although many minerals phases are identified from the database as potential precipitates,

SI data is only presented for possible carbonate products as many of the other minerals selected by PHREEQC are thermodynamically unrealistic under the experimental conditions. Of the carbonate minerals identified by the database, hydromagnesite and magnesite are of the most interest. The leach solution had SI values for hydromagnesite and magnesite of -10.07 and -0.65, respectively. These negative values are largely due to the lack of DIC in the solution. Magnesium carbonation SI values could not be determined for the BG-11 solution because it did not contain magnesium. On day 0, all of the sampling locations in the bioreactor had hydromagnesite SI values near 0, ranging from -0.36 to 0.51. Magnesite had slightly higher value ranging from 1.39 to 1.45.

Upon addition of the feedstock solutions to the bioreactor, the SI values for all of the carbonate minerals increased. The SI of hydromagnesite increased from the leach solution value of -10.07 to 3.03 at the 0 m sampling location. The average hydromagnesite SI value for the entire system increased over time to day 39, followed by a decrease over the remainder of the experiment (Figure 3.20A). Throughout the time during which the leach solution was being added to the bioreactor, the average value was always above 1.25. The highest system average of 3.64 occurred on day 39. Down the length of the bioreactor, the hydromagnesite SI behaved differently at different times during the experiment. The average over the course of the experiment at the 0 m sampling location was 1.94 (Figure 3.20B). This value increased slightly over the first few metres, followed by a system low average at 5 m of 1.62. This point corresponds to the second BG-11 inflow location. The 6 m sampling location had the highest average of 2.44. On day 14, the SI fluctuated down the length of the system, with an overall trend of decreasing with length. The SI was relatively stable down the length of the system on day 39, having the highest overall values with all of the sampling locations between 3.14 and 3.97. Day 53 showed similar stability with slightly lower SI values, ranging from 2.83 to 3.24. Day 67 was the final sampling day of the experiment, occurring after one week of a 5 L/day inflow rate, and demonstrated a large increase in hydromagnesite SI down the length of the bioreactor. The 0 m sampling location had a value of -0.56, which was one of the few times during the carbonation experiment the hydromagnesite SI dropped below zero (Figure 3.20B). The SI increased to 2.31 by 3 m down the system, followed by a

slight drop to 3.12 at 5 m. Beyond the halfway mark, the SI value jumped to 3.02 at 6 m, and remained steady around 3.0 for the remaining length of the bioreactor.

The magnesite SI value changes were smaller and less frequent than those observed for hydromagnesite, although similar trends can be seen. The system average SI for magnesite on day 0 was 1.43, which increased over time to a value of 2.09 on day 39 (Figure 3.21A). This was followed by a decrease over the remainder of the experiment, dropping to 1.62 by day 67. Down the length of the bioreactor, the experimental average magnesite SI by sampling location remained relatively steady, ranging between 1.72 and 1.86. Like hydromagnesite, the 5 m sampling location had the lowest value. On day 14, the magnesite SI fluctuated down the length of the system, exhibiting an overall decreased down the length of the bioreactor. On day 39, the SI was relatively stable down the length of the system, having the highest overall values with all sampling locations having magnesite SI values between 1.94 and 2.17. The SI was also consistent between sampling locations on day 53, with values ranging from 2.83 to 3.24. Day 67, the final day of the experiment, demonstrated an increase in magnesite SI down the length of the bioreactor. The 0 m sampling location had a value of 1.2, which, like hydromagnesite was one of the lowest SI values measured during the carbonation experiment (Figure 3.21B). The SI increased to 1.63 by 3 m, and remained constant at this value until 5 m. After 5 m, the magnesite SI increased slightly down the remaining length, reaching 1.81 by the end of the bioreactor.

Another piece of information that PHREEQC is able to determine is the saturation state of CO_2 in the experimental water. At no point during the experiment did the water in the bioreactor approach saturation (SI=0) in terms of gaseous CO_2. With atmospheric CO_2 being the only available source of the DIC that was measured in the water samples, some atmospheric CO_2 must have is dissolved into the bioreactor, acting as the carbon source for carbonate mineralisation. The negative SI values observed for CO_2 at all sampling locations on every sampling day indicates that the system was never saturated in CO_2, which is important to the carbonation potential of the system (Appendix E).

Table 3.3 Average concentrations (mM) of major cations and anions in water samples collected from the bioreactor on different days during the carbonation experiment.

Day	Ca^{2+}	K^+	Mg^{2+}	Mn^{2+}	Na^+	Si^{4+}	Cl^-	NO_2^-	NO_3^-	PO_4^{3-}	SO_4^{2-}
						Ion concentration (mM)					
0	0.06	1.71	2.60	0.00	94.47	0.02	2.98	ND	ND	ND	66.14
7	0.12	1.36	4.22	0.00	88.73	0.01	2.52	0.36	3.31	0.18	75.72
14	0.16	1.59	7.38	0.00	93.71	0.01	3.41	0.22	4.82	0.12	40.97
21	0.28	1.97	12.54	0.00	97.74	0.01	5.37	0.54	9.50	0.13	130.21
39	1.11	1.71	18.05	0.00	82.59	0.01	3.43	0.03	4.15	0.02	50.34
46	0.56	1.64	28.01	0.00	91.19	0.01	4.63	0.02	5.88	0.02	60.92
53	1.12	1.78	42.69	0.00	93.41	0.01	6.37	0.03	8.87	0.02	79.12
60	1.80	2.02	56.56	0.00	76.24	0.01	7.84	0.05	14.3	0.02	91.28
67	2.47	2.02	68.80	0.00	78.55	0.01	9.25	0.08	16.9	0.02	106.98

ND: no data

Table 3.4 Average concentrations (mM) of major cations and anions in water samples collected at 1 m increments down the length of the bioreactor during the carbonation experiment.

Sample Point	Ca^{2+}	K$^+$	Mg^{2+}	Mn^{2+}	Na$^+$	Si^{4+}	Cl$^-$	NO$_2^-$	NO$_3^-$	PO$_4^{3-}$	SO$_4^{2-}$
						Ion concentration (mM)					
Full BG-11	0.78	3.97	0.01	0.02	88.42	ND	2.26	ND	74.87	6.10	ND
Half BG-11	0.34	1.46	ND	0.01	45.85	ND	0.92	ND	30.67	2.28	0.01
Leach solution	8.16	1.21	196.12	0.06	0.08	0.22	24.13	ND	ND	ND	407.32
0 m	2.63	1.86	45.72	ND	89.33	0.03	8.03	0.27	15.59	0.05	71.44
1 m	1.42	2.17	42.14	ND	93.13	0.02	7.40	0.29	13.09	0.06	67.53
2 m	1.24	2.07	38.78	ND	91.79	0.02	6.37	0.25	10.54	0.03	60.83
3m	1.10	1.97	35.72	ND	88.80	0.01	6.14	0.26	11.00	0.05	57.26
4 m	1.01	1.97	33.37	ND	85.82	0.01	6.04	0.30	11.50	0.08	56.13
5 m	0.93	1.91	31.14	ND	84.48	ND	5.54	0.24	12.77	0.12	54.47
6 m	0.76	1.70	27.92	ND	90.16	ND	4.76	0.16	6.15	0.10	47.72
7 m	0.65	1.54	24.61	ND	90.37	ND	4.61	0.12	5.27	0.08	47.77
8 m	0.51	1.54	21.80	ND	87.82	ND	4.20	0.04	4.43	0.06	44.78
9 m	0.45	1.54	19.92	ND	90.00	ND	3.98	0.02	4.01	0.05	38.66
10 m	0.41	1.45	18.83	ND	87.90	ND	3.77	0.02	3.76	0.04	40.36
Outflow	0.39	1.43	17.43	ND	73.66	ND	3.39	0.02	3.56	0.05	36.86

ND: not detected
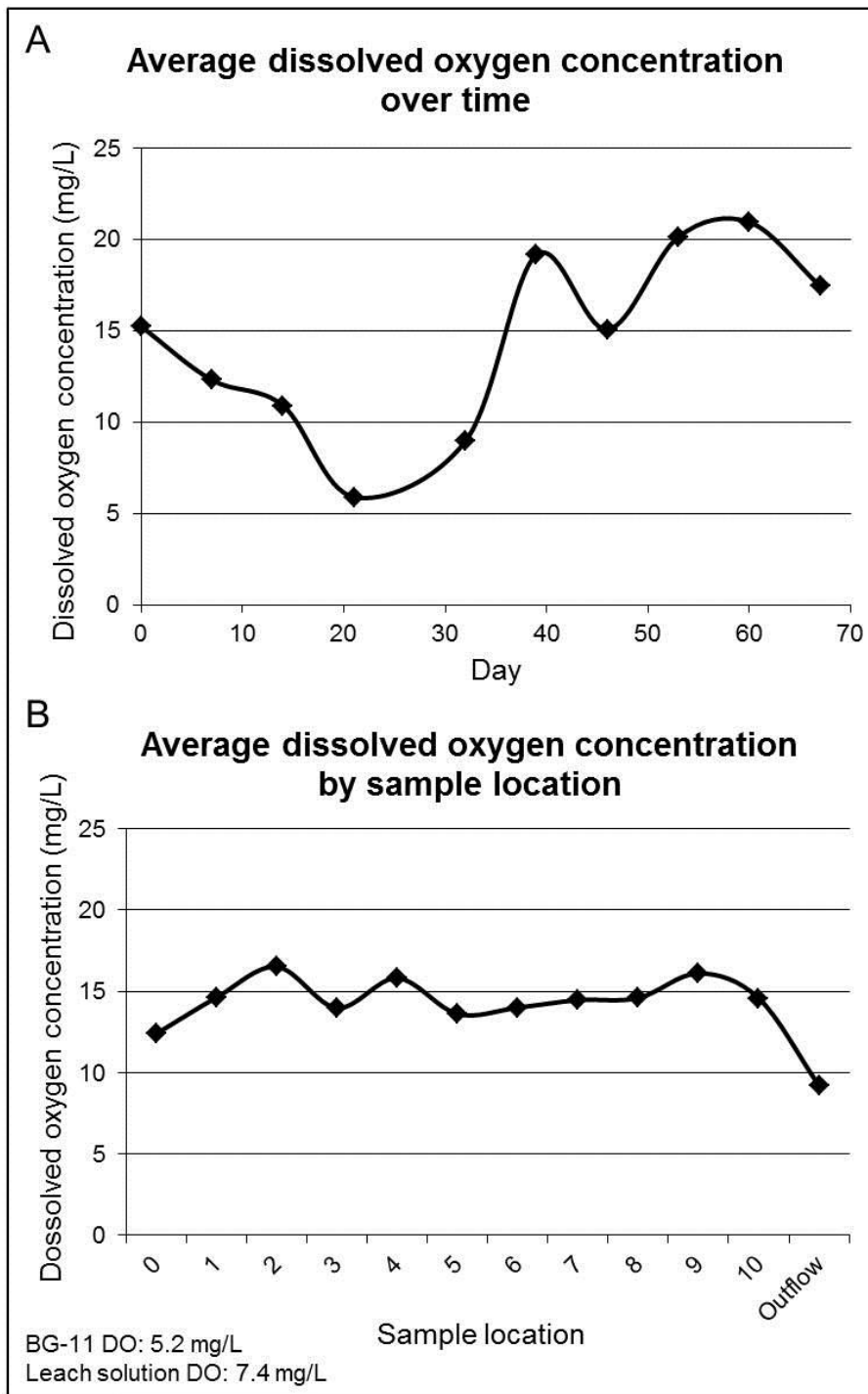
Figure 3.12 Average dissolved oxygen concentration over A) time as a system average and B) space as a sample location average.
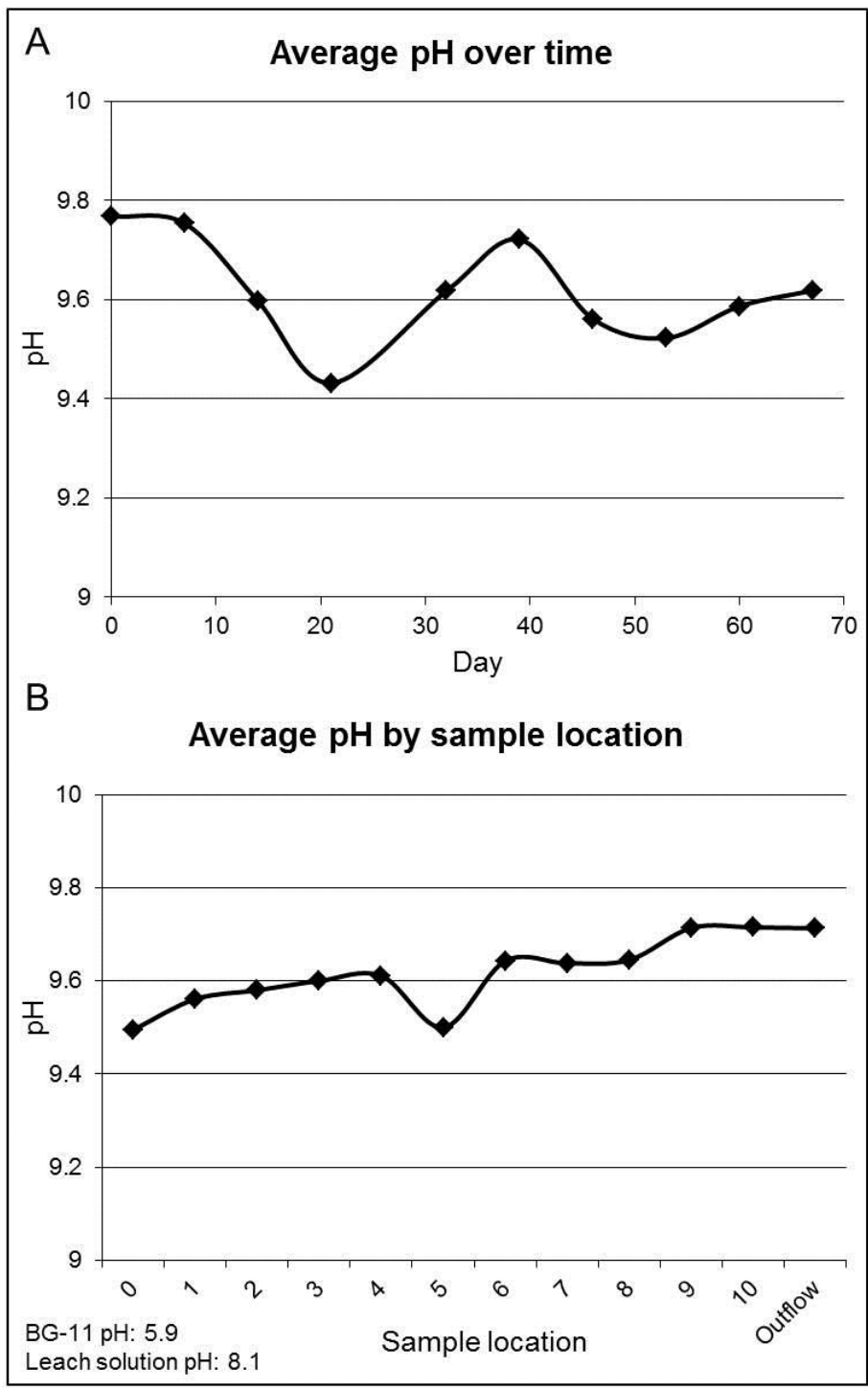
Figure 3.13 Average pH over A) time as a system average and B) space as a sample location average.
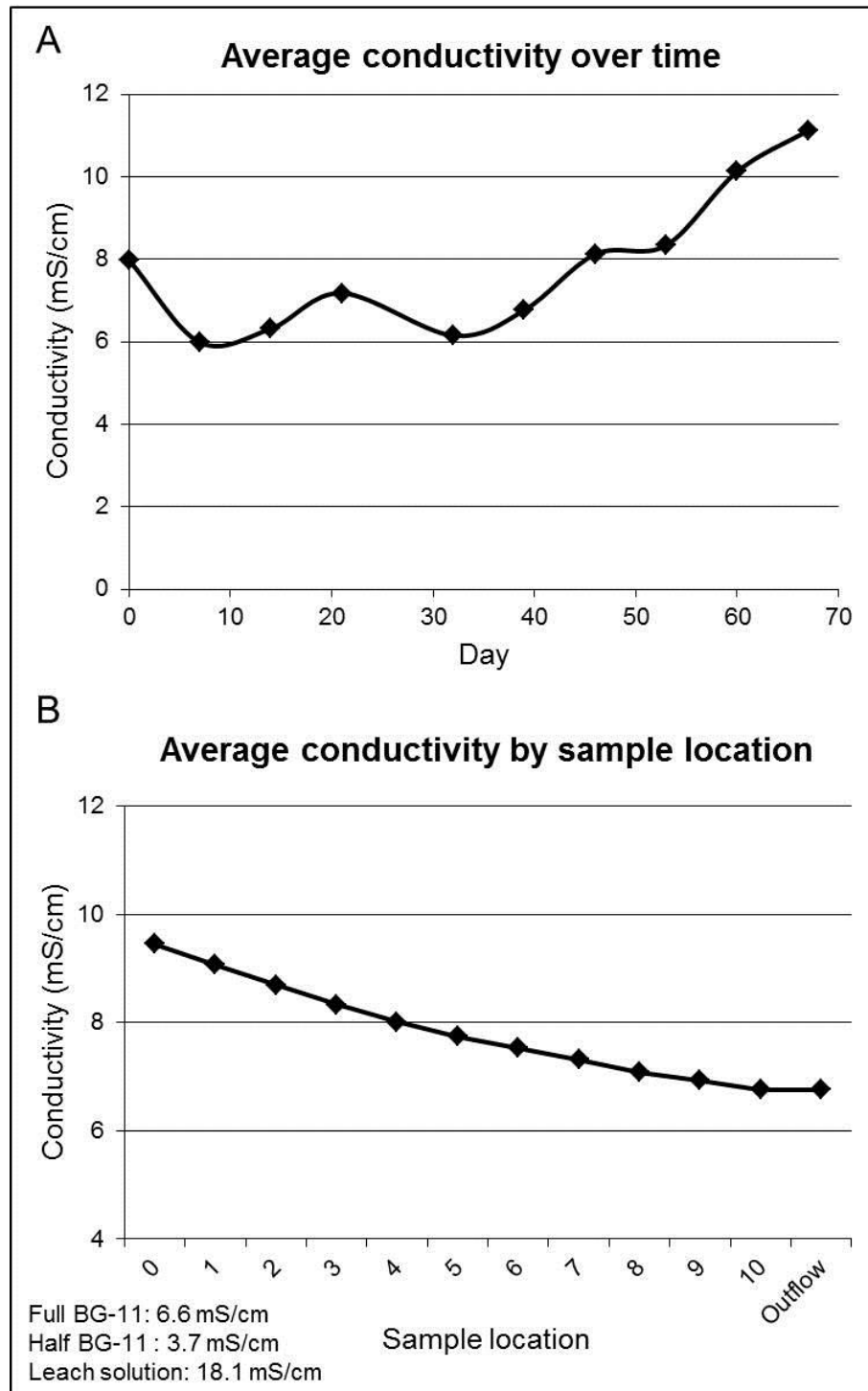
Figure 3.14 Average conductivity over A) time as a system average and B) space as a sample location average.
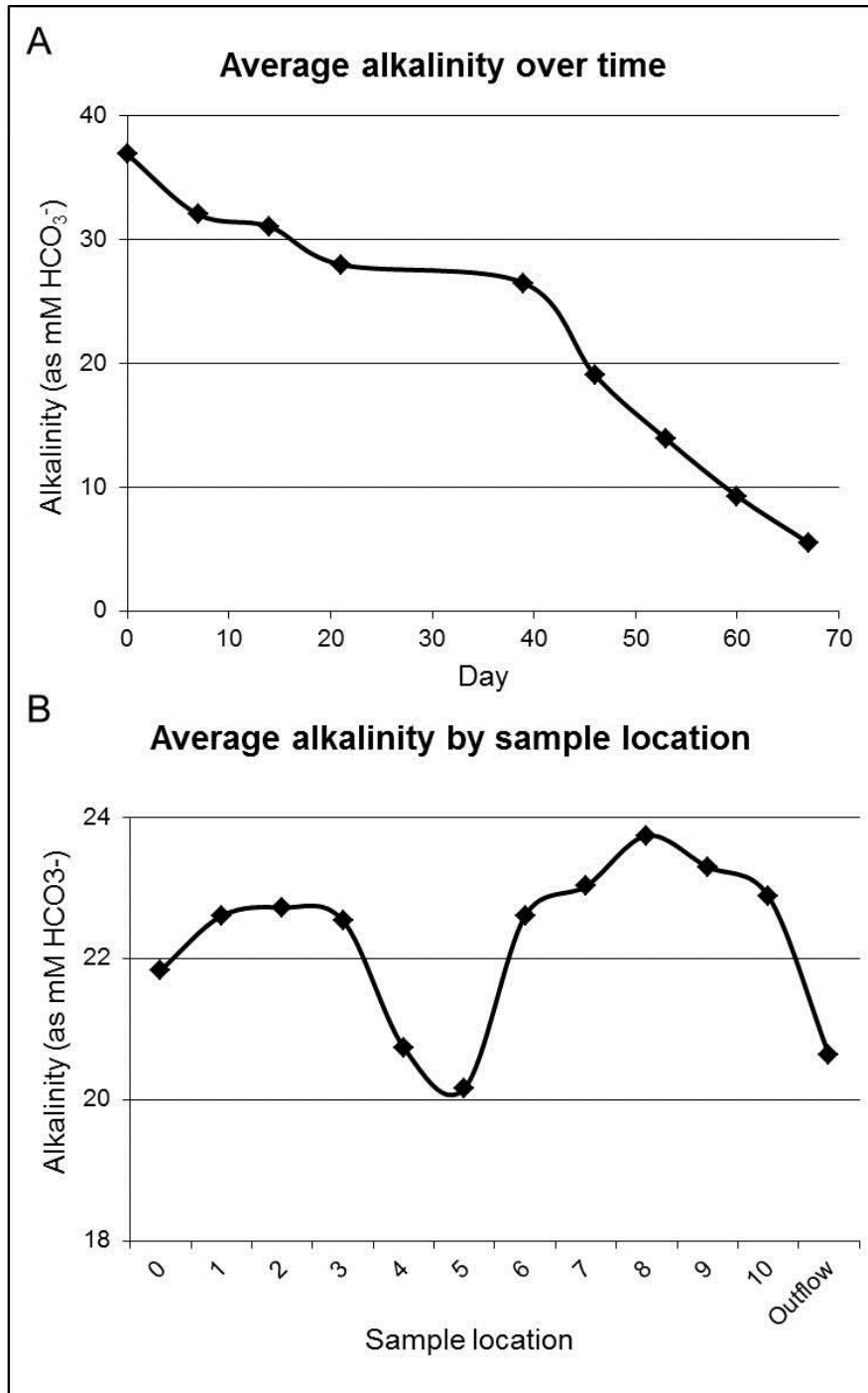
Figure 3.15 Average alkalinity over A) time as a system average and B) space as a sample location average.
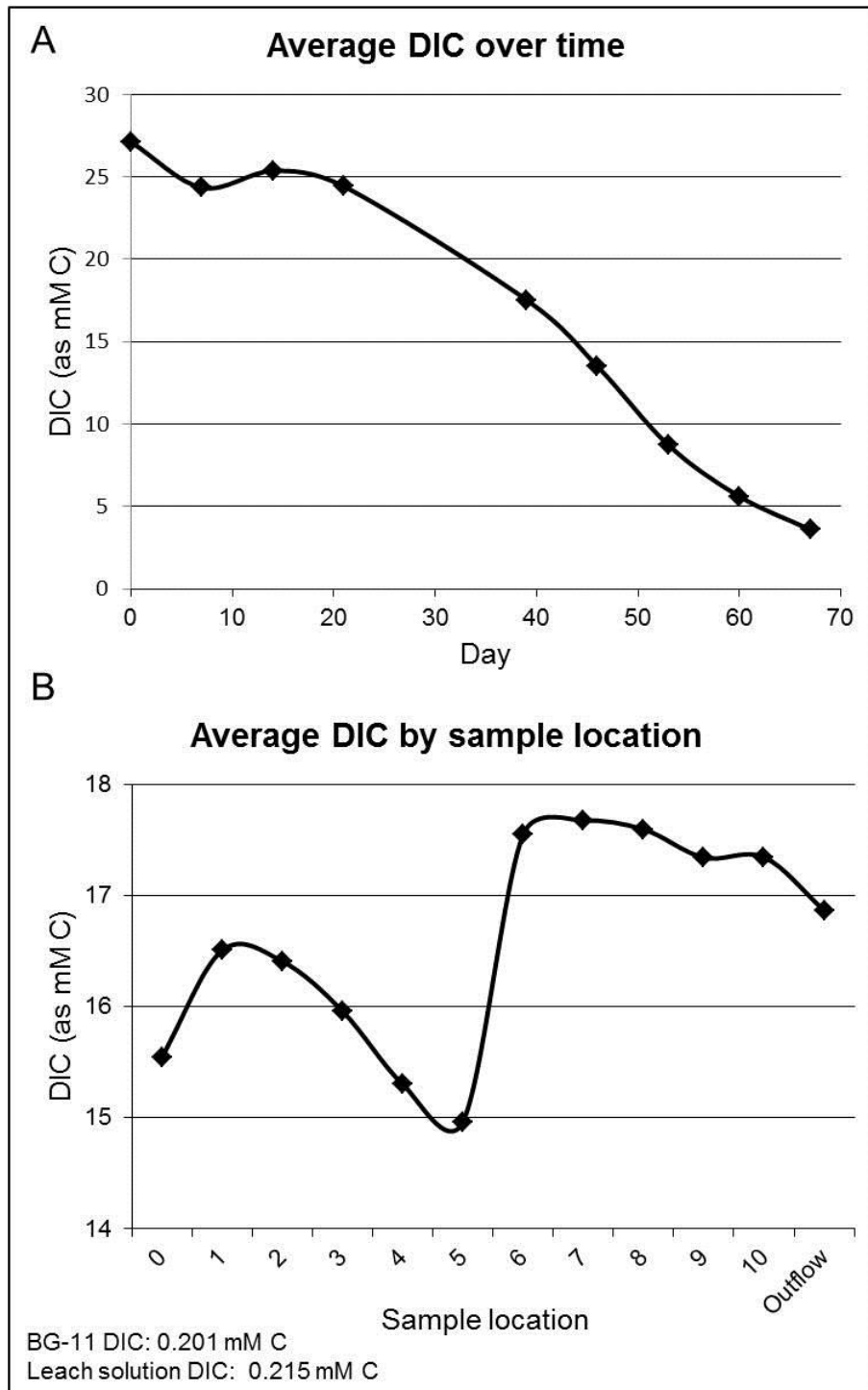
Figure 3.16 Average dissolved inorganic carbon concentration over A) time as a system average and B) space as a sample location average.
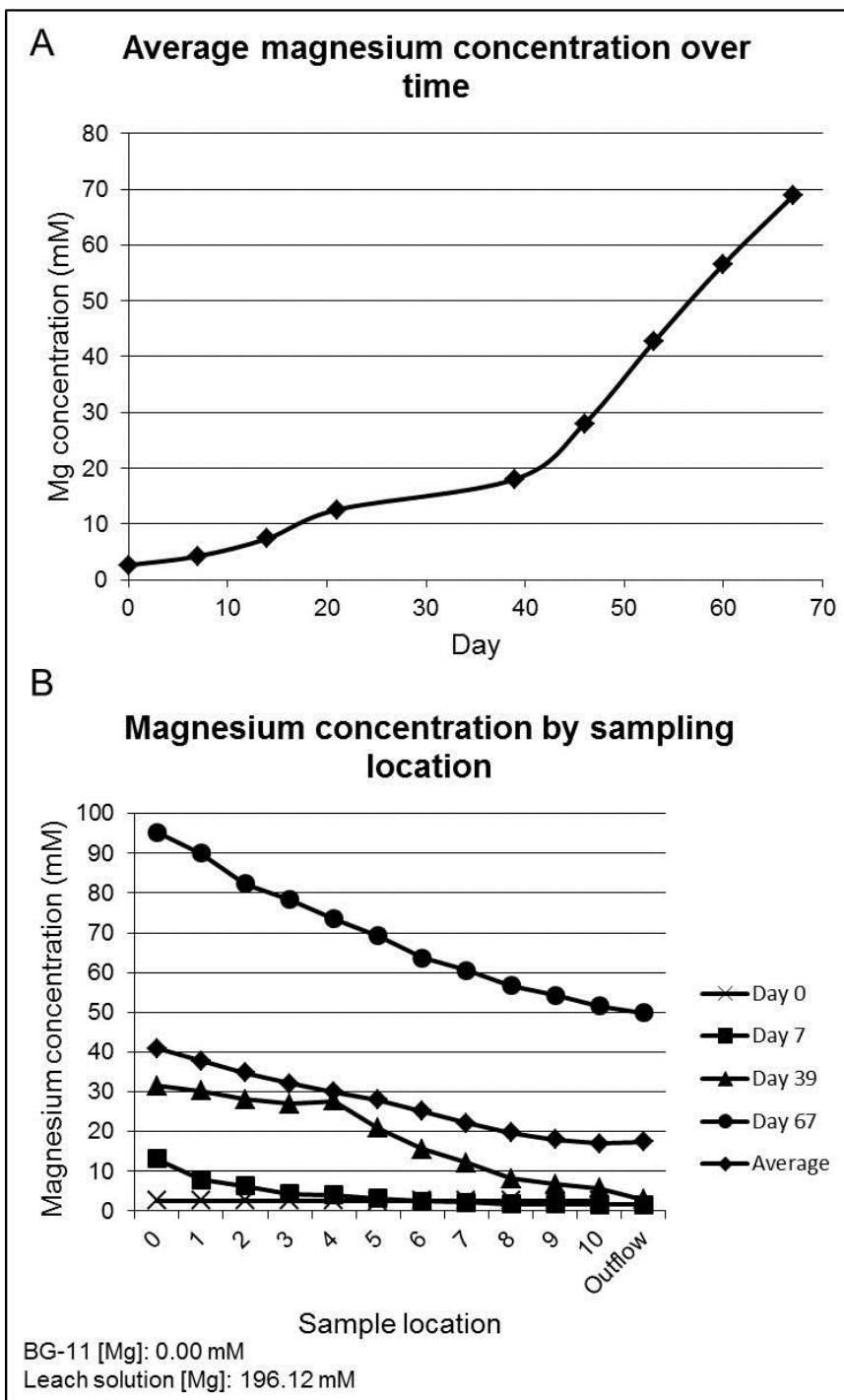
Figure 3.17 Average magnesium concentration over A) time as a system average and B) space on key days throughout the experiment as well as sample location averages for the entire experiment.
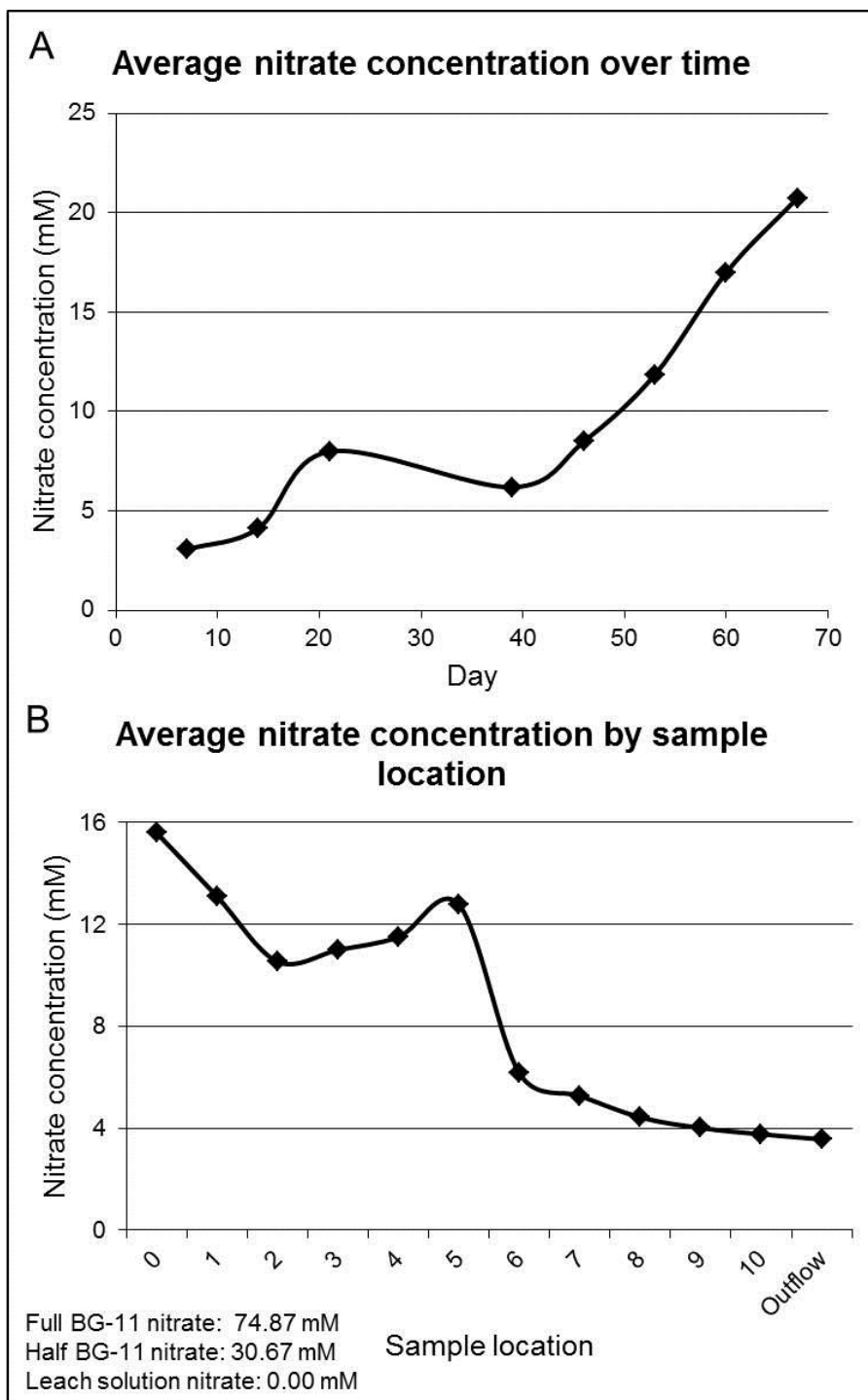
Figure 3.18 Average nitrate concentration over A) time as a system average and B) space as a sample location average.
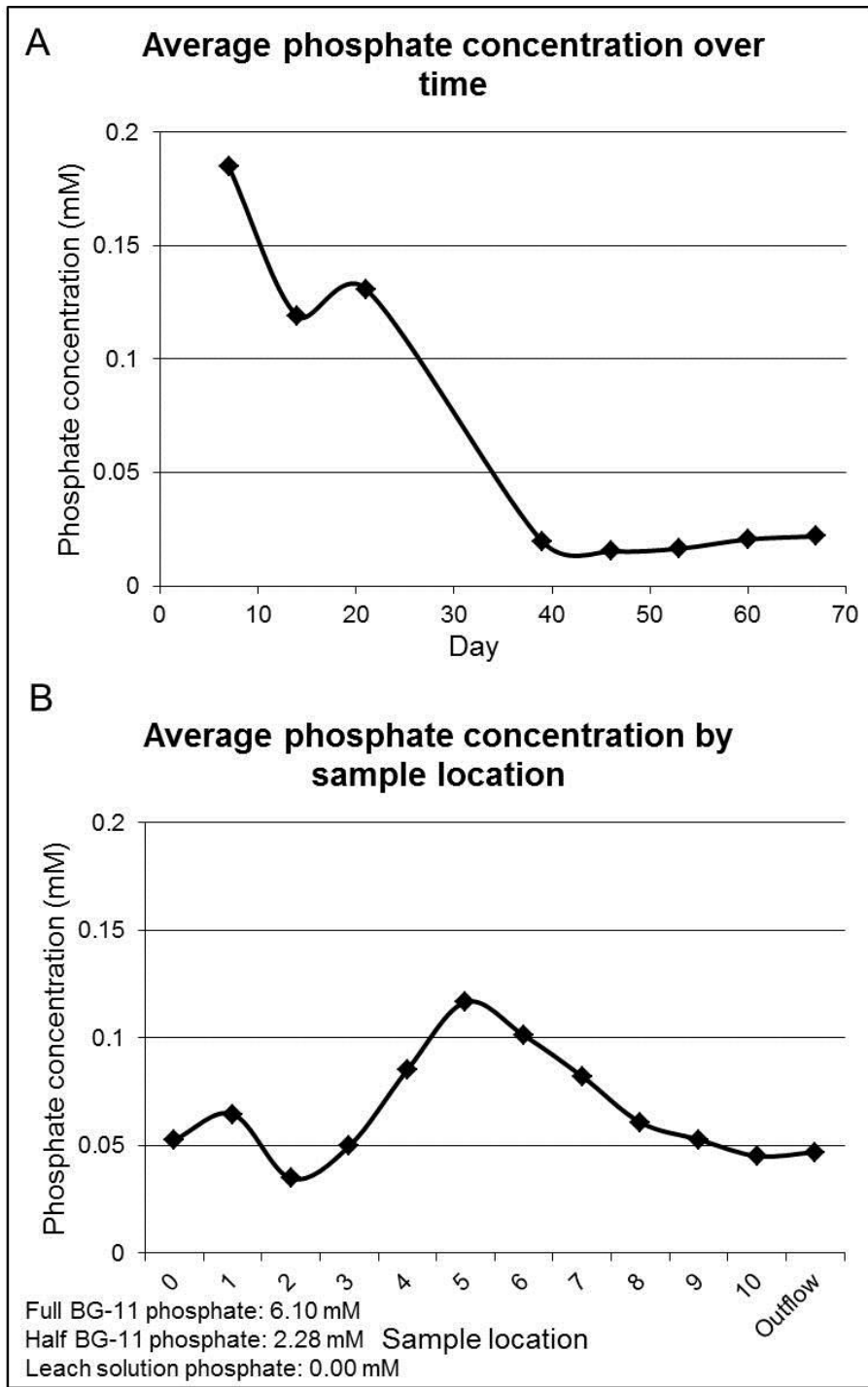
Figure 3.19 Average conductivity over A) time as a system average and B) space as a sample location average.
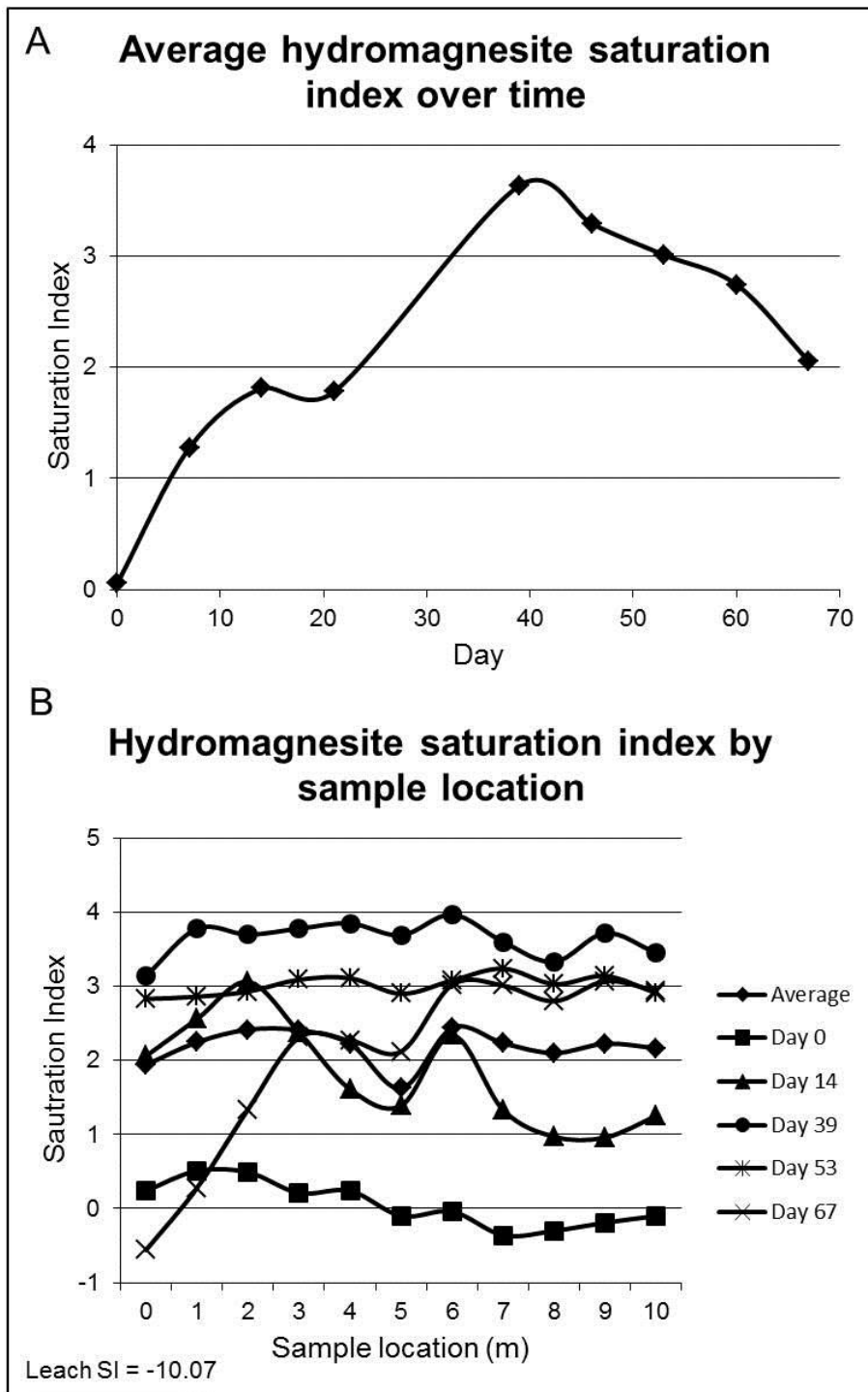
Figure 3.20 Saturation index values for hydromagnesite over A) time as a system average and B) space on key days throughout the experiment as well as sample location averages for the entire experiment.

100
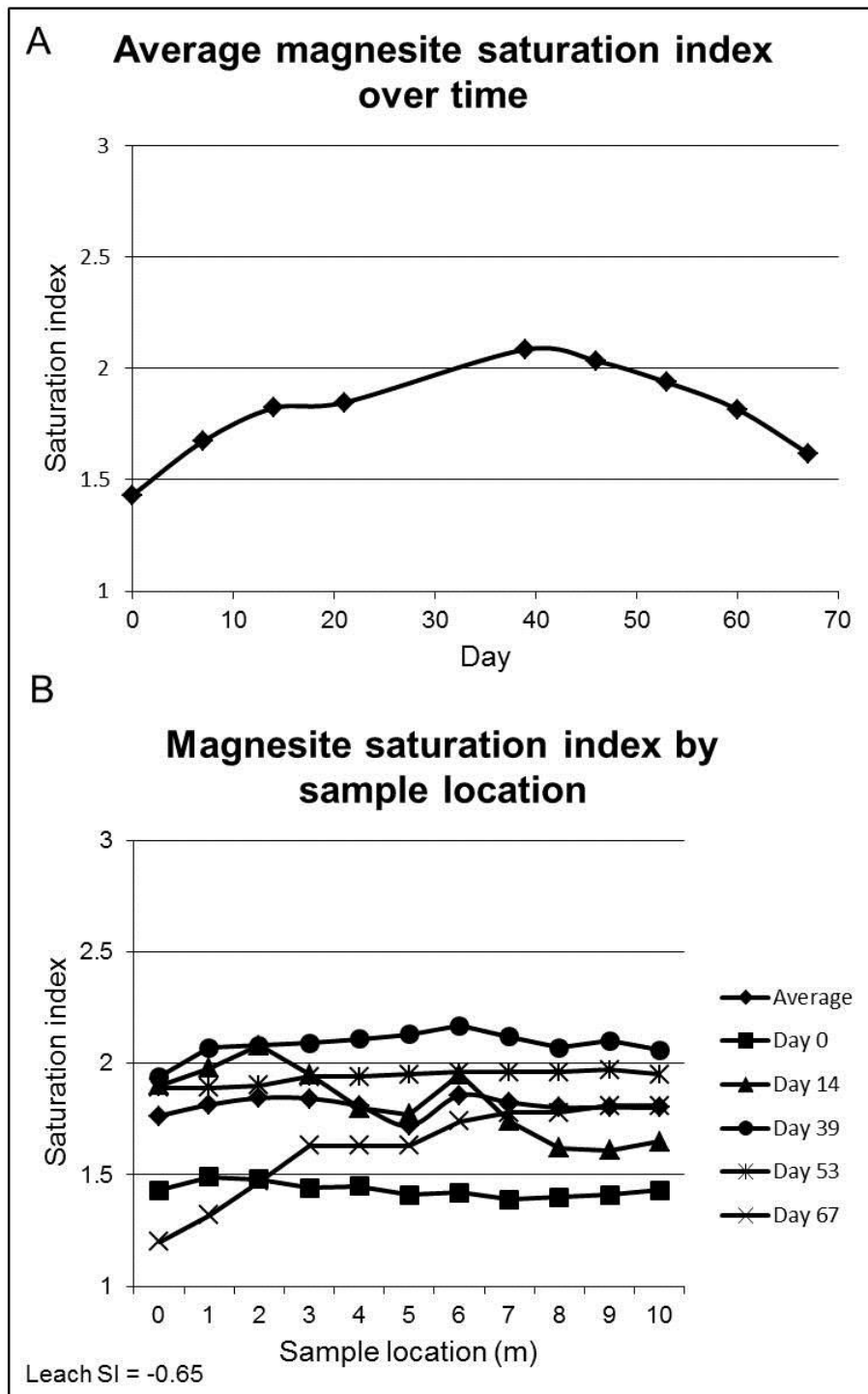
Figure 3.21 Saturation index values for magnesite over A) time as a system average and B) space on key days throughout the experiment as well as sample location averages for the entire experiment.

3.3.4   *Microbe and mineral characterisation*

X-ray diffraction of the microbial mat sample collected prior to starting the experiment indicated only thenardite [Na_2SO_4], which was not observed with SEM and aragonite [$CaCO_3$]; however, the aragonite mineralisation appears to be minimal based on the weak signal collected (Figure 3.22A). The thenardite is likely to be a product of the high sodium and sulfate concentrations in the bioreactor. For the samples collected from the 0 m, 5 m, and 10 m sampling locations during the experiment, the best XRD pattern is presented for each sampling location from either day 28 or day 67. This is due to the low counts measured as a result of the mixed mineral-organic nature of the samples. XRD of the 0 m sample (day 28) indicated the presence of aragonite, magnesite [$MgCO_3$], dypingite [$Mg_5(CO_3)_4(OH)_2 \cdot 8H_2O$], nesquehonite [$MgCO_3(H_2O)_3$], and struvite [$NH_4MgPO_4 \cdot 6H_2O$] (Figure 3.22B). The 5 m and 10 m samples (day 67) both contained aragonite, magnesite, hydromagnesite [$Mg_5(CO_3)_4(OH)_2 \cdot 4H_2O$], and nesquehonite (Figure 3.23). Dypingite and hydromagnesite are very similar minerals in terms of crystal morphology and chemistry, with the primary difference between them being the degree of hydration of the mineral.

SEM-EDS allowed for characterisation of the microbe-mineral relationships present in the bioreactor, and corresponded well with the mineralogy identified with XRD. The microbial mat sample collected prior to starting the carbonation experiment contained filamentous cyanobacteria reaching >200 μm in length. These filaments were straight and cylindrical, with few to no constrictions at the cross walls, and they were accompanied by minor helical filamentous and coccoid bacterial cells (Figure 3.24). No mineral precipitation was observed in this sample. Of the samples collected on day 14, 28, and 67, variations in mineral precipitation appeared to correlate with the location within the bioreactor, and not with time passed in the experiment. All samples examined exhibited some evidence of magnesium carbonate mineralisation, often with several forms of mineral precipitation being observed in a single sample.

The most common magnesium carbonate mineral morphology observed consisted of thin, platy crystals of hydromagnesite reaching 15 μm in diameter (Figure 3.25). The crystals strongly resembled those identified in Chapter 2. They were generally associated with

filamentous cyanobacteria cells similar to the cells described for the time zero sample, as well as large amounts of extra polymeric substances (EPS). In some cases, the EPS appeared to be contained within the mineral plates.

The second type of mineral precipitation observed consisted of small rhombohedral crystals of magnesite (Figure 3.26). The magnesite grains reached 3 μm in size along their longest axis, though most were less than one micron. The crystals were primarily composed of Mg-C-O; however, some grains contained 1-2 wt% calcium. The grains were always observed amongst plates of hydromagnesite, and generally at boundaries between the plates. A similar relationship between magnesite and hydromagnesite was also documented by Power et al. (2012) in samples of the Atlin playa sediments.

Two carbonate precipitation morphologies were observed directly on microbial cells, and appeared to correspond to cell morphology. Many of the filamentous cyanobacterial cells were encased in a nanometer-scale crystalline coating which generally contained large amounts of EPS (Figure 3.27). When analysed with EDS, this mineral phase was composed of Mg-C-O, although the carbon content was extremely high due to some of the signal being generated by the cells. Many examples of empty magnesium carbonate casts were observed and exhibited the morphology of the cyanobacterium cells, even after the cells were no longer present (Figure 3.27B). The mineralisation appeared to encase a framework of EPS outside the filaments, with occasional crystals of what appeared to be submicron sized hydromagnesite plates beginning to form (Figure 3.27D). In rare cases, small individual crystals were seen adhering to filaments without a continuous carbonate coating (Figure 3.27C). These nanometer-scale grains resembled the larger magnesite crystals seen in many of the microbial mat samples. The second form of carbonate precipitate observed directly on microbial cells occurred as a nanometer-scale acicular precipitate on coccoid cells (Figure 3.28). The precipitate contained a mix of magnesium and calcium, present as ~4.5 wt % and ~9 wt %, respectively.

Rosettes of curved platy Mg-C-O crystals were observed in the 1 m microbial mat sample (Figure 3.29). Some of these crystals contained up to 7 wt% calcium. Although some

individual rosettes reached diameters of 6 μm, most were on the order of 3 μm in size, constituting clusters of adjacent rosettes reaching 15 μm in diameter. This form of mineralisation was always covered in large amounts of EPS. The rosettes strongly resembled the dypingite crystal aggregates identified by Power et al. (2007) from the Atlin wetland. With dypingite only being identified by XRD in the 0 m sample, and this crystal morphology only having been observed near the start of the bioreactor, it stands to reason that these rosettes are composed of dypingite. The combined XRD and SEM-EDS results indicate that significantly more hydromagnesite precipitated during the carbonation experiment than dypingite. Nesquehonite, which forms abiotically through dehydration, was not observed in any of the samples using SEM. The nesquehonite identified with XRD was likely to have been a product of drying the microbial mat samples or was formed as an evaporative phase on the surface of the water in the bioreactor and became adhered to the microbial mat as it was removed from the water during sampling. This is supported by the fact that PHREEQC did not indicate supersaturation of nesquehonite in the bioreactor water at any point during the experiment (Appendix E).

The aragonite identified with XRD was primarily observed as clusters of prismatic crystals reaching 6 μm in length (Figure 3.30A). Although the aragonite contained mainly calcium, carbon, and oxygen, some crystals contained 1-2 wt% magnesium. The crystals were similar to those documented by Power et al. (2009) from sediments in the Atlin wetland. The other morphology observed for calcium carbonate consisted of pseudohexagonal crystals reaching 40 μm in size (Figure 3.30D and 3.30E).

Struvite was identified with XRD in the 0 m and 5 m samples. The mineral was observed with SEM-EDS in the microbial mat samples collected at 1 m increments between 0 m and 3 m, and between 5 m and 8 m. Although the phase identified was a good match for struvite using XRD, when analysed with EDS the crystals were shown to be composed of magnesium, phosphorus, carbon, and oxygen (Figure 3.31). This varies from the standard chemical formula of [$NH_4MgPO_4 \cdot 6H_2O$] for struvite. No nitrogen was ever identified with EDS. The relative proportions of carbon and phosphorus varied between mineral grains. In many cases, microbes could be seen adhering to the struvite crystals,

particularly along edges and fractures, likely acquiring phosphate from the mineral phase. Also, the struvite crystals became smaller and more fragmented with increasing distance from the phosphate source, suggesting that dissolution was occurring.

Many of the microbial mat samples examined showed the occurrence of multiple forms of magnesium carbonate precipitation in close proximity to each other (Figure 3.32). The mixed mineralisation included hydromagnesite, magnesite, aragonite, carbonate coatings on filaments, and acicular precipitates on coccoid cells. The presence of multiple mineral phases together demonstrated that mineralisation type was not closely tied to specific sites in the bioreactor. There were, however, general trends observed in terms of the types of carbonate mineral formation. It appeared that the carbonate coatings seen on cells, particularly the filaments, were found more commonly in the upper 5 m of the bioreactor with large amounts concentrated at the 0 m location. Although hydromagnesite was found throughout the bioreactor, little was observed in the 0 m samples. Magnesite was not observed in mat samples collected at locations from 0 m to 3 m. Magnesite crystals became more abundant over time and down the length of the bioreactor. Moreover, the size of the magnesite crystals increased as a function of distance from the start of the bioreactor.
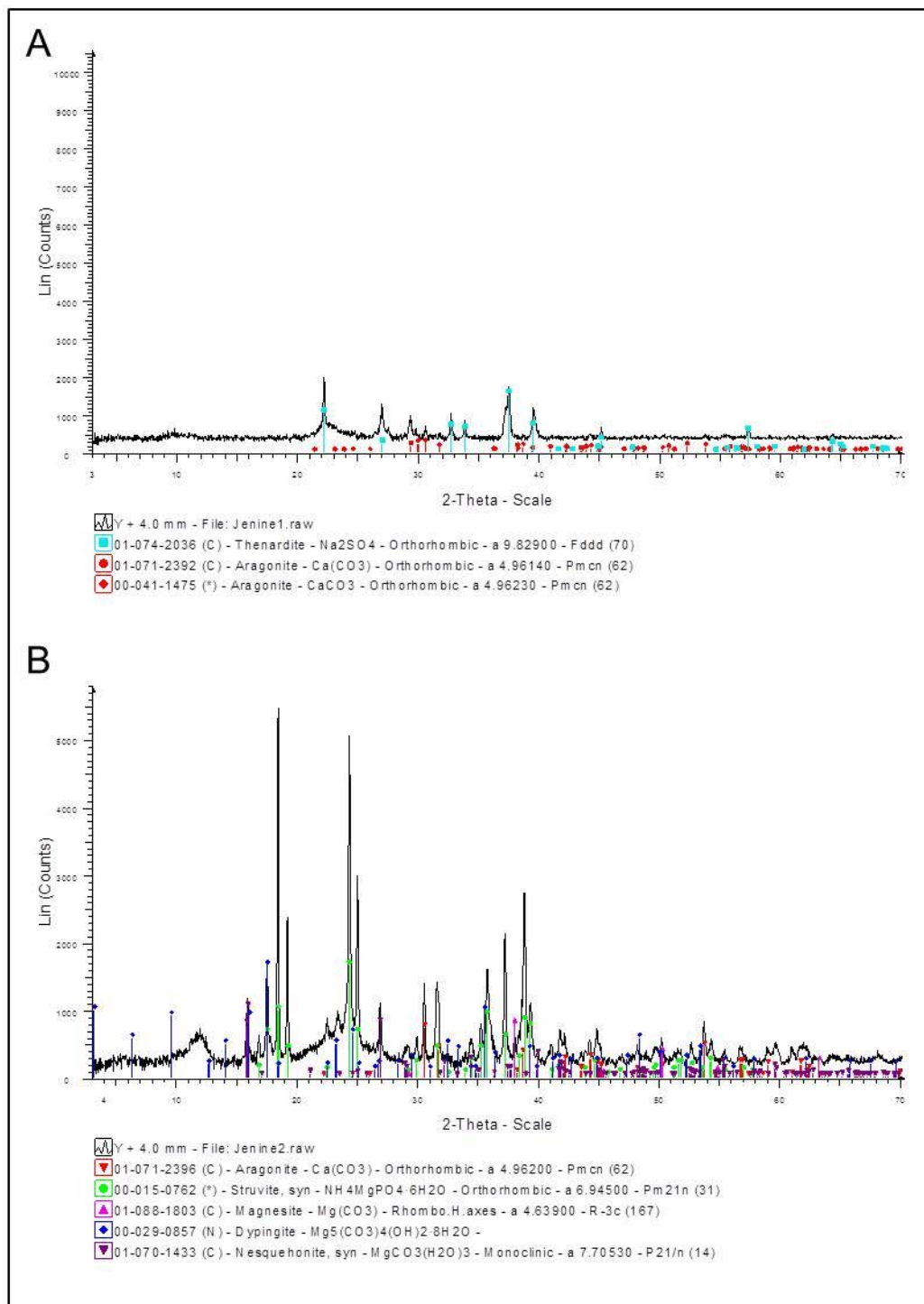
Figure 3.22 XRD pattern for samples of microbial mat collected at A) the start of the experiment and B) on day 28 at the 0 m sampling point in the bioreactor.
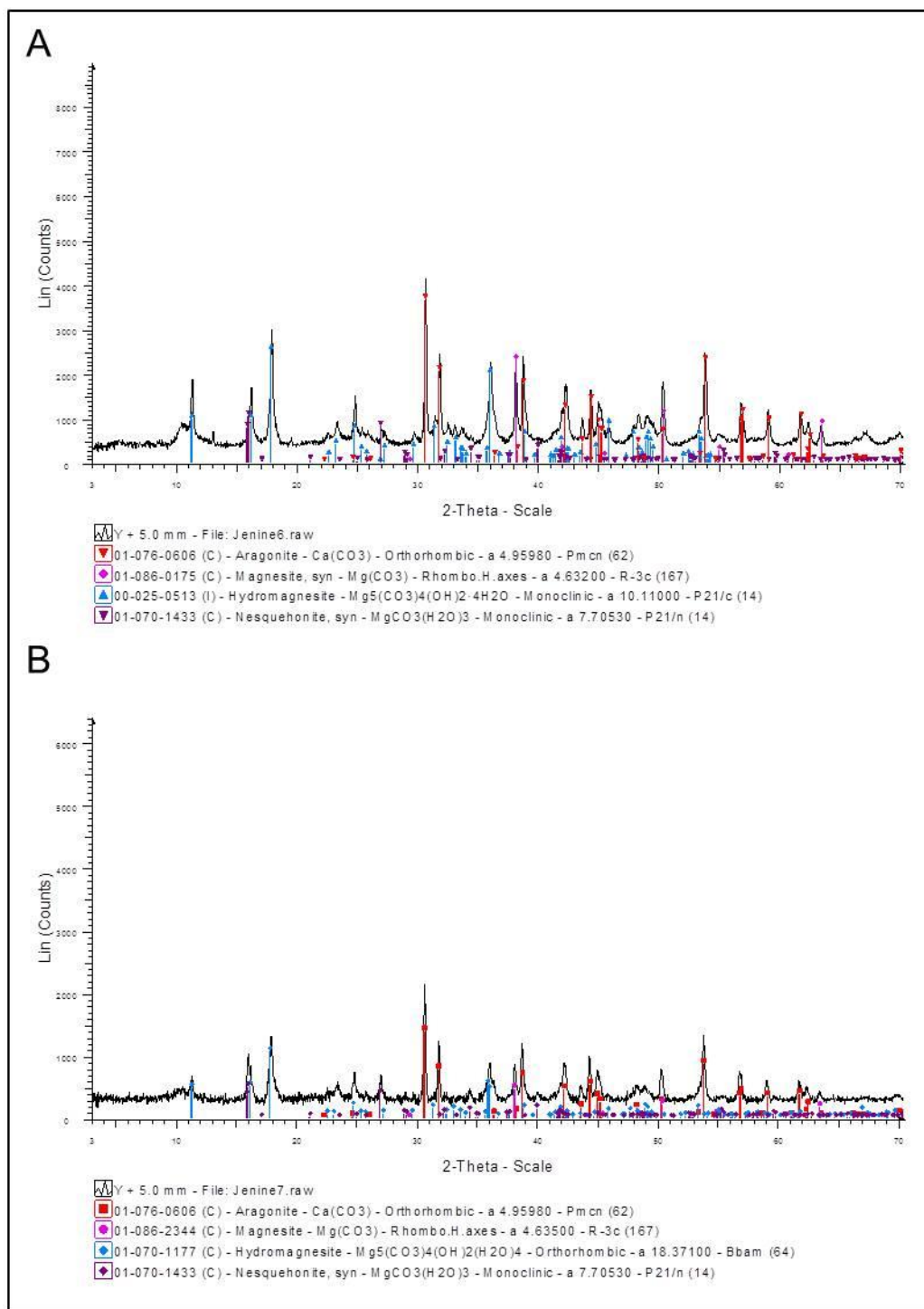
Figure 3.23 XRD pattern for powdered microbial mat samples collected on day 67 at A) the 5 m sampling location and B) the 10 m sampling location in the bioreactor.
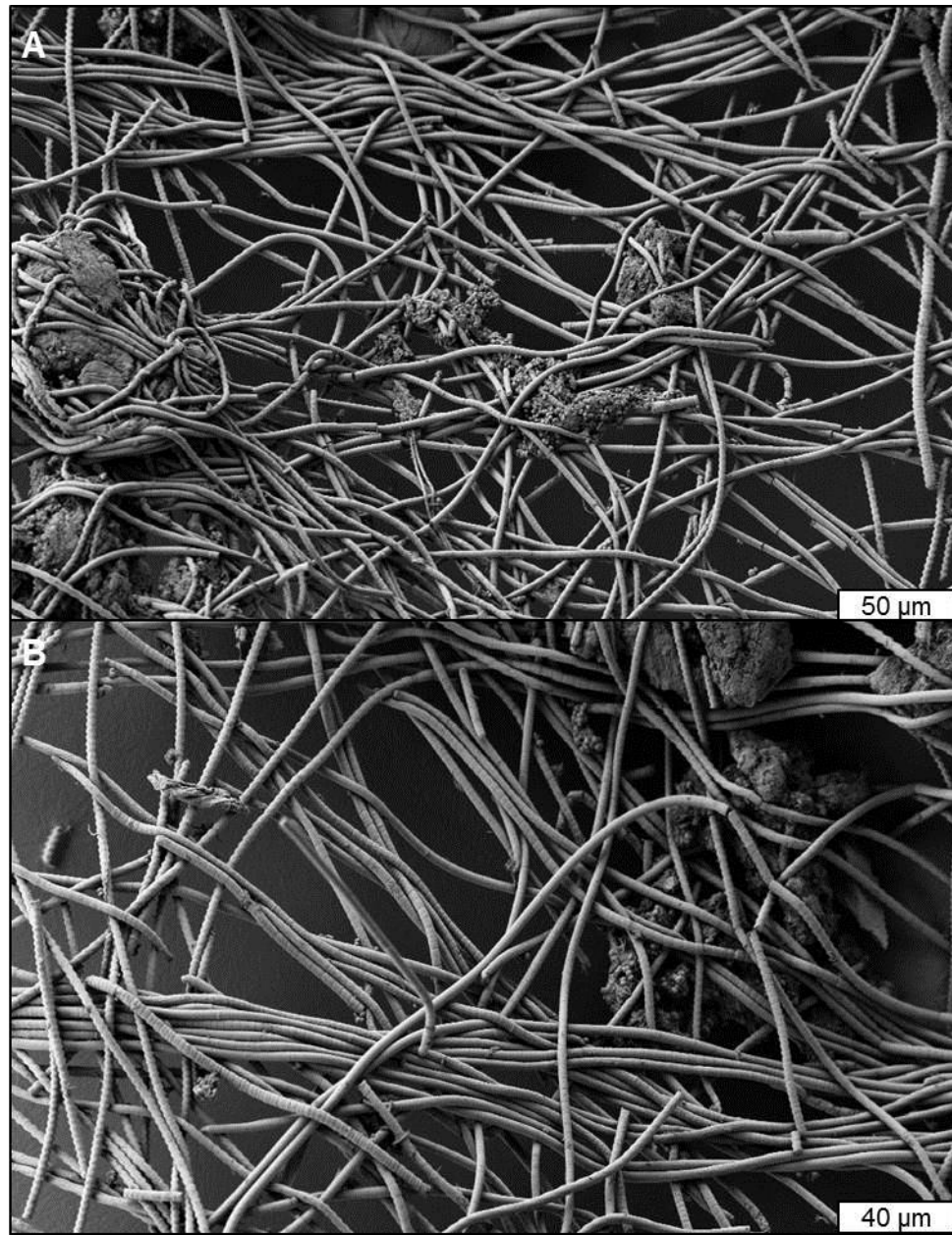
Figure 3.24 SEM of the filamentous cyanobacteria cells found in the microbial mat sampled from the bioreactor prior to the start of the carbonation experiment.
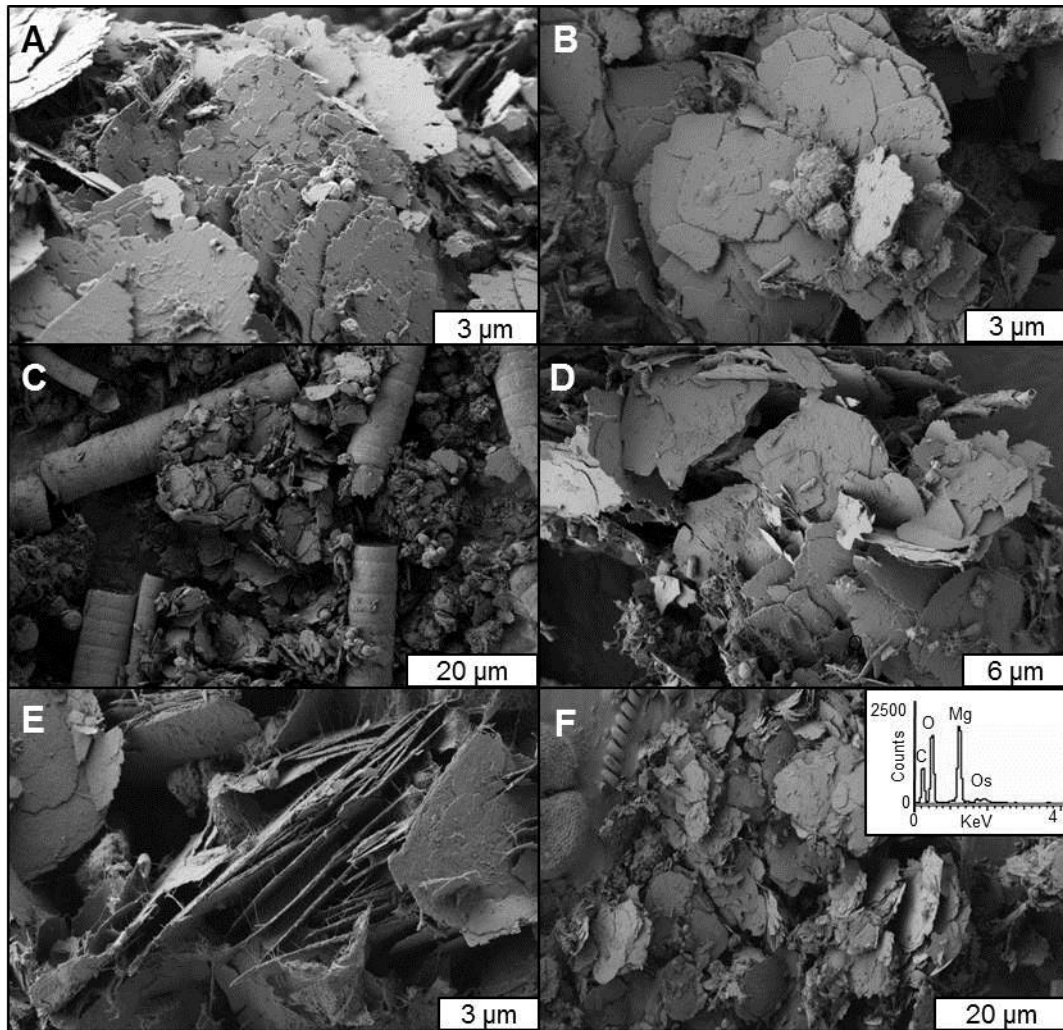
Figure 3.25 Scanning electron microscopy of hydromagnesite plates observed in samples from day 14 at 10 m (A and B); and day 67 at 5 m with cyanobacteria filaments (C), 6 m (D), and 7 m (E and F). Inset of F) EDS spectrum of the hydromagnesite.
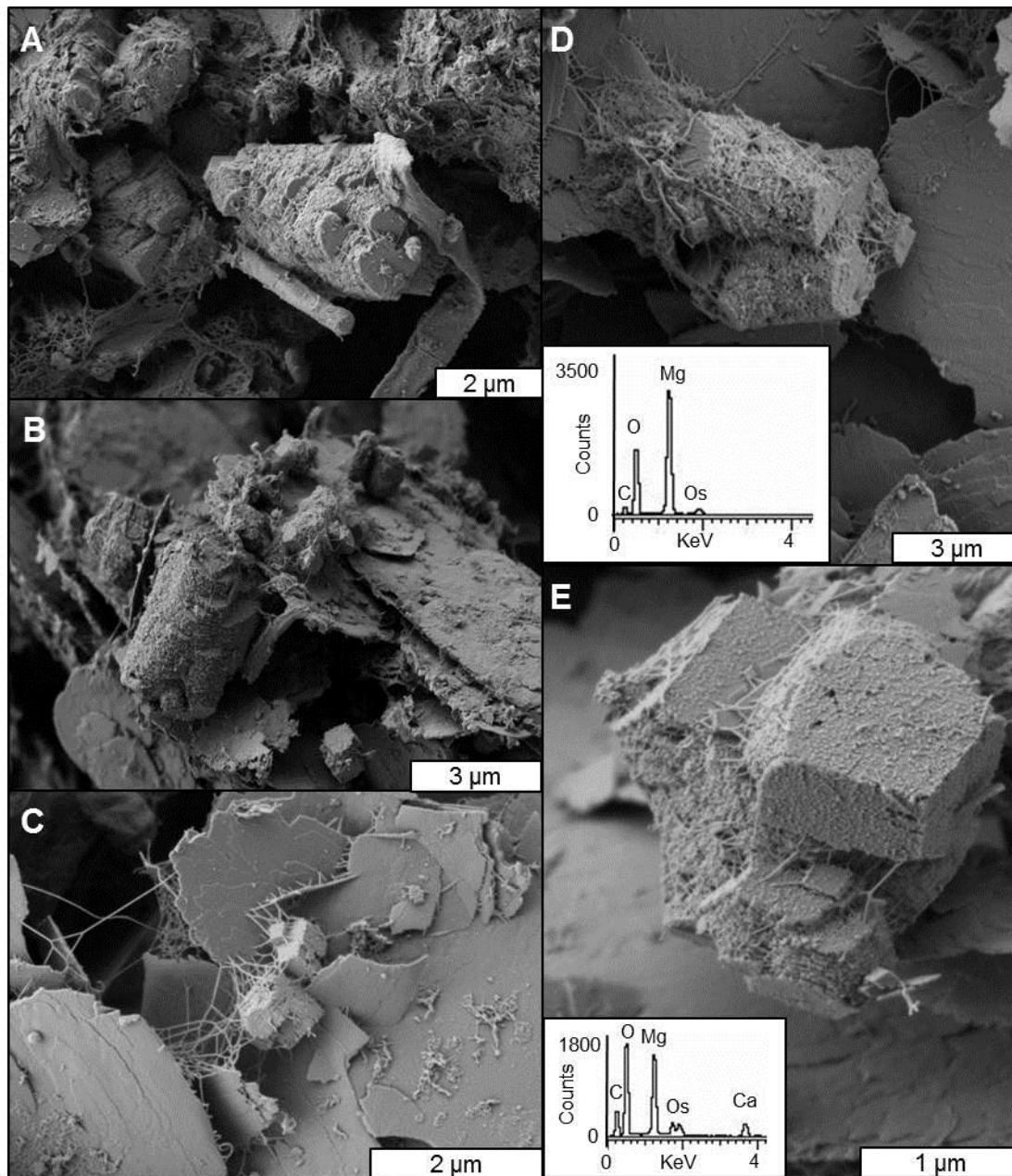
Figure 3.26 Rhombohedral magnesite crystals found associated with hydromagnesite in the microbial mat samples collected during the carbonation experiment. Samples collected on day 14 (A) and day 28 (B) at 10 m; and day 67 at 6 m (C and D), and 7 m (E). EDS spectra for the magnesite in D and E are shown, with the grain in E containing some calcium.
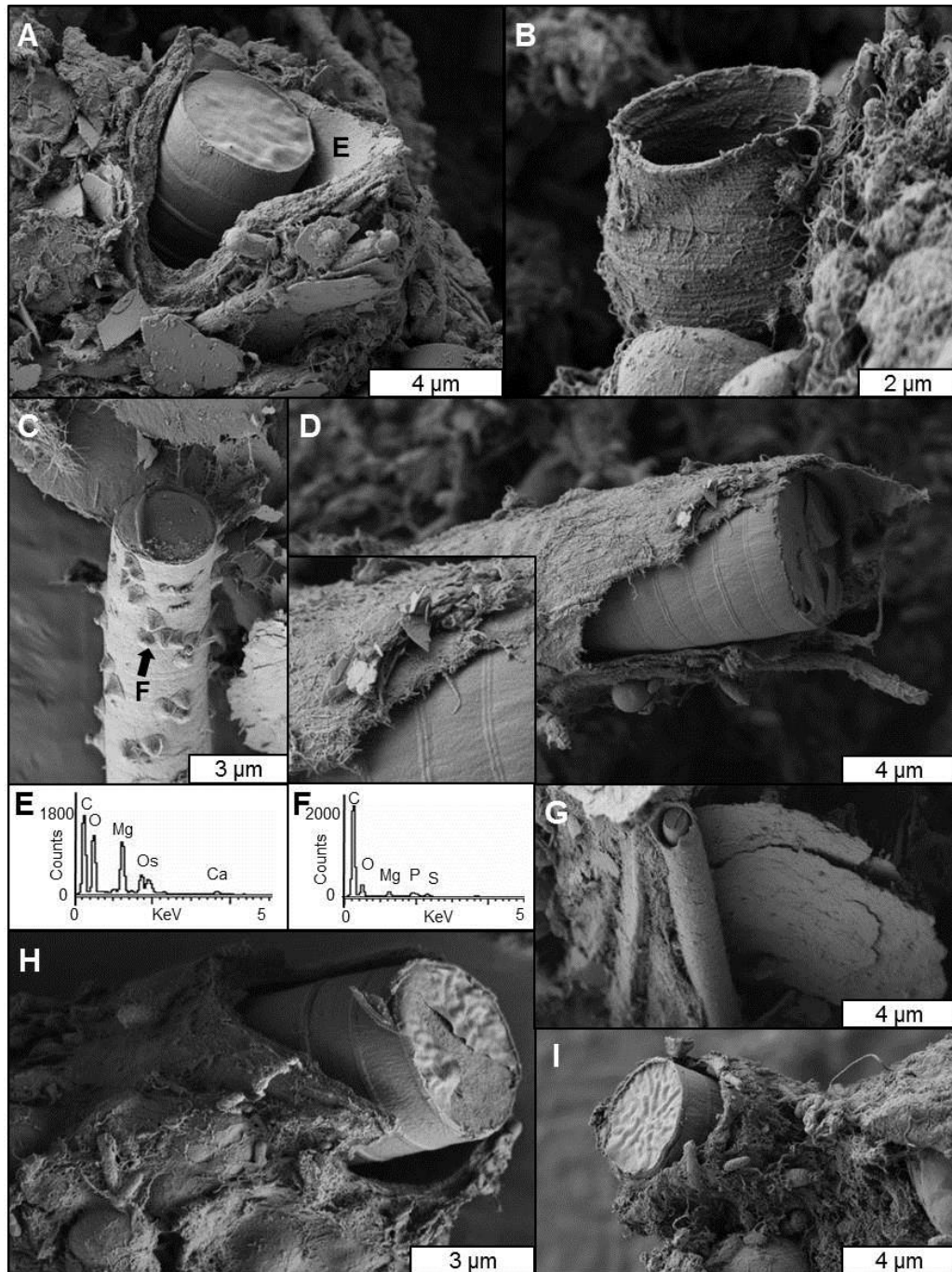
Figure 3.27 A) SEM of cyanobacteria filaments encased in magnesium carbonate and EPS sampled on day 14 at 10 m (EDS spectra shown in E). B) A magnesium carbonate cast left behind after a cell has died and C) nanometre-scale crystals adhered to a filament sampled at 2 m on day 67 (EDS spectra corresponding to C) shown in F). D) A cyanobacterium covered in magnesium carbonate and EPS sampled on day 67 at 6 m, with small plates of hydromagnesite forming on top of the precipitate coating (inset). G)-I) cyanobacteria filaments coated in carbonate precipitate sampled on day 67 at 7 m, 8 m, and 10 m.
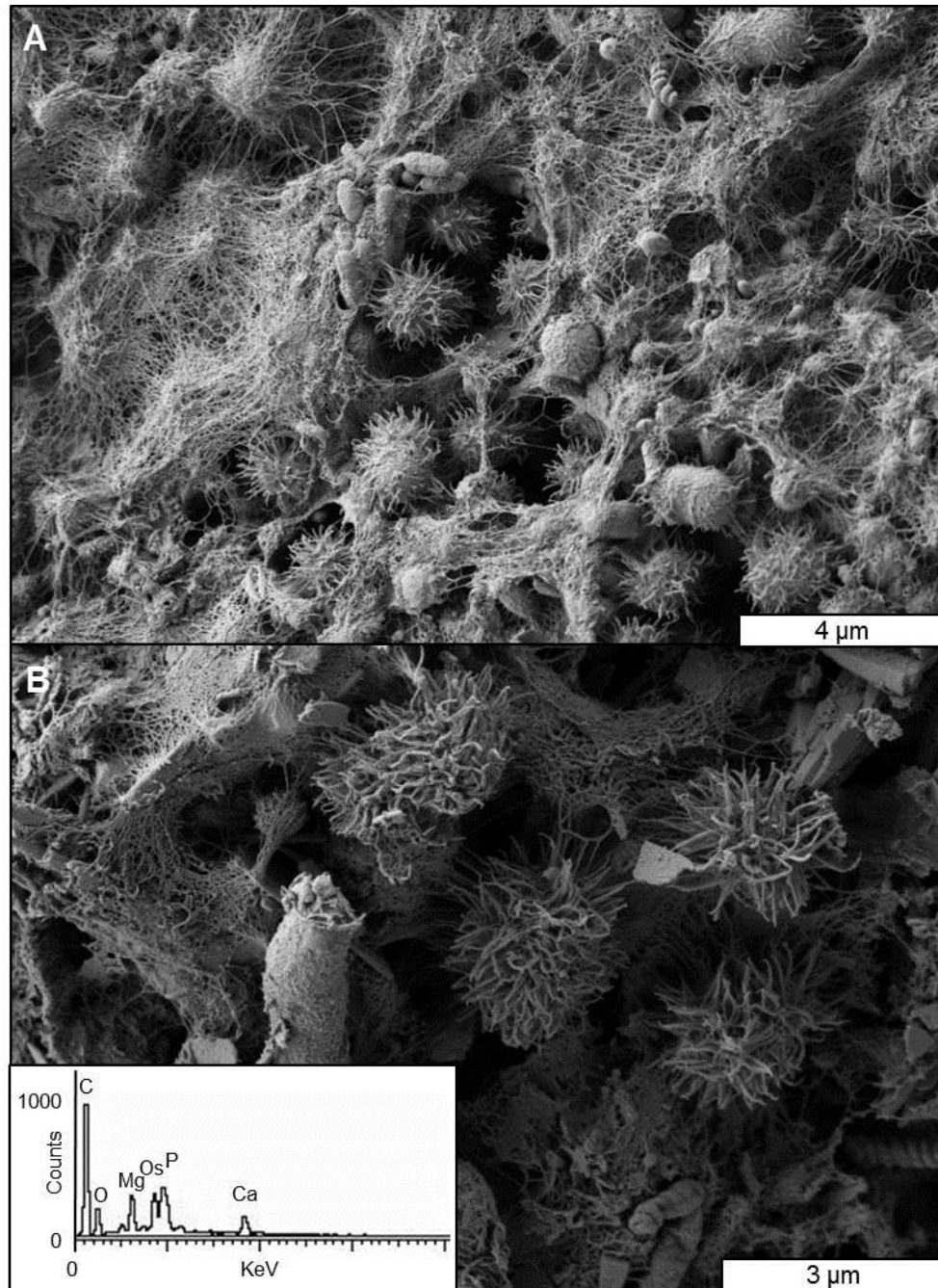
Figure 3.28 SEM of the large amount of EPS generated in the bioreactor along with the nanometer-scale acicular mineral precipitate found coating coccoid cells within the microbial mat. Samples taken on day 14 from A) 0 m and B) 10 m. Inset in B) is the spectrum generated by EDS of these precipitates.
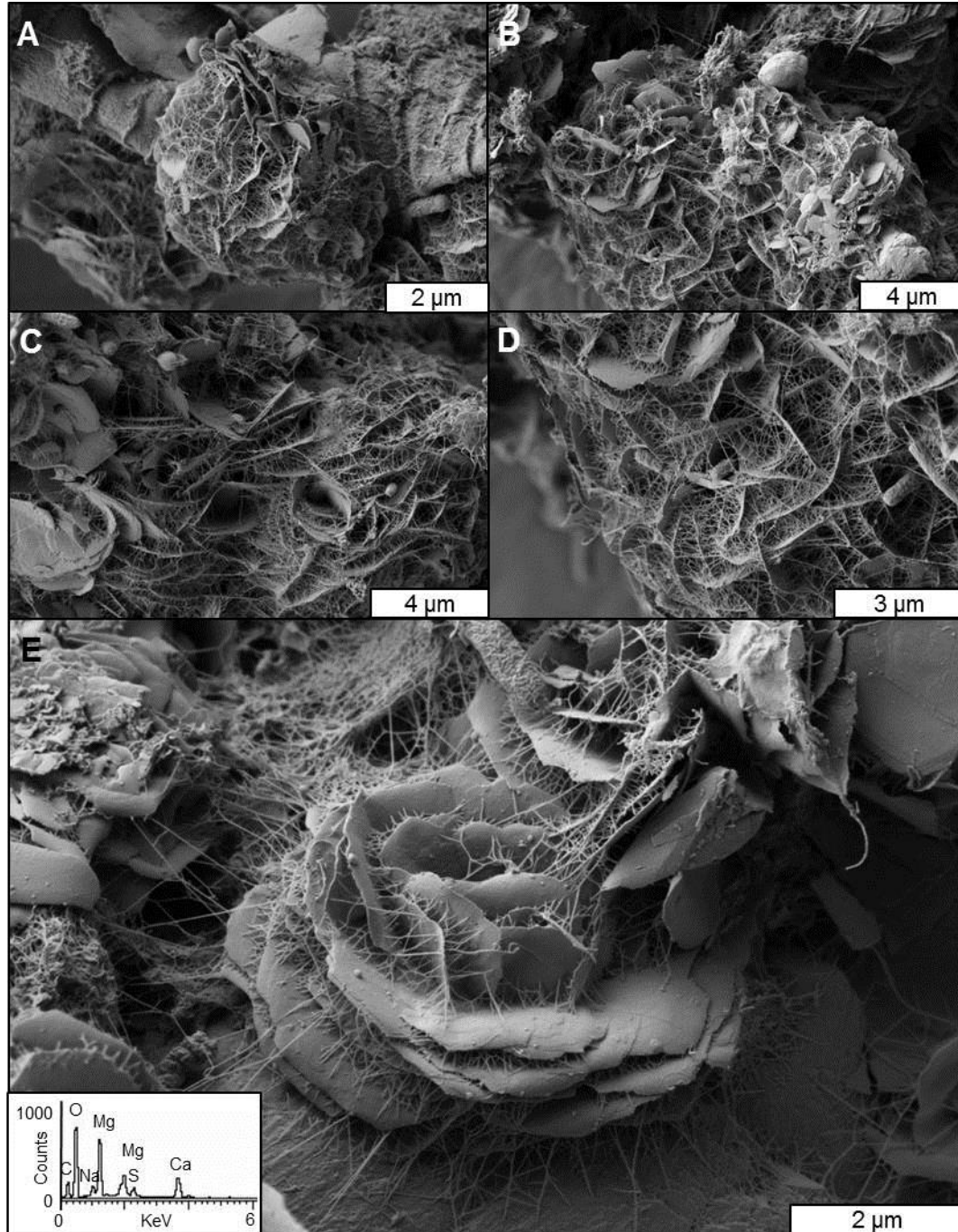
Figure 3.29 Scanning electron microscopy of the dypingite rosettes observed in the microbial mat samples. All of these examples were observed in a sample of mat collected on day 67 from the 1 m location, with the inset of E) showing the corresponding EDS spectrum.
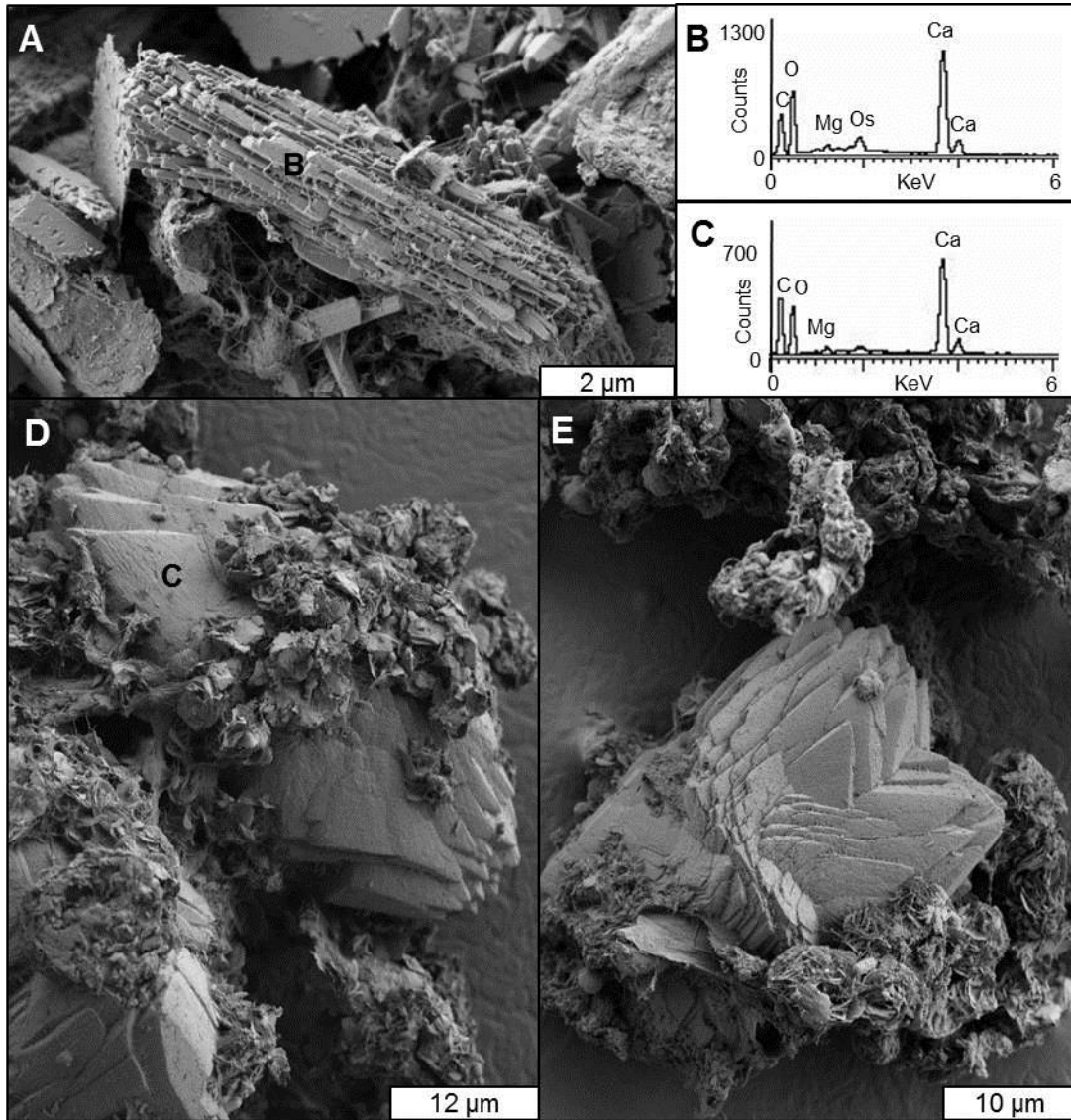
Figure 3.30 SEM of the aragonite observed in the microbial mat samples. A) prismatic aragonite crystals in a sample from 10 m on day 14, with the corresponding EDS spectra shown in B). C) EDS spectra of the larger aragonite crystals observed in a sample from 1 m on day 67, as shown in D) and E).
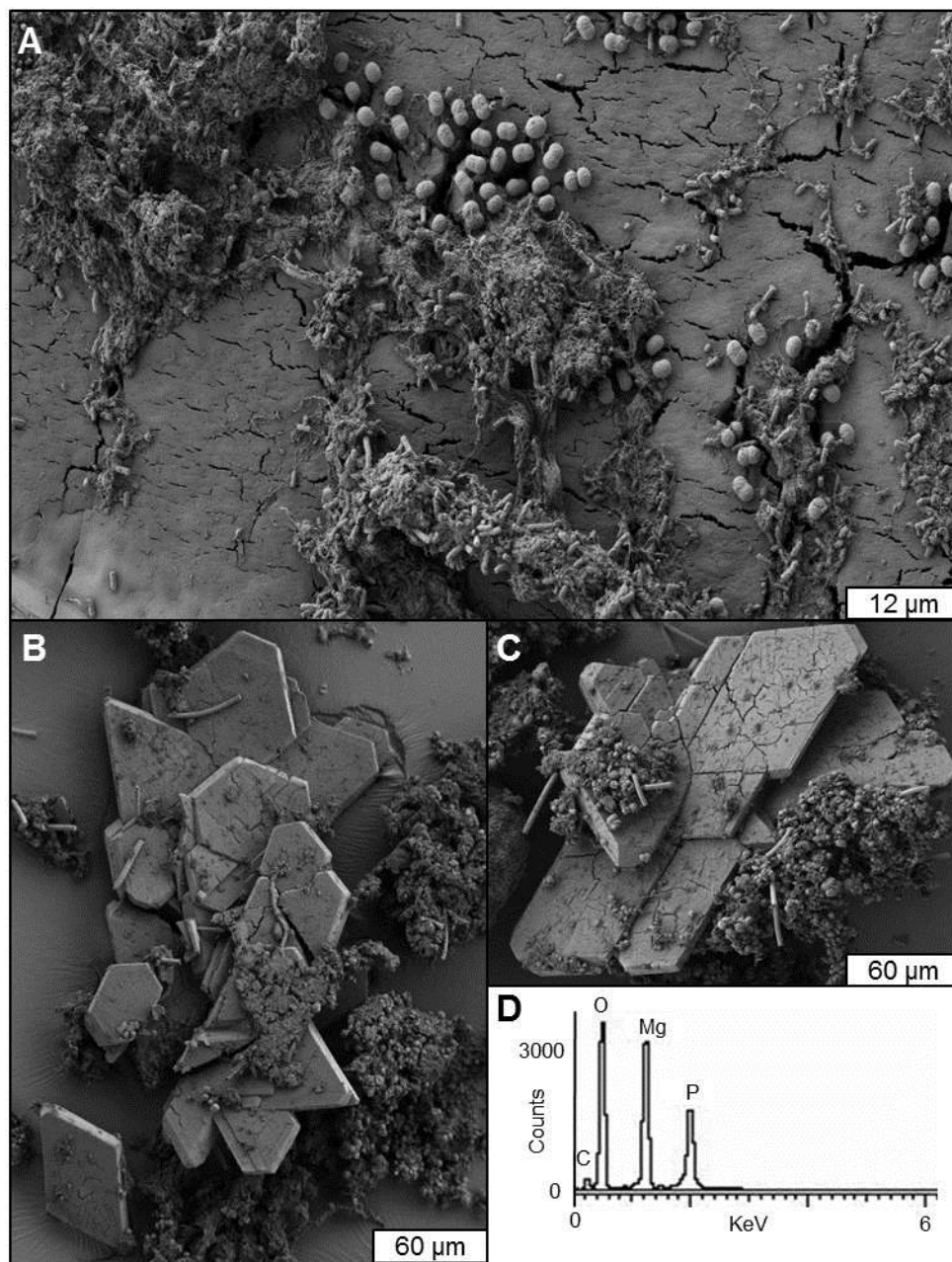
Figure 3.31 SEM of the struvite found precipitated at the 0 m sampling location on A) day 67 and B)-C) day 14. D) Representative EDS spectrum of the struvite observed in the microbial mat samples.
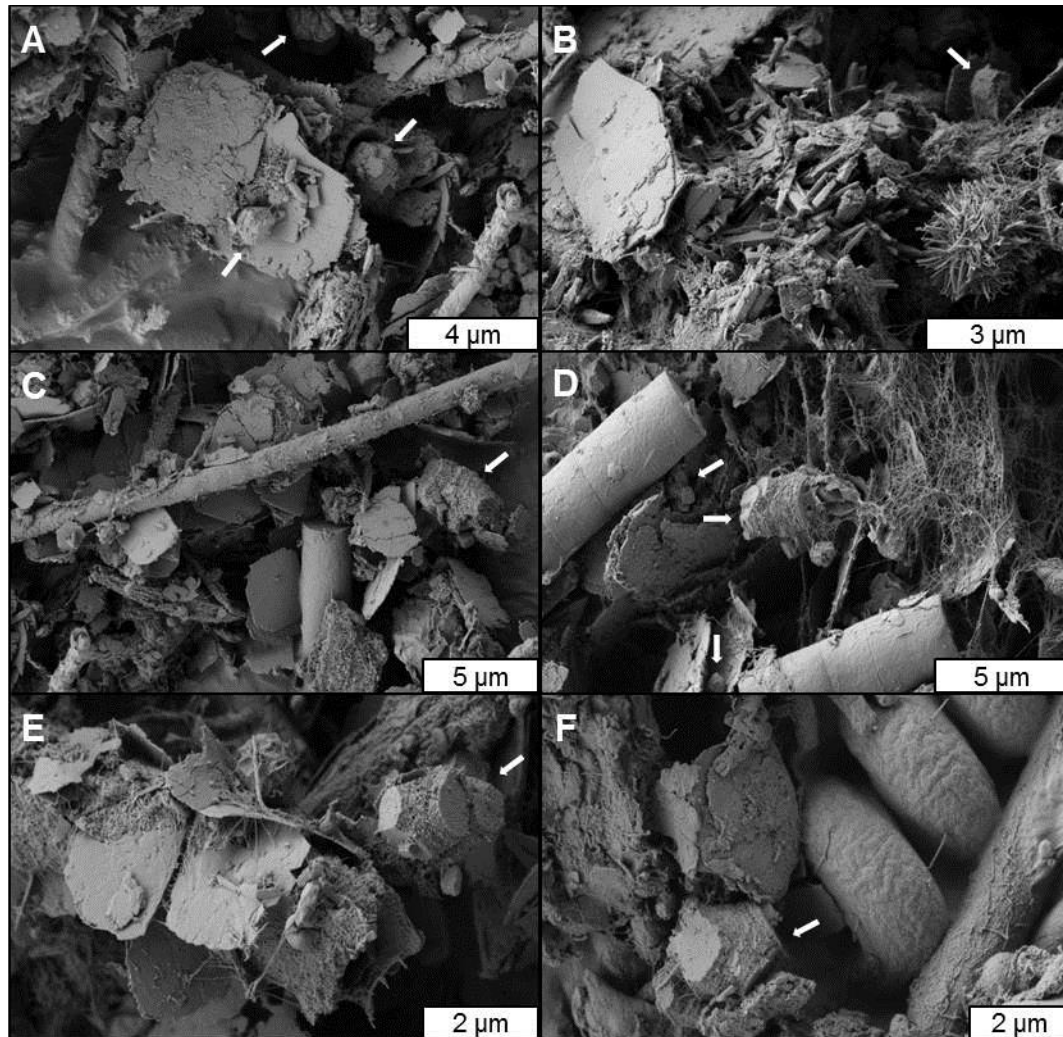
Figure 3.32 Scanning electron microscopy of the occurrence of multiple types of magnesium carbonate mineralisation in several individual samples. These samples were collected on: A)-C) day 14 at 10 m, D) day 28 at 10 m, E) day 67 at 7 m, and F) day 67 at 9 m. These images demonstrate the ability of the bioreactor to precipitate, hydromagnesite, magnesite, aragonite, carbonate coatings on filaments, and acicular precipitates on coccoid cells within microns of each other.

3.4   **Discussion**

3.4.1   Magnesium leaching at high acid concentrations

The results of the leaching experiment showed that the amount of material leached from the chrysotile fibres increased with increasing acid concentration (Stumm 1992; Park and Fan 2004). This trend was observed for most flasks; however, both the XRF and ICP results indicate there was less magnesium leached in flask 4 than in flask 3. This difference may be due to the magnesium sulfate minerals that were observed with SEM-EDS in flask 4, which would have consumed some of the soluble magnesium generated by the leaching process. The concentration of sulfate increased with increasing sulfuric acid concentration, making precipitation of these minerals possible. Secondary minerals may have also inhibited further leaching of chrysotile by precipitating on the surface of the chrysotile fibres, blocking the reactive surfaces and preventing more magnesium from being leached. The precipitation of secondary minerals on the chrysotile may have been particularly relevant because of the way magnesium is leached from chrysotile. Luce et al. (1972) demonstrated that chrysotile exposed to high concentrations of acid initially exhibits a rapid exchange of magnesium for $[H^+]$ on the surface of the chrysotile fibres, followed by the slower removal of internal magnesium over time. Depending on when the magnesium sulfate precipitation occurred, it may have prevented some of the extraction of internal magnesium. The siloxane layer, the silica-rich layer in sheet silicate minerals, is another factor which may play a role in controlling the rate of chrysotile dissolution (Park et al. 2003; Park and Fan 2004). During the early stages of leaching, the siloxane layer dissolves more slowly than the magnesium-rich layers, limiting the rate at which the acid can access the magnesium in the chrysotile.

The inability of flasks 2, 3, and 4 to approach a neutral pH indicates that the concentration of $[H^+]$ was much greater than that of magnesium in the chrysotile. Although these flasks leached more magnesium than those with a lower acid concentration, the acidic leach solutions generated in flasks 2, 3, and 4 would have to be neutralised before they could be used as a starting point for a carbonate precipitation process. Such a method was proposed by Park and Fan (2004) by neutralizing acidic leach solutions with NH_4OH to increase the pH to 9.5. Once at 9.5, the solution was

exposed pure CO_2 gas, resulting in the precipitation of $MgCO_3 \cdot 3H_2O$. Another method proposed to solve this problem is the use of neutral organic salts instead of strong acids to leach the magnesium (Krevor and Lackner 2011). Compounds such as sodium oxalate and sodium citrate were shown to leach magnesium out of antigorite at a neutral pH, eliminating the need for a neutralisation process after leaching.

Studies using both acidic and circum-neutral pH values for leaching found that the mineral dissolution rate increased with increasing temperature, reaction time, leach solvent concentration, and mineral surface area; the subsequent carbonate precipitation was more successful at higher CO_2 concentrations (Park et al. 2003; Park and Fan 2004; Alexander et al. 2007; Krevor and Lackner 2011). Although adjusting these reaction conditions is possible in laboratory trials, doing so may not be realistic during field-scale implementation of carbonation reactions. As a result, bioleaching has been studied as a method for dissolving waste rock for carbonate mineralisation purposes (Power et al. 2010). Exposing magnesium-rich tailings to a consortium of *Acidothiobacillus* spp. and a substance such as pyrite or elemental sulfur results in the generation of acid capable of dissolving the tailings. The dissolution process produces soluble magnesium, which can be used in 'downstream' carbonate precipitation reactions. The process of dissolving the tailings neutralises the generated acid, preventing the release of acid into the environment.

3.4.2 The influence of microbial activity on water chemistry

The excess microbial growth in the bioreactor during the first 3 weeks resulted in the formation of a pellicle. A pellicle is a type of biofilm that forms at the air-water interface in natural environments (Davey and O'Toole 2000). This likely occurred by sections of mat being buoyed up to the surface of the water by photosynthetically generated oxygen bubbles trapped within the mat. Pieces of floating and overturned microbial mat were observed in the wetland at the Atlin field site. The microbes in these floating pieces of mat were then able to grow over the surface of the water, eventually connecting to each other to form a continuous sheet. It appears that the pellicle was able to attach to the edges of the bioreactor, fully sealing in the water below. The surface cover restricted gas exchange between the bioreactor water and the atmosphere. A large amount of the

oxygen generated by the cyanobacteria in the pellicle would have been released directly into the atmosphere, instead of contributing to the dissolved oxygen in the bioreactor water. With the submerged cyanobacteria receiving little sunlight due to the overlying pellicle, their photosynthesis would have been restricted. The heterotrophs present in the bioreactor quickly consumed the dissolved oxygen present in the water, leading to the drop in DO documented during the presence of the pellicle. Although the cyanobacteria would still be able to produce oxygen in this suboxic environment, other forms of bacterial metabolism would be taking place under these conditions. The sediments used to line the bottom of the bioreactor were anoxic at the time of collection from the wetland, and were inhabited by sulfate reducing-bacteria (SRB) (Power et al. 2009). The activity of these organisms would have been encouraged by the lack of oxygen in the bioreactor. SRBs use sulfate (SO_4^{2-}) as a terminal electron acceptor during the oxidation of organic compounds, resulting in the production of hydrogen sulfide (H_2S) (Equation 5) (Trudinger 1985; Langke and Southam 2006). The H_2S generated by the SRBs could then be utlised by purple sulfur bacteria, which use H_2S to perform anoxygenic photosynthesis, producing elemental sulfur (Pfennig 1977; Cohen et al. 1986).

$$2\ CH_2O + SO_4^{2-} \rightarrow H_2S + 2\ HCO_3^- \tag{5}$$

It is likely that the microbial activity had a diurnal effect on the water chemistry. During the day, cyanobacteria would have been performing oxygenic photosynthesis. The cells used sunlight to generate chemical energy as adenosine triphosphate (ATP) and nicotinamide adenine dinucleotide phosphate (NADPH), while also producing oxygen by splitting water to produce electrons (Bryant and Frigaard 2006). The electrons are used to fix carbohydrates from CO_2. Simultaneously, the purple sulfur bacteria would be completing anoxygenic photosynthesis. At night, the cyanobacteria would only be able to complete the light-independent portion of photosynthesis, which consists of carbon fixation. With no photosynthetic generation of oxygen during the night, the diurnal drop in DO would have resulted in an increase in SRB activity, generating H_2S for use by the purple sulfur bacteria the following day. This cyclical daily transition between O_2 and H_2S production has been documented in natural microbial mat settings (Jørgensen et al. 1979).

3.4.3 *Water chemistry and mineral precipitation*

The experiment described in this chapter differed from the carbonation experiment described in Chapter 2 in that a dissolved source of inorganic carbon was not provided. As a result, dissolving CO_2 from the atmosphere into the bioreactor water became an additional step required for carbonate precipitation to take place. The results of this study demonstrate that atmospheric CO_2 can act as a carbon source for carbonate precipitation under the right water chemistry conditions. Such a demonstration is important because dissolution of atmospheric CO_2 into water is often the rate-limiting step in many mineral carbonation experiments (Power et al. 2011). Based on the PHREEQC results, the water was still undersaturated in CO_2 and never reached equilibrium with the atmosphere throughout the duration of the experiment. It is possible that some of the CO_2 used in carbonate precipitation was generated through biological processes. Heterotrophic oxidation of photosynthetically derived organic compounds such as acetate (CH_3COO^-) contribute to DIC by producing dissolved CO_2 or HCO_3^- (Von Knorre et al. 2000; Power et al. 2011; Sánchez-Román et al. 2011). In microbial mat systems, organics oxidised by heterotrophs are largely derived from atmospheric carbon fixed by phototrophic organisms, acting as an indirect pathway for transferring atmospheric CO_2 into the water. Heterotrophic activity, therefore, may have been partially responsible for the patterns observed in the alkalinity and DIC measured in the bioreactor. Both of these parameters exhibited increases immediately following the addition of the BG-11 solution at 0 m and 5 m. These locations had the highest concentrations of nutrients, likely resulting in a localised increase in heterotrophic activity. This increase likely caused a downstream increase in heterotrophy-generated DIC, which was observed immediately after the nutrient addition from 1 m to 2 m, and 6 m to 8 m. The pH drop at 5 m was likely also caused by the addition of nutrient at that location. Not only was the pH of the BG-11 solution much lower than that of the water in the bioreactor, but dissolution of heterotroph generated CO_2 at that location would have caused a decrease in pH. Beyond the 5 m location, autotroph activity resumed to dominate the microbial activity in the system, driving the pH back up with photosynthetically generated OH^-.

The conductivity in the bioreactor decreased continuously and evenly down the length of the system. This is in contrast to the behavior of the conductivity in the carbonation experiment described in Chapter 2, which decreased in the first 2 m of the system, but remained relatively constant for the remaining length of the bioreactor. The difference is important because in the current experiment, the bioreactor was able to remove magnesium continually from solution, instead of being limited to carbonate formation only in the upper few metres of the system. This is particularly notable because the concentration of magnesium being added was up to five times higher than in the experiment described in Chapter 2. At leach solution inflow rates of 1 - 3 L/day, the system was able to precipitate carbonate minerals at a rate which reduced the conductivity to the value measured in the system prior to starting the experiment. At inflow rates of 4 and 5 L/day, although magnesium was being removed from the water demonstrating that the carbonation potential of the bioreactor had not yet been exhausted, the magnesium concentration and conductivity values began to increase. It is quite likely that if the length of the bioreactor was greater, perhaps 20 m, the conductivity and magnesium concentration would have decreased further. In this experiment, it appears that the system was able to manage the lower flow rates, as indicated by the way the magnesium concentration and the conductivity were reduced to equal or lower than the respective time zero values.

Based on the reduction of the magnesium concentration, the rate of magnesium carbonate precipitation can be deduced for specific times during the carbonation experiment, as outlined below. Mineral precipitation is closely linked to the state of mineral saturation in the bioreactor water. The conditions in the bioreactor were able to increase the SI for hydromagnesite from the -10.07 value determined for the leach solution, to above zero (<4). These values are not as high as those achieved in Chapter 2, likely because of the lack of a soluble inorganic carbon source in the current experiment. Another cause of this difference is that alkalinity, as opposed to a direct DIC measurement, was used to represent carbon when determining the SI values reported in Chapter 2. Although a large portion of the alkalinity was represented by DIC, it was likely an overestimate of the amount of carbon in the system because other compounds would have contributed to the total alkalinity measured.

Hydromagnesite precipitation was still successful in the present experiment, due to the higher magnesium concentration used and the higher pH achieved as a result of the higher concentration of BG-11 supplied to the microorganisms. These results indicate that saturation index cannot be used as a rigid guide for determining if a solution will be able to produce magnesium carbonate minerals. For instance, the carbonation experiment described in Chapter 2 yielded many hydromagnesite SI values greater than 4 that did not result in precipitation. This is in contrast to the current experiment, which did not produce any SI values above 4, although hydromagnesite was observed at all sampling locations in the bioreactor. It appears that although the balance between pH, the availability of dissolved inorganic carbon, and magnesium concentration can result in a wide range of possible saturation indices, different combinations of these factors can result in successful magnesium carbonate precipitation.

With the above observations in mind, the following interpretations can be made regarding the relationship between water chemistry, saturation index, and mineral precipitation. The changes in magnesium concentration in the system indicated that the greatest carbonation rate was achieved between day 60 and day 67, when the leach solution was being added to the system at the highest implemented flow rate of 5 L/day. Based on the magnesium concentration and the conductivity measurements documented on day 67, carbonate precipitation was taking place throughout the entire bioreactor. At this time, the hydromagnesite SI values were among the lowest observed at any point during the experiment, ranging from -0.56 at 0 m, to 3.07 at 9 m. These values, particularly those from the first few metres of the system, do not seem appropriate for a high rate of carbonate precipitation. The inconsistency would likely be resolved if more frequent samples had been taken throughout the last week of the experiment. The system average DO concentration on day 60 was an experiment high of 21.0 mg/L and the average pH was 9.59, indicating that the bioreactor was in good 'health' at this time. In the following week, the DO and the pH dropped at the start of the bioreactor, corresponding to the region of the system with the lowest SI values. It is likely that with the good state of the pH and DO on day 60, and the increased inflow of magnesium to 5 L/day, the first few days of the last week of experimentation exhibited the large amount of carbonate precipitation (based on magnesium concentration). It may be that the rapid carbonate

formation resulted in the cyanobacteria becoming trapped in carbonate and shielded from the sun, slowing photosynthesis and nutrient absorption from the water. This would have resulted in the observed drop in both pH and DO. On day 67, the DIC concentration was less than half of what it was on day 60, which also indicates fast precipitation of carbonate and removal of DIC from solution. It is likely that if the experiment had continued beyond day 67, the rapid carbonate mineralisation would have been detrimental to the cyanobacteria, even though it resulted in the greatest amount of precipitation. The addition of 5000 ppm magnesium at a rate of 5 L/day was likely approaching the upper limits of the system's ability to consume magnesium through carbonate precipitation. In order to maintain the biogeochemical conditions required for successful carbonation, reducing either the flow rate or the magnesium concentration would likely be necessary if this process is to be implemented over a longer period of time.

3.4.4   *Carbonate mineral morphology*

The relationship observed between magnesium carbonate type and location in the bioreactor can be explained by basic precipitation kinetics. Fine-grained mineral crystals such as the nanometre-scale precipitates observed as casts and acicular crystals directly on the microbial cells are the result of fast precipitation from solution. This relationship is also seen in minerals forming from melts in igneous systems (Swanson 1977; Toramaru 1991). Melts that undergo fast cooling result in a high density of nucleation sites and generate rocks composed of many small crystals rather than fewer large ones. From this information, it is logical that mineral grain size would increase down the length of the bioreactor and over time. Of the carbonate minerals, calcium carbonate has been examined in the most detail in terms of precipitation kinetics and conditions for supersaturation (Pokrovsky 1998; Spanos and Koutsoukos 1998; Aizenberg et al. 1999; Kile et al. 2000; Naka and Chujo 2001; Roqué et al. 2004; Tong et al. 2004). The size and abundance of carbonate crystals precipitating from solution is dependent on the balance between crystal nucleation rate and crystal growth rate. Solutions with a higher degree of supersaturation encourage mineral nucleation, resulting in a high density of individual crystals (Spanos and Koutsoukos 1998; Tong et al. 2004). This is in contrast to solutions

with a low degree of supersaturation, in which crystal growth is favoured over nucleation of new crystals, resulting in fewer, larger mineral crystals. The relationship between the degree of saturation and crystal formation method can be applied to the mineralisation trends observed during the carbonation experiment. The magnesium carbonate coatings documented on the microbial cells is composed of nanometre-scale mineral grains. The coatings were more abundant in the upper portion of the bioreactor, which had access to a high concentration of magnesium, causing a degree of supersaturation high enough to enable a high nucleation rate of these nanometre-scale carbonate crystals. Further downstream, the lower magnesium concentration encouraged crystal growth, rather than crystal nucleation, resulting in the formation of micron-scale grains of hydromagnesite and magnesite.

The presence of the microorganisms in the bioreactor adds another factor to the carbonate precipitation kinetics taking place in the system. Studies have demonstrated the ability of organic compounds, such as aspartic and glutamic acid, to form complexes with cations resulting in carbonate mineralisation (Roqué et al. 2004; Tong et al. 2004). The concentration of these compounds influences the morphology of the crystals produced, indicating that crystal nucleation can be carefully controlled by the presence of substances that can act as nucleation sites for precipitation (Aizenberg et al. 1999). In the presence of microorganisms, nucleation sites are present largely in the form of EPS. Cations such as magnesium and calcium are able to bind to anionic functional groups in the EPS, including carboxyl groups, resulting in localised areas of high cation concentrations around the cells (Braissant et al. 2009). These cations are held into place, making the EPS a reservoir of cations, to which low molecular weight organic carbon compounds can attach. During metabolism in the microbial mat, these compounds become oxidised to form bicarbonate, which can then react with the cations to form carbonate minerals (Braissant et al. 2009). Depending on the strength of the bond connecting the cation to the EPS, mineral precipitates may remain attached to the cell, as in the case of the carbonate coatings observed in the present study, or be released like many of the hydromagnesite plates seen in the microbial mat samples. Once nucleation has occurred, the crystals are able to continue growing, independently of the microorganism. This process highlights the fact that microbial mats must be actively

producing EPS and metabolising in order for carbonate precipitation to occur. In addition to cyanobacteria, SRBs are known to enable calcium carbonate precipitation by driving the water chemistry conditions towards carbonate supersaturation and the generation of EPS (Braissant et al. 2007; Gallagher et al. 2012). This may have played a role in carbonation reactions in the bioreactor during the time in the carbonation experiment when the DO concentration was low. Precipitation of carbonate minerals in microbial mats can eventually lead to the lithification of the mat, a process of which there are many examples in both modern environments and the rock record (Grotzinger and James 2000; Dupraz and Visscher 2005; Altermann et al. 2006; Braissant et al. 2007; Aloisi 2008).

The ability of microorganisms to enable carbonate precipitation is particularly important to magnesium carbonates because magnesium carbonate minerals are much more difficult to form than calcium carbonate minerals. Abiotic precipitation of magnesite at temperatures below 80°C is inhibited by the amount of energy required for the spiral step crystal growth pattern by which magnesite is formed (Saldi et al. 2009). Hydrated magnesium carbonates such as nesquehonite and hydromagnesite form much more readily, largely because of the degree of hydration that commonly occurs with magnesium (Hänchen et al. 2008; Saldi et al. 2009). A stable, octahedrally coordinated shell of six water molecules typically surrounds a magnesium ion in solution (Kluge and Weston 2005). Disruption of this shell, through a process such as the magnesium ion becoming bound to EPS through the process outlined above, is required in order for magnesite precipitation to occur. It is difficult for complete dehydration of the magnesium to take place, which is why hydrated magnesium carbonate minerals form more readily than magnesite (Saldi et al. 2009). With the number of factors that must be in place for low temperature magnesite precipitation to occur, the microbially aided magnesite formed in the current study and in other studies is notable (Thompson and Ferris 1990).

The hydration energy of magnesium (1926 kJ/mol) compared to calcium (1579 kJ/mol) results in the exchange of the water molecules in calcium's hydration shell occurring approximately one thousand times faster than around magnesium, and is one of the reasons why calcium carbonate minerals form more easily than magnesium carbonates

(Slaughter and Hill 1991; Wright and Wacey 2005; Fenter et al. 2007). Of the possible calcium carbonate minerals, only aragonite was identified in the bioreactor. Aragonite was not a targeted form of carbonate mineralisation in this study and that which formed was minimal compared to the amount of magnesium carbonate generated. As a result, aragonite was not included in the carbon storage rate calculations outlined below. The presence of aragonite, however, does demonstrate a common geochemical feature of calcium carbonate minerals. Many studies have shown that the presence of a high dissolved magnesium concentration inhibits the formation of calcite and allows only aragonite to form (Berner 1975; Zhang and Dawe 2000; Stashans and Chamba 2010). Dissolved magnesium is able to substitute for calcium in the crystal lattice of calcite, resulting in a change in the crystal structure, inhibiting further growth. In a solution supersaturated in $CaCO_3$ containing magnesium, the growth rate of calcite decreases with increasing magnesium concentration (Zhang and Dawe 2000). Aragonite crystal growth is not influenced by the presence of dissolved magnesium, thus allowing for the aragonite precipitation that took place in the bioreactor.

3.4.5   *Quantifying mineral precipitation rate*

Using the water chemistry data outlined above, mineral precipitation and carbon storage rates were calculated for this carbonation experiment. The carbonate mineralisation that took place in this experiment was much more complex than that observed in the experiment describe in Chapter 2. Several carbonate species were identified with XRD, and different mineralisation morphologies were documented with SEM-EDS. The presence of the struvite also complicates quantification of the magnesium carbonate precipitation because its formation consumed some of the soluble magnesium. This problem was overcome by using the change in phosphate concentration as a guide for how much struvite was precipitated. A large drop in phosphate concentration was documented from the BG-11 solution added to the 0 m and 5 m locations. As these locations exhibited the most struvite, it is likely that a large amount of phosphate was 'consumed' by struvite precipitation at these sites. There was also, however, a large amount of microbial mat growth throughout the bioreactor to the extent that the pellicle developed, which could have only taken place in the presence of readily available

phosphate. It is also important to note the presence of cells attached to the struvite crystals and the degradation of the crystals with increasing distance from the phosphate source, both of which indicate dissolution of the struvite. It is likely that as phosphate was removed from solution by microbial activity, the dissolved phosphate was replenished by that stored in the struvite, making this mineral only a temporary intermediate phase. With these observations in mind, a conservative estimate of 50:50 was made in terms of the amount of phosphate being tied up in struvite versus biomass in the bioreactor.

The chemistry data collected on day 67 was used to calculate the carbonate formation rate, because the week during which the leach solution was added at a rate of 5 L/day exhibited the greatest quantity of magnesium consumption. Even with some of the magnesium being lost to struvite formation, 73% of the added magnesium was used for carbonate precipitation (Appendix F). The first week of the carbonation experiment exhibited a higher proportion of magnesium removed of 98%; however, the last week of the experiment still had the greatest magnitude of precipitation due to the higher rate of magnesium addition. Between day 60 and day 67, 5 mol or 123 g of Mg was used to in the process of carbonate minerals. It becomes necessary to consider which carbonate end product is being made. Hydromagnesite was the most common carbonate formed, but a large amount of magnesite was also produced. Due to the mixed precipitation that occurred, an exact value cannot be determined for the carbon storage rate achieved. A value can, however, be assigned for each of hydromagnesite and magnesite, providing a range in which the rate achieved would fall. Using the water chemistry data, the flow rate, and the surface area of the microbial mat in the bioreactor, it was calculated that either 472 g hydromagnesite or 476 g of magnesite could have formed in the bioreactor between day 60 and day 67 (Appendix F). If this process is extrapolated to the scale of a microbial carbonation pond at a mine tailings storage facility, these values translate into carbon storage rates of 61 and 65 tonnes of C/ha of pond/year, respectively. These rates represent both biological and mineral storage. The hydration of hydromagnesite results in its slightly greater precipitation mass, but also makes it slightly less efficient in terms of carbon stored per atom of magnesium used in comparison to anhydrous magnesite.

3.4.6   *Applications to carbon sequestration*

Application of this range of 61-65 tonnes of C/ha of pond/year to the Mount Keith Nickel Mine in Western Australia, which has ~1900 ha of tailings, predicts the storage of 422 000 to 450 000 tonnes of CO_2 per year. In 2004, the Mount Keith Mine emitted ~382 000 tonnes of CO_2 equivalent, demonstrating that the proposed method of carbon storage is capable of sequestering mine-scale quantities of CO_2 (Power et al. 2011b). The achievement of a carbon storage rate almost twice the 33 tonnes of C/ha of pond/year achieved in the experiment described in Chapter 2 demonstrates that the information gathered in Chapter 2 was applied effectively in the present experiment by adjusting the experimental conditions in order to encourage greater carbonation. This was primarily in the form of a higher BG-11 concentration and having a second BG-11 inflow location to ensure that nutrients were reaching all regions of the bioreactor. With the information collected in the present experiment, the carbonate precipitation rate could potentially be increased further. This would be important if this process were to be implemented at a mine facility as a long-term, low risk method for reducing net carbon emissions.

3.5   Conclusion

Characterisation of the Clinton Creek chrysotile tailings indicated that fibrous chrysotile is present as veins which cross cut the serpentine wall rock. Carbonate alteration of the chrysotile was observed with SEM-EDS. A leaching experiment was completed using the fibrous chrysotile and demonstrated a relationship between acid concentration, pH, and leached ion concentrations. Higher acid concentrations generally led to greater amounts of leached ions; however, high concentrations of strong acids cannot always be neutralized through the leaching process. Neutralisation is critical if the leach solution is going to be used in a carbonation process, because carbonate minerals cannot form in acidic solutions. In the leaching experiment described above, a chrysotile:acid ratio of 1:1 yielded the best results in terms of releasing the most magnesium into solution while still attaining a neutral pH. Magnesium was the most abundant element leached from the chrysotile, with a concentration of 4932 ppm in the 1:1 flask. When chrysotile fibres were examined with SEM-EDS, chemical weathering of the fibres was observed, with the degree of weathering increasing with increasing acid concentration. Secondary sulfate

minerals were observed in the material generated by the highest acid concentration. These additional phases may have inhibited magnesium leaching from the underlying chrysotile by covering the reactive surfaces of the fibres.

Using the information gathered in the leaching experiment, a synthetic leach solution containing 5000 ppm magnesium was designed to represent a solution that would be produced at a mine site by leaching an ultramafic tailings pile. The solution, along with a BG-11 growth medium, was added to the phototrophic flow-through bioreactor used in Chapter 2. The carbonation experiment examined the ability of the microbial consortium to induce carbonate mineral precipitation in the absence of an added dissolved inorganic carbon source such as that supplied to the system in the carbonation experiment outlined in Chapter 2. Monitoring of the water chemistry conditions indicated that a high pH (>9.4) and high concentrations of magnesium and dissolved inorganic carbon are critical for carbonate precipitation. The primary carbonate product generated was hydromagnesite accompanied by magnesite, aragonite, and minor dypingite. SEM-EDS observations indicated that cell exteriors and extracellular polymeric substances play an important role as nucleation sites for carbonate precipitation. In many cases, entire cyanobacteria filaments were observed entombed in magnesium carbonate coatings, which appeared to contain a framework of EPS. Cell coatings were composed of small crystals, which resulted from rapid crystal nucleation.

The saturation indices identified for hydromagnesite were lower than those determined in Chapter 2. This is likely due to this experiment not having a source of dissolved inorganic carbon. In spite of this, greater carbonate precipitation rates were achieved. The highest precipitation rate occurred at the time during which the leach solution was being added to the bioreactor at the highest rate of 5 L/day. If all of the carbonation occurred as hydromagnesite and was extrapolated to the scale of a mine site carbonation pond, a rate of 61 tonnes of C/h of pond/year was achieved. A slightly higher rate of 65 tonnes of C/h of pond/year was attained if all of the precipitation were to occur as magnesite. These results are encouraging for the potential of this biogeochemical process to be implemented at a mine tailings storage facility as a carbon sequestration strategy.

3.6 **References**

Aizenberg, J., Black, A.J., and Whitesids, G.M. 1999. Control of crystal nucleation by patterned self-assembled monolayers. Nature, **398**: 495-498.

Al, T.A., Martin, C.J., and Blowes, D.W. 2000. Carbonate-mineral/water interactions in sulfide-rich mine tailings. Geochimica et Cosmochimica Acta, **64**: 3933-3948.

Aloisi, G. 2008. The calcium carbonate saturation state in cyanobacterial mats throughout Earth's history. Geochimica et Cosmochimica Acta, **72**: 6037-6060.

Altermann, W., Kazmierczak, J., Oren, A., and Wright, D.T. 2006. Cyanobacterial calcification and its rock-building potential during 3.5 billion years of Earth history. Geobiology, **4**: 147-166.

Bea, S.A., Wilson, S.A., Mayer, K.U., Dipple, G.M., Power, I.M., and Gamazo, P. 2012. Reactive transport modeling of natural carbon sequestration in ultra-mafic mine tailings. Vadose Zone Journal, **11**.

Berner, R.A. 1975. The role of magnesium in the growth of calcite and aragonite from sea water. Geochimica et Cosmochimica Acta, **39**: 489-504.

Braissant, O., Decho, A.W., Dupraz, C., Glunk, C., Przekop, K.M., and Visscher, P.T. 2007. Exopolymeric substances of sulfate-reducing bacteria: Interactions with calcium at alkaline pH and implication for formation of carbonate minerals. Geobiology, **5**: 401-411.

Braissant, O., Decho, A.W., Przekop, K.M., Gallagher, K.L., Glunk, C., Dupraz, C., and Visscher, P.T. 2009. Characteristics and turnover of exopolymeric substances in a hypersaline microbial mat. FEMS Microbiology Ecology, **67**: 293-307.

Bryant, D.A. and Frigaard, N.-U. 2006. Prokaryotic photosynthesis and phototrophy illuminated. Trends in Microbiology, **14**: 11.

Burner, R.V. and Moore, L.S. 1987. Microbialites: organosedimentary deposits of benthic microbial communities. Palaios, **2**: 241-254.

Cohen, Y., Jørgensen, B.B., Revsbech, N.P., and Poplawski, N.P. 1986. Adaptation of hydrogen sulfide of oxygenic and anoxygenic photosynthesis among cyanobacteria. Applied and Environmental Microbiology, **51**: 398-407.

Davey, M.E. and O'Toole, G.A. 2000. Microbial biofilms: from ecology to molecular genetics. Microbiology and Molecular Biology Reviews, **64**: 847-867.

Dupraz, C. and Visscher, P.T. 2005. Microbial lithification in marine stromatolites and hypersaline mats. Trends in Microbiology, **13**: 429-438.

Fagerlund, J., Teir, S., Nduagu, E., and Zevenhoven, R. 2009. Carbonation of magnesium silicate mineral using a pressurised gas/solid process. Energy Procedia, **1**: 4907-4914.

Fenter P., Zhang, Z., Park, C., Sturchio, N.C., Hu, X.M., and Higgins, S.R. 2007. Structure and reactivity of dolomite (104)-water interface: New insights into the dolomite problem. Geochimica et Cosmochimica Acta, **71**: 566-579.

Gallagher, K.L., Kading, T.J., Braissant, O., Dupraz, C., and Visscher, P.T. 2012. Inside the alkalinity engine: the role of electron donors in the organomineralization potential of sulfate-reducing bacteria. Geobiology, **10**: 518-530.

Grotzinger, J.P. and James, N.P. 2000. Precambrian carbonates: evolution of understanding. In Carbonate Sedimentation and Diagenesis in the Evolving Precambrian World. SEPM Special Publication, **67**: 3-19.

Hänchen, M., Prigiobbe, V., Baciocchi, R., and Mazzotti, M. 2008. Precipitation in the Mg-carbonate system - effects of temperature and CO_2 pressure. Chemical Engineering Science, **63**: 1012-1028.

Harrison, A.L., Power, I.M., and Dipple, G.M. 2013. Accelerated carbonation of brucite in mine tailings for carbon sequestration. Environmental Science & Technology, **47**: 126-134.

Htoon, M. Geology of the Clinton Creek asbestos deposit, Yukon Territory. M.Sc. dissertation. The University of British Columbia, Vancouver, British Columbia, Canada, 1979.

Huot, F., Beaudoin, G., Hebert, R., Constantin, M., Bonin, G., and Dipple, G. 2003. Evaluation of southern Québec asbestos residues for CO2 sequestration by mineral carbonation: Preliminary results: Joint Annual Meeting of the Geological and Mineralogical Associations of Canada, Vancouver, Canada, May 25–28, 2003, Proceedings.

IPCC, 2007. Climate Change 2007: The physical science basis. Contribution of Working Group I to the Fourth Assessment Report of the Intergovernmental Panel on Climate Change [Solomon, S., Qin, D., Manning, M., Chen, Z., Marquis, M., Averyt, K.B., Tignor, M., and Miller, H.L. (eds)]. Cambridge University Press, Cambridge, United Kingdom and New York, NY, USA, pp. 96.

Jørgensen, B.B., Revsbech, N.P., Blackburn, T.H., and Cohen, Y. 1979. Diurnal cycling of oxygen and sulfide microgradients and microbial photosynthesis in a cyanobacterial mat. Applied and Environmental Microbiology, **38**: 46-58.

Kile, D.E., Eberl, D.D., Hoch, A.R., and Reddy M.M. 2000. An assessment of calcite crystal growth mechanisms based on crystal size distribution. Geochimica et Cosmochimica Acta, **64**: 2937-2950.

Kluge, S. and Weston, J. 2005. Can a hydroxide ligand trigger a change in the coordination number of magnesium ions in biological systems. Biochemistry, **44**: 4877-4885.

Köhler, P., Hartmann, J., and Wolf-Gladrow, D.A. 2010. Geoengineering potential of artificially enhanced silicate weathering of olivine. Proceedings of the National Academy of Sciences of the United States of America, **107**: 20228-20233.

Koukouzas, N., Gemeni, V., and Ziock, H.J. 2009. Sequestration of CO_2 in magnesium silicates, in Western Macedonia, Greece. International Journal of Mineral Processing, **93**: 179-186.

Krevor, S.C.M. and Lackner, K.S. 2011. Enhancing serpentine dissolution kinetics for mineral carbon dioxide sequestration. International Journal of Greenhouse Gas Control, **5**: 1073-1080.

Kump, L.R., Brantley, S.L., and Arthur, M.A. 2000. Chemical weathering, atmospheric CO_2, and climate. Annual Reviews in Earth and Planetary Sciences, **28**: 611-667.

Lacis, A.A., Schmidt, G.A., Rind, D., and Ruedy, R.A. 2010. Atmospheric CO_2: Principle control knob governing Earth's temperature. Science, **330**: 356-359.

Lackner, K.S. 2003. Climate change: a guide to CO_2 sequestration. Science, **300**: 1677-1678.

Lackner, K.S., Wendt, C.H., Butt, D.P., Joyce, G.L., and Sharp, D.H. 1995. Carbon dioxide disposal in carbonate minerals. Energy, **20**: 1153-1170.

Lahav, O., Morgan, B.E., and Loewenthal, R.E. 2001. Measurement of pH, alkalinity and acidity in ultra-soft waters. Water SA, **27**: 423-431.

Lammers, K., Murphy, R., Riendeau, A., Smirnov, A., Schoonon, M.A.A., and Strongin, D.R. 2011. CO_2 Sequestration through mineral carbonation of iron oxyhydroxides. Environmental Science and Technology, **45**: 10422-10428.

Lengke, M.F., and Southam, G. 2006. Bioaccumulation of gold by sulfate-reducing bacteria cultured in the presence of gold(I)-thiosulfate complex. Geochimica et Cosmochimica Acta, **70**: 3646-3661.

Luce, R.W., Bartlett, R.W., and Parks, G.A. 1972. Dissolution kinetics of magnesium silicates. Geochimica et Cosmochimica Acta, **36**: 35-50.

Molson, J.W., Fala, O., Aubertin, M., and Bussière, B. 2005. Numerical simulations of pyrite oxidation and acid mine drainage in unsaturated waste rock piles. Journal of Contaminant Hydrology, **78**: 343-371.

Naka, K. and Chujo, Y. 2001. Control of crystal nucleation and growth of calcium carbonate by synthetic Substrates. Chemical Materials, **13**: 3245-3259.

Natural Resources Canada. Provincial and Territorial Reference Maps.6. Available at: http://atlas.nrcan.gc.ca/site/english/maps/reference/outlineprov_terr/ yuk_outline (accessed April 9, 2013).

Nothdurft, L.D., Webb, G.E., Buster, N.A., Holmes, C.W., Sorauf, J.E., and Kloprogge, J.T. 2005. Brucite microbialites in living coral skeletons: Indicators of extreme microenvironments in shallow-marine settings. Geology, **33**: 169-172.

Paktunc, A.D. and Davé, N.K. 2002. Formation of secondary pyrite and carbonate minerals in the Lower Williams Lake tailings basin, Elliot Lake, Ontario, Canada: American Mineralogist, **87**: 593-602.

Park, A.-H.A., Jadhav, R., and Fan, L-S. 2003. CO_2 sequestration: Chemically enhanced aqueous carbonation of serpentine. The Canadian Journal of Chemical Engineering, **81**: 885-890.

Park, A.-H.A. and Fan, L-S. 2004. CO_2 mineral sequestration: physically activated dissolution of serpentine and pH swing process. Chemical Engineering Science, **59**: 5241-5247.

Parkhurst, D.L. and Appelo, C.A.J. 1999. User's guide to PHREEQC (version 2) - A computer program for speciation, batch-reaction, one-dimensional transport and inverse geochemical calculations. Water-Resources Investigations Report 99-4259, U.S. Geologic Survey, Denver.

Pentecost, A. 1995. Significance of the biomineralizing microniche in a Lyngbya (cyanobacterium) travertine. Geomicrobiology Journal, **13**: 213-222.

Peters, K.E., Walters, C.C., and Moldowan, J.M. 2005. The Biomarker Guide Volume I Biomarkers and Isotopes in the Environment and Human History; Cambridge University Press: Cambridge, U.K., pp 1155.

Pfennig, N. 1977. Phototrophic green and purple bacteria: A comparative, systematic survey. Annual Reviews in Microbiology, **31**: 275-290.

Pokrovsky, O.S. 1998. Precipitation of calcium and magnesium carbonates from homogeneous supersaturated solutions. Journal of Crystal Growth, **186**: 233-239.

Pokrovsky, O.S. and Schott, J. 2000. Kinetics and mechanism of forsterite dissolution at 25°C and pH from 1 to 12. Geochimica et Cosmochimica Acta, **64**: 3313-3325.

Pokrovsky, O.S. and Schott, J. 2004. Experimental study of brucite dissolution and precipitation in aqueous solutions: surface speciation and chemical affinity control. Geochimica et Cosmochimica Acta, **68**: 31-45.

Power, I.M., Wilson, S.A., Thom, J.M., Dipple, G.M., and Southam, G. 2007. Biologically induced mineralisation of dypingite by cyanobacteria from an alkaline wetland near Atlin, British Columbia, Canada. Geochemical Transactions, **8**: 13.

Power, I.M., Wilson, S.A., Thom, J.M., Dipple, G.M., Gabites, J.E., and Southam, G. 2009. The hydromagnesite playas of Atlin, British Columbia, Canada: A biogeochemical model for CO_2 sequestration. Chemical Geology, **260**: 286-300.

Power, I.M., Dipple, G.M., and Southam, G. 2010. Bioleaching of ultramafic tailings by *Acidithiobacillus* spp. for CO_2 sequestration. Environmental Science & Technology, **44**: 456-462.

Power, I.M., Wilson, S.A., Small, D.P., Dipple, G.M., and Southam, G. 2011. Modern carboante microbialites from an asbestos open pit pond, Yukon, Canada. Geobiology, **9**: 180-195.

Power, I.M., Wilson, S.A., Small, D.P., Dipple, G.M., Wan, W.K., and Southam, G. 2011. Microbially mediated mineral carbonation: Roles of phototrophy and heterotrophy. Environmental Science & Technology, **45**: 9061-9068.

Power, I.M., Wilson, S.A., Dipple, G.M., and Harrison, A.L. 2012. Hydromagnesite-magnesite playas: A model for carbon storage: 22nd V.M. Goldschmidt Conference, Montréal, Canada, June 24-29.

Pronost, J., Beaudoin, G., Tremblay, J., Larachi, F., Duchesne, J., Hébert, R., and Constantin, M. 2011. Carbon sequestration kinetic and storage capacity of ultramafic mining waste. Environmental Science & Technology, **45**: 9413-9420.

Pronost, J., Beaudoin, G., Lemieux, J.-M., Hébert, R., Constantin, M, Marcouiller, S., Klein, M., Duchesne, J., Molson, J.W., Larchi, F., and Maldague, X. 2012. CO_2-depleted warm air venting from chrysotile milling waste (Thetford Mines, Canada): Evidence for in-situ carbon capture from the atmosphere. Geology, **40**: 275-278.

Renforth, P. 2012. The potential of enhanced weathering in the UK. International Journal of Greenhouse Gas Control, **10**: 229-243.

Renforth, P. and Manning, D.A.C. 2011. Laboratory carbonation of artificial silicate gels enhanced by citrate: Implications for engineered pedogenic carbonate formation. International Journal of Greenhouse Gas Control, **5**: 1578-1586.

Roqué, J., Molera, J., Vendrell-Saz, M., and Salvadó, N. 2004. Crystal size distributions of induced calcium carbonate crystals in polyaspartic acid and *Mytilus edulis* acidic organic proteins aqueous solutions. Journal of Crystal Growth, **262**: 543-553.

Saldi, G.D., Jordan, G., Schott, J., and Oelkers, E.H. 2009. Magnesite growth rates as a function of temperature and saturation state. Geochimica et Cosmochimica Acta, **73**: 5646-5657.

Sánchez-Román, M., Romanek, C.S., Fernández-Remolar, D.C., Sánchez-Navas, A., McKenzie, J.A., Pibernat, R.A., and Vasconcelos, C. 2011. Aerobic biomineralization of Mg rich carbonates: Implications for natural environments. Chemical Geology, **281**: 143-150.

Schultze-Lam, S., Fortin, D., Davis, B.S., and Beveridge, T.J. 1996. Mineralization of bacterial surfaces. Chemical Geology, **132**: 171-181.

Seifritz, W. 1990. CO_2 disposal by means of silicates. Nature, **345**: 486.

Slaughter, M. and Hill, R.J. 1991. The influence of organic matter in organogenic dolomitization. Journal of Sedimentary Petrology, **61**: 296-303.

Spanos, N. and Koutsoukos, P.G. 1998. Kinetics of precipitation of calcium carbonate in alkaline pH at constant supersaturation. Spontaneous and seeded growth. Journal of Physical Chemistry, **102**: 6679-6684.

Stashans, A. and Chamba, G. 2010. A new insight on the role of Mg in calcite. International Journal of Quantum Chemistry, **111**: 2436-2443.

Stumm, W. 1992. Chemistry of the solid-water interface. Wily-Interscience Publication, New York, pp. 523-598.

Swanson, S.E. 1977. Relation of nucleation and crystal-growth rate to the development of granitic textures. American Mineralogist, **62**: 966-978.

Thompson, J.B. and Ferris, F.G. 1990. Cyanobacterial precipitation of gypsum, calcite, and magnesite from natural alkaline water. Geology, **18**: 995-998.

Tong, H., Ma, W., Wang, L., Wan, P., Hu, J., and Cao, L. 2004. Control over the crystal phase, shape, size and aggregation of calcium carbonate via a L-aspartic acid inducing process. Biomaterials, **25**: 3923-3929.

Toramaru, A. 1991. Model of nucleation and growth of crystals in cooling magmas. Contributions to Mineralogy and Petrology, **108**: 106-117.

Trudinger, P.A., Chambers, L.A., and Smith, J.W. 1985. Low temperature sulphate reduction: biological versus abiological. Canadian Journal of Earth Sciences, **22**: 1910-1918.

Vermilyea, D.A. 1969. The dissolution of MgO and Mg(OH)$_2$ in aqueous solutions. Journal of Electrochemical Society, **116**: 1179-1183.

von Knorre, H. and Krumbein, W.E., 2000, Bacterial calcification. In: Riding, R.E., Awramik, S.M. (eds). Microbial Sediments. Springer, Berlin, pp. 331.

Vonshak, A. 1986. Laboratory techniques for the cultivation of microalgae. In: Richmond, A. (eds). CRC handbook of microalgae mass culture. CRC Press Inc., Bocca Raton, pp. 117.

Washbourne, C.L., Renforth, P., and Manning, D.A.C. 2012. Investigating carbonate formation in urban soils as a method for capture and storage of atmospheric carbon. Science of the Total Environment, **431**: 166-175.

White, A.F., Blum, A.E., Schulz, M.S., Bullen, T.D., Harden, J.W., and Peterson, M.L. 1996. Chemical weathering rates of a soil chronosequence on granitic alluvium: I. Quantification of mineralogical and surface area changes and calculation of primary silicate reaction rates. Geochimica et Cosmochimica Acta, **60**: 2533-2550.

Wilson, S.A. Mineral traps for greenhouse gases in mine tailings: A protocol for verifying and quantifying CO$_2$ sequestration in ultramafic mines. Ph.D. Dissertation, The University of British Columbia, Vancouver, British Columbia, Canada, 2009.

Wilson, S.A., Raudsepp, M., and Dipple, G.M. 2009. Quantifying carbon fixation in trace minerals from processed kimberlite: A comparative study of quantitative methods using X-ray powder diffraction data with applications to the Diavik Diamond Mine, Northwest Territories. Canada. Applied Geochemistry, **24**: 2312-2331.

Wilson, S.A., Dipple, G.M., Power, I.M., Thom, J.M., Anderson, R.G., Raudsepp, M., Gabite, J.E., and Southam, G. 2009. Carbon dioxide fixation within mine wastes of ultramafic-hosted ore deposits: examples from the Clinton Creek and Cassiar chrysotile deposits, Canada. Economic Geology, **104**: 95-112.

Wilson, S.A., Barker, S.L.L., Dipple, G.M., and Atudorei, V. 2010. Isotopic disequilibrium during uptake of atmospheric CO$_2$ into mine process waters: implications for CO$_2$ sequestration. Environmental Science and Technology, **44**: 9522-9529.

Wilson, S.A., Dipple, G.M., Power, I.M., Barker, S.L.L., Fallon, S.J., and Southam, G. 2011. Subarctic weathering of mineral wastes provides a sink for atmospheric CO_2. Environmental Science and Technology, **45**: 7727-7736.

Winsborough, B.M. and Golubic, S. 1987. The role of diatoms in stromatolites growth - 2 examples from modern fresh-water settings. Journal of Phycology, **23**: 195-201.

Wright, D.T. and Wacey, D. 2005. Precipitation of dolomite using sulphate-reducing bacteria from the Coorong Region, South Australia: Significance and implications. Sedimentology, **52**: 987-1008.

Yukon Government Publication, 2010, Abandoned Mines. Whitehorse, Yukon, Canada, pp. 9.

Zevenhoven, R., Teir, S., and Eloneva, S. 2008. Heat optimization of a staged gas-solid mineral carbonation process for long-term CO_2 storage. Energy, **33**: 362-370.

Zhang, Y. and Dawe, R.A. 2000. Influence of Mg^{2+} on the kinetics of calcite precipitation and calcite crystal morphology. Chemical Geology, **163**: 129-138.

Chapter 4

4   Summary

Fossil fuel use by humans over the past 250 years has caused an increase in the concentration of atmospheric CO_2 from 280 ppm to 390 ppm (IPCC 2007; Lacis 2010). This increase has led to an enhanced greenhouse effect, causing an increase in global air temperatures and subsequent sea level rise, and loss of polar ice and snowpack. The carbon-dependent nature of modern society is unlikely to change to alternative fuel sources fast enough to nullify this problem, making strategies for sequestering some of this excess CO_2 essential for minimising the environmental problems caused by human CO_2 production (Broecker 2007). One sink for sequestrating anthropogenic carbon is carbonate minerals, which will likely be the sink for almost all carbon emissions on a time scale of 1 Ma (Seifritz 1990; Kump et al. 2000).

4.1   Biogenic magnesium carbonation reactions

The two carbonation experiments completed in this study modeled different environments, one naturally occurring and one manmade, in which magnesium carbonate precipitation has been documented. The experiment completed in Chapter 2 modeled the biogeochemical conditions of the Atlin, British Columbia wetland and hydromagnesite playa. This field site is known for the precipitation of several magnesium carbonate minerals from the wetland water, which is fed by magnesium-rich groundwater derived from the surrounding ultramafic country rock (Hansen et al. 2005; Power et al. 2007; Power et al. 2009). The bioreactor system successfully demonstrated hydromagnesite precipitation from solution. This was achieved by the cyanobacteria inducing water chemistry conditions required for mineral formation and providing sites for crystal nucleation. Through photosynthetic production of hydroxyl ions, the phototrophic microbes were able to drive the pH above 9.0, which, combined with the high magnesium and dissolved inorganic carbon content of the feedstock solution, made the system supersaturated in regards to hydromagnesite. Carbonate formation was likely even more favourable directly around the microbial cells through the generation of water chemistry

microenvironments. Such microenvironments are known to have a pH value one unit higher than that measured for the bulk solution, causing a photosynthetically induced increase in the CO_3^{2-} concentration (Dittrich et al. 2003; Bissett et al. 2008; Obst et al. 2009b; Power et al. 2011). These chemical conditions combined with the presence of the microorganisms to enable carbonate formation. Extracellular polysaccharides act as nucleation sites for mineral precipitation through producing areas of increased cation concentrations (Dittrich et al. 2003; Bissett et al. 2008; Braissant et al. 2009; Obst et al. 2009a; Obst et al. 2009b; Power et al. 2011). This occurs through the attachment of cations, in this case magnesium, to organic ligands, such as carboxyl groups that contribute to the net negatively charged cell surfaces. The localised concentration of magnesium, combined with the high CO_3^{2-} content, allows hydromagnesite precipitation to occur from solutions that would not generate this mineral abiotically. The highest rate of hydromagnesite precipitation documented in the bioreactor translated to a carbon sequestration rate of 33 t C/ha/year.

The carbonation experiment in Chapter 3 demonstrated the process of magnesium carbonate precipitation from mine waste products. Carbonation reactions have been documented at several mines which produce ultramafic tailings (Wilson 2009; Wilson et al. 2009a; Wilson et al. 2009b; Wilson et al. 2010; Wilson et al. 2011; Pronost et al. 2011). In Chapter 3, the process was accelerated at a rate beyond what occurs passively at mine tailing storage facilities. The chemistry of a realistic mine tailings leach water was determined in a leaching experiment using chrysotile from the abandoned Clinton Creek Asbestos Mine (Yukon, Canada). The chrysotile was reacted with a range of acid concentrations, generating solutions with varying chemistry. The best leach solution was produced by a chrysotile:acid ratio of 1:1, generating the highest dissolved magnesium concentration while still reaching a neutral pH through the acid neutralisation leaching reactions. A synthetic version of this solution, containing 5000 ppm magnesium, was added to the bioreactor for a second carbonation experiment. This experiment differed from the first one in that no source of dissolved inorganic carbon was provided to the system, forcing it to use atmospheric CO_2 as the carbon source for carbonate precipitation. The magnesium concentration being added to the bioreactor was five times higher than that used in the first experiment, and the magnesium inflow rate was

increased from 1 L/day to 5 L/day over the course of the experiment. In response to the nutrient limitation problems experienced in the Chapter 2 experiment which limited carbonate precipitation, a higher BG-11 concentration was used in Chapter 3. The latter experiment successfully produced hydromagnesite and magnesite, as well as minor dypingite and aragonite. The mineralisation differs from the precipitation achieved in the experiment described in Chapter 2 because multiple carbonate minerals and morphologies were produced. The hydromagnesite and magnesite were present as platelets and rhombohedral crystals, respectively, while magnesium carbonate coatings were identified on many of the microbial cells present in the bioreactor. The coatings were composed of nanometre-scale casts directly on the cells, and appeared to contain a framework of EPS. Several examples of casts left behind after the entombed cells had died were observed. All of the mineralisation took place at an alkaline pH (>9.4), and provided information regarding the relative precipitation conditions found in different parts of the bioreactor. The first few metres of the bioreactor contained primarily the carbonate coatings, with some hydromagnesite platelets also visible. The size of the hydromagnesite crystals increased over both time and distance down the bioreactor. Magnesite crystals were not observed in the first 3 m of the bioreactor. Beyond the 3 m location, both magnesite crystal frequency and magnesite crystal size increased with increasing distance down the system. The nano-scale coatings represent a high crystal nucleation rate compared to the hydromagnesite and magnesite grains, the latter of which demonstrate a balance between crystal nucleation rate and crystal growth rate. Crystal nucleation dominated the system over the first few metres because of the higher magnesium concentration making carbonate formation more favourable (Spanos and Koutsoukos 1998; Tong et al. 2004). At a leach solution inflow rate of 1 L/day, the bioreactor was able to consume the added magnesium and reduce the dissolved magnesium concentration to equal or less than the starting system concentration. As the flow rate was increased, the bioreactor was not able to keep up with the magnesium addition, resulting in an overall increase in the magnesium concentration in the system over time. Since carbonate precipitation was observed right to the end of the bioreactor channel, a longer channel would likely have been able to manage the higher magnesium inflow rate. The greatest carbon storage rate was achieved at the fastest flow rate of 5

L/day. The rate was calculated to be between 61 and 65 t of C/ha/year, depending on if the end product is hydromagnesite or magnesite.

Two main factors can be identified to account for the differences observed between the mineralisation in the two carbonation experiments. The first is the availability of nutrients in each of these experiments. During the first carbonation experiment, it became apparent that nutrient availability plays an important role in the bioreactor's ability to induce carbonation reactions. Low nutrient availability in the lower portion of the bioreactor prevented active growth and EPS production by the microbial consortium, two factors which are critical to biogenically induced hydromagnesite precipitation. In contrast, the second carbonation experiment had problems with microbial mat overgrowth as opposed to nutrient limitation. This occurred in the form of a pellicle on the surface of the bioreactor water and resulted in a large drop in the dissolved oxygen concentration. While the pellicle was present, the levels of anoxygenic photosynthesis and sulfate reduction in the bioreactor increased through the metabolic activity of purple sulfur bacteria and sulfate reducing bacteria, respectively. A reduction in carbonate mineral precipitation was observed during this stage of the experiment, demonstrating the importance of the health of the microbial community to the success of carbonate precipitation. In spite of this problem, which demonstrated that the pellicle growth needed to be 'controlled', the second carbonation experiment exhibited carbonate mineralisation at all locations in the bioreactor. This contrasts with the first experiment in which mineral precipitation was limited to the top 2 m of the system.

The second factor which influences the potential for carbonate precipitation is the mineral saturation index of the water, which is primarily determined by the combination of pH, magnesium concentration, and dissolved inorganic carbon concentration. Magnesium carbonate precipitation occurs when these three factors are optimised in the presence of suitable nucleation sites. Water chemistry modeling software indicated different saturation indices for hydromagnesite for each of the carbonation experiments. Chapter 2 had much higher saturation indices than Chapter 3, with maximum values for hydromagnesite of 6.14 and 3.97, respectively. In spite of this, the second experiment exhibited a much higher carbon storage rate as well as precipitation of multiple

magnesium carbonate phases throughout the entire bioreactor. The improvement in the processes decribed in Chapter 2 and Chapter 3 is especially notable because in the second experiment no carbon source was provided other than atmospheric CO_2, and the availability of CO_2 is usually the rate limiting factor in carbonate formation (Vermilyea 1969; Pokrovsky and Schott 2000; Pokrovsky and Schott 2004; Wilson et al. 2010; Harrison et al. 2013). The higher rate of carbonate precipitation in the second experiment is likely due to a combination of the higher magnesium concentration and the higher nutrient availability allowing for increased photosynthesis, which in turn encourages the generation of more EPS and a higher pH. The combination of these factors, which would have been particularly enhanced in microenvironments surrounding the microbial cells, would have compensated for the lower availability of dissolved inorganic carbon compared to the first experiment. The two carbonation experiments also differ in the duration of active precipitation. In the first experiment, the carbon storage rate was highest at the very start and decreased over time. However, with increased nutrient amendments, the bioreactor was able to continue carbonation reactions throughout the entire duration of the second experiment, demonstrating that microbial growth and EPS production kept up with the rate of precipitation. The observations made in this study indicate that it is difficult to use saturation index alone to predict if a particular solution will result in magnesium carbonate formation, since solutions of very different chemistries are capable of producing the same saturation index value. It is clear, however, that multiple biogeochemical factors must be in place for successful microbially enabled magnesium carbonate precipitation.

4.2 *In situ* application to mine tailings

The carbon storage rates achieved in this experiment raise the potential for a similar carbon sequestration strategy to be implemented at mine sites. Piles of milled tailings provide an excellent magnesium source, which would have to be leached either chemically or biologically. Bioleaching of magnesium has been explored as a method of releasing magnesium from ultramafic tailings (Power et al. 2010). Once leached, the dissolved magnesium would be directed into a carbonation pond in which a microbial consortium comparable to the one used in this study would grow. With the source of

magnesium and exposure to the atmosphere, the only other resource needed would be essential nutrients like phosphorus and nitrogen. Addition of these nutrients would be relatively easy, not unlike fertilising crops. The exact design of the carbonation system would be specific to each mine, as it would be dependent on the structure and hydrogeology of the site. In most cases, however, little infrastructure or energy input would be required to implement this method of carbon storage. This study demonstrated that the microbial community was able to tolerate the 5000 ppm magnesium concentration that was produced when mine waste products were leached. The rate of leach solution addition would be dependent on the surface area of the carbonation pond and how rapidly carbonation reactions are taking place. Site monitoring would likely be required during the early stages of pond establishment in order to maintain the health of the microbial community, by refining the balance between magnesium addition, microbial growth, and carbonation reaction rates. A possible area of exploration for enhancing this process is using captured CO_2 from a point source as the carbon source for carbonation by bubbling it into the pond. Further investigation would be required before this method could be used at a mine. Atmospheric CO_2, however, appears to act as a sufficient carbon source for successful microbially accelerated magnesium carbonate precipitation. This, and other, methods of carbon sequestration deserve consideration for mitigating climate change and the associated environmental challenges society will face in the coming centuries.

4.3   **References**

Bissett, A., Reimer, A., de Beer, D., Shiraishi, F., and Arp, G. 2008. Metabolic microenvironmental control by photosynthetic biofilms under changing macroenvironmental temperature and pH conditions. Applied Environmental Microbiology, **74**: 6306-6312.

Braissant, O., Decho, A.W., Przekop, K.M., Gallagher, K.L., Glunk, C., Dupraz, C., and Visscher, P.T. 2008. Characteristics and turnover of exopolymeric substances in a hypersaline microbial mat. FEMS Microbiology Ecology, **67**: 293-307.

Broecker, W.S. 2007. CO_2 arithmetic. Science, **315**: 1371.

Dittrich, M., Müller, B., Mavrocordatos, D., and Wehril, B. 2003. Induced calcite precipitation by cyanobacterium Synechococcus. Acta Hydrochimica Hydrobiologica, **31**: 162-169.

Hansen, L.D., Dipple, G.M., Gordon, T.M., and Kellett, D.A. 2005. Carbonated serpentinite (listwanite) at Atlin, British Columbia: A geological analogue to carbon dioxide sequestration. Canadian Mineralogist, **43**: 225-239.

Harrison, A.L., Power, I.M., and Dipple, G.M. 2013. Accelerated carbonation of brucite in mine tailings for carbon sequestration. Environmental Science & Technology, **47**: 126-134.

IPCC, 2007. Climate Change 2007: The physical science basis. Contribution of Working Group I to the Fourth Assessment Report of the Intergovernmental Panel on Climate Change [Solomon, S., Qin, D., Manning, M., Chen, Z., Marquis, M., Averyt, K.B., Tignor, M., and Miller, H.L. (eds)]. Cambridge University Press, Cambridge, United Kingdom and New York, NY, USA, pp. 96.

Kump, L.R., Brantley, S.L., and Arthur, M.A. 2000. Chemical weathering, atmospheric CO_2, and climate. Annual Reviews in Earth and Planetary Sciences, **28**: 611-667.

Lacis, A.A., Schmidt, G.A., Rind, D., and Ruedy, R.A. 2010. Atmospheric CO_2: Principle control knob governing Earth's temperature. Science. **330**: 356-359.

Obst, M., Wehrli, B., and Dittrich, M. 2009. $CaCO_3$ nucleation by cyanobacteria: Laboratory evidence for a passive, surface-induced mechanism. Geobiology, **7**: 324-347.

Obst, M., Dynes, J.J., Lawrence, J.,R., Swerhone, G.D.W., Benzerara, K., Karunakaran, C., Kaznatcheev, K., Tyliszczak, T. and Hitchock, A.P. 2009. Precipitation of amorphous $CaCO_3$ (aragonite-like) by cyanobacteria: A STXM study of the influence of EPS on the nucleation process. Geochimica et Cosmochimica Acta. **72**: 4180-4198.

Pokrovsky, O.S. and Schott, J. 2000. Kinetics and mechanism of forsterite dissolution at 25°C and pH from 1 to 12. Geochimica et Cosmochimica Acta, **64**: 3313-3325.

Pokrovsky, O.S. and Schott, J. 2004. Experimental study of brucite dissolution and precipitation in aqueous solutions: surface speciation and chemical affinity control. Geochimica et Cosmochimica Acta, **68**: 31-45.

Power, I.M., Wilson, S.A., Thom, J.M., Dipple, G.M., and Southam, G. 2007. Biologically induced mineralisation of dypingite by cyanobacteria from an alkaline wetland near Atlin, British Columbia, Canada. Geochemical Transactions, **8**: 13.

Power, I.M., Wilson, S.A., Thom, J.M., Dipple, G.M., Gabites, J.E., and Southam, G. 2009. The hydromagnesite playas of Atlin, British Columbia, Canada: A biogeochemical model for CO_2 sequestration. Chemical Geology, **260**: 286-300.

Power, I.M., Dipple, G.M., and Southam, G. 2010. Bioleaching of ultramafic tailings by *Acidithiobacillus* spp. for CO_2 sequestration. Environmental Science & Technology, **44**: 456-462.

Power, I.M., Wilson, S.A., Small, D.P., Dipple, G.M., Wan, W.K., and Southam, G. 2011. Microbially mediated mineral carbonation: Roles of phototrophy and heterotrophy. Environmental Science & Technology, **45**: 9061-9068.

Pronost, J., Beaudoin, G., Tremblay, J., Larachi, F., Duchesne, J., Hébert, R., and Constantin, M. 2011. Carbon sequestration kinetic and storage capacity of ultramafic mining waste. Environmental Science & Technology, **45**: 9413-9420.

Seifritz, W. 1990. CO_2 disposal by means of silicates. Nature, **345**: 486.

Spanos, N. and Koutsoukos, P.G. 1998. Kinetics of precipitation of calcium carbonate in alkaline pH at constant supersaturation. Spontaneous and seeded growth. Journal of Physical Chemistry, **102**: 6679-6684.

Tong, H., Ma, W., Wang, L., Wan, P., Hu, J., and Cao, L. 2004. Control over the crystal phase, shape, size and aggregation of calcium carbonate via a L-aspartic acid inducing process. Biomaterials, **25**: 3923-3929.

Vermilyea, D.A. 1969. The dissolution of MgO and $Mg(OH)_2$ in aqueous solutions. Journal of Electrochemical Society, **116**: 1179-1183.

Wilson, S.A. Mineral traps for greenhouse gases in mine tailings: A protocol for verifying and quantifying CO2 sequestration in ultramafic mines. Ph.D. Dissertation, The University of British Columbia, Vancouver, British Columbia, Canada, 2009.

Wilson, S.A., Raudsepp, M., and Dipple, G.M. 2009. Quantifying carbon fixation in trace minerals from processed kimberlite: A comparative study of quantitative methods using X-ray powder diffraction data with applications to the Diavik Diamond Mine, Northwest Territories. Canada. Applied Geochemistry, **24**: 2312-2331.

Wilson, S.A., Dipple, G.M., Power, I.M., Thom, J.M., Anderson, R.G., Raudsepp, M., Gabite, J.E., and Southam, G. 2009. Carbon dioxide fixation within mine wastes of ultramafic-hosted ore deposits: examples from the Clinton Creek and Cassiar chrysotile deposits, Canada. Economic Geology, **104**: 95-112.

Wilson, S.A., Barker, S.L.L., Dipple, G.M., and Atudorei, V. 2010. Isotopic disequilibrium during uptake of atmospheric CO_2 into mine process waters:

implications for CO_2 sequestration. Environmental Science and Technology, **44**: 9522-9529.

Wilson, S.A., Dipple, G.M., Power, I.M., Barker, S.L.L., Fallon, S.J., and Southam, G. 2011. Subarctic weathering of mineral wastes provides a sink for atmospheric CO_2. Environmental Science and Technology, **45**: 7727-7736.

Appendices

Appendix A: Media Recipes for Chapter 2

A- 1 Standard BG-11 media recipes used during the growth phase, and the modified recipe used during the carbonation phase.

Chemical	Standard BG-11 medium	Carbonation phase inflow solution
	g/L of solution	
$NaNO_3$	1.5	0.6336
K_2HPO_4	0.04	0.057
$MgSO_4 \cdot 7H_2O$	0.075	10.11
$CaCl_2 \cdot 2H_2O$	0.036	0.0152
Citric Acid	0.006	0.0025
Ferric Ammonium Citrate	0.006	0.0025
EDTA (Disodium Salt)	0.001	0.0004
Na_2CO_3	0.02	6.9274
Trace Metal Mix (below)	1	0.4224
$Na_2SiO_3 \cdot 9H_2O$		0.5800

A- 2 Trace metal mix recipe used in the BG-11 media.

Chemical	g/L ddH_2O
H_3BO_3 (Baker 0084)	2.86
$MnCl_2 \cdot 4H_2O$ (Baker 2540)	1.81
$ZnSO_4 \cdot 7H_2O$ (SigmaZ 0251)	0.22
$Na_2MoO_4 \cdot 2H_2O$ (JT Baker 3764)	0.39
$CuSO_4 \cdot 5H_2O$ (MCIB2M11)	0.079
$Co(NO_3)_2 \cdot 6H_2O$ (Mallinckroft 4544)	0.0494

Appendix B: PHREEQC data for Chapter 2

All solutions were run at 22 °C.

The high cation-anion balance error measured for some of the solutions is due to the lack of SO_4^{2-} data.

B- 1 Inflow solution chemistry

Concentration (mM)	0 m
Ca	0.076
K	0.385
Mg	38.298
Na	89.848
Si	1.872
P	0.301
S(6)	52.514
Cl	0.322
N(5)	0.466
pH	8.32
Alkalinity as HCO_3^-	69.358
Percent error*	-3.34

* = 100*(Cation-|Anion|)/(Cation+|Anion|)

B- 2 PHREEQC modeling output

Phase	Chemical Formula	Saturation Index
Afwillite	Ca3Si2O4(OH)6	-30.73
Akermanite	Ca2MgSi2O7	-13.26
Anhydrite	CaSO4	-2.58
Antarcticite	CaCl2:6H2O	-16.24
Anthophyllite	Mg7Si8O22(OH)2	11.81
Antigorite	Mg48Si34O85(OH)62	118.63
Aphthitalite	NaK3(SO4)2	-12.14
Aragonite	CaCO3	0.04
Arcanite	K2SO4	-7.31
Artinite	Mg2CO3(OH)2:3H2O	-0.66
Bassanite	CaSO4:0.5H2O	-3.22
Bischofite	MgCl2:6H2O	-13.85
Bloedite	Na2Mg(SO4)2:4H2O	-6.2

Brucite	Mg(OH)2	-2.02
Brushite	CaHPO4:2H2O	-16.05
Burkeite	Na6CO3(SO4)2	-13.92
C	C	-36.98
Ca	Ca	-110.74
Ca2Cl2(OH)2:H2O	Ca2Cl2(OH)2:H2O	-26.66
Ca4Cl2(OH)6:13H2O	Ca4Cl2(OH)6:13H2O	-45.17
Calcite	CaCO3	0.19
Carnallite	KMgCl3:6H2O	-20.95
CaSO4:0.5H2O(beta)	CaSO4:0.5H2O	-3.4
Chalcedony	SiO2	1.05
Chloromagnesite	MgCl2	-31.55
Chrysotile	Mg3Si2O5(OH)4	6.44
CO2(g)	CO2	-1.91
Coesite	SiO2	0.51
Cristobalite(alpha)	SiO2	0.77
Cristobalite(beta)	SiO2	0.32
Dicalcium_silicate	Ca2SiO4	-16.73
Diopside	CaMgSi2O6	-0.41
Dolomite	CaMg(CO3)2	4.22
Dolomite-dis	CaMg(CO3)2	2.66
Dolomite-ord	CaMg(CO3)2	4.23
Enstatite	MgSiO3	0.27
Epsomite	MgSO4:7H2O	-2.25
Foshagite	Ca4Si3O9(OH)2:0.5H2O	-27.63
Gaylussite	CaNa2(CO3)2:5H2O	-4.62
Glauberite	Na2Ca(SO4)2	-5.89
Gypsum	CaSO4:2H2O	-2.37
Gyrolite	Ca2Si3O7(OH)2:1.5H2O	-7.69
H2(g)	H2	-24.71
H2O(g)	H2O	-1.67
Halite	NaCl	-6.41
Hatrurite	Ca3SiO5	-41.57
HCl(g)	HCl	-18.39
Hexahydrite	MgSO4:6H2O	-2.49
Hillebrandite	Ca2SiO3(OH)2:0.17H2O	-16.35
Huntite	CaMg3(CO3)4	5.77
Hydromagnesite	Mg5(CO3)4(OH)2:4H2O	2.16
Hydrophilite	CaCl2	-24.03
Hydroxylapatite	Ca5(OH)(PO4)3	-2.08
K	K	-57.54
K2CO3:1.5H2O	K2CO3:1.5H2O	-13.62
K3H(SO4)2	K3H(SO4)2	-19.5

Kainite	KMgClSO4:3H2O	-11.12
Kalicinite	KHCO3	-5.26
Kieserite	MgSO4:H2O	-3.94
KMgCl3	KMgCl3	-38.15
KMgCl3:2H2O	KMgCl3:2H2O	-30.77
KNaCO3:6H2O	KNaCO3:6H2O	-8.15
Lansfordite	MgCO3:5H2O	-0.1
Larnite	Ca2SiO4	-18.04
Leonite	K2Mg(SO4)2:4H2O	-9.29
Lime	CaO	-21.14
Magnesite	MgCO3	2.39
Mercallite	KHSO4	-12.49
Merwinite	MgCa3(SiO4)2	-24.91
Mg	Mg	-90.6
Mg1.25SO4(OH)0.5:0.5H2O	Mg1.25SO4(OH)0.5:0.5H2O	-5.96
Mg1.5SO4(OH)	Mg1.5SO4(OH)	-6.41
MgCl2:2H2O	MgCl2:2H2O	-22.35
MgCl2:4H2O	MgCl2:4H2O	-16.84
MgCl2:H2O	MgCl2:H2O	-25.74
MgOHCl	MgOHCl	-13.6
MgSO4	MgSO4	-9.2
Mirabilite	Na2SO4:10H2O	-3.18
Monohydrocalcite	CaCO3:H2O	-0.66
Monticellite	CaMgSiO4	-6.41
Na	Na	-51.55
Na2CO3	Na2CO3	-6.74
Na2CO3:7H2O	Na2CO3:7H2O	-5.41
Na2O	Na2O	-53.84
Na2SiO3	Na2SiO3	-10.91
Na3H(SO4)2	Na3H(SO4)2	-15.14
Na4Ca(SO4)3:2H2O	Na4Ca(SO4)3:2H2O	-9.93
Na4SiO4	Na4SiO4	-45.53
Nahcolite	NaHCO3	-2.44
Natron	Na2CO3:10H2O	-5.03
Natrosilite	Na2Si2O5	-9.47
Nesquehonite	MgCO3:3H2O	-0.63
Niter	KNO3	-6.77
NO2(g)	NO2	-10.9
O2(g)	O2	-34.71
Okenite	CaSi2O4(OH)2:H2O	-4.1
Oxychloride-Mg	Mg2Cl(OH)3:4H2O	-8.87
Pentahydrite	MgSO4:5H2O	-2.83
Periclase	MgO	-7.13

Picromerite	K2Mg(SO4)2:6H2O	-8.97
Pirssonite	Na2Ca(CO3)2:2H2O	-4.78
Polyhalite	K2MgCa2(SO4)4:2H2O	-12.88
Portlandite	Ca(OH)2	-11
Pseudowollastonite	CaSiO3	-5.09
Quartz	SiO2	1.33
Rankinite	Ca3Si2O7	-22.56
Sepiolite	Mg4Si6O15(OH)2:6H2O	10.77
Si	Si	-115.59
SiO2(am)	SiO2	0.02
Starkeyite	MgSO4:4H2O	-3.21
Sylvite	KCl	-8.02
Syngenite	K2Ca(SO4)2:H2O	-8.49
Tachyhydrite	Mg2CaCl6:12H2O	-48.2
Talc	Mg3Si4O10(OH)2	11.09
Thenardite	Na2SO4	-4.11
Thermonatrite	Na2CO3:H2O	-6.5
Tobermorite-11A	Ca5Si6H11O22.5	-23.6
Tobermorite-14A	Ca5Si6H21O27.5	-21.73
Tobermorite-9A	Ca5Si6H6O20	-27.14
Tremolite	Ca2Mg5Si8O22(OH)2	12.12
Tridymite	SiO2	1.14
Trona-K	K2NaH(CO3)2:2H2O	-14.45
Whitlockite	Ca3(PO4)2	-3.12
Wollastonite	CaSiO3	-4.85
Xonotlite	Ca6Si6O17(OH)2	-38.53

B- 3 One week into carbonation phase (Day 63)

Concentration (mM)	0 m	2 m	4 m	6 m	8 m
Ca	0.0389	0.0419	0.0412	0.0372	0.0287
K	1.8031	1.9974	2.2174	2.2506	2.3683
Mg	16.2896	12.7931	10.7000	9.2000	6.2937
Na	75.2501	71.3354	69.5955	67.8556	59.5911
Si	0.8342	0.7155	0.7731	0.8306	0.7838
N(5)	0.9224	0.2532	0.0221	0.0000	0.0000
P	0.0808	0.0532	0.0382	0.0335	0.0103
Alkalinity as HCO_3^-	55.00	50.00	47.5000	45.00	40.00
pH	8.980	9.02	9.15	9.24	9.30
Percent error*	39.4600	38.9700	38.7700	38.7400	34.9700

* = 100*(Cation-|Anion|)/(Cation+|Anion|)

B- 4 PHREEQC modeling output for day 63

Phase	Formula	Saturation index by sample location				
		0 m	2 m	4 m	6 m	8 m
Afwillite	Ca3Si2O4(OH)6	-28.45	-28.25	-27.63	-27.3	-27.36
Akermanite	Ca2MgSi2O7	-10.89	-10.83	-10.26	-9.94	-10.06
Anthophyllite	Mg7Si8O22(OH)2	16.15	15.42	16.47	17.16	16.56
Antigorite	Mg48Si34O85(OH)62	158.09	154.61	161.99	166.73	163.37
Aragonite	CaCO3	0.28	0.33	0.37	0.36	0.26
Artinite	Mg2CO3(OH)2:3H2O	0.82	0.71	0.86	0.93	0.74
Brucite	Mg(OH)2	-0.87	-0.89	-0.73	-0.63	-0.68
Brushite	CaHPO4:2H2O	-16.99	-17.07	-17.26	-17.38	-17.91
C	C	-40.45	-40.68	-41.37	-41.86	-42.19
Ca	Ca	-110.99	-110.95	-111	-111.07	-111.19
Calcite	CaCO3	0.43	0.48	0.52	0.5	0.41
Chalcedony	SiO2	0.59	0.52	0.51	0.51	0.47
Chrysotile	Mg3Si2O5(OH)4	8.97	8.76	9.22	9.52	9.31
CO2(g)	CO2	-2.73	-2.8	-2.97	-3.1	-3.19
Coesite	SiO2	0.05	-0.03	-0.04	-0.04	-0.07
Cristobalite(alpha)	SiO2	0.31	0.23	0.22	0.22	0.19
Cristobalite(beta)	SiO2	-0.15	-0.22	-0.23	-0.23	-0.26
Dicalcium_silicate	Ca2SiO4	-15.05	-14.9	-14.48	-14.26	-14.29
Diopside	CaMgSi2O6	0.89	0.83	1.19	1.4	1.28
Dolomite	CaMg(CO3)2	4.79	4.75	4.78	4.73	4.5
Dolomite-dis	CaMg(CO3)2	3.23	3.19	3.22	3.17	2.94
Dolomite-ord	CaMg(CO3)2	4.8	4.76	4.79	4.74	4.51
Enstatite	MgSiO3	0.95	0.86	1.01	1.11	1.03
Foshagite	Ca4Si3O9(OH)2:0.5H2O	-24.74	-24.51	-23.68	-23.24	-23.34
Gaylussite	CaNa2(CO3)2:5H2O	-3.93	-3.91	-3.79	-3.78	-3.95
Gyrolite	Ca2Si3O7(OH)2:1.5H2O	-6.94	-6.93	-6.53	-6.31	-6.41
H2(g)	H2	-26.03	-26.11	-26.37	-26.55	-26.67
H2O(g)	H2O	-1.67	-1.66	-1.66	-1.66	-1.66
Hatrurite	Ca3SiO5	-38.82	-38.55	-37.92	-37.59	-37.62
Hillebrandite	Ca2SiO3(OH)2:0.17H2O	-14.67	-14.52	-14.1	-13.88	-13.91
Huntite	CaMg3(CO3)4	6.98	6.76	6.77	6.67	6.16
Hydromagnesite	Mg5(CO3)4(OH)2:4H2O	4.6	4.23	4.35	4.34	3.73
Hydroxylapatite	Ca5(OH)(PO4)3	-2.75	-2.78	-2.91	-3.05	-4.64
K	K	-56.81	-56.76	-56.72	-56.71	-56.68
K2CO3:1.5H2O	K2CO3:1.5H2O	-11.67	-11.56	-11.37	-11.3	-11.22
K2O	K2O	-72.54	-72.36	-72.01	-71.81	-71.64
K8H4(CO3)6:3H2O	K8H4(CO3)6:3H2O	-41.95	-41.64	-41.24	-41.22	-41.09
Kalicinite	KHCO3	-4.7	-4.68	-4.67	-4.7	-4.71
KNaCO3:6H2O	KNaCO3:6H2O	-6.94	-6.9	-6.77	-6.72	-6.72

Lansfordite	MgCO3:5H2O	0.22	0.14	0.12	0.1	-0.04
Larnite	Ca2SiO4	-16.36	-16.21	-15.79	-15.57	-15.6
Lime	CaO	-20.07	-19.96	-19.74	-19.63	-19.63
Magnesite	MgCO3	2.72	2.63	2.62	2.59	2.45
Merwinite	MgCa3(SiO4)2	-21.48	-21.31	-20.53	-20.1	-20.21
Mg	Mg	-90.77	-90.87	-90.97	-91.05	-91.22
Monohydrocalcite	CaCO3:H2O	-0.41	-0.37	-0.33	-0.34	-0.44
Monticellite	CaMgSiO4	-4.65	-4.63	-4.26	-4.06	-4.13
Na	Na	-51.57	-51.59	-51.6	-51.61	-51.66
Na(g)	Na	-65.25	-65.27	-65.28	-65.29	-65.34
Na2CO3	Na2CO3	-6.3	-6.32	-6.25	-6.22	-6.29
Na2CO3:7H2O	Na2CO3:7H2O	-4.96	-4.99	-4.91	-4.88	-4.96
Na2O	Na2O	-52.56	-52.52	-52.28	-52.12	-52.1
Na2SiO3	Na2SiO3	-10.09	-10.13	-9.89	-9.73	-9.75
Na4SiO4	Na4SiO4	-43.45	-43.44	-42.96	-42.63	-42.64
Nahcolite	NaHCO3	-2.63	-2.68	-2.73	-2.78	-2.86
Natron	Na2CO3:10H2O	-4.57	-4.6	-4.53	-4.49	-4.57
Natrosilite	Na2Si2O5	-9.12	-9.23	-9	-8.84	-8.9
Nesquehonite	MgCO3:3H2O	-0.31	-0.4	-0.41	-0.43	-0.57
Niter	KNO3	-5.71	-6.22	-7.23		
NO2(g)	NO2	-11.9	-12.54	-13.85		
O2(g)	O2	-32.06	-31.9	-31.38	-31.02	-30.78
Okenite	CaSi2O4(OH)2:H2O	-3.95	-3.99	-3.79	-3.68	-3.75
Periclase	MgO	-5.98	-6	-5.84	-5.74	-5.79
Pirssonite	Na2Ca(CO3)2:2H2O	-4.09	-4.07	-3.95	-3.93	-4.11
Portlandite	Ca(OH)2	-9.93	-9.82	-9.61	-9.5	-9.49
Pseudowollastonite	CaSiO3	-4.48	-4.44	-4.24	-4.13	-4.16
Quartz	SiO2	0.86	0.79	0.78	0.78	0.75
Rankinite	Ca3Si2O7	-20.28	-20.08	-19.46	-19.13	-19.2
Sepiolite	Mg4Si6O15(OH)2:6H2O	12.6	12.07	12.66	13.06	12.66
Si	Si	-118.69	-118.93	-119.45	-119.82	-120.09
SiO2(am)	SiO2	-0.44	-0.52	-0.53	-0.53	-0.56
Talc	Mg3Si4O10(OH)2	12.69	12.33	12.78	13.07	12.8
Thermonatrite	Na2CO3:H2O	-6.05	-6.08	-6	-5.97	-6.05
Tobermorite-11A	Ca5Si6H11O22.5	-21.03	-20.9	-19.89	-19.34	-19.55
Tobermorite-14A	Ca5Si6H21O27.5	-19.16	-19.03	-18.01	-17.47	-17.67
Tobermorite-9A	Ca5Si6H6O20	-24.57	-24.44	-23.43	-22.88	-23.09
Tremolite	Ca2Mg5Si8O22(OH)2	16.31	15.84	17	17.71	17.2
Tridymite	SiO2	0.68	0.6	0.59	0.59	0.56
Trona-K	K2NaH(CO3)2:2H2O	-12.68	-12.62	-12.48	-12.46	-12.47
Whitlockite	Ca3(PO4)2	-3.92	-3.98	-4.14	-4.27	-5.33
Wollastonite	CaSiO3	-4.24	-4.2	-4	-3.89	-3.92

Xonotlite	Ca6Si6O17(OH)2	-34.9	-34.66	-33.42	-32.77	-32.97

B- 5 Two weeks into carbonation phase (Day 70)

Concentration (mM)	0 m	2 m	4 m	6 m	8 m
Ca	0.0312	0.0449	0.0424	0.0457	0.0417
K	1.8107	2.0102	1.9693	1.7468	2.1023
Mg	18.7577	17.0300	15.4258	17.8116	14.8910
Na	88.7342	86.1244	80.0348	79.5998	81.3397
Si	0.3308	0.1546	0.1316	0.2841	0.2876
N(5)	0.6451	0.2306	0.1321	0.3129	0.0000
P	0.0429	0.0278	0.0176	0.0349	0.0080
Alkalinity as HCO_3^-	60.00	57.00	52.50	56.00	52.50
pH	9.19	9.3	9.27	9.21	9.19
Percent error*	45.08	45.89	45.48	44.36	45.04

* = 100*(Cation-|Anion|)/(Cation+|Anion|)

B- 6 PHREEQC modeling output (day 70)

		Saturation index by sample location				
Phase	Formula	0 m	2 m	4 m	6 m	8 m
Afwillite	Ca3Si2O4(OH)6	-28.72	-28.43	-28.69	-28.2	-28.37
Akermanite	Ca2MgSi2O7	-10.98	-10.88	-11.17	-10.65	-10.86
Anthophyllite	Mg7Si8O22(OH)2	15.16	13.26	12.33	14.87	14.2
Antigorite	Mg48Si34O85(OH)62	161.58	156.41	151	160.83	156.05
Aragonite	CaCO3	0.27	0.46	0.42	0.44	0.39
Artinite	Mg2CO3(OH)2:3H2O	1.41	1.57	1.43	1.42	1.22
Brucite	Mg(OH)2	-0.45	-0.29	-0.37	-0.42	-0.53
Brushite	CaHPO4:2H2O	-17.59	-17.68	-17.83	-17.5	-18.1
C	C	-41.54	-42.14	-42.01	-41.67	-41.58
Ca	Ca	-111.17	-111.04	-111.04	-110.99	-111.02
Calcite	CaCO3	0.41	0.6	0.56	0.58	0.53
Chalcedony	SiO2	0.1	-0.28	-0.33	0.03	0.05
Chrysotile	Mg3Si2O5(OH)4	9.25	8.97	8.64	9.21	8.91
CO2(g)	CO2	-2.98	-3.14	-3.13	-3.03	-3.02
Coesite	SiO2	-0.45	-0.82	-0.87	-0.51	-0.5
Cristobalite(alpha)	SiO2	-0.19	-0.56	-0.61	-0.25	-0.24
Cristobalite(beta)	SiO2	-0.64	-1.02	-1.06	-0.7	-0.69
Dicalcium_silicate	Ca2SiO4	-15.07	-14.75	-14.91	-14.7	-14.82

Diopside	CaMgSi2O6	0.56	0.31	0.08	0.68	0.53
Dolomite	CaMg(CO3)2	4.94	5.13	5.03	5.09	4.95
Dolomite-dis	CaMg(CO3)2	3.38	3.57	3.47	3.53	3.39
Dolomite-ord	CaMg(CO3)2	4.95	5.14	5.04	5.1	4.96
Enstatite	MgSiO3	0.88	0.66	0.54	0.85	0.75
Foshagite	Ca4Si3O9(OH)2:0.5H2O	-25.27	-25.01	-25.37	-24.59	-24.83
Gaylussite	CaNa2(CO3)2:5H2O	-3.64	-3.41	-3.55	-3.57	-3.62
Gyrolite	Ca2Si3O7(OH)2:1.5H2O	-7.95	-8.38	-8.63	-7.7	-7.8
H2(g)	H2	-26.45	-26.67	-26.61	-26.49	-26.45
H2O(g)	H2O	-1.67	-1.67	-1.67	-1.67	-1.67
Hatrurite	Ca3SiO5	-38.61	-37.94	-38.15	-38.02	-38.2
Hillebrandite	Ca2SiO3(OH)2:0.17H2O	-14.69	-14.37	-14.53	-14.32	-14.44
Huntite	CaMg3(CO3)4	7.48	7.67	7.44	7.58	7.27
Hydromagnesite	Mg5(CO3)4(OH)2:4H2O	5.71	5.87	5.54	5.65	5.19
Hydroxylapatite	Ca5(OH)(PO4)3	-4.08	-3.64	-4.21	-3.39	-5.3
K	K	-56.81	-56.77	-56.77	-56.83	-56.75
K2CO3:1.5H2O	K2CO3:1.5H2O	-11.5	-11.35	-11.4	-11.54	-11.39
K2O	K2O	-72.12	-71.81	-71.88	-72.11	-71.98
K8H4(CO3)6:3H2O	K8H4(CO3)6:3H2O	-41.79	-41.49	-41.67	-42.02	-41.42
Kalicinite	KHCO3	-4.74	-4.74	-4.76	-4.78	-4.7
KNaCO3:6H2O	KNaCO3:6H2O	-6.7	-6.61	-6.68	-6.77	-6.7
Lansfordite	MgCO3:5H2O	0.39	0.39	0.33	0.37	0.28
Larnite	Ca2SiO4	-16.38	-16.06	-16.22	-16.01	-16.13
Lime	CaO	-19.84	-19.49	-19.54	-19.62	-19.68
Magnesite	MgCO3	2.89	2.89	2.82	2.86	2.78
Merwinite	MgCa3(SiO4)2	-21.34	-20.89	-21.23	-20.78	-21.07
Mg	Mg	-90.77	-90.83	-90.85	-90.78	-90.85
Monohydrocalcite	CaCO3:H2O	-0.43	-0.24	-0.28	-0.26	-0.31
Monticellite	CaMgSiO4	-4.48	-4.35	-4.54	-4.3	-4.46
Na	Na	-51.51	-51.52	-51.54	-51.55	-51.54
Na(g)	Na	-65.18	-65.2	-65.22	-65.23	-65.22
Na2CO3	Na2CO3	-5.99	-5.95	-6.05	-6.09	-6.09
Na2CO3:7H2O	Na2CO3:7H2O	-4.65	-4.61	-4.71	-4.75	-4.75
Na2O	Na2O	-52.01	-51.81	-51.92	-52.05	-52.07
Na2SiO3	Na2SiO3	-10.03	-10.21	-10.37	-10.14	-10.15
Na4SiO4	Na4SiO4	-42.82	-42.8	-43.08	-42.98	-43.01
Nahcolite	NaHCO3	-2.61	-2.67	-2.71	-2.68	-2.67
Natron	Na2CO3:10H2O	-4.27	-4.23	-4.33	-4.36	-4.36
Natrosilite	Na2Si2O5	-9.55	-10.11	-10.32	-9.72	-9.72
Nesquehonite	MgCO3:3H2O	-0.14	-0.14	-0.2	-0.16	-0.25
Niter	KNO3	-5.87	-6.27	-6.51	-6.19	

NO2(g)	NO2	-12.48	-13.14	-13.32	-12.83	
O2(g)	O2	-31.22	-30.78	-30.9	-31.14	-31.22
Okenite	CaSi2O4(OH)2:H2O	-4.71	-5.11	-5.26	-4.61	-4.66
Periclase	MgO	-5.56	-5.4	-5.48	-5.53	-5.64
Pirssonite	Na2Ca(CO3)2:2H2O	-3.8	-3.57	-3.7	-3.73	-3.77
Portlandite	Ca(OH)2	-9.7	-9.35	-9.41	-9.48	-9.55
Pseudowollastonite	CaSiO3	-4.74	-4.77	-4.87	-4.59	-4.64
Quartz	SiO2	0.37	-0.01	-0.05	0.31	0.32
Rankinite	Ca3Si2O7	-20.56	-20.27	-20.53	-20.03	-20.21
Sepiolite	Mg4Si6O15(OH)2:6H2O	11.33	9.7	9.1	11.07	10.7
Si	Si	-120.03	-120.84	-120.77	-120.17	-120.08
SiO2(am)	SiO2	-0.94	-1.32	-1.36	-1	-0.99
Talc	Mg3Si4O10(OH)2	11.98	10.95	10.53	11.82	11.54
Thermonatrite	Na2CO3:H2O	-5.74	-5.7	-5.8	-5.84	-5.84
Tobermorite-11A	Ca5Si6H11O22.5	-22.81	-23.33	-23.89	-22.1	-22.36
Tobermorite-14A	Ca5Si6H21O27.5	-20.94	-21.46	-22.02	-20.23	-20.49
Tobermorite-9A	Ca5Si6H6O20	-26.35	-26.87	-27.43	-25.64	-25.9
Tremolite	Ca2Mg5Si8O22(OH)2	14.94	13.42	12.54	15.02	14.44
Tridymite	SiO2	0.18	-0.19	-0.24	0.12	0.13
Trona-K	K2NaH(CO3)2:2H2O	-12.49	-12.39	-12.49	-12.6	-12.44
Whitlockite	Ca3(PO4)2	-4.89	-4.71	-5.07	-4.5	-5.75
Wollastonite	CaSiO3	-4.5	-4.53	-4.63	-4.34	-4.4
Xonotlite	Ca6Si6O17(OH)2	-36.44	-36.61	-37.22	-35.51	-35.84

B- 7 Four weeks into carbonation phase (Day 84)

Concentration (mM)	0 m	2 m	4 m	6 m	8 m
Ca	0.0664	0.0619	0.0302	0.0499	0.0494
K	1.1893	1.3529	1.4450	1.4859	1.6164
Mg	26.1209	26.4912	20.2797	18.3464	17.6882
Na	94.3889	97.4337	96.1288	97.4337	97.4337
Si	0.4962	0.3218	0.0370	0.0561	0.0687
N(5)	2.1448	1.2772	0.5080	0.1758	0.0197
P	0.1038	0.0725	0.0214	0.0000	0.0062
Alkalinity as HCO_3^-	65.00	62.50	60.00	57.50	55.00
pH	9.04	9.13	9.12	9.13	9.19
Percent error*	47.84	52.54	48.74	49.64	51.65

* = 100*(Cation-|Anion|)/(Cation+|Anion|)

B- 8 PHREEQC modeling output (day 84)

Phase	Formula	Saturation index by sample location				
		0 m	2 m	4 m	6 m	8 m
Afwillite	Ca3Si2O4(OH)6	-28.04	-28.08	-30.96	-29.89	-29.45
Akermanite	Ca2MgSi2O7	-10.5	-10.51	-13.19	-12.38	-11.94
Anthophyllite	Mg7Si8O22(OH)2	16.09	15.54	7.09	8.34	9.54
Antigorite	Mg48Si34O85(OH)62	163.22	164.14	125.68	130.62	137.52
Aragonite	CaCO3	0.53	0.52	0.22	0.44	0.45
Artinite	Mg2CO3(OH)2:3H2O	1.34	1.56	1.31	1.25	1.35
Brucite	Mg(OH)2	-0.58	-0.4	-0.54	-0.56	-0.46
Brushite	CaHPO4:2H2O	-16.88	-17.14	-17.88		-18.2
C	C	-40.76	-41.26	-41.18	-41.24	-41.58
Ca	Ca	-110.79	-110.84	-111.16	-110.93	-110.95
Calcite	CaCO3	0.68	0.67	0.37	0.59	0.6
Chalcedony	SiO2	0.32	0.1	-0.84	-0.66	-0.6
Chrysotile	Mg3Si2O5(OH)4	9.32	9.41	7.12	7.41	7.83
CO2(g)	CO2	-2.8	-2.94	-2.9	-2.93	-3.02
Coesite	SiO2	-0.22	-0.45	-1.38	-1.21	-1.14
Cristobalite(alpha)	SiO2	0.04	-0.19	-1.12	-0.95	-0.88
Cristobalite(beta)	SiO2	-0.41	-0.64	-1.57	-1.4	-1.34
Dicalcium_silicate	Ca2SiO4	-14.69	-14.65	-16.26	-15.6	-15.32
Diopside	CaMgSi2O6	0.96	0.82	-1.52	-0.95	-0.62
Dolomite	CaMg(CO3)2	5.26	5.29	4.89	5.07	5.08
Dolomite-dis	CaMg(CO3)2	3.7	3.73	3.33	3.51	3.52
Dolomite-ord	CaMg(CO3)2	5.27	5.3	4.9	5.08	5.09
Enstatite	MgSiO3	0.98	0.94	-0.14	0.02	0.18
Foshagite	Ca4Si3O9(OH)2:0.5H2O	-24.29	-24.42	-28.57	-27.09	-26.47
Gaylussite	CaNa2(CO3)2:5H2O	-3.45	-3.39	-3.68	-3.45	-3.41
Gyrolite	Ca2Si3O7(OH)2:1.5H2O	-7.11	-7.52	-10.99	-9.99	-9.59
H2(g)	H2	-26.15	-26.33	-26.31	-26.33	-26.45
H2O(g)	H2O	-1.67	-1.67	-1.67	-1.67	-1.67
Hatrurite	Ca3SiO5	-38.15	-37.97	-39.91	-39.02	-38.63
Hillebrandite	Ca2SiO3(OH)2:0.17H2O	-14.31	-14.27	-15.88	-15.22	-14.94
Huntite	CaMg3(CO3)4	7.92	8.02	7.41	7.51	7.53
Hydromagnesite	Mg5(CO3)4(OH)2:4H2O	5.81	6.14	5.59	5.4	5.52
Hydroxylapatite	Ca5(OH)(PO4)3	-1.81	-2.32	-5.19		-5.47
K	K	-57	-56.95	-56.92	-56.9	-56.86
K2CO3:1.5H2O	K2CO3:1.5H2O	-11.99	-11.84	-11.76	-11.74	-11.64
K2O	K2O	-72.8	-72.51	-72.46	-72.42	-72.22
K8H4(CO3)6:3H2O	K8H4(CO3)6:3H2O	-43.39	-43.08	-42.68	-42.62	-42.42
Kalicinite	KHCO3	-4.9	-4.89	-4.83	-4.83	-4.83

KNaCO3:6H2O	KNaCO3:6H2O	-6.99	-6.88	-6.83	-6.81	-6.75
Lansfordite	MgCO3:5H2O	0.45	0.49	0.39	0.34	0.35
Larnite	Ca2SiO4	-16	-15.96	-17.57	-16.91	-16.64
Lime	CaO	-19.76	-19.62	-19.96	-19.72	-19.61
Magnesite	MgCO3	2.94	2.98	2.88	2.84	2.84
Merwinite	MgCa3(SiO4)2	-20.78	-20.65	-23.67	-22.62	-22.07
Mg	Mg	-90.59	-90.59	-90.71	-90.76	-90.78
Mg(g)	Mg	-110.58	-110.58	-110.7	-110.74	-110.76
Monohydrocalcite	CaCO3:H2O	-0.17	-0.18	-0.48	-0.26	-0.25
Monticellite	CaMgSiO4	-4.31	-4.22	-5.63	-5.23	-4.97
Na	Na	-51.48	-51.47	-51.47	-51.47	-51.46
Na2CO3	Na2CO3	-6.06	-5.99	-5.98	-5.97	-5.95
Na2CO3:7H2O	Na2CO3:7H2O	-4.73	-4.66	-4.65	-4.64	-4.61
Na2O	Na2O	-52.26	-52.05	-52.08	-52.05	-51.92
Na2SiO3	Na2SiO3	-10.06	-10.07	-11.04	-10.83	-10.64
Na4SiO4	Na4SiO4	-43.11	-42.91	-43.9	-43.66	-43.35
Nahcolite	NaHCO3	-2.55	-2.59	-2.56	-2.57	-2.6
Natron	Na2CO3:10H2O	-4.34	-4.27	-4.26	-4.25	-4.22
Natrosilite	Na2Si2O5	-9.35	-9.6	-11.49	-11.11	-10.86
Nesquehonite	MgCO3:3H2O	-0.08	-0.04	-0.15	-0.19	-0.18
Niter	KNO3	-5.54	-5.71	-6.08	-6.52	-7.44
NO2(g)	NO2	-11.66	-12.07	-12.44	-12.92	-13.99
O2(g)	O2	-31.82	-31.46	-31.5	-31.46	-31.22
Okenite	CaSi2O4(OH)2:H2O	-4.17	-4.49	-6.7	-6.11	-5.88
Periclase	MgO	-5.69	-5.51	-5.65	-5.67	-5.57
Pirssonite	Na2Ca(CO3)2:2H2O	-3.61	-3.55	-3.84	-3.6	-3.57
Portlandite	Ca(OH)2	-9.62	-9.49	-9.82	-9.58	-9.48
Pseudowollastonite	CaSiO3	-4.44	-4.53	-5.8	-5.38	-5.21
Quartz	SiO2	0.6	0.37	-0.56	-0.39	-0.33
Rankinite	Ca3Si2O7	-19.87	-19.92	-22.8	-21.73	-21.28
Sepiolite	Mg4Si6O15(OH)2:6H2O	12.18	11.54	5.38	6.34	7.12
Si	Si	-119.2	-119.78	-120.68	-120.54	-120.72
SiO2(am)	SiO2	-0.71	-0.94	-1.87	-1.7	-1.63
Talc	Mg3Si4O10(OH)2	12.51	12.14	7.99	8.62	9.17
Thermonatrite	Na2CO3:H2O	-5.82	-5.75	-5.74	-5.72	-5.7
Tobermorite-11A	Ca5Si6H11O22.5	-21.06	-21.74	-29.03	-26.78	-25.88
Tobermorite-14A	Ca5Si6H21O27.5	-19.19	-19.87	-27.16	-24.91	-24.01
Tobermorite-9A	Ca5Si6H6O20	-24.6	-25.28	-32.57	-30.32	-29.42
Tremolite	Ca2Mg5Si8O22(OH)2	16.28	15.64	6.79	8.57	9.78
Tridymite	SiO2	0.41	0.18	-0.75	-0.58	-0.51
Trona-K	K2NaH(CO3)2:2H2O	-12.92	-12.81	-12.71	-12.69	-12.62
Whitlockite	Ca3(PO4)2	-3.4	-3.78	-5.59		-5.89

Wollastonite	CaSiO3	-4.19	-4.28	-5.56	-5.14	-4.97
Xonotlite	Ca6Si6O17(OH)2	-34.61	-35.16	-42.79	-40.29	-39.28

B- 9 Six weeks into carbonation phase (Day 98)

Concentration (mM)	0 m	2 m	4 m	6 m	8 m
Ca	0.0656	0.0585	0.0515	0.0492	0.0463
K	1.1304	1.0024	1.1720	1.0604	1.2635
Mg	40.1302	38.0601	26.7378	22.5513	20.9324
Na	138.5055	145.6468	113.5772	110.3448	104.7405
Si	0.7111	0.3788	0.1375	0.1263	0.1179
N(5)	4.7734	1.3917	0.6451	0.3000	0.0648
P	0.1464	0.0945	0.0502	0.0202	0.0000
S(6)	74.2167	41.9486	44.9672	56.6254	60.7890
N(3)	0.1193	0.1452	0.1204	0.0865	0.0561
Cl	0.5811	0.6291	0.6939	0.7221	0.7927
Alkalinity as HCO_3^-	62.50	57.50	55.00	60.00	48.75
Percent error*	1.16	29.87	9.37	-7.04	-9.5

* = 100*(Cation-|Anion|)/(Cation+|Anion|)

B- 10 PHREEQC modeling output (day 98)

		Saturation index by sample location				
Phase	Formula	0 m	2 m	4 m	6 m	8 m
Afwillite	Ca3Si2O4(OH)6	-29.03	-28.49	-29.5	-29.65	-29.65
Akermanite	Ca2MgSi2O7	-11.44	-10.82	-11.95	-12.15	-12.18
Anhydrite	CaSO4	-2.63	-2.89	-2.88	-2.84	-2.8
Antarcticite	CaCl2:6H2O	-15.92	-15.85	-15.84	-15.89	-15.81
Anthophyllite	Mg7Si8O22(OH)2	14.75	15.34	10.85	9.96	9.68
Antigorite	Mg48Si34O85(OH)62	150.11	161.88	139.6	134.35	133.01
Aphthitalite	NaK3(SO4)2	-10.38	-10.91	-10.61	-10.57	-10.3
Aragonite	CaCO3	0.27	0.35	0.32	0.32	0.24
Arcanite	K2SO4	-6.29	-6.6	-6.36	-6.36	-6.17
Artinite	Mg2CO3(OH)2:3H2O	0.72	1.39	1.07	0.93	0.82
Bassanite	CaSO4:0.5H2O	-3.27	-3.54	-3.52	-3.48	-3.45
Bischofite	MgCl2:6H2O	-13.42	-13.27	-13.37	-13.48	-13.43
Bloedite	Na2Mg(SO4)2:4H2O	-5.67	-6	-6.21	-6.17	-6.17
Brucite	Mg(OH)2	-0.98	-0.47	-0.65	-0.73	-0.74
Brushite	CaHPO4:2H2O	-16.73	-17.11	-17.31	-17.7	
Burkeite	Na6CO3(SO4)2	-12.22	-12.35	-12.76	-12.59	-12.73
C	C	-39.89	-41.11	-41.12	-41.22	-41.35

Ca	Ca	-110.91	-110.92	-111.01	-111.09	-111.09
Ca2Cl2(OH)2:H2O	Ca2Cl2(OH)2:H2O	-25.41	-24.91	-24.97	-25.04	-24.94
Ca4Cl2(OH)6:13H2O	Ca4Cl2(OH)6:13H2O	-42.07	-40.71	-40.9	-41.02	-40.88
Calcite	CaCO3	0.41	0.5	0.46	0.46	0.39
Carnallite	KMgCl3:6H2O	-19.83	-19.66	-19.64	-19.8	-19.63
CaSO4:0.5H2O(beta)	CaSO4:0.5H2O	-3.45	-3.71	-3.7	-3.66	-3.62
Chalcedony	SiO2	0.51	0.14	-0.27	-0.31	-0.34
Chloromagnesite	MgCl2	-31.12	-30.97	-31.06	-31.18	-31.12
Chrysotile	Mg3Si2O5(OH)4	8.48	9.26	7.92	7.59	7.51
Cl2(g)	Cl2	-45.3	-45.21	-45.12	-45.09	-45.01
CO2(g)	CO2	-2.61	-2.95	-2.92	-2.9	-2.99
Coesite	SiO2	-0.03	-0.4	-0.81	-0.85	-0.88
Cristobalite(alpha)	SiO2	0.23	-0.14	-0.55	-0.59	-0.62
Cristobalite(beta)	SiO2	-0.22	-0.59	-1	-1.04	-1.07
Dicalcium_silicate	Ca2SiO4	-15.41	-14.93	-15.47	-15.55	-15.54
Diopside	CaMgSi2O6	0.48	0.67	-0.39	-0.57	-0.62
Dolomite	CaMg(CO3)2	4.79	5.04	4.85	4.8	4.62
Dolomite-dis	CaMg(CO3)2	3.23	3.48	3.29	3.24	3.06
Dolomite-ord	CaMg(CO3)2	4.8	5.04	4.86	4.81	4.63
Enstatite	MgSiO3	0.76	0.9	0.32	0.2	0.16
Epsomite	MgSO4:7H2O	-2.2	-2.38	-2.47	-2.49	-2.48
Foshagite	Ca4Si3O9(OH)2:0.5H2O	-25.54	-24.94	-26.43	-26.64	-26.65
Gaylussite	CaNa2(CO3)2:5H2O	-3.65	-3.38	-3.58	-3.54	-3.74
Glauberite	Na2Ca(SO4)2	-5.46	-5.88	-5.99	-5.88	-5.85
Gypsum	CaSO4:2H2O	-2.42	-2.68	-2.67	-2.63	-2.59
Gyrolite	Ca2Si3O7(OH)2:1.5H2O	-7.46	-7.71	-9.07	-9.24	-9.28
H2(g)	H2	-25.81	-26.25	-26.27	-26.33	-26.35
H2O(g)	H2O	-1.67	-1.67	-1.67	-1.67	-1.67
Halite	NaCl	-5.99	-5.9	-5.96	-5.97	-5.95
Hatrurite	Ca3SiO5	-39.32	-38.41	-39.02	-39.12	-39.1
HCl(g)	HCl	-18.7	-18.87	-18.83	-18.85	-18.82
Hexahydrite	MgSO4:6H2O	-2.43	-2.61	-2.7	-2.73	-2.72
Hillebrandite	Ca2SiO3(OH)2:0.17H2O	-15.03	-14.55	-15.09	-15.17	-15.16
Huntite	CaMg3(CO3)4	7.01	7.59	7.12	6.95	6.56
Hydromagnesite	Mg5(CO3)4(OH)2:4H2O	4.55	5.71	4.96	4.66	4.23
Hydrophilite	CaCl2	-23.71	-23.64	-23.63	-23.68	-23.6
Hydroxylapatite	Ca5(OH)(PO4)3	-2.25	-2.54	-3.28	-4.49	
K	K	-57.1	-57.12	-57.06	-57.11	-57.04
K2CO3:1.5H2O	K2CO3:1.5H2O	-12.33	-12.29	-12.1	-12.13	-12.06
K2O	K2O	-73.33	-72.94	-72.79	-72.84	-72.67
K3H(SO4)2	K3H(SO4)2	-18.47	-19.27	-18.87	-18.84	-18.55

K8H4(CO3)6:3H2O	K8H4(CO3)6:3H2O	-44.35	-44.86	-44.07	-44.14	-44.05
Kainite	KMgClSO4:3H2O	-10.37	-10.53	-10.51	-10.57	-10.45
Kalicinite	KHCO3	-4.97	-5.12	-5.01	-5.01	-5.03
Kieserite	MgSO4:H2O	-3.88	-4.06	-4.15	-4.18	-4.17
KMgCl3	KMgCl3	-37.03	-36.86	-36.84	-37	-36.83
KMgCl3:2H2O	KMgCl3:2H2O	-29.65	-29.48	-29.46	-29.61	-29.45
KNaCO3:6H2O	KNaCO3:6H2O	-7.13	-7.01	-7	-7	-7.02
Lansfordite	MgCO3:5H2O	0.23	0.4	0.26	0.2	0.09
Larnite	Ca2SiO4	-16.72	-16.24	-16.78	-16.86	-16.85
Leonite	K2Mg(SO4)2:4H2O	-8.22	-8.7	-8.56	-8.58	-8.38
Lime	CaO	-20.21	-19.78	-19.85	-19.87	-19.85
Magnesite	MgCO3	2.73	2.89	2.75	2.69	2.59
Mercallite	KHSO4	-12.48	-12.97	-12.81	-12.78	-12.68
Merwinite	MgCa3(SiO4)2	-22.17	-21.12	-22.32	-22.54	-22.55
Mg	Mg	-90.66	-90.59	-90.79	-90.93	-90.96
Mg1.25SO4(OH)0.5:0.5H2O	Mg1.25SO4(OH)0.5:0.5H2O	-5.64	-5.7	-5.83	-5.88	-5.87
Mg1.5SO4(OH)	Mg1.5SO4(OH)	-5.83	-5.76	-5.94	-6	-6
MgCl2:2H2O	MgCl2:2H2O	-21.92	-21.77	-21.86	-21.98	-21.92
MgCl2:4H2O	MgCl2:4H2O	-16.41	-16.26	-16.35	-16.47	-16.41
MgCl2:H2O	MgCl2:H2O	-25.31	-25.15	-25.25	-25.36	-25.31
MgOHCl	MgOHCl	-12.86	-12.53	-12.67	-12.77	-12.74
MgSO4	MgSO4	-9.14	-9.32	-9.41	-9.43	-9.42
Mirabilite	Na2SO4:10H2O	-2.72	-2.87	-2.99	-2.92	-2.93
Misenite	K8H6(SO4)7	-80.59	-83.86	-82.67	-82.49	-81.7
Monohydrocalcite	CaCO3:H2O	-0.43	-0.35	-0.38	-0.38	-0.46
Monticellite	CaMgSiO4	-4.98	-4.41	-5.06	-5.21	-5.22
Na	Na	-51.37	-51.33	-51.44	-51.46	-51.49
Na(g)	Na	-65.05	-65.01	-65.12	-65.14	-65.17
Na2CO3	Na2CO3	-5.99	-5.81	-5.98	-5.94	-6.06
Na2CO3:7H2O	Na2CO3:7H2O	-4.66	-4.47	-4.64	-4.61	-4.73
Na2O	Na2O	-52.38	-51.85	-52.06	-52.04	-52.07
Na2SiO3	Na2SiO3	-9.99	-9.83	-10.44	-10.47	-10.53
Na3H(SO4)2	Na3H(SO4)2	-14.92	-15.5	-15.63	-15.51	-15.51
Na4Ca(SO4)3:2H2O	Na4Ca(SO4)3:2H2O	-9.03	-9.61	-9.83	-9.66	-9.64
Na4SiO4	Na4SiO4	-43.17	-42.47	-43.29	-43.31	-43.38
Na6Si2O7	Na6Si2O7	-62	-61.15	-62.57	-62.62	-62.75
Nahcolite	NaHCO3	-2.42	-2.5	-2.57	-2.54	-2.65
Natron	Na2CO3:10H2O	-4.28	-4.09	-4.26	-4.22	-4.35
Natrosilite	Na2Si2O5	-9.1	-9.31	-10.33	-10.4	-10.48
Nesquehonite	MgCO3:3H2O	-0.3	-0.13	-0.27	-0.33	-0.44
Niter	KNO3	-5.32	-5.87	-6.13	-6.53	-7.12

NO(g)	NO	-4.92	-5.27	-5.36	-5.57	-5.78
NO2(g)	NO2	-11	-11.97	-12.32	-12.72	-13.4
O2(g)	O2	-32.51	-31.63	-31.59	-31.47	-31.43
Okenite	CaSi2O4(OH)2:H2O	-4.25	-4.57	-5.45	-5.56	-5.59
Oxychloride-Mg	Mg2Cl(OH)3:4H2O	-7.1	-6.26	-6.57	-6.75	-6.73
Pentahydrite	MgSO4:5H2O	-2.77	-2.95	-3.04	-3.06	-3.05
Periclase	MgO	-6.09	-5.58	-5.76	-5.84	-5.85
Picromerite	K2Mg(SO4)2:6H2O	-7.9	-8.38	-8.24	-8.26	-8.06
Pirssonite	Na2Ca(CO3)2:2H2O	-3.8	-3.53	-3.73	-3.7	-3.9
Polyhalite	K2MgCa2(SO4)4:2H2O	-11.91	-12.91	-12.74	-12.69	-12.42
Portlandite	Ca(OH)2	-10.08	-9.65	-9.72	-9.74	-9.72
Pseudowollastonite	CaSiO3	-4.7	-4.65	-5.12	-5.18	-5.19
Quartz	SiO2	0.79	0.41	0.01	-0.04	-0.06
Rankinite	Ca3Si2O7	-20.86	-20.32	-21.33	-21.48	-21.48
Sepiolite	Mg4Si6O15(OH)2:6H2O	11.68	11.49	8.34	7.77	7.57
Si	Si	-118.33	-119.58	-120.03	-120.19	-120.26
SiO2(am)	SiO2	-0.52	-0.89	-1.3	-1.34	-1.37
Starkeyite	MgSO4:4H2O	-3.15	-3.33	-3.43	-3.45	-3.44
Sylvite	KCl	-7.32	-7.31	-7.19	-7.23	-7.12
Syngenite	K2Ca(SO4)2:H2O	-7.53	-8.09	-7.84	-7.8	-7.58
Tachyhydrite	Mg2CaCl6:12H2O	-47.02	-46.64	-46.83	-47.11	-46.92
Talc	Mg3Si4O10(OH)2	12.04	12.08	9.93	9.52	9.38
Thenardite	Na2SO4	-3.64	-3.8	-3.91	-3.85	-3.85
Thermonatrite	Na2CO3:H2O	-5.75	-5.56	-5.73	-5.7	-5.82
Tobermorite-11A	Ca5Si6H11O22.5	-22.21	-22.29	-25.08	-25.43	-25.51
Tobermorite-14A	Ca5Si6H21O27.5	-20.34	-20.43	-23.21	-23.57	-23.64
Tobermorite-9A	Ca5Si6H6O20	-25.75	-25.83	-28.62	-28.97	-29.04
Tremolite	Ca2Mg5Si8O22(OH)2	14.85	15.27	11	10.22	10
Tridymite	SiO2	0.6	0.23	-0.18	-0.22	-0.25
Trona-K	K2NaH(CO3)2:2H2O	-13.13	-13.17	-13.05	-13.05	-13.09
Whitlockite	Ca3(PO4)2	-3.54	-3.88	-4.35	-5.15	
Wollastonite	CaSiO3	-4.46	-4.4	-4.88	-4.94	-4.95
Xonotlite	Ca6Si6O17(OH)2	-36.21	-35.87	-38.73	-39.1	-39.15

Appendix C: Feedstock solution recipes for Chapter 3

C- 1 BG-11 media recipes used in Chapter 3

	g/L of solution	
Chemical	Full strength BG-11 medium	Half strength BG-11 medium
$NaNO_3$	5.250	2.625
K_2HPO_4	0.680	0.340
$CaCl_2 \cdot 2H_2O$	0.126	0.063
Citric Acid	0.021	0.0105
Ferric Ammonium Citrate	0.021	0.0105
EDTA (Disodium Salt)	0.0035	0.00175
Na_2CO_3	0.070	0.035
Trace Metal Mix (below)	3.500	1.750

C- 2 Leach solution recipe

Chemical	Leach solution (g/L)
$MgSO_4 \cdot 7H_2O$	50.714
$CaCl_2$	1.315
$Na_2SiO_3 \cdot 9H2O$	0.506
$MnCl2 \cdot 4H2O$	0.072
KCl	5.720E-04
$ZnSO_4$	6.596E-05
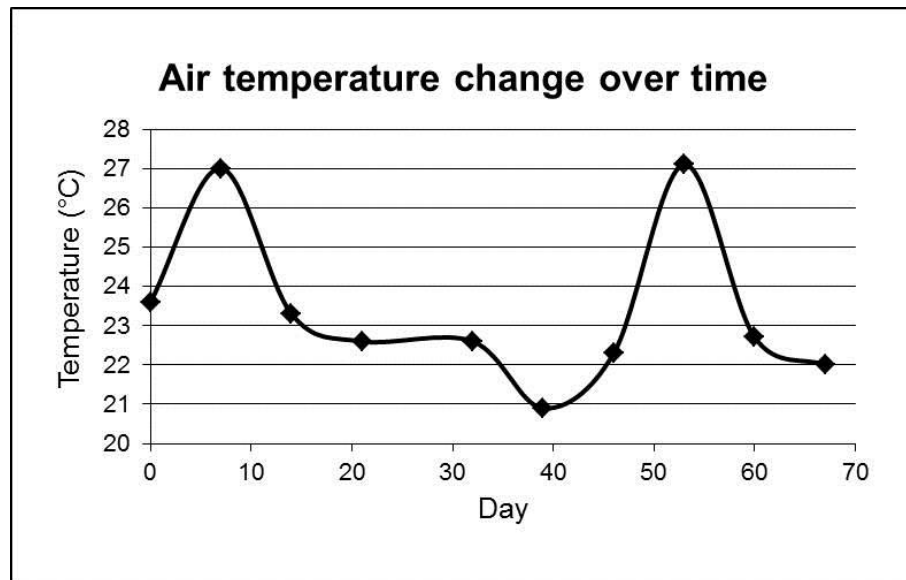
Figure C-1 Air temperature in the greenhouse at the time of sampling.

Appendix D: Additional SEM figures of the leached chrysotile fibres from Chapter 3
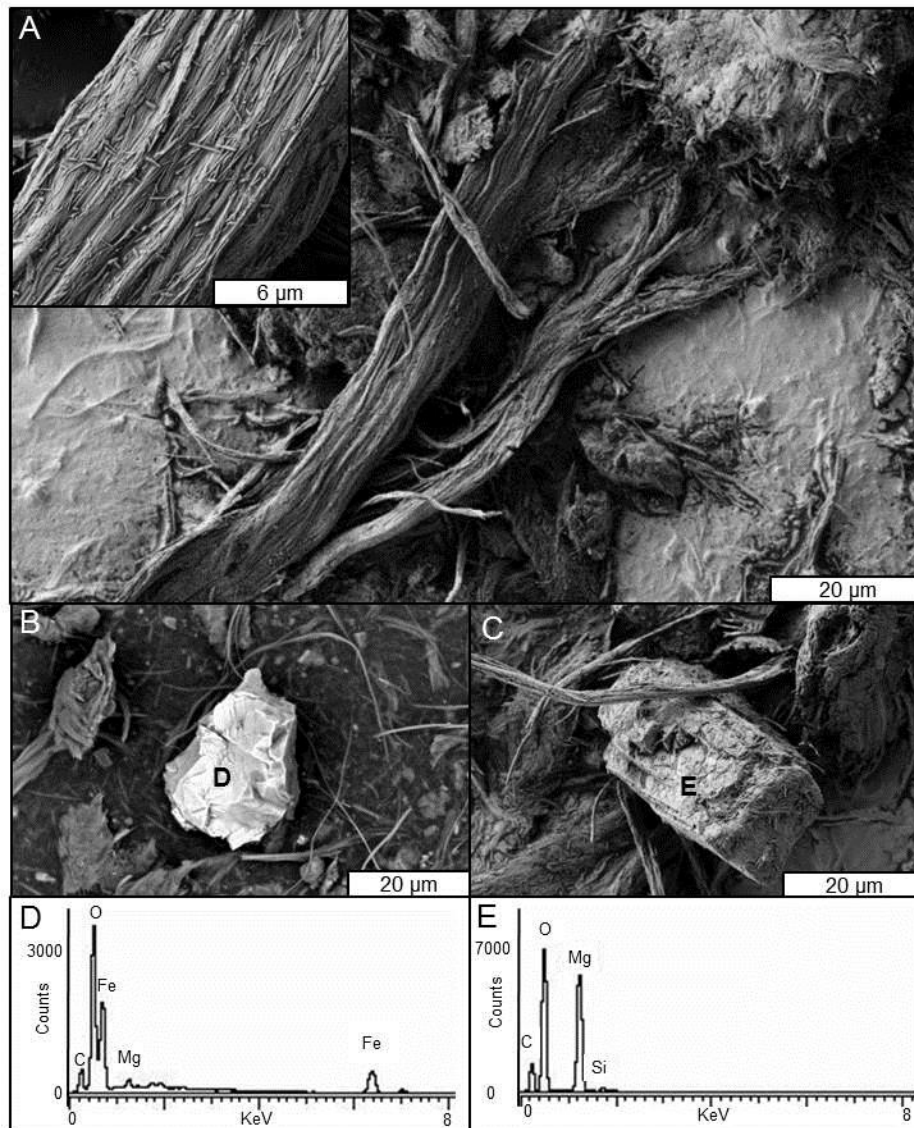
Figure D-1 A) Scanning electron microscopy of fibres from the control flask. Grains of B) magnetite and C) magnesite found in the fibres (corresponding EDS spectra in D and E, respectively).
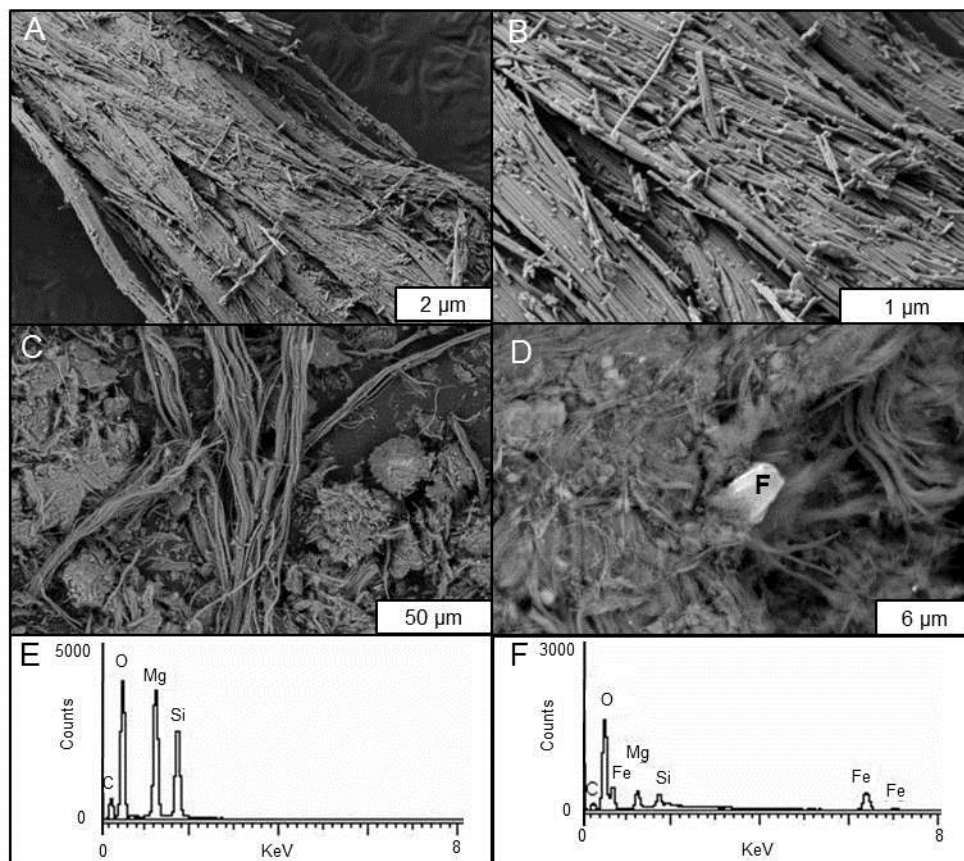
Figure D-2 A)-C) Scanning electron microscopy of fibres from flask 0.25. D) A magnetite grain in chyrostile. E) and F) EDS spectra for chrysotile fibres and magnetite, respectively.
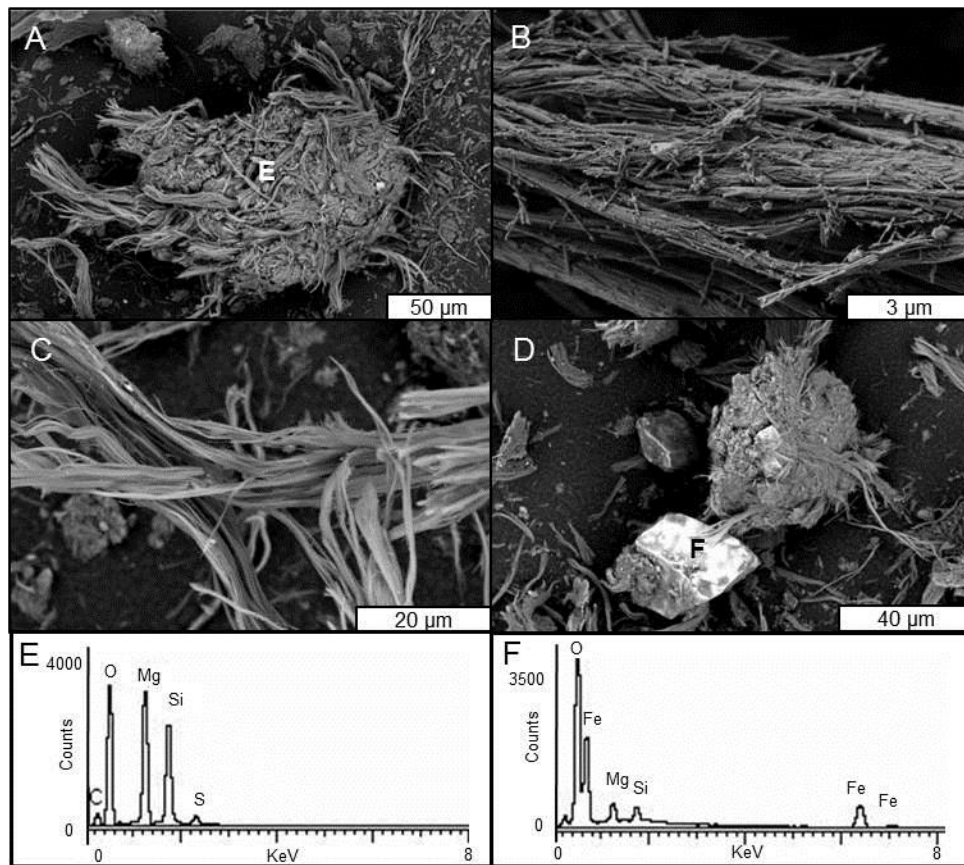
Figure D-3 A)-D) Scanning electron microscopy of chrysotile fibres in flask 0.5. E) EDS spectra corresponding to fibres in A. F) EDS spectra of the magnetite grain in D.
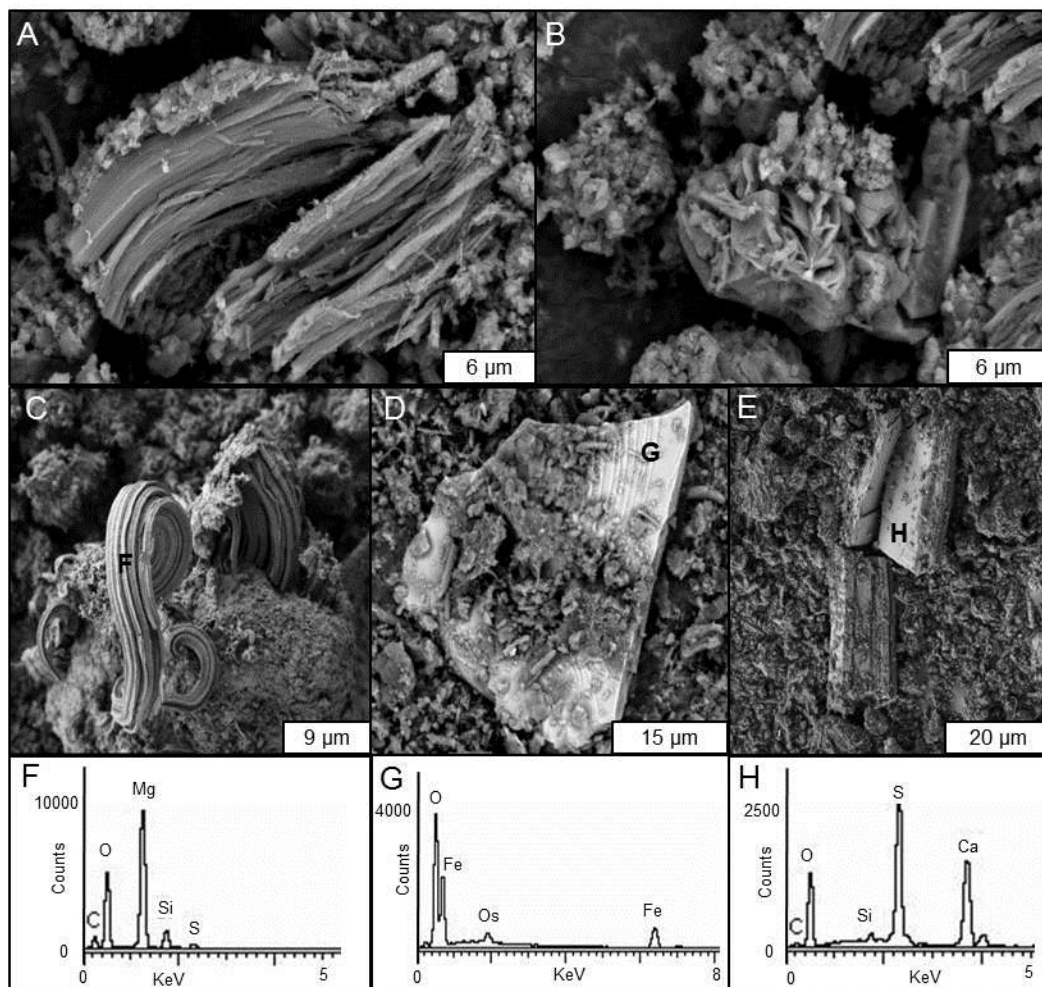
Figure D-4 A)-C) Scanning electron microscopy of chrysotile fibres showing chemical weathering sampled from flask 2 D) A large magnetite grain and E) calcium sulfate crystals found in the fibres. F)-H) EDS spectra corresponding to locations marked in C)-E), respec
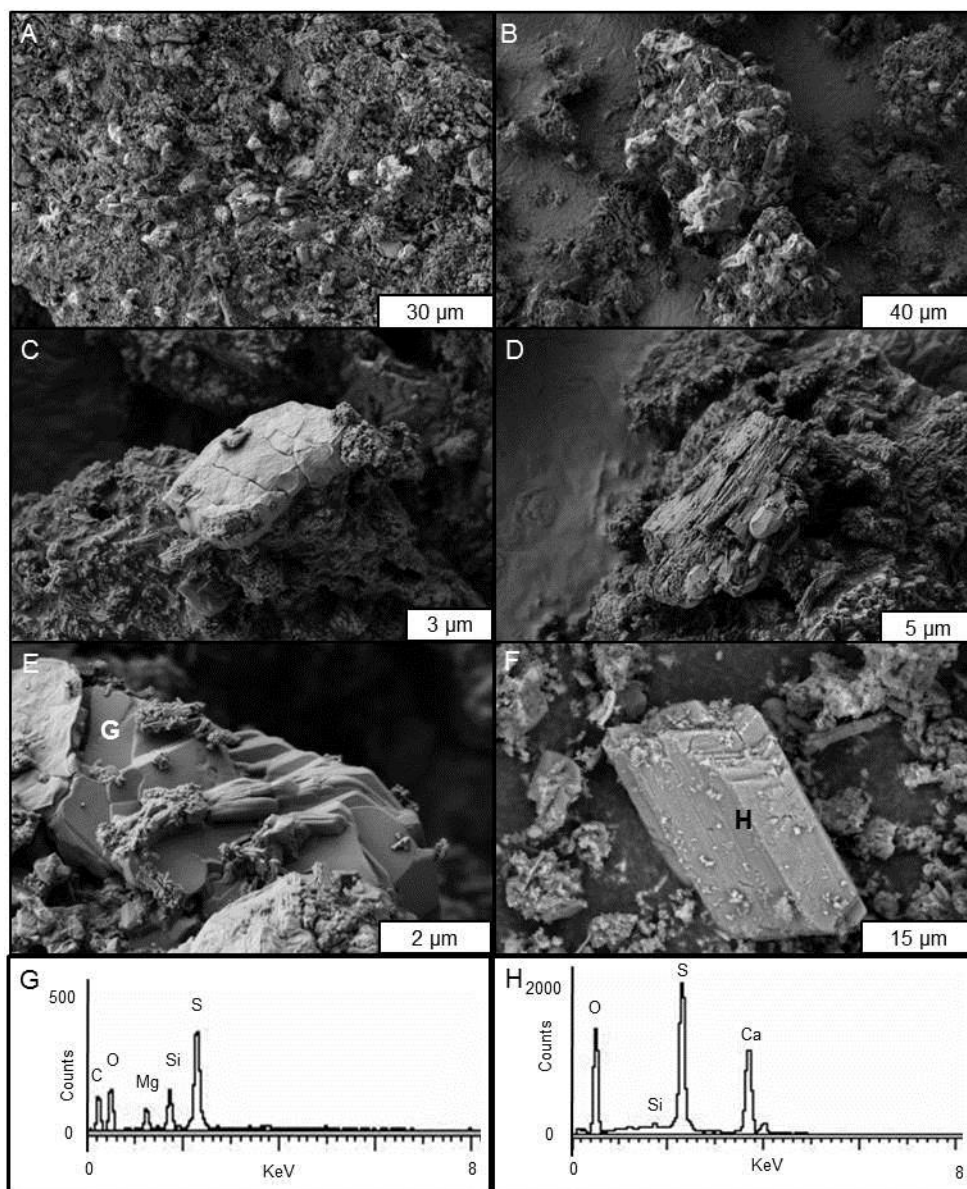
Figure D-5 A)-F) Scanning electron microscopy of the chemically weather chrysotile fibres in flask 3. Sulfate minerals can be seen as the brighter phase in all of the images, with EDS spectra for the sulfate grains in E) and F) shown in G) and H), respectively.

Appendix E: Saturation Indices as determined by PHREEQC

All solutions were run at 23.5°C.

E- 1 Inflow solution chemistry

Element	Inflow solution chemistry by IC and ICP-AES (mg/L)		
	Full strength BG-11	Half strength BG-11	Leach solution
Ca	31.200	13.713	327.000
Fe	0.868	0.805	24.329
K	155.267	85.350	4767.750
Mn	1.220	0.697	3.994
Na	1919.000	1054.000	51.700
Zn	0.097	0.067	6.058
Cl	90.817	32.600	863.472
N(5)	9309.000	1901.667	0.000
P	477.060	216.333	0.000
S(6)	5.982	1.380	25130.000
C(4)	2.410	2.410	2.580
pH	5.9	5.9	7.99
Charge balance error*	-77.14	-49.63	-33.57

* = 100*(Cation-|Anion|)/(Cation+|Anion|)

E- 2 Inflow SI values

Phase	Inflow solution saturation indices		
	Full strength BG-11	Half strength BG-11	Leach solution
aragonite	-5.07	-5.1	-1.6
calcite	-4.93	-4.96	-1.45
CO2(g)	-3.11	-3.11	-4.82
dolomite	ND	ND	-0.47
Hmg	ND	ND	-10.07
landsfordite	ND	ND	-3.19
magnesite	ND	ND	-0.65
nesquehonite	ND	ND	-3.68

ND: not determined

E- 3 Day 0 chemistry

	Sample location chemistry (mg/L) by IC and ICP-AES on (day 0)										
Element	0 m	1 m	2 m	3 m	4 m	5 m	6 m	7 m	8 m	9 m	10 m
Ca	2.91	2.95	2.62	2.42	2.35	2.28	2.30	2.26	2.17	2.21	2.13
K	52.80	56.40	57.80	59.70	63.70	65.00	72.30	75.40	77.50	76.60	77.50
Mg	62.50	64.80	64.20	62.80	62.50	60.70	64.20	64.20	63.60	63.80	63.20
Mn	0.01	0.01	0.01	0.01	0.01	0.01	0.01	0.01	0.01	0.01	0.01
Na	1660.00	1890.00	2040.00	2120.00	2330.00	2240.00	2320.00	2410.00	2410.00	2370.00	2100.00
Si	0.42	0.45	0.48	0.43	0.44	0.42	0.37	0.41	0.45	0.44	0.40
Cl	64.90	75.60	82.90	93.00	104.00	109.00	116.00	129.00	130.00	131.00	125.00
S(6)	4740.00	5520.00	5760.00	6060.00	6530.00	6550.00	6810.00	7140.00	7050.00	7050.00	6680.00
C(4)	301.46	355.10	365.79	371.85	383.13	407.08	413.98	433.84	439.13	445.32	448.55
pH	9.84	9.87	9.87	9.82	9.84	9.75	9.74	9.66	9.67	9.69	9.7
Charge balance error*	-17.28	-19.04	-17.55	-18.28	-17.46	-19.78	-19.86	-20.44	-19.86	-20.79	-24.11

* = 100*(Cation-|Anion|)/(Cation+|Anion|)

E- 4 Day 7 chemistry

	Sample location chemistry (mg/L) by IC and ICP-AES on (day 7)										
Element	0 m	1 m	2 m	3 m	4 m	5 m	6 m	7 m	8 m	9 m	10 m
Ca	15.80	8.87	7.58	6.17	6.04	5.78	3.28	2.46	1.89	1.73	1.83
K	71.40	64.90	64.70	67.70	70.30	76.70	63.30	62.30	55.70	60.30	62.50
Mg	321.00	202.00	169.00	121.00	117.00	96.60	78.00	68.40	58.40	59.30	56.50
Mn	0.06	0.05	0.06	0.07	0.07	0.07	0.02	0.00	0.00	0.00	0.00
Na	2256.00	2402.00	2480.00	2503.00	2467.00	2447.00	2485.00	2601.00	2618.00	2716.00	2600.00
Si	0.77	0.58	0.54	0.49	0.48	0.44	0.48	0.37	0.41	0.41	0.40
Zn	0.01	0.00	0.01	0.01	0.02	0.02	0.00	0.00	0.01	0.00	0.02
Cl	169.00	137.00	146.00	104.00	103.00	96.40	85.60	84.40	86.10	87.20	90.70
N(3)	23.09	26.00	31.63	35.12	35.50	37.84	34.60	2.71	0.00	0.00	0.00

Element											
N(5)	435.00	269.00	350.00	355.00	378.00	912.00	85.10	4.30	0.82	0.63	0.49
P	4.95	19.40	7.76	13.90	38.70	42.30	53.80	29.60	15.50	13.60	11.20
S(6)	3580.00	3140.00	3270.00	2620.00	2660.00	5090.00	2690.00	2660.00	2810.00	2800.00	3070.00
C(4)	312.95	336.54	335.79	335.88	339.89	337.62	387.01	407.66	398.48	389.42	391.27
pH	9.62	9.66	9.59	9.69	9.74	9.63	9.77	9.77	9.82	9.91	9.92
Charge balance error*	3.49	12.08	7.9	13.72	10.18	-25.68	20.39	29.37	27.98	29.97	23.88

* = 100*(Cation-|Anion|)/(Cation+|Anion|)

E- 5 Day 14 chemistry

Element	Sample location chemistry (mg/L) by IC and ICP-AES on (day 14)										
	0 m	1 m	2 m	3 m	4 m	5 m	6 m	7 m	8 m	9 m	10 m
Ca	18.60	15.80	12.90	9.58	8.67	8.07	3.93	0.82	2.04	1.84	1.69
K	95.20	89.10	90.60	80.10	95.50	86.40	70.80	37.90	64.10	64.70	61.50
Mg	409.00	382.00	326.00	282.00	230.00	235.00	170.00	140.00	86.30	72.80	66.10
Mn	0.07	0.06	0.05	0.05	0.05	0.07	0.00	0.00	0.00	0.00	0.00
Na	2417.00	2561.00	2581.00	2542.00	2492.00	2551.00	2642.00	2700.00	2831.00	2873.00	2960.00
Si	0.69	0.63	0.56	0.43	0.42	0.42	0.41	0.38	0.38	0.37	0.35
Zn	0.00	0.00	0.00	0.00	0.00	0.01	0.00	0.01	0.00	0.00	0.00
Cl	281.00	240.00	51.10	134.00	202.00	186.00	72.50	137.00	112.00	107.00	94.20
N(3)	25.60	22.90	5.87	14.00	24.40	22.50	7.99	14.90	3.19	0.00	0.00
N(5)	988.00	812.00	191.00	512.00	784.00	557.00	45.60	49.70	4.30	0.00	0.00
P	9.54	11.00	2.33	5.88	13.20	20.90	8.83	21.00	21.50	21.90	16.30
S(6)	5020.00	4820.00	1990.00	2920.00	4410.00	4480.00	2000.00	4200.00	3879.79	3700.00	3210.00
C(4)	310.16	331.77	334.99	329.55	336.36	350.40	411.58	422.01	401.55	448.51	451.24
pH	9.37	9.48	9.48	9.47	9.48	9.42	9.55	9.58	9.76	9.81	9.89
Charge balance error*	-17.77	-10.82	43.49	12.32	-13.01	-6.66	44.24	11.14	18	20.02	27.6

* = 100*(Cation-|Anion|)/(Cation+|Anion|)

E- 6 Day 21 chemistry

Element	Sample location chemistry (mg/L) by IC and ICP-AES on (day 21)										
	0 m	1 m	2 m	3 m	4 m	5 m	6 m	7 m	8 m	9 m	10 m
Ca	28.90	25.20	21.90	19.70	16.40	15.40	8.15	5.47	4.09	2.92	2.30
K	112.00	110.00	104.00	98.20	107.00	124.00	84.40	79.30	74.70	72.70	74.20
Mg	615.00	574.00	552.00	510.00	416.00	353.00	342.00	274.00	229.00	154.00	110.00
Mn	0.13	0.07	0.06	0.06	0.06	0.09	0.02	0.00	0.00	0.01	0.00
Na	2395.00	2559.00	2746.00	2612.00	2567.00	2458.00	2887.00	2870.00	2968.00	3058.00	3150.00
Si	0.67	0.60	0.46	0.45	0.41	0.30	0.41	0.40	0.40	0.37	0.32
Zn	0.01	0.00	0.00	0.00	0.00	0.02	0.00	0.00	0.00	0.00	0.00
Cl	322.00	304.00	302.00	301.00	279.00	241.00	210.00	179.00	163.00	142.00	131.00
N(3)	44.30	55.50	53.10	49.00	57.50	32.90	16.70	22.30	1.47	0.00	0.00
N(5)	1710.00	1230.00	676.00	925.00	1170.00	2020.00	81.00	46.70	1.54	0.00	0.00
P	10.90	9.18	9.39	14.50	14.80	31.90	14.40	14.90	14.10	15.00	17.60
S(6)	6270.00	6320.00	6330.00	5940.00	5390.00	4200.00	5410.00	5330.00	5170.00	4800.00	4130.00
C(4)	252.92	310.28	337.46	331.69	313.30	203.40	416.23	402.13	427.64	440.01	457.61
pH	9.26	9.35	9.37	9.33	9.30	8.90	9.46	9.47	9.50	9.66	9.76
Charge balance error*	-31.28	-23.26	-10.78	-16.82	-21.3	-30.99	8.49	7.99	11.76	14.27	20.98

* = 100*(Cation-|Anion|)/(Cation+|Anion|)

E- 7 Day 39 chemistry

Element	Sample location chemistry (mg/L) by IC and ICP-AES on (day 39)										
	0 m	1 m	2 m	3 m	4 m	5 m	6 m	7 m	8 m	9 m	10 m
Ca	372.00	36.60	33.40	30.40	30.00	21.30	13.20	9.55	5.67	4.78	4.11
K	81.00	82.30	77.60	81.50	80.30	81.60	79.30	83.70	87.80	87.80	80.70
Mg	767.00	768.00	743.00	745.00	793.00	618.00	480.00	387.00	271.00	231.00	201.00
Mn	0.11	0.12	0.09	0.06	0.05	0.03	0.02	0.02	0.02	0.01	0.02

Element											
Na	1912.00	2209.00	2281.00	2227.00	2203.00	2270.00	2872.00	2859.00	2723.00	3067.00	3387.00
Si	0.35	0.35	0.32	0.33	0.32	0.30	0.31	0.32	0.33	0.33	0.34
Zn	0.00	0.00	0.00	0.00	0.00	0.00	0.00	0.00	0.01	0.01	0.00
Cl	199.00	193.00	185.00	176.00	177.00	158.00	145.00	136.00	121.00	118.00	115.00
N(3)	0.81	1.41	2.12	3.03	3.65	3.01	2.18	2.31	1.39	0.33	0.00
N(5)	570.00	529.00	502.00	505.00	500.00	459.00	213.00	131.00	40.80	8.01	0.95
P	0.00	1.72	0.00	1.45	1.61	2.33	4.89	5.21	5.31	3.40	2.87
S(6)	4920.00	4840.00	4710.00	4470.00	4550.00	4080.00	3970.00	3840.00	3570.00	3530.00	3460.00
C(4)	160.47	173.49	186.64	186.07	188.09	244.39	287.31	309.71	351.77	364.28	160.47
pH	9.67	9.72	9.67	9.68	9.67	9.60	9.72	9.69	9.73	9.90	9.88
Charge balance error*	5.78	6.05	8.43	9.74	10.31	10.88	25.63	26.92	27.37	32.87	37.21

* = 100*(Cation-|Anion|)/(Cation+|Anion|)

E- 8 Day 46 chemistry

	Sample location chemistry (mg/L) by IC and ICP-AES on (day 46)										
Element	0 m	1 m	2 m	3 m	4 m	5 m	6 m	7 m	8 m	9 m	10 m
Ca	44.10	41.70	39.80	38.50	37.50	37.40	28.80	18.40	15.40	13.10	11.70
K	22.00	84.50	83.50	83.70	86.00	81.50	86.70	85.90	85.60	86.50	85.10
Mg	1099.00	1052.00	1025.00	1003.00	959.00	999.00	854.00	653.00	587.00	539.00	513.00
Mn	0.26	0.20	0.17	0.12	0.11	0.10	0.03	0.00	0.00	0.00	0.00
Na	1972.00	2145.00	1964.00	2077.00	1891.00	2501.00	2895.00	3186.00	3011.00	3469.00	3059.00
Si	0.35	0.34	0.32	0.31	0.31	0.30	0.28	0.24	0.23	0.24	0.24
Zn	0.00	0.00	0.00	0.00	0.00	0.00	0.00	0.00	0.00	0.00	0.00
Cl	226.00	228.00	216.00	216.00	215.00	213.00	200.00	188.00	175.00	173.00	171.00
N(3)	0.82	0.79	0.92	1.34	1.63	1.72	2.21	2.56	1.73	1.39	1.39
N(5)	651.00	615.00	608.00	603.00	593.00	618.00	438.00	298.00	221.00	187.00	167.00
P	1.63	1.16	1.57	1.64	1.73	1.79	5.17	2.56	1.38	0.82	0.54
S(6)	5760.00	5780.00	5590.00	5550.00	5540.00	5490.00	5220.00	5090.00	4870.00	4870.00	4840.00

	0 m	1 m	2 m	3 m	4 m	5 m	6 m	7 m	8 m	9 m	10 m
C(4)	138.84	151.35	152.96	155.25	147.10	150.54	217.80	250.94	248.13	251.45	255.27
pH	9.53	9.56	9.56	9.55	9.54	9.57	9.50	9.52	9.54	9.59	9.59
Charge balance error*	0.94	3.6	1.54	3.18	-1.06	9.74	18.08	21.5	22.04	27.73	2.51

* = 100*(Cation-|Anion|)/(Cation+|Anion|)

E- 9 Day 53 chemistry

	Sample location chemistry (mg/L) by IC and ICP-AES on (day 53)										
Element	0 m	1 m	2 m	3 m	4 m	5 m	6 m	7 m	8 m	9 m	10 m
Ca	76.30	72.70	72.20	65.70	63.90	62.80	55.20	49.10	31.40	29.30	28.10
K	22.50	95.70	93.40	92.40	93.50	88.50	90.40	88.60	92.80	96.10	88.50
Mg	1450.00	1426.00	1435.00	1362.00	1325.00	1334.00	1295.00	1190.00	1106.00	1038.00	1058.00
Mn	0.33	0.22	0.19	0.11	0.09	0.08	0.04	0.02	0.00	0.00	0.00
Na	2124.00	2447.00	2369.00	2466.00	2864.00	2393.00	2601.00	2777.00	2882.00	2803.00	3348.00
Si	0.67	0.52	0.48	0.34	0.31	0.27	0.23	0.19	0.15	0.13	0.13
Zn	0.00	0.00	0.00	0.00	0.00	0.00	0.00	0.00	0.00	0.00	0.00
Cl	300.00	299.00	295.00	286.00	288.00	280.00	274.00	270.00	249.00	251.00	255.00
N(3)	1.15	1.29	1.26	1.73	1.73	2.12	2.96	3.53	1.97	1.29	1.22
N(5)	845.00	806.00	791.00	738.00	738.00	703.00	636.00	627.00	517.00	510.00	507.00
P	2.72	1.99	2.00	1.72	1.58	2.20	4.52	3.67	1.76	0.00	0.00
S(6)	8120.00	8060.00	7950.00	7700.00	7720.00	7590.00	7360.00	7430.00	6820.00	6920.00	6980.00
C(4)	111.40	109.85	110.46	119.51	119.62	141.75	130.43	128.37	143.95	144.49	149.08
pH	9.50	9.52	9.53	9.55	9.57	9.43	9.52	9.61	9.51	9.57	9.49
Charge balance error*	-8.02	-2.2	-2.02	0.14	4.3	-0.26	4.7	3.57	10.23	6.77	13.81

* = 100*(Cation-|Anion|)/(Cation+|Anion|)

E- 10 Day 60 chemistry

Element	Sample location chemistry (mg/L) by IC and ICP-AES on (day 60)										
	0 m	1 m	2 m	3 m	4 m	5 m	6 m	7 m	8 m	9 m	10 m
Ca	117.00	112.00	102.00	92.90	93.00	89.30	87.90	85.90	69.40	62.50	58.90
K	98.50	98.00	95.40	97.10	95.60	95.00	96.60	95.30	91.40	99.60	98.70
Mg	1913.00	1871.00	1786.00	1694.00	1703.00	1713.00	1704.00	1640.00	1545.00	1487.00	1476.00
Mn	0.18	0.13	0.10	0.06	0.05	0.03	0.02	0.00	0.03	0.02	0.02
Na	1885.00	1940.00	2005.00	2078.00	2104.00	2409.00	2030.00	2315.00	2354.00	2367.00	2202.00
Si	1.21	1.00	0.75	0.44	0.41	0.28	0.25	0.21	0.12	0.07	0.07
Zn	0.00	0.00	0.00	0.00	0.00	0.00	0.00	0.00	0.00	0.00	0.00
Cl	356.00	367.00	355.00	347.00	346.00	341.00	328.00	335.00	323.00	324.00	319.00
N(3)	1.19	1.37	1.49	1.99	2.25	3.01	4.02	5.03	4.39	3.51	2.86
N(5)	1344.00	1287.00	1208.00	1146.00	1165.00	1086.00	1035.00	1016.00	946.00	887.00	862.00
P	3.00	2.23	2.10	1.51	2.33	3.96	3.98	3.52	2.41	1.22	0.84
S(6)	9600.00	9670.00	9600.00	9450.00	9460.00	9260.00	8990.00	9170.00	8880.00	4480.00	8820.00
C(4)	61.82	62.92	70.13	79.21	75.34	93.30	84.97	88.71	100.00	71.63	105.96
pH	9.40	9.48	9.58	9.60	9.61	9.47	9.66	9.71	9.66	9.68	9.63
Charge balance error*	-8.02	-16.11	-15.71	-15.17	-14.97	-8.35	-11.19	-9.61	-8.64	20.87	-10.61

* = 100*(Cation-|Anion|)/(Cation+|Anion|)

E- 11 Day 67 chemistry

Element	Sample location chemistry (mg/L) by IC and ICP-AES on (day 67)										
	0 m	1 m	2 m	3 m	4 m	5 m	6 m	7 m	8 m	9 m	10 m
Ca	170.00	162.00	142.00	136.00	128.00	124.00	107.00	102.00	93.20	86.90	81.10
K	80.00	84.30	97.40	97.60	98.40	97.20	101.00	97.90	103.00	106.00	104.00
Mg	2318.00	2286.00	2179.00	2161.00	2108.00	2061.00	1964.00	1931.00	1872.00	1850.00	1817.00
Mn	0.25	0.15	0.06	0.03	0.03	0.02	0.02	0.02	0.02	0.02	0.02
Na	1468.00	1631.00	1965.00	2017.00	2018.00	1980.00	2618.00	2513.00	2539.00	2858.00	2686.00

	1	2	3	4	5	6	7	8	9	10	11
Si	1.18	0.82	0.36	0.20	0.15	0.14	0.08	0.08	0.06	0.00	0.05
Zn	0.00	0.00	0.00	0.00	0.00	0.01	0.00	0.00	0.00	0.00	0.00
Cl	423.00	424.00	419.00	411.00	410.00	407.00	396.00	386.00	386.00	380.00	373.00
N(3)	1.68	2.05	2.79	3.34	3.63	3.74	6.32	6.23	6.31	6.09	5.69
N(5)	1192.00	1235.00	1368.00	1402.00	1400.00	1394.00	1335.00	1261.00	1250.00	1196.00	1164.00
P	7.29	4.61	3.59	2.25	2.36	3.06	1.83	1.49	0.69	0.29	0.24
S(6)	11640.00	11590.00	11490.00	11260.00	11120.00	11030.00	10870.00	10480.00	10720.00	10570.00	10370.00
C(4)	29.01	31.03	36.17	45.75	45.34	48.96	54.25	62.56	69.09	71.04	72.28
pH	9.12	9.30	9.53	9.70	9.70	9.62	9.87	9.78	9.68	9.75	9.70
Charge balance error*	-20.43	-19.35	-18.92	-18.13	-18.67	-19.74	-12.45	-11.45	-13.46	-8.59	-9.85

* = 100*(Cation-|Anion|)/(Cation+|Anion|)

E- 12 Aragonite SI values

Day	Saturation index by sample location										
	0 m	1 m	2 m	3 m	4 m	5 m	6 m	7 m	8 m	9 m	10 m
0	0.24	0.28	0.23	0.17	0.16	0.13	0.12	0.08	0.08	0.1	0.1
7	0.83	0.66	0.56	0.55	0.52	0.33	0.27	0.22	0.15	0.14	0.17
14	0.67	0.71	0.76	0.57	0.49	0.44	0.39	-0.36	0.11	0.12	0.14
21	0.63	0.73	0.74	0.67	0.56	0.05	0.51	0.34	0.27	0.23	0.2
39	1.75	0.88	0.86	0.82	0.81	0.78	0.72	0.63	0.5	0.51	0.46
46	0.71	0.75	0.74	0.73	0.7	0.71	0.75	0.66	0.61	0.57	0.54
53	0.76	0.74	0.75	0.76	0.76	0.77	0.73	0.72	0.56	0.56	0.51
60	0.56	0.59	0.65	0.68	0.66	0.68	0.72	0.75	0.71	0.55	0.67
67	0.21	0.32	0.43	0.57	0.54	0.55	0.61	0.63	0.62	0.62	0.59

E- 13 Calcite SI values

Day	Saturation index by sample location										
	0 m	1 m	2 m	3 m	4 m	5 m	6 m	7 m	8 m	9 m	10 m
0	0.38	0.42	0.37	0.31	0.3	0.27	0.27	0.23	0.22	0.24	0.25
7	0.98	0.8	0.71	0.69	0.67	0.48	0.42	0.37	0.29	0.29	0.31
14	0.82	0.85	0.9	0.72	0.63	0.58	0.54	-0.22	0.25	0.27	0.29
21	0.78	0.88	0.89	0.81	0.7	0.19	0.66	0.49	0.41	0.37	0.34
39	1.89	1.02	1	0.97	0.95	0.93	0.87	0.77	0.65	0.66	0.6
46	0.86	0.89	0.89	0.88	0.85	0.85	0.89	0.8	0.76	0.72	0.69
53	0.9	0.89	0.89	0.91	0.9	0.91	0.87	0.86	0.7	0.71	0.66
60	0.71	0.74	0.8	0.83	0.81	0.83	0.86	0.89	0.85	0.7	0.81
67	0.36	0.46	0.57	0.71	0.69	0.69	0.75	0.78	0.76	0.77	0.74

E- 14 $CO_2(g)$ SI values

Day	Saturation index by sample location										
	0 m	1 m	2 m	3 m	4 m	5 m	6 m	7 m	8 m	9 m	10 m
0	-4.72	-4.7	-4.7	-4.62	-4.64	-4.49	-4.47	-4.34	-4.35	-4.37	-4.37
7	-4.5	-4.49	-4.38	-4.5	-4.56	-4.42	-4.52	-4.5	-4.58	-4.72	-4.73
14	-4.19	-4.3	-4.3	-4.27	-4.26	-4.16	-4.24	-4.26	-4.51	-4.53	-4.64
21	-4.17	-4.19	-4.18	-4.12	-4.1	-3.8	-4.16	-4.17	-4.18	-4.36	-4.47
39	-5.09	-5.04	-4.92	-4.94	-4.93	-4.67	-4.74	-4.63	-4.59	-4.83	-4.77
46	-4.9	-4.9	-4.89	-4.87	-4.86	-4.92	-4.62	-4.55	-4.57	-4.63	-4.61
53	-4.99	-5.03	-5.04	-5.03	-5.06	-4.77	-4.94	-5.07	-4.85	-4.92	-4.8
60	-5.15	-5.26	-5.36	-5.32	-5.36	-5.05	-5.4	-5.45	-5.3	-5.56	-5.21
67	-5.08	-5.32	-5.6	-5.78	-5.78	-5.6	-5.98	-5.76	-5.53	-5.64	-5.54

E- 15 Dolomite SI values

Day	Saturation index by sample location										
	0 m	1 m	2 m	3 m	4 m	5 m	6 m	7 m	8 m	9 m	10 m
0	3.44	3.54	3.49	3.39	3.38	3.31	3.33	3.25	3.25	3.29	3.31
7	4.64	4.35	4.14	4.07	4.01	3.54	3.58	3.56	3.47	3.51	3.51
14	4.35	4.47	4.61	4.3	4.06	3.99	4.11	3.16	3.5	3.51	3.57
21	4.27	4.49	4.53	4.4	4.18	3.15	4.28	4.02	3.92	3.83	3.75
39	5.46	4.73	4.72	4.7	4.7	4.69	4.67	4.53	4.36	4.4	4.3
46	4.47	4.54	4.54	4.53	4.46	4.5	4.62	4.52	4.45	4.41	4.37
53	4.43	4.41	4.43	4.48	4.47	4.5	4.46	4.46	4.3	4.31	4.24
60	3.99	4.05	4.19	4.27	4.23	4.29	4.36	4.41	4.4	4.18	4.37
67	3.19	3.42	3.68	3.98	3.95	3.96	4.12	4.19	4.18	4.21	4.18

E- 16 Hydromagnesite SI values

Day	Saturation index by sample location										
	0 m	1 m	2 m	3 m	4 m	5 m	6 m	7 m	8 m	9 m	10 m
0	0.24	0.51	0.49	0.21	0.24	-0.1	-0.04	-0.36	-0.3	-0.19	-0.1
7	3.03	2.4	1.77	1.61	1.46	-0.08	0.51	0.68	0.67	1.04	0.94
14	2.06	2.56	3.06	2.38	1.61	1.39	2.34	1.33	0.97	0.96	1.25
21	1.81	2.43	2.58	2.26	1.7	-1.22	2.5	2.03	1.92	1.86	1.7
39	3.14	3.78	3.7	3.78	3.85	3.69	3.97	3.6	3.33	3.72	3.45
46	3.17	3.36	3.36	3.32	3.11	3.34	3.46	3.31	3.23	3.29	3.23
53	2.83	2.86	2.93	3.09	3.11	2.9	3.08	3.24	3.03	3.14	2.91
60	1.75	2.03	2.51	2.72	2.67	2.57	3.1	3.26	3.25	3.15	3.18
67	-0.56	0.28	1.34	2.31	2.27	2.12	3.02	3.01	2.8	3.07	2.94

E- 17 Landsfordite SI values

Day	Saturation index by sample location										
	0 m	1 m	2 m	3 m	4 m	5 m	6 m	7 m	8 m	9 m	10 m
0	-1.1	-1.05	-1.05	-1.09	-1.09	-1.13	-1.11	-1.15	-1.14	-1.12	-1.1
7	-0.5	-0.62	-0.73	-0.79	-0.83	-1.11	-1.01	-0.99	-0.97	-0.94	-0.97
14	-0.64	-0.56	-0.46	-0.59	-0.74	-0.76	-0.59	-0.79	-0.92	-0.92	-0.89
21	-0.68	-0.56	-0.53	-0.58	-0.69	-1.22	-0.54	-0.64	-0.66	-0.71	-0.76
39	-0.6	-0.46	-0.45	-0.44	-0.43	-0.41	-0.36	-0.42	-0.46	-0.43	-0.47
46	-0.56	-0.52	-0.52	-0.52	-0.56	-0.53	-0.44	-0.46	-0.48	-0.48	-0.48
53	-0.64	-0.64	-0.63	-0.6	-0.6	-0.58	-0.58	-0.58	-0.58	-0.57	-0.59
60	-0.89	-0.86	-0.78	-0.73	-0.75	-0.71	-0.67	-0.65	-0.62	-0.69	-0.62
67	-1.34	-1.22	-1.07	-0.91	-0.92	-0.91	-0.81	-0.76	-0.76	-0.73	-0.73

E- 18 Magnesite SI values

Day	Saturation index by sample location										
	0 m	1 m	2 m	3 m	4 m	5 m	6 m	7 m	8 m	9 m	10 m
0	1.43	1.49	1.48	1.44	1.45	1.41	1.42	1.39	1.4	1.41	1.43
7	2.03	1.91	1.8	1.75	1.71	1.43	1.52	1.56	1.54	1.59	1.57
14	1.9	1.98	2.08	1.95	1.8	1.77	1.95	1.74	1.62	1.61	1.65
21	1.86	1.97	2.01	1.95	1.85	1.32	1.99	1.9	1.87	1.83	1.77
39	1.94	2.07	2.08	2.09	2.11	2.13	2.17	2.12	2.07	2.1	2.06
46	1.98	2.02	2.02	2.02	1.98	2.01	2.09	2.08	2.06	2.06	2.05
53	1.89	1.89	1.9	1.94	1.94	1.95	1.96	1.96	1.96	1.97	1.95
60	1.65	1.68	1.76	1.81	1.79	1.83	1.87	1.89	1.92	1.85	1.92
67	1.2	1.32	1.47	1.63	1.63	1.63	1.74	1.78	1.78	1.81	1.81

E- 19 Nesquehonite SI values

Day	Saturation index by sample location										
	0 m	1 m	2 m	3 m	4 m	5 m	6 m	7 m	8 m	9 m	10 m
0	-1.59	-1.53	-1.54	-1.58	-1.58	-1.61	-1.6	-1.64	-1.63	-1.61	-1.59
7	-0.99	-1.11	-1.22	-1.27	-1.32	-1.6	-1.5	-1.46	-1.48	-1.43	-1.45
14	-1.12	-1.04	-0.94	-1.07	-1.23	-1.25	-1.08	-1.28	-1.4	-1.41	-1.37
21	-1.17	-1.05	-1.02	-1.07	-1.18	-1.7	-1.03	-1.12	-1.15	-1.2	-1.25
39	-1.09	-0.95	-0.94	-0.93	-0.91	-0.89	-0.85	-0.9	-0.95	-0.92	-0.96
46	-1.04	-1.01	-1	-1.01	-1.05	-1.01	-0.93	-0.94	-0.96	-0.96	-0.97
53	-1.13	-1.13	-1.12	-1.09	-1.09	-1.07	-1.07	-1.06	-1.06	-1.05	-1.08
60	-1.38	-1.34	-1.27	-1.22	-1.24	-1.19	-1.16	-1.14	-1.11	-1.18	-1.1
67	-1.83	-1.7	-1.55	-1.39	-1.4	-1.39	-1.29	-1.25	-1.24	-1.21	-1.22

Appendix F: Carbon storage calculation

$$\text{Total phosphate decrease} = [PO_4^{2-}] \text{ BG-11} - [PO_4^{2-}] \text{at 10 m on day 67} \qquad (1)$$
$$2.327 \text{ mM} - 0.0017 \text{ mM} = 2.325 \text{ mM}$$

$$\textit{If half of the phosphate is used in struvite, then:} \qquad (2)$$
$$2.325 \div 2 = 1.163 \text{ mM } [Mg^{2+}] \text{ lost to struvite precipitation}$$

$$[Mg^{2+}] \text{ in leach solution} - [Mg^{2+}] \text{ in struvite} - [Mg^{2+}] \text{ at 10 m} = [Mg^{2+}] \text{ used} \qquad (3)$$
$$\textit{for carbonate precipitation:}$$
$$197.203 \text{ mM} - 1.163 \text{ mM} - 51.655 \text{ mM} = 144.385 \text{ mM}$$

$$\textit{Leach solution added at 5 L/day for 7 days:} \qquad (3)$$
$$144.385 \text{ mM} = 0.144385 \text{ mol/L} \times 35 \text{ L} = 5.053 \text{ mol of Mg consumed}$$

$$\text{Mass of Mg} = n_{Mg} \times \textit{molar mass of Mg:} \qquad (4)$$
$$5.053 \text{ mol} \times 24.31 \text{ g/mol} = 122.850 \text{ g of Mg}$$

$$[Mg^{2+}] \times \textit{volume} = \textit{mass of Mg removed from solution} \qquad (5)$$
$$684.1 \text{ mg/L} \times 35.00 \text{ L} = 23944 \text{ mg} = 23.94 \text{ g}$$

$$\textit{Mass Mg / molar mass Mg} = \textit{moles Mg removed from solution} \qquad (6)$$
$$23.94 \text{ g} \div 24.305 \text{ g/mol} = 0.9850 \text{ mol of Mg}$$

$$\textit{5 Mg atoms needed per crystal of hydromagnesite produced:} \qquad (7)$$
$$\text{Moles Mg} \div 5 = \text{moles hydromagnesite produce} = 0.9850 \text{ mol} \div 5 = 0.1970$$
$$\text{mol}$$

$$\textit{Two possible magnesium carbonate mineral products:} \qquad (8)$$
$$\text{Hydromagnesite} \qquad\qquad\qquad \text{Magnesite}$$

$$\textit{Magnesium used per unit of mineral made:} \qquad (9)$$
Mg:mineral 1:5, 1.011 mol of   Mg:mineral 1:1, 5.053 mol of
hydromagnesite made   magnesite made

$$\textit{Mass of mineral made} = \textit{mol} \times \textit{molar mass of mineral} \qquad (10)$$
$$1.011 \times 467.5 \text{ g/mol} = 472.500 \text{ g} \qquad 5.053 \times 84.31 \text{ g/mol} = 426.058 \text{ g}$$

$$\textit{Moles of CO}_2 \textit{ consumed:} \qquad (11)$$
$$1.011 \text{ mol} \times 14 = 14.150 \text{ mol} \qquad\qquad 5.053 \text{ mol} \times 3 = 15.160 \text{ mol}$$

$$\textit{Mass of CO}_2 \textit{ consumed} = \textit{moles} \times \textit{molar mass of CO}_2 \qquad (12)$$
$$14.150 \text{ mol} \times 44.0 \text{ g/mol} = 622.588 \text{ g} \qquad 15.160 \text{ mol} \times 44.0 \text{ g/mol} = 667.058 \text{ g}$$

$$\textit{CO}_2 \textit{ consumption per unit area} = \textit{mass} \div \textit{mat surface area} \qquad (13)$$
$$622.588 \text{ g} \div 1.46 \text{ m}^2 = 426.430 \text{ g of} \qquad 667.058 \text{ g} \div 1.46 \text{ m}^2 = 456.899 \text{ g of}$$

CO_2 consumed /m^2 of mat CO_2 consumed /m^2 of mat

Annual CO_2 consumption rate per unit area: (14)

426.430 g/m^2 × (365/7) = 22235.279   456.899 g/m^2 × (365/7) = 23823.513
g of CO_2 consumed /m^2 of mat/year =   g of CO_2 consumed /m^2 of mat/year =
22235.279 t of CO_2 consumed /km^2 23823.513 t of CO_2 consumed /km^2
of mat/year   of mat/year

In hectares/year: (15)

22235.279 t of CO_2/km^2/year ÷ 100 =   23823.513 t of CO_2/km^2/year ÷ 100 =
222.353 t of CO_2/ha/year   238.235 t of CO_2/ha/year

The mass of carbon sequestered based on the molar mass of CO_2 and carbon: (16)

222.353 t of CO_2/ha/year × (12.01   238.235 t of CO_2/ha/year × (12.01
g/mol ÷ 44.01 g/mol) = 60.642 t of   g/mol ÷ 44.01 g/mol) = 64.973 t of
C/ha/year   C/ha/year

Curriculum Vitae

Name: Jenine McCutcheon

Post-secondary Education:

2011 - 2013 M.Sc. Geology, The University of Western Ontario London, Ontario, Canada

2007 - 2011 B.Sc. Honours Specialization Geology and Biology, The University of Western Ontario London, Ontario, Canada

Select Awards:

2013 NSERC Alexander Graham Bell Canadian Graduate Scholarship (Ph.D.)

2013 Female Student-Athlete Community Service Award, Ontario University Athletics

2012 - 2013 NSERC Alexander Graham Bell Canadian Graduate Scholarship (M.Sc.)

2011 - 2012 J.P. Bickell Ontario Graduate Scholarship

2011 Western Gold Medal, The University of Western Ontario

2010 - 2011 J.P. Bickell Foundation Mining Scholarship

Related Work Experience:

2013 Teaching Assistant, ES 1022B (Earth Rocks), The University of Western Ontario

2011 Teaching Assistant, ES 2265A (Paleobiology and Paleoecology), The University of Western Ontario

2011 Geomicrobiology Research Assistant, Department of Earth Sciences, The University of Western Ontario, Supervisor: Dr. G. Southam

2010 NSERC Undergraduate Student Research Award (USRA), Supervisor: Dr. G. Osinski, The University of Western Ontario (Impact crater geology)

2009 NSERC USRA, Supervisor: Dr. C. Tsujita, The University of Western Ontario (Invertebrate Paleontology and Paleobiogeography)

Publications:

Power, I.M., Wilson, S., Harrison, A., Dipple, G., **McCutcheon, J.**, Southam, G., and Kenward, P. 2013. A depositional model for hydromagnesite-magnesite playa. Sedimentology, (Under review: SED-2013-OM-062).

Osinski, G.R., Tornabene, L., Banerjee, N., Cockell, C., Flemming, R., Izawa, M., **McCutcheon J.**, Parnell, J., Preston, L., Pickersgill, A., Pontefract, A., Sapers, H., and Southam, G. 2013. Impact-generated hydrothermal systems on Earth and Mars. Icaarus, 224 (2): 347-363.

McCutcheon, J., Power, I.M., Small, D., Harrison, A.L., Pirani, A., Dipple, G., and Southam, G. (2012) Microbially-accelerated carbon mineralization: Applications to carbon sequestration in mine waste. Carbon Management Canada Conference, Gatineau, Canada, May 22-25.

McCutcheon, J., Power, I.M., Harrison, A., Small, D., Pirani, A., Dipple, G., and Southam, G. (2012) Microbially-accelerated carbon sequestration: magnesium carbonate mineralization in mine waste. 22nd V.M. Goldschmidt Conference, Montréal, Canada, June 24-29.

Dipple, G., Southam, G., Mayer, U., Hitch, M., Power, I.M., Bea, S., Harrison, A.L., and **McCutcheon, J.** (2012) Carbon Mineralization in Mine Waste. Carbon Management Canada Conference, Gatineau, Canada, May 22-25.

Power, I.M., Southam, G., Wilson, S.A., Dipple, G.M., **McCutcheon, J.**, and Harrison, A.L. (2012) Microbially mediated mineral carbonation: Implications for CO_2 sequestration in mine wastes. Canadian Society of Microbiologists, 62nd Annual Meeting, Vancouver, Canada, June 20-23.